Nickel Based Nanoalloys as Reduction Electrocatalysts for Solar Fuel Production

Natalie Estelle Pridmore

Doctor of Philosophy

University of York

Chemistry

September 2015

Abstract

In order to optimise the efficiency of solar fuel devices, development of cheap, active and stable reduction electrocatalysts for solar fuel production is crucial. To this end, ligand stabilised nickel nanoalloys of around 10 nm with relatively small size distributions, have been synthesised for a variety of compositions utilising first row transition metals (Cr, Fe, Co and Cu). Bi- and trimetallic nanoalloys have been synthesised and good control over composition was demonstrated. Synthesised nanoalloys were electrochemically tested to assess their proton and CO_2 reduction activities. All nanoalloys showed higher hydrogen evolution reaction (HER) activity than pure nickel. For bimetallic nanoalloys, in pH 1, a general increase in HER activity with increased electron negativity was observed. The $Ni_{0.5}Cu_{0.3}Co_{0.2}$ nanoalloy showed the highest HER activity at pH 1, whereas the $Ni_{0.5}Co_{0.3}Fe_{0.2}$ nanoalloy was most active for HER in pH 13. Little difference between the activities for all nanoalloys was observed at pH 7. The nanoalloys showed differing selectivity's for CO_2 reduction products. Solution based CO_2 reduction products were detected at low overpotentials (below -0.789 V vs RHE, pH 6.8), although low faradaic efficiencies (< 1%) were observed.

High resolution scanning electron microscopy (HR-SEM) was used to attempt to analyse the nanoalloys after deposition onto the electrodes and after electrochemical testing. The results indicated the presence of sub-monolayer coverage, therefore increasing the nanoalloy coverage without large amounts of agglomeration occurring could result in the observation of higher current densities at lower overpotentials. The stability of the nanoalloy electrodes was also investigated and no decrease in HER activity was observed over 12 hours at -0.5 V vs RHE. Moreover, repeated cycling resulted in an increase in activity being observed. This may be due to leaching of elements overtime.

A procedure has been developed using a range of techniques to analyse nanoalloy composition, test proton and CO_2 reduction activities and assess stability. This has not only allowed for direct comparison between different materials studied, it also provides a framework for future investigations of nanoalloys for (photo)electrochemical proton and CO_2 reduction.

Table of Contents

Table of Figures

Table of Tables

Acknowledgements

Declaration

The research presented in this thesis was carried out at the University of York between October 2011 and August 2015. This work is, to the best of my knowledge, original and my own, except for the following:

- Electron diffraction and some EDX measurements were taken by Dr Robert Mitchell (JEOL Nanocentre)

- Elemental Analyses were performed by Dr Graeme McAllister

- HR-SEM was performed by (LENFF, Leeds)

- NMR measurements were run by Mr Ben Coulson (PhD student)

- H_2 GC calibration was carried out by Miss Danielle Jowett (PhD student)

- Mass spectroscopy was carried out by Mr Karl Heaton.

This thesis has not been submitted for any other degree at this or any other University.

1   Introduction

1.1   The Energy Crisis

Due to environmental considerations, including the rising levels of CO_2 and the depleting reserves of fossil fuels, the development of clean energy technologies is necessary.[1] Unlike fossil fuels, solar energy is a decentralized and limitless, renewable resource. The available solar power striking the earth's surface at any one instant is equal to 130 million, 500 MW power plants[1] and more energy from sunlight strikes the Earth's surface in one hour (4.3 × 10^{20} J) than the total energy consumption of the whole planet in a year (4.1 × 10^{20} J).[2] One of the main problems with solar energy is storing the energy for later use (such as at night or when it is cloudy), this can be overcome by converting the solar energy into chemical fuels. In this case the energy is stored in the chemical bonds allowing for storage, distribution and use when required.

Solar fuels are particularly attractive as they can be created using abundant precursors, such as water or carbon dioxide. Examples of solar fuels include hydrogen, carbon monoxide and methanol all of which are important industrial feedstocks and in the case of hydrogen and methanol, possible transport fuels.

1.2   Solar Fuel Production

Fuels, such as hydrogen, can be produced electrochemically; the full cell reaction for hydrogen production via water splitting is shown in equation 1-1 and the half-cell reactions can be seen in equations 1-2 and 1-3.

$$2H_2O \longrightarrow 2H_2 + O_2 \qquad \Delta G_0 = +237\ kJ\ mol^{-1} \qquad \text{Equation 1-1}$$

$$4H^+ + 4e^- \longrightarrow 2H_2 \qquad\qquad\qquad 0.00\ V \qquad \text{Equation 1-2}$$

$$2H_2O \longrightarrow O_2 + 4H^+ + 4e^- \qquad +1.23\ V \qquad \text{Equation 1-3}$$
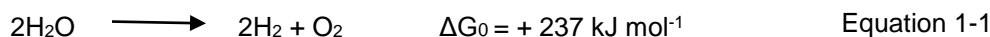
To make this a sustainable process, the electricity used can be provided by a renewable source or alternatively a method of harvesting the light can be incorporated into the electrochemical cell. These photoelectrochemical cells commonly use semiconductors to

harvest the incident photons and may also employ these semiconductors as the catalysts for the redox reactions.

1.2.1 Photocatalytic Semiconductors

One method of producing solar fuels is to use photocatalytic semiconductors, such as TiO_2 to mediate conversion of the solar energy into chemical potential energy.[1] Photocatalytic semiconductors have an electronic band structure consisting of a conduction band and a valence band separated by an energy difference known as a band gap. When the semiconductor is irradiated with light of energy greater than or equal to that of the band gap, an electron will be excited from the valence band into the conduction band, leaving a positive hole in the valence band. These electron/hole pairs may recombine or they could facilitate redox reactions at the surface of the semiconductor.[1]

For example, as the free energy change for conversion of one water molecule to H_2 and ½ O_2 is 237 kJ mol^{-1}, from the Nernst equation it can be seen that in order to facilitate hydrogen and oxygen production, the semiconductor must absorb radiant light with photon energies greater than 1.23 eV (< 1000 nm).[2] To account for overpotentials (the deviation of measured potential from the thermodynamic potential), the actual energy needed is often reported as 1.6 – 2.4 eV.[2]

1.2.1.1 Challenges for Solar Fuel Production

Photocatalytic semiconductors share the same main challenges as many of the other methods for producing solar fuels. One is maximising the range of wavelengths that the material can utilise. Many common semiconductors, including TiO_2, have band gaps larger than 3.0 eV (413 nm)[1] and as a consequence they are only active under ultra-violet (UV) radiation and therefore can only harness a small percentage of the total incident light that reaches the Earth's surface.[1, 3] More recently visible light active materials have been the focus of investigations for hydrogen production including $BiVO_4$, Fe_2O_3, WO_3, and TaON.[4]

The second challenge is improving the activity and selectivity of the catalytic reactions. As catalysis occurs at the surface, increasing the surface area helps to increase activity as well

as light collection. This can be accomplished using nanoparticles or by creating porous structures.[5]

The third challenge is ensuring a long enough lifetime of the excited state to facilitate reaction. To extend the lifetime of the excited state, recombination of electron/hole pairs must be limited, usually by spatially separating them. In addition to the catalytic behaviour of the co-catalyst(s) they can also reduce the rate of electron/hole recombination.[3, 6, 7] For metal co-catalysed hydrogen production the metal Fermi energy must be more positive than the conduction band of the semiconductor but more negative than the proton reduction potential. Electrons will then move from the conduction band of the semiconductor onto the metal and as the holes remain in the valence band of the semiconductor, recombination is prevented (Figure 1-1 1-1).[8-10]
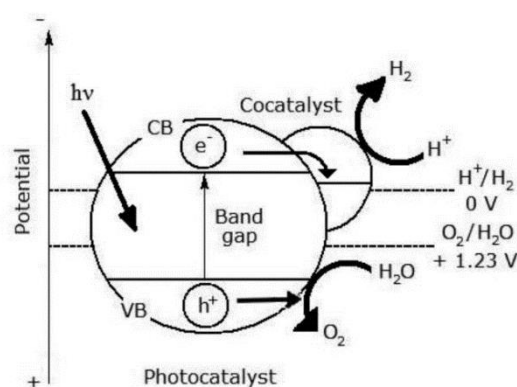
Figure 1-1 Idealised photocatalytic system of water splitting with a co-catalyst adapted with permission from A. Kudo and Y. Miseki, *Chem. Soc. Rev.*, 2009, **38**, 253-278.[1] Copyright 2012 American Chemical Society.

Electrons move from the semiconductor conduction band to the conduction band of the co-catalyst, which has a less negative potential. Hydrogen production occurs on the co-catalyst and oxygen production takes place on the semiconductor as the hole remains in the valence band of the semiconductor. Alternatively another co-catalyst or separate photocatalytic semiconductor and co-catalyst could be employed for the water oxidation reaction, either in solution or as part of a monolithic device.[1, 11]

The conduction and valence band positions of different known semiconductors make it unlikely that one material will be suitable for both the oxidation and reduction reactions and be able to absorb visible light (see Figure 1-2). Doping of materials with nitrogen can raise the valence band position and therefore increase the absorbance range of the material. However, it is more likely that a commercial device will employ different semiconductors for the two half reactions, in tandem, to maximise efficiency.
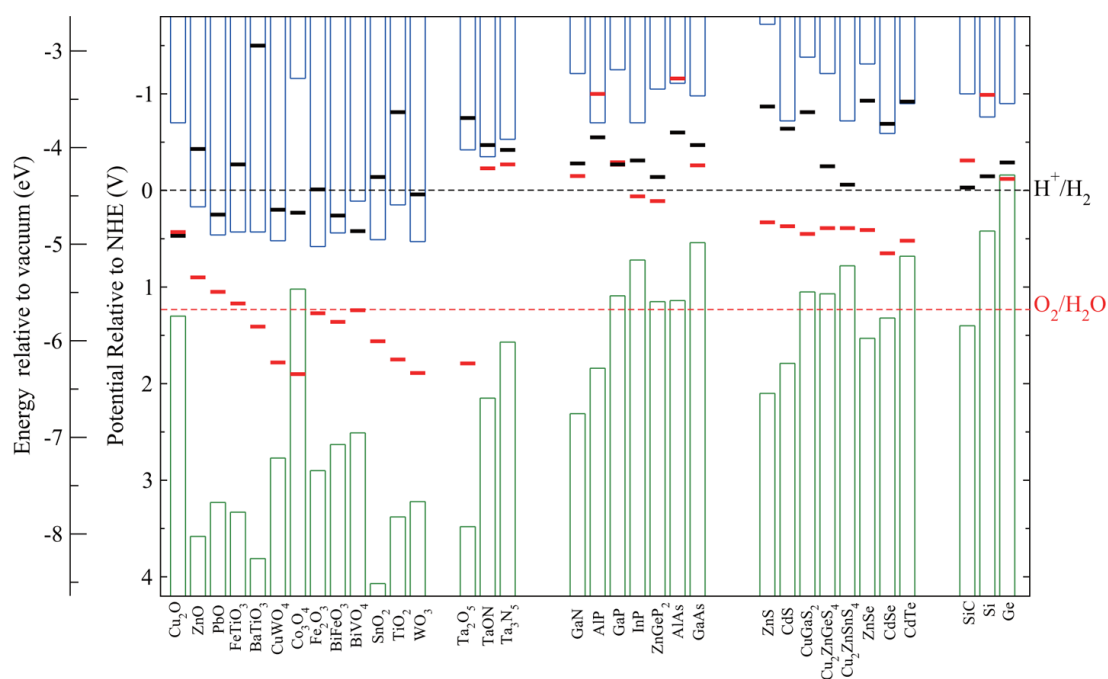
Figure 1-2 Band edge positions with respect to the vacuum level and the normal hydrogen electrode (NHE) for selected semiconductors at pH 0. Showing conduction band edges (top blue columns), valence band edges (bottom green columns) and their band gaps. Calculated oxidation (red bars) and reduction (black bars) potentials relative are given and the two dashed lines indicate the water redox reaction potentials. Reprinted with permission from S. Chen and L.-W. Wang, *Chem. Matter.*, 2012, **24**, 3659-3666.[4] Copyright 2012 American Chemical Society.

1.2.2   Theoretical Photoelectrochemical Water Splitting Device Setups

To be commercially viable, a scalable solar H_2 production method, with costs comparable to those of H_2 production via steam reforming of natural gas (2-3 US$ Kg^{-1}),[12] must be developed. This requires a balance between maximising both energy conversion efficiency and device longevity while at the same time minimising system complexity and production costs.[12]

Constructing wireless photoelectrochemical water splitting devices from semiconductor materials can be done in a number of ways. This includes using a single n-type

semiconductor photoanaode and connecting to a metal cathode back contact (Figure 1-3 a); using n- and p-type semiconductors for the anode and cathode materials respectively in a dual semiconductor cell (Figure 1-3 b); using an n-type semiconductor photoanaode in series with a p-n photovoltaic (PV) connected to a metal cathode (Figure 1-3 c) or using multiple PV cells connected in series and integrated to a metal anode and cathode (Figure 1-3 d) this last option is essentially a PV-photoelectrochemical cell.[2]
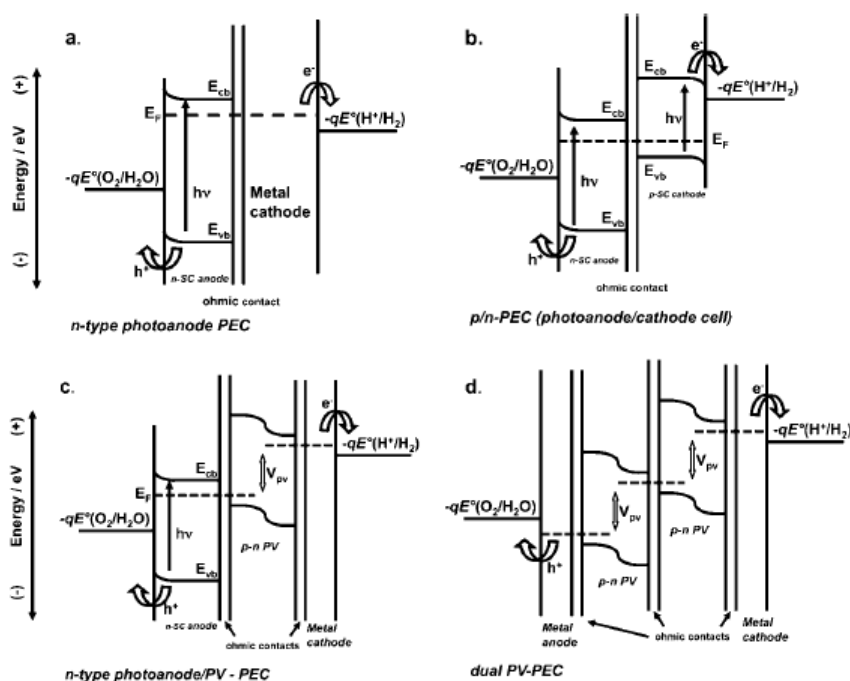
Figure 1-3 Schematics of different possible conformations of photoelectrical water splitting devices using semiconductors, reprinted with permission from M. G. Walter, E. L. Warren, J. R. Mckone, S. W. Boettcher, Q. Mi, E. A. Santori and N. S. Lewis, *Chem. Rev.*, 2010, **110**, 6446-6473.[2] Copyright 2010 American Chemical Society.

In the case of a single semiconductor and metal cathode combination (Figure 1-3a), the photoanode material often shows good stability but large energy loses result in the requirement for materials with band gaps greater than 3.0 eV which limits the maximum efficiency obtainable, as only a small part of the solar spectrum can be harvested.[12] Connecting multiple PV cells in series can generate sufficient voltage to split water, for example using three pn-silicon solar cells that each generate 0.5-0.6 V at their maximum power point.[12]

1.2.3 Photoelectrochemical Water Splitting Devices

In recent years a number of model devices for complete water splitting have been developed, in both wired[11] and wireless configurations.[11] All incorporate PV technology as this provides higher efficiencies (greater hydrogen production at lower overpotentials) even though it increases fabrication and system costs.[2, 13] To date, the highest reported solar-to-hydrogen efficiencies (> 12 %) are by Khaselev and Turner[14] and more recently Luo and co-workers[15].

1.2.3.1 High Efficiency Devices

Khaselev and Turner used a solid state tandem cell consisting of a photoanode made up of a GaAs bottom cell connected to a GaInP top cell through a tunnel diode interconnect and a Pt cathode, operating in 3 M H_2SO_4 (Figure 1-4). The use of the two semiconductors, with varying band gaps, allows for the absorption of visible (by GaInP, 1.83 eV) and near infrared radiation (by GaAs, 1.42 eV). This ability to absorb a wider range of wavelengths allows for the higher efficiencies observed.[14]
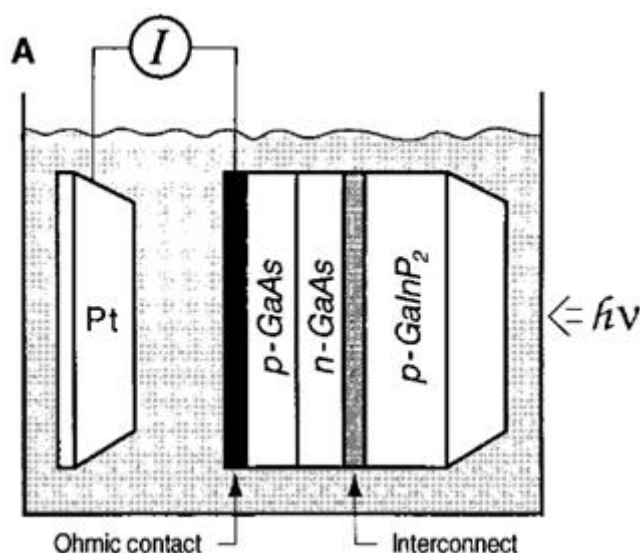
Figure 1-4 Schematic of the tandem monolithic device developed by Khaselev and Turner. Reprinted with permission from O. Khaselev and J. A. Turner, *Science*, 1998, **280**, 425-427.[14] Copyright 1998 American Chemical Society.

Alternatively, Luo and co-workers used a perovskite tandem cell (Figure 1-5) incorporating $CH_3NH_3PbI_3$. The same Earth-abundant catalyst, a NiFe layered double hydroxide, was used for hydrogen and oxygen evolution. Operating in 1 M NaOH; a solar-to-hydrogen efficiency of 12.3% was obtained. However, longevity was an issue with this device as cell lifetime was limited by the instability of the perovskite.[15]
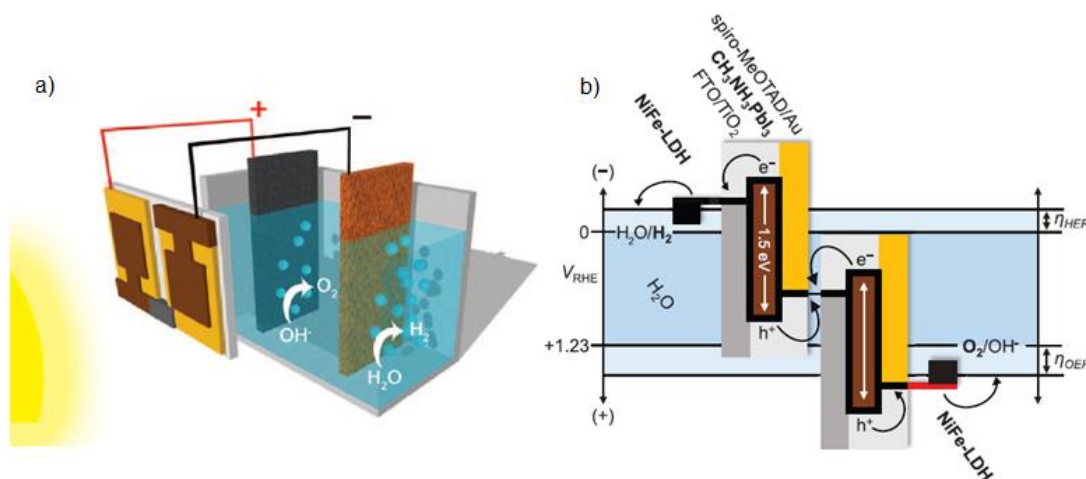
Figure 1-5 a) Schematic diagram and b) generalised energy schematic of Luo and co-workers perovskite tandem cell. Reprinted with permission from J. Luo, J.-H. Im, M. T. Mayer, M. Schreier, M. K. Nazeeruddin, N. -G. Park, S. D. Tilley, H. J. Fan and M. Gratzel, *Science*, 2014, **345**, 1593-1596.[15] Copyright 2014 American Chemical Society.

Both of the previously mentioned cells operate in very harsh acid or alkaline conditions. Whereas Reece and co-workers reported an artificial leaf system operating at pH 7 (Figure 1-6). It uses 3 Si junctions, a cobalt based oxygen evolution catalyst and a NiMoZn HER catalyst. It can operate in both wired and wireless configurations. The wired configuration had an efficiency of 7.7 % whereas the wireless efficiency was much lower but believed to be possible to have a minimal efficiency of 4.7 % with the proper engineering.[11]
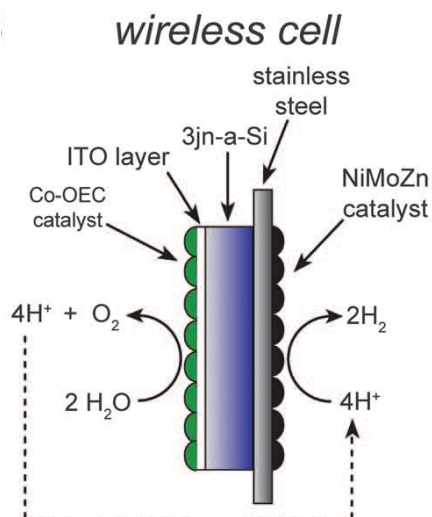
Figure 1-6 Schematic of the wireless solar water splitting device developed by Reece and co-workers. Reprinted with permission from S. Y. reece, J. A. Hamel, K. Sung, T. D. Jarvi, A. J. Esswein, J. J. H. Pijpers and D. G. Nocera, *Science*, 2011, **334**, 645-648.[11] Copyright 2011 American Chemical Society.

Instead of reducing protons to hydrogen, CO_2 can be used as a reactant and reduced to a number of useful hydrocarbon products (see section 1.5 for more details). Monolithic devices have been developed for CO_2 reduction in aqueous solutions (Figure 1-7). Arai and co-workers have reported a solar to chemical energy conversion efficiency of 4.6% for CO_2 photoreduction to formate. Using IrOx/SiGe-jn/CC/p-RuCP, under simulated solar light irradiation (1 sun, AM1.5, 0.25 cm^2). In CO_2-saturated phosphate buffer solution (pH 6.4).[16]
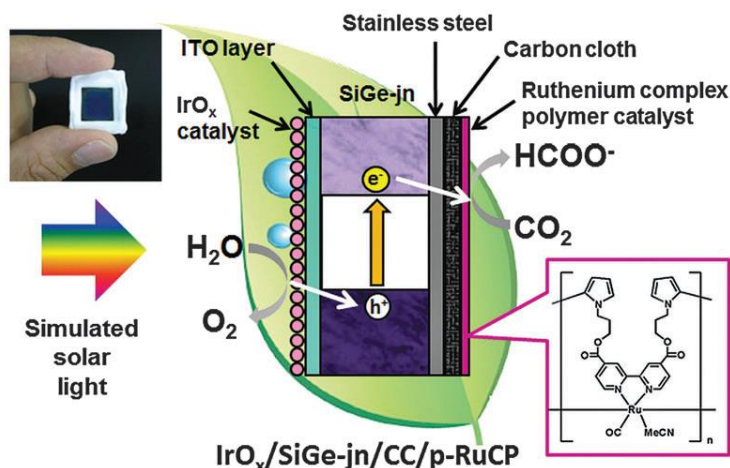
Figure 1-7 Schematic illustration of the IrO$_x$/SiGe-jn/CC/p-RuCP monolithic tablet-shaped device for CO$_2$ photoreduction from Arai and co-workers. Reprinted with permission from T. Arai, S. Sato and T. Marikawa, *Energy Environ. Sci.*, 2015, **8**, 1998-2002.[16] Published by The Royal Society of Chemistry.

1.2.3.2   Device Limitations

The main limitation of the mentioned devices is stability. Either the catalyst or perovskite degrades appreciably over time resulting in a large decrease in efficiency.[11, 14, 15]

One way to improve activity is to utilize more active catalysts for the oxidation and reduction reactions as this would result in lower overpotentials and therefore higher efficiencies.[2] A good catalyst must be active at low overpotentials, robust enough to maintain its efficiency over the lifetime of a commercial device and, in the case of CO$_2$ reduction it needs to be selective (see section 1.5 for more details).[2 17]

1.3   Development of Reduction Electrocatalysts

As well as potentially increasing activity, the use of a catalyst lowers the activation energy required for the reaction to occur. Electrochemically this is referred to as the overpotential and is the difference between a reaction's thermodynamic equilibrium potential and the applied potential required for reaction to occur.[18] The better the catalyst the lower the overpotential and the higher the reaction rate and efficiency of the system.[18]

Promising reduction catalysts are generally tested electrochemically, to assess their activity and the overpotentials required. The standard electrochemical setup consists of a three-electrode electrochemical cell with a working electrode (material being investigated on a conductive support), counter electrode (to complete the circuit, often platinum) and a reference electrode (to measure the charge passed, for example Ag/AgCl). To test the catalytic ability of a material for reduction processes the potential is swept from positive to negative and the current is recorded. The potential required to reach a current density of 10 mA cm^{-2} is often reported as a measure of the materials activity as this is believed to be the current density required for operation in a working device with 10 % efficiency.[11, 14, 19] The voltage required depends on the redox reaction, for HER where the standard thermodynamic reduction potential is 0 V (vs. RHE, pH = 0), a good electrocatalyst should give high current densities below -0.2 V (vs. RHE).[19] An effective catalyst must also have good stability over the timescale of a commercial device and this is often the limiting factor for reasonably active materials.[2]

1.3.1   Electrochemical Screening Methods

The most commonly used electrocatalyst for HER is platinum, due to its high activity at low overpotential. The potential required to achieve a current density of 10 mA cm^{-2} is around -0.06 V (vs. RHE).[19] However, platinum is non-abundant, expensive and also catalyses the back reaction of hydrogen and oxygen to water.[20] The best electrocatalysts for producing various products from CO_2 reduction include gold[21] and tin,[22] again these are not particularly abundant elements therefore alternatives need to be developed. Although far more abundant copper electrodes have shown the most promise for solution based hydrocarbon products they have low selectivity, require high overpotentials and are not very stable.[23, 24] Therefore, it is clear alternative reduction catalysts need to be developed.

1.3.1.1   *Comparing Activities of Reported Catalysts*

The development of alternative electrocatalysts for these reactions has been a large area of research in recent years; however, comparison between studies is not always straight forward and can therefore hinder identification of suitable materials for further development.

One of the main problems of attempting to compare between studies is the variations in the conditions used.[25-27] Differences in pH and electrolyte concentration can make a large difference to the activity and stability of a material.[28] Also, not all studies investigate the stability of their materials and although the use of the potential required for a 10 mA cm^{-2} current density is becoming a conventional activity indicator, it is not always reported. The best method for directly comparing electrocatalytic activity of various materials is to test a whole range under exactly the same conditions.

1.3.1.2   *Electrodeposition as a Synthesis Method for Fast Material Screening*

One of the most commonly used synthesis methods for screening new electrocatalytic materials is electrodeposition. This involves the deposition of catalyst particles onto a supporting electrode (often copper or nickel) and is achieved by applying a potential to a solution of the metal salts. By changing the relative concentrations of the metals present in solution, moderate control over the final composition can be obtained. However, due to possible leaching of elements during electrolysing, it can be difficult to determine the exact composition of the active catalyst. Reasonably large particles, in the micrometre or hundreds of nanometre range, are formed giving a much rougher surface and larger surface area than a normal bulk alloy. The rough surface of the electrocatalyst can lead to improved activity due to an increase in surface area and therefore, being able to separate out the intrinsic activity of the material and any surface enhancement is important when screening new materials.

Recently McCrory and co-workers have tested a number of electrodeposited materials known for HER or ORR activity in acidic and basic solutions.[19] The reason for this study was that it is often difficult to compare the activity of catalysts between different studies as no standard methods of testing exist. Therefore, to effectively compare various potentially promising electrocataysts; they synthesised and tested all materials under the same conditions. This allowed for direct comparison of catalytic activity and identification of the best materials to investigate further. However, the elemental composition of the catalysts was not investigated and this is known to have a large impact on activity.

The problem with electrodeposited catalysts is that if deposited on a photocatalytic semiconductor they may hinder light absorption and therefore overall efficiency. Using a layer of nanoparticles, rather than a relatively thick electrodeposited film would prevent this

problem. Also the use of nanoparticles can further enhance surface area and allow for synthesis of alloy compositions that cannot be accessed in the bulk. Although electrodeposition can be a useful method for initial screening it cannot be used to synthesise small nanoparticles (in the tens of nanometres). Therefore, as nanomaterials can show different activity to the bulk, screening of electrodeposited materials may not give an accurate indication of activity seen for corresponding compositions on the nanoscale. Consequently, alternative screening methods need to be developed and employed for the study of nanoparticle electrocatalysts.

1.3.1.3   Combinatorial Screening Methods

Another method for initially screening a large range of materials, which is becoming increasingly common, is the combinatorial approach.[29] Combinatorial screening allows for the simultaneous potentiostatic control and measurement of current at a large number of electrodes[30] which allows for direct comparison of materials and compositions. Most often, electrodeposition is used to construct the combinatorial array of materials and has been shown to provide a fast method for initial screening in order to determine which material to investigate further.[29, 31, 32] When creating combinatorial libraries, it is common to vary the composition of two or more components across the sample to theoretically cover the whole compositional range.[29] Thin film deposition techniques are often employed in the synthesis of these samples (Figure 1-8).[29] Although some synthetic methods, such as co-evaporation, are not always readily reproducible and can suffer from contamination problems.[29, 33]
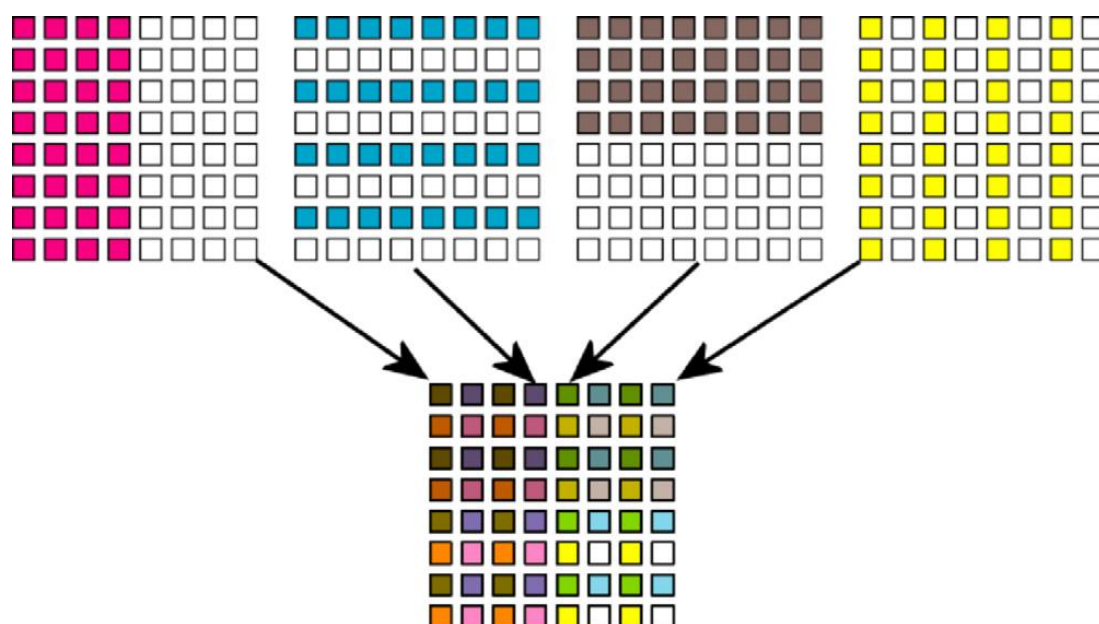
Figure 1-8 Example of sample preparation for combinatorial screening. Thin film deposition and masking technologies can be used to create 2^n-1 material compositions. In this example, four individual layers result in 15 compositions. Reprinted with permission from T. M. Muster, A. Trichi, T. A. Markley, D. Lau, P. Martin, A. Bradbury, A. Bendavid and S. Dligatch, *Electrochim. Acta*, 2011, **56**, 9679-9699.[29] Copyright 2011 Elsevier Ltd.

The combinatorial method is becoming more common as a way of designing new electrocatalytic materials.[29, 34, 35] Although this technique can be used to evaluate the effect of particle size on activity,[34] the particles are still agglomerated and so may not have as high activity as nanoparticles and may also interfere with the light harvesting ability of the semiconductor if the film is too thick.

Therefore, as well as being expensive and time consuming to initially setup, the combinatorial method is only useful for initial screening of materials. Further investigation would then require the synthesis of nanoparticles of materials and compositions expected to have good activity.[35] Consequently, if possible materials can be identified by other means; it may be advantageous to proceed directly from nanoparticle synthesis.

1.3.1.4 Electrochemical Screening of Nanoparticle Materials

To electrochemically test nanoparticle materials, such as for applications in fuel cells, the commonly used method involves initially depositing nanoparticles on a high surface area carbon support and this is then deposited onto the electrode (often glassy carbon).[36-43]

Ideally, the nanoparticles should be deposited directly onto the electrode surface without first adding a support.[28]

Nanoparticles have been deposited directly onto TiO_2 films supported on fluorine or indium doped tin oxide (FTO or ITO) transparent conductive glass.[44] This is beneficial as it allows for analysis of activity directly on the semiconductor material. It also allows for investigations of photoelectrocatalytic activity without having to change the electrode setup.

To be effective, the screening method needs to be quick and straight forward. Although the use of semiconductor films on FTO electrodes would be advantageous for photoelectrocatalytic testing, it is a time consuming process for initial electrocatalytic screening. It is clear that development of a quick and simple procedure for electrocatalytically testing nanoparticles would be beneficial.

1.3.2 Stability Tests

As well as catalytic activity, assessing the stability of catalytic materials is also important. To be viable for use in a commercial device the catalyst must be stable over the lifetime of the device. Unfortunately, few studies investigate the stability of their catalysts and a lot of the recently reported active catalysts have poor longevity. This is due to the tendency of materials to oxidise over time[45] or in some cases the leaching of elements leads to a reduction in activity.[11]

Various methods have been employed to test stability including chronoamperometry (holding at a potential and measuring the current over time) and cyclic voltammetry (sweeping the potential from more positive to more negative and back multiple times, usually between100 and 5000). Electrochemical impedance spectroscopy can also be employed to investigate corrosion activity of the catalyst.[46]

1.4 Electrocatalysts for Hydrogen Production

Hydrogen is an important clean energy alternative to fossil fuels as a chemical feed stock and possible transport fuel. Currently, hydrogen is mainly produced by steam methane reforming, using natural gas as the feed stock (Equation 1-4).[47] Consequently a large amount of CO_2 is released, as a by-product making it a non-sustainable process. By

contrast, hydrogen produced from photoelectrolysis of water would be a sustainable process using abundant resources, water and sunlight, to produce hydrogen (Equation 1-2).[47]

$$CO_2 + 2H_2O \rightarrow 4H_2 + CO_2 \qquad \text{Equation 1-4}$$

The hydrogen evolution reaction (HER,) is the cathodic half reaction of water splitting[18] The thermodynamic standard reduction potential of the HER is defined as $E^0_{H2/H2O} = 0$ V *versus* a normal hydrogen electrode at pH = 0.

In order for solar fuels to be a viable alternative to fossil fuels cost effective, efficient and stable devices need to be developed. Catalysts are often employed to reduce overpotentials required and enhance the rate of reaction, therefore increasing efficiency.

1.4.1   HER Mechanism

The hydrogen evolution reaction (HER, Equation 1-5), at a solid surface, involves two of three steps which are shown in Equations 1-5 to 1-9 the mechanism of steps 1 and 3 depends on whether the solution is acidic ((1A) and (3A)) or basic/neutral (3A and 3B). The first step involves hydrogen adsorption onto the metal surface (Volmer step, Equation 1-5 or 1-6), this adsorbed species can then either combine with another adsorbed hydrogen (Tafel step, Equation 1-7) or with a species in solution (Heyrovsky step, Equation 1-8 or 1-9) to produce dihydrogen.

Step 1A:	$M + H^+ + e^- \rightarrow M\text{-}H_{ads}$	Equation 1-5
Step 1B:	$H_2O + M + e^- \rightarrow M\text{-}H_{ads} + OH^-$	Equation 1-6
Step 2:	$2M\text{-}H_{ads} \rightarrow H_2 + 2M$	Equation 1-7
Step 3A:	$M\text{-}H_{ads} + H^+ + e^- \rightarrow H_2 + M$	Equation 1-8
Step 3B:	$M\text{-}H_{ads} + H_2O + e^- \rightarrow H_2 + M + OH^-$	Equation 1-9
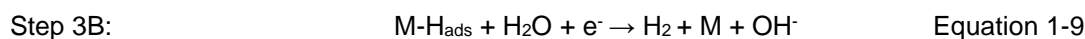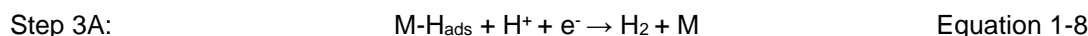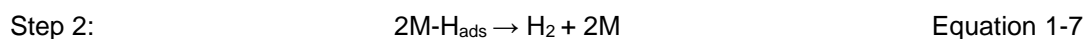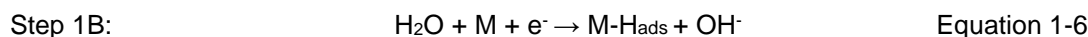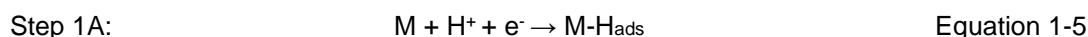
The identity of the rate determining step depends on the structure and composition of the catalyst used. Many active materials operate via the Tafel step at low overpotentials,[26] suggesting desorption of produced hydrogen is the rate limiting step. The speed of proton adsorption and hydrogen desorption will depend on the M-H bond strength of the catalyst.

1.4.2 Correlation Between HER Activity and M-H Bond Strength

Trassatti[48] has shown that a metals activity for proton reduction is linked to the strength of the metal-hydrogen bond it forms (figure 1-9). Exchange current density has been used as an indicator of a metals activity; this is the current density flowing, in both directions, at equilibrium (see chapter 3 section 3.1). A large exchange current density indicates a fast reaction while a small exchange current density indicates a slow reaction. The maximum of the volcano curve should correspond to $\Delta G° = 0$, where $\Delta G°$ is the standard free energy of hydrogen adsorption and occurs at intermediate bond strengths. For weaker M-H bonds, the metals do not adsorb hydrogen ($\Delta G° > 0$) and for stronger M-H bonds, metals adsorb hydrogen ($\Delta G ° < 0$).[48] However, if the M-H bond is too strong, the rate of dihydrogen production will decrease. This is consistent with the Sabatier principle which states that, for heterogeneous catalysis and electrocatalysis, optimal catalytic activity requires a catalytic surface that has intermediate bonding energies with the reaction intermediate.[18]
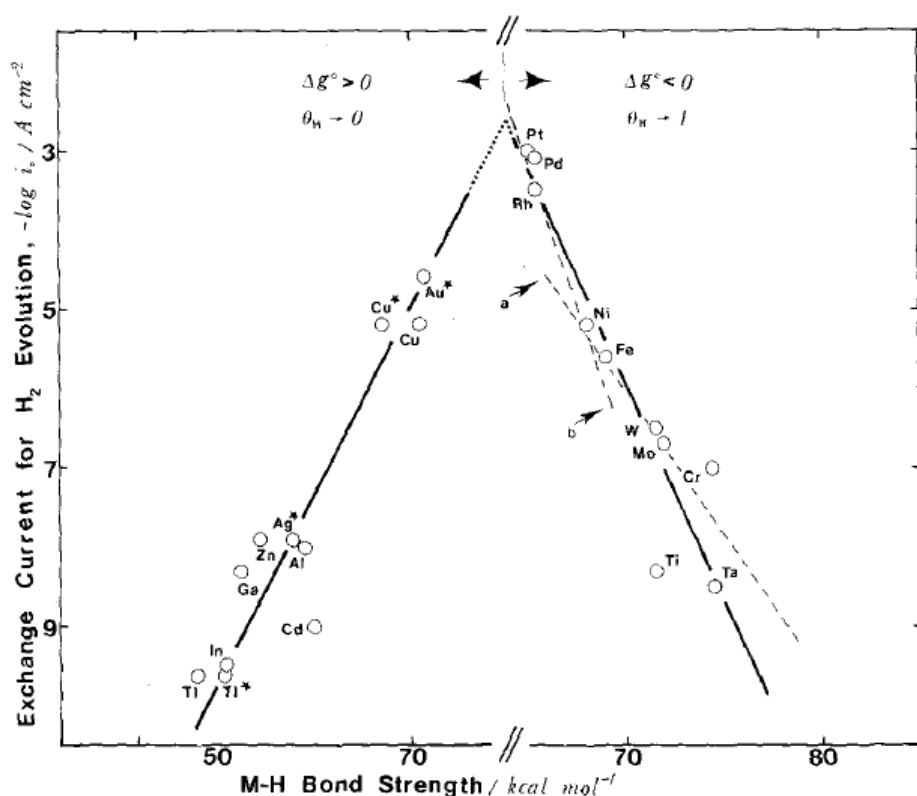
Figure 1-9 Exchange currents for electrolytic hydrogen evolution *vs.* strength of metal-hydrogen bond derived from heat of hydride formation in the case of *sp* metals, and from heat of adsorption from gas phase in the case of transition metals. Starred values refer to spectroscopic dissociation heat. Arrows indicate theoretical slopes for (a) ion + atom, (b) combination reaction. Reprinted with permission from S. Trasatti, *J. Electroanal. Chem.*, 1972, **39**, 163-184.[48] Copyright 1972 Elsevier B. V.

These measurements have been conducted in acidic conditions and as the reduction potential for hydrogen production is pH dependant may not be the same in basic conditions. Unfortunately, comparable collected values of the exchange current densities, in highly alkaline conditions, are not readily available. However, work by Miles[49] has measured the overpotentials required, by various transition metals, to achieve a set current density (Figure 1-10).
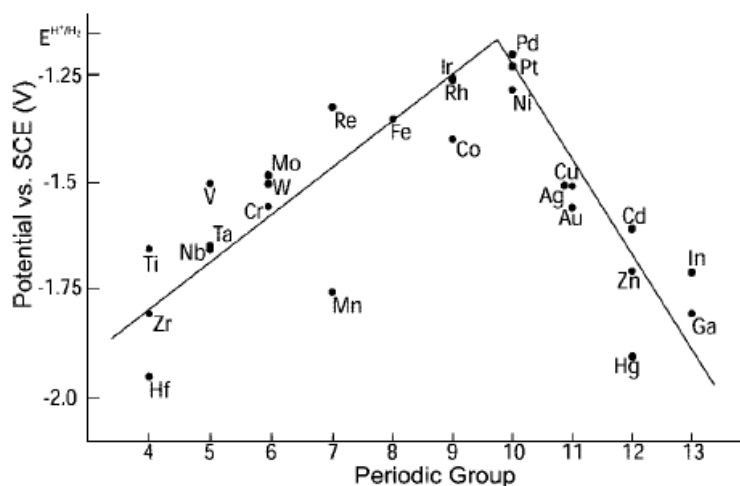
Figure 1-10 The volcano relation (in 30 wt % base solution) based on potentials required to attain a current density of 2 mA cm^{-2} as measured by Miles[49] reprinted with permission from M. G. Walter, E. L. Warren, J. R. Mckone, S. W. Boettcher, Q. Mi, E. A. Santori and N. S. Lewis, *Chem. Rev.*, 2010, **110**, 6446-6473.[2] Copyright 2010 American Chemical Society.

In acidic media, platinum, which has intermediate M-H bond strength, is expectedly a good catalyst for the proton reduction reaction. The collected data for alkaline media shows a similar trend, again with platinum the most active, followed by the other group 10 metals. This suggests the predominant HER mechanism for a given metal is the same in acidic and basic media.[2] It also explains why platinum has been widely used as a catalyst for HER. However, as previously stated, using platinum is not feasible in the long term so alternatives need to be developed.

1.4.3 Catalysts for HER

Many materials have been investigated as alternatives to platinum as HER electrocatalysts. One option is to alloy platinum with other metals often in the form of core-shell nanoparticles, with a more abundant metal in the centre and a thin layer of platinum on the surface. This

strategy reduces the platinum content while maximising the platinum surface area and so does not reduce the activity. In fact alloying has been shown to increase the activity compared to pure platinum.[50] Nevertheless, there is still a drive to move away from platinum completely.

1.4.3.1   Non-noble Metal Alloy Catalysts for HER

Many alternative materials have been investigated, with a focus on trying to utilise more abundant and readily available materials (Figure 1-11). Therefore, first row transition metals especially iron,[26, 51, 52] cobalt,[51, 53] nickel,[11, 26, 51-54] copper[53] and zinc[11, 26, 53] are often incorporated. Although less abundant and more expensive, molybdenum[11, 55] and tungsten[56] have also received a lot of attention due to the high HER activities observed when these materials are incorporated, especially with nickel.[2, 11, 26, 57, 58]
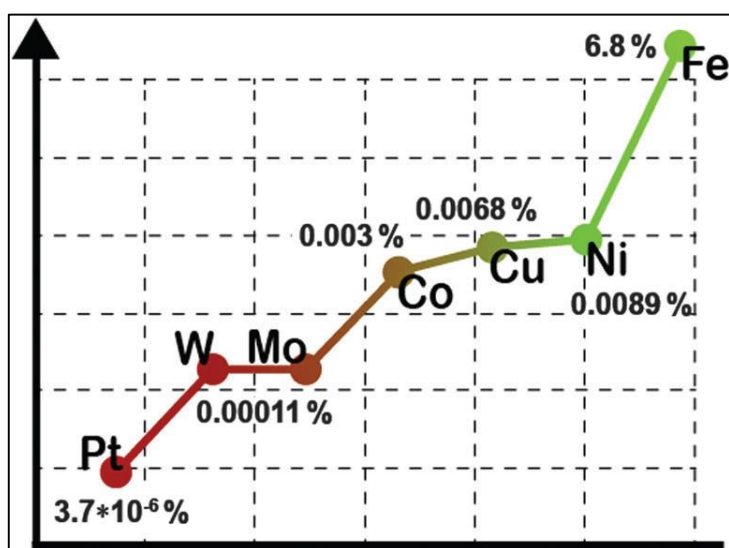
Figure 1-11 Crustal abundance of some metals commonly used for constructing HER Electrocatalysts, adapted with permission from X. Zou and Y. Zhang, *Chem. Soc. Rev.*, 2015, **44**, 5148-5180.[46] Published by The Royal Society of Chemistry.

Navarro-Flores and co-workers investigated Ni-alloy electrodeposits, including Ni-Mo and Ni-W, for HER activity. They reported overpotentials of -75 mV and -85 mV respectively for a current density of -1 mA cm^{-2} in 0.5 M H_2SO_4.[26] Although current densities of -10 mA cm^{-2} are required for an efficient device the low overpotentials are promising. However, these

materials are not stable for long periods of time in acidic conditions[26] and their relatively low abundance also makes them less desirable than other materials.

As well as combinations of metals, alloys incorporating non-metallic elements specifically boron,[2, 55] carbon,[2, 55, 56] nitrogen,[2] phosphorous[2, 28] and sulphur[46] have been investigated. In 1973, Levy and Boudart discovered the platinum-like catalytic behaviour of tungsten carbide.[56] This was attributed to the similarities between the d-band electronic density of states of platinum and tungsten carbide.[56] More recently, a lot of research has focussed on metal carbides for the HER. Mo_2C and MoC materials have been investigated and Wan and co-workers have demonstrated the importance of structure on activity with β- Mo_2C being most active for HER in acidic conditions.[59] Vrubel and Hu have shown that β- Mo_2C is a stable electrocatalyst in both acidic and basic conditions over 45 hours at -0.20 V vs RHE.[55] The overpotentials required for a current density of 10 mA cm^{-2} were -0.23 V and -0.20 V in acid and base respectively.[55] Ideally the overpotential should be as low as possible and although many materials have shown lower overpotentials than this, few have shown as good stability. However, most work with carbides has focussed on W and Mo when ideally the employment of less expensive and more abundant elements would be preferred.

1.4.3.2 Molecular HER Catalysts

Alloys are not the only HER active catalysts and investigation of hydrogenases (hydrogen enzymes)[60] and molecular species as electrocatalysts for HER has also increased in recent years.[61-69] Moreover, many molecular catalytsts developed focus on nickel and iron in attempts to mimic the active site of [NiFe] and [FeFe] hydrogenases.[61-64, 69] However, higher overpotentials and much lower current densities (normally μA rather than mA) are generally observed for molecular catalysts.[61, 62, 65, 67-69] Martindale and co-workers investigated solar hydrogen production using carbon quantum dots and a molecular nickel catalyst. They found that the stability of their molecular Ni catalyst limited activity and that overall activity could be improved by adding more catalyst every few hours.[66] However, this is not ideal in a working device. Therefore, focusing on alloyed materials appears to be the most likely route to developing a catalyst with high enough activity and stability.

1.4.3.3   Nickel HER Electrocatalysts

Among the elements most commonly incorporated in alloys for electrocatalysis are molybdenum and nickel.[26] Although good activities have been achieved, there are often stability issues with these materials.[46] As nickel is by far the more abundant of these two materials, focussing on the development of nickel alloy electrocatalysts for HER is advisable.

As a relatively cheap, abundant and readily available material, nickel is a promising alternative to platinum for HER. Ni/NiO core/shell nanoparticles have been shown to be effective proton reduction catalysts on photocatalytic semiconductors, without catalysing the back reaction. However, there are longevity issues with this material.[45] Alloying nickel has been shown to improve both the corrosion resistance and activity, as the influence of different neighbouring atoms can lead to the observation of different, and often better, catalytic activity than that shown by the monometallic particles.[70]

Some nickel alloys have already been identified as electrocatalysts for HER including NiCo,[51, 52] NiCu,[54] NiFe,[26, 51, 71] NiMo,[26, 72-74] NiW,[26, 75] NiCoFe,[76] NiCoZn,[53] NiFeZn,[77] NiMoZn[11, 26] and Ni_2P.[28] However, with the exception of Ni_2P, all these materials were synthesised by electrodeposition and therefore the exact composition and structure of the active catalyst is often unknown. Also, stability was either poor or untested.

The Ni_2P nanoparticle electrocatalyst showed good activity in 0.5 M H_2SO_4 with a current density of 10 mA cm^{-2} achieved at an overpotential of around 0.1 V. This activity is not as high as that of NiMo but the latter rapidly degrades under acidic conditions.[28, 58] The main problem with this material is that the synthesis involves the high-temperature decomposition of a phosphine which can liberate phosphorus. This means this reaction should be considered as highly corrosive and flammable and therefore should only be carried out by appropriately trained personnel, under rigorously air-free conditions which is not conducive to scaling up.[28]

Many nickel alloys show relevant activity in thermal applications, for example; Ni_xFe_{1-x} and Ni_xRu_{1-x} (0 < x < 1) alloy nanoparticles have been shown to exhibit comparable activity to platinum for the decomposition of ammonia borane (NH_3BH_3) to dihydrogen, in water[78, 79] and Ni_xCu_{1-x} (0 < x < 1) nanoparticles exhibit a range of thermal catalytic activity including BH_4^- reduction,[42] and H_2 production via steam reforming.[80] Plus many [NiFe] molecular catalysts, that model the active site of [NiFe] hydrogenase, have also been investigated for hydrogen

reduction.[81] NiCr has been investigated for dental applications due to its corrosion resistance and a NiCuFe alloy has shown good stability in sea water.[82]

Although NiMo has shown reasonable activity; to improve stability and reduce cost development of alloy electrocatalysts utilising first row transition metals for the HER should be focussed on.

1.5   Electrocatalysts for CO_2 reduction

Rising atmospheric CO_2 levels have been linked to environmental concerns, resulting in a need to develop 'carbon neutral' processes in order to maintain environmental stability by keeping the overall level of CO_2 constant.[83] Therefore, the development of efficient CO_2 reduction catalysts is required. Many useful products can be produced by CO_2 reduction including formic acid, carbon monoxide, methane, ethylene, ethanol and methanol. For example, methanol has been used as a transportation fuel in either modfied internal combustion engines or direct methanol fuel cells,[84] and also as a raw material for the synthesis of important platform chemicals for methyl *tert*-butyl ether, chloromethane, acetic acid and formaldehyde[85, 86] Alternatively it can be converted to ethylene which is used in the production of hydrocarbon fuels.[84]

Hydrothermal CO_2 reduction, into methanol and formic acid by aluminum and a copper catalyst with yields of up to 5.4 and 70 % respectively, has been reported by Lyu and co-workers.[86] Compared to thermocatalytic CO_2 reduction, (photo)electrocatalytic CO_2 reduction has the advantage of operating at ambient temperature and lower partial pressures of reactant gases.[87] The identity and distribution of products formed is affected by many factors including electrolyte composition, pH value, applied potential, cathode composition and surface morphology.[87, 88] The source of this behaviour is the relative thermodynamic reduction potentials for the various CO_2 reduction reactions (Equation 1-10 to Equation 1-16).[83] Directly reducing CO_2 to $CO_2^{\cdot-}$ (-1.9 V vs SHE) has a much higher reduction potential than reduction to various products.[83, 87]

$$CO_2 + 2H^+ + 2e^- \rightarrow HCO_2H \qquad \text{-0.61 V vs SHE} \qquad \text{Equation 1-10}$$

$$CO_2 + 2H^+ + 2e^- \rightarrow CO + H_2O \qquad \text{-0.53 V vs SHE} \qquad \text{Equation 1-11}$$

$$2CO_2 + 2H^+ + 2e^- \rightarrow H_2C_2O_4 \qquad \text{-0.49 V vs SHE} \qquad \text{Equation 1-12}$$

$$CO_2 + 4H^+ + 4e^- \rightarrow HCHO + H_2O \qquad \text{-0.48 V vs SHE} \qquad \text{Equation 1-13}$$

$$CO_2 + 6H^+ + 6e^- \rightarrow CH_3OH + H_2O \qquad \text{-0.38 V vs SHE} \qquad \text{Equation 1-14}$$

$$CO_2 + 8H^+ + 8e^- \rightarrow CH_4 + 2H_2O \qquad \text{-0.24 V vs SHE} \qquad \text{Equation 1-15}$$

$$CO_2 + 4H^+ + 4e^- \rightarrow C + 2H_2O \qquad \text{-0.2 V vs SHE} \qquad \text{Equation 1-16}$$

The exact mechanism of CO_2 reduction to give various products is still debated and generally unknown. However, most theories agree it begins with the reductive adsorption of CO_2 on the catalyst surface leading to the formation of a COOH intermediate. The adsorbed COOH is reduced and reacts with another proton and electron, giving CO and H_2O. The first two steps are fundamentally electrochemical, each involving the transfer of an electron and a proton, and the final step is the nonelectrochemical release of CO from the electrode. Therefore, the binding strengths of the the various products and intermediates has a large effect on the overall product distribution.[21] Therefore, the overpotentials required for each possible CO_2 reduction reaction, vary depending on the electrode material giving rise to a range of products depending on the potential used. Consequently, identifying and developing new catalytic materials for selective CO_2 reduction has been of great importance.

1.5.1   Adsorption behaviour of various metals and effect on CO_2 reduction activity

Just as the M-H bond strength is important for the activity of catalysts for hydrogen production, the CO adsorption strength of metals affects the CO_2 reduction products formed. Pure metals in aqueous solutions can be divided into four main groups. The first group of metals produce predominately hydrogen; examples include Ni, Fe, Pt and Ti. This is due to having the ability to evolve hydrogen at low overpotentials combined with a high CO adsorption strength. As a consequence, CO_2 reduced to CO binds very strongly to the surface and so prevents further reduction.[23] However, operating under a pure CO_2 atmosphere can lead to an improvement in the hydrogen evolution activity, compared to operation under an inert (argon) atmosphere, due to the effect the CO_2 binding has on the surface of the metal.[23, 24]

The second group of metals mainly produce formic acid and include Sn, In, Tl, Pb, Hg, Bi and Cd. This is due to a high overpotential for hydrogen evolution and a low CO adsorption strength, meaning the breaking of the C-O bond in CO_2 cannot be catalysed by these metals and so a wider range of products are not produced. [23]

The third group of metals produce mainly CO and this group includes Au, Ag, Zn and Ga. They have a medium ovepotential for hydrogen evolution and a weak CO adsorption ability, and form CO at less negative potentials than formic acid. [23]

Finally, there are some metals that produce various hydrocarbons (particularly methane, ethylene and methanol), including Cu, Mo and Ru. These metals have a higher CO adsorption strength than the previous group which allows for the formation of various hydrocarbons as well as CO. [23]

1.5.2   Known materials for CO_2 reduction

Gold is characteristic in selectively generating CO.[21] Tin has been shown to produce CO, formate and hydrogen.[22, 88] The relative Faradaic efficiencies (FE) are dependent on the potential used and increased selectivity for CO and formate over H_2 were observed when a thin SnO_x layer was present on the surface of the electrode.[22] Lv and co-workers have demonstrated high FE (>70 %) for CO_2 reduction to formate at higher overpotentials (-1.8 V vs Ag/AgCl),[88] again illustrating the importance of the reaction conditions as well as the catalyst employed.

Cu is the only one found to possess high faradaic efficiency towards CO_2 electroreduction to methane (CH_4) and ethylene (C_2H_4). As well as producing a range of other hydrocarbon products with lower faradaic efficiencies. One of the main drawbacks of copper electrodes is that they rapidly lose CO_2 reduction activity if impurities are present in the electrolyte solution.[89]

As mentioned for HER electrocatalysts, the use of alloy materials could help improve stability and may also be able to direct CO_2 reduction product selectivity.

1.6   Nanomaterials

If these catalysts are going to be used on photocatalytic semiconductors it is also important for the particles to be discontinuous and smaller than the wavelength of incident photons, so the light absorption properties are not affected.[2] To get the best activity the alloy material needs to be as small as possible. The use of nanoparticles can also provide large surface areas and allow control over composition and morphology.

Compared to bulk materials, metal nanoparticles have a large proportion of atoms at or near to the particle surface and consequently these nanoparticles often show different structures and properties to those observed in the bulk materials.[70, 90] Also, as electrocatalysis occurs on the surface, providing a large surface area negates the need for a high catalyst loading[18] and therefore lowers cost.

Nickel nanoparticles have previously been synthesised and used for hydrogen production[91] both electrocatalytically[91] and on photocatalytic semiconductors,[45] however there are longevity issues with this material.[45] It may be possible to improve the longevity of the nickel catalyst by forming an alloy with other transition metals. This could also lead to an enhancement in activity due to synergistic effects.[70] As nanoparticles, the alloys may also display different properties from the equivalent bulk alloy due to finite size effects. For example, elements that are immiscible in the bulk may readily mix in finite clusters.[70]

1.6.1   Mixing and Ordering in Bimetallic Nanoalloys

Many factors affect the mixing and ordering in bimetallic nanoalloys, including the relative bond strengths, the atomic sizes, the surface energies of the bulk elements and the strength with which each element binds to the support or surface ligands. If homonuclear bonds are stronger than the heteronuclear bonds, segregation will be favoured and the species forming the strongest homonuclear bonds tends to be in the centre. The smaller atoms will also tend to occupy the more sterically confined core. Whereas the element with the lowest surface energy will tend to segregate to the surface and the element that binds most strongly to the support or ligands may be pulled towards the surface. It is clear that the arrangement for a particular bimetallic nanoparticle depends on the balance of these factors and therefore, the selection of experimental synthetic method and conditions is very important.[70]

This results in four main types of possible mixing patterns that the nanoalloy may adopt.[70] The first is the core-shell structure (Figure 1-12 a), this is very common and involves a core made of one type of atom (A) surrounded by a shell of another (B), though there may be some mixing between the shells. Subcluster segregated nanoalloys are also theoretically possible although there are currently no known examples of this type of mixing. It would consist of A and B subclusters (Figure 1-12 b), which may share a mixed interface (left) or only have a small number of A-B bonds (right). A much more common possibility is mixed nanoalloys (Figure 1-12 c). They can be ordered (left) or random (i.e., a solid solution, right, often referred to as alloyed nanoparticles in the literature[70]). The final option is multishell nanoalloys, which contain layered alternating –A-B-A- shells (Figure 1-12 d)); a few examples of this pattern have been reported.[92-95]
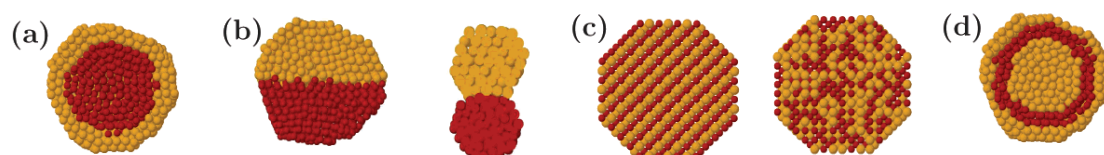
Figure 1-12 Schematic representation of some possible nanoalloy mixing patterns: (a) core-shell, (b) subcluster segregated, (c) mixed, (d) three shell. The pictures show cross sections of the clusters. Reprinted with permission from R. Ferrando, J. Jellinek and R. L. Johnston, *Chem. Rev.*, 2008, **108**, 845-910.[70] Copyright 2008 American Chemical Society.

Both core-shell and mixed nanoalloy electrocatalysts have previously been studied for fuel production.[96, 97] The use of the core-shell structure is often employed to reduce the overall amount of platinum used but maintain or improve its activity by alloying it with a cheaper metal.[50, 98] Alloys using only relatively cheap, abundant and readily available elements have also been investigated. Often these materials are prepared by electrodepositon however this method does not allow for good control of the synthesised composition.[11] Also, it does not produce nanoparticles and the thickness of the film produced may inhibit the absorption properties of the photocatalytic semiconductor, in the solar water splitting device.

1.6.2   Nanoalloy Synthesis Methods

When synthesising nanoalloys the goal is to obtain mono-disperse, regularly shaped materials that all have the same composition. To achieve this the synthesis method used must be considered carefully.

There are many methods for synthesising nanoalloys. Synthesising nanoalloys directly on a support material is often a simple reaction with very few steps, but it can be hard to control size distribution and ensure a uniform composition in all individual nanoparticles.[90] Pulsed laser deposition techniques can give better size control but it is still difficult to ensure the composition in all nanoparticles.[99] Using ligand stabilised methods allows for good control of the size and composition of the nanoalloys formed[42, 100] and can prevent aggregation of the formed nanoparticles.[38, 101]

1.6.2.1 Ligand Stabilised Nanoalloy Synthesis

Various stabilising ligands can be used including coordination of bulky phosphorous, nitrogen or sulphur donors providing steric stabilisation.[70, 100] Alternatively electrostatic stabilization could be used in this case, aggregation is prevented due to Coulombic repulsion between nanoparticles, arising from the electrical double layer of ions adsorbed at the particle surface (e.g., when preparing sodium citrate gold sols).[102]

However, the use of ligand stabilised nanoparticles generally necessitates the removal of the ligands from deposited nanoparticles before use. This is due to the inhibition of electron transfer that is often caused by the presence of the stabilising ligands. In order to remove the ligands, samples are normally heated to temperatures above 400 °C. Therefore, sintering and growth of the particles can occur and needs to be considered during synthesis.

1.6.2.2 Mechanism of Nanoparticle Formation

The formation of nanoparticles from metal salt precursors occurs in several steps (Figure 1-13). Initially, the metal salt is reduced to give zero valent metal atoms. These atoms eventually form an irreversible "seed" of stable metal nuclei by colliding in solution with other metal ions, metal atoms or clusters. These "seeds" continue to grow to produce the metal nanoparticles.[100] Careful consideration of the temperature, time, stabilising ligands and reductants are important for controlling the average size and size dispersion of the nanopartilces formed.
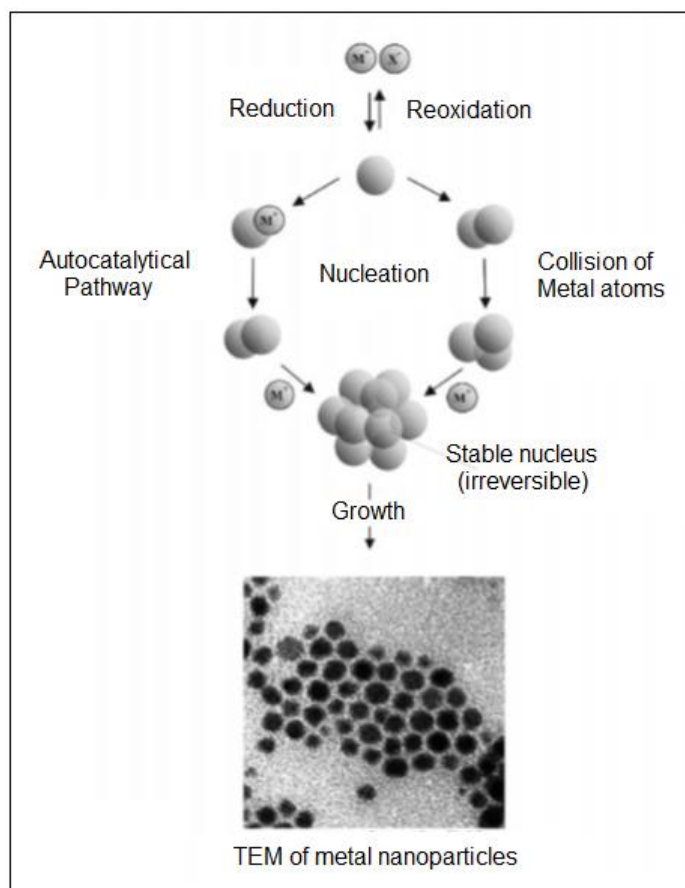
Figure 1-13 Schematic of the mechanism for nanoparticle synthesis, showing nucleation and particle growth. Reprinted with permission from R. Ferrando, J. Jellinek and R. L. Johnston, *Chem. Rev.*, 2008, **108**, 845-910.[70] Copyright 2008 American Chemical Society.

1.7 Conclusions

Solar fuels could provide a useful alternative to fossil fuels as both chemical feedstocks and transport fuels. One of the key areas to improve the efficiency of a solar fuel device is the development of catalysts with low activity and good longevity. Current active materials are not very stable and many of the most common are very expensive (e.g. platinum). Therefore, new reduction electrocatalysts that employ cheap and abundant materials need to be developed. Nickel is already known to have reasonable HER activity, therefore alloying with other first row transition metals could improve both activity and stability. Using nanoalloys allows for higher surface areas with less material, again minimising costs. The small size of the nanoalloys would also enable deposition onto a photocatalytic semiconductor without inhibiting its absorption properties. Unlike other synthesis methods, using ligand stabilised nanoalloys would allow for good control of the size and composition of materials produced.

1.8 Aims

42

This work aims to investigate nickel based nanoalloy materials as proton and CO_2 reduction catalysts, with a focus on first row transition metals. Synthesis and characterisation of a range of nickel nanoalloys will be discussed (Chapter 2). Electrochemical analysis of proton (Chapter 3) and CO_2 (Chapter 4) reduction activities and stabilities will be presented and comparison of the different materials will be given.

2 Nanoalloy Synthesis

2.1 Introduction

Whether being used as part of a complete solar device or as an electrocatalyst with a renewable energy power source, the production of solar fuels from water and carbon dioxide requires appropriate catalysts. The most commonly used catalyst for hydrogen evolution is platinum[20, 48, 50] however, due to its expense and rarity, alternative catalysts need to be developed. Many nickel alloys have been investigated for the HER and often show good activity but not always good stability.[11] However, various nickel alloys have been shown to have good stability in corrosive environments,[82, 103] therefore with the right combination of elements a nickel alloy may present a stable and active reduction catalyst.

As catalysis occurs at the surface, increasing the surface area helps to increase activity of the metal catalyst while at the same time decreasing the amount of material that is required and therefore decreasing costs. To get the best activity the material needs to be as small as possible. The use of nanoparticles can provide large surface areas while still allowing for control over composition and morphology. Also, elements that would be immiscible in the bulk can often form nanoalloys as the formation enthalpies become more negative for nanomaterials.[42, 70, 79] Therefore, using nanoparticles allows for easier synthesis of certain alloys, including NiCu[42] and NiRu.[79] To determine which phases are expected to be thermodynamically stable for a synthesised bulk alloy phase diagrams are used.[104]

2.1.1 Phase Diagrams

Phase diagrams are used to show the relationships between the various phases within a system that appear under equilibrium conditions. A single component phase diagram is a one- or two-dimensional plot showing the phase changes of a substance with change in temperature and/or pressure (Figure 2-1 (left)). For systems with two or more components, two- or three-dimensional plots are used to describe the phase relationships in the system. Often the diagram is simplified by only considering atmospheric pressure and assessing the effect of composition and temperature. In these cases, the phase diagrams often show mixed phase as well as single phase fields (Figure 2-1 (right)).[104]
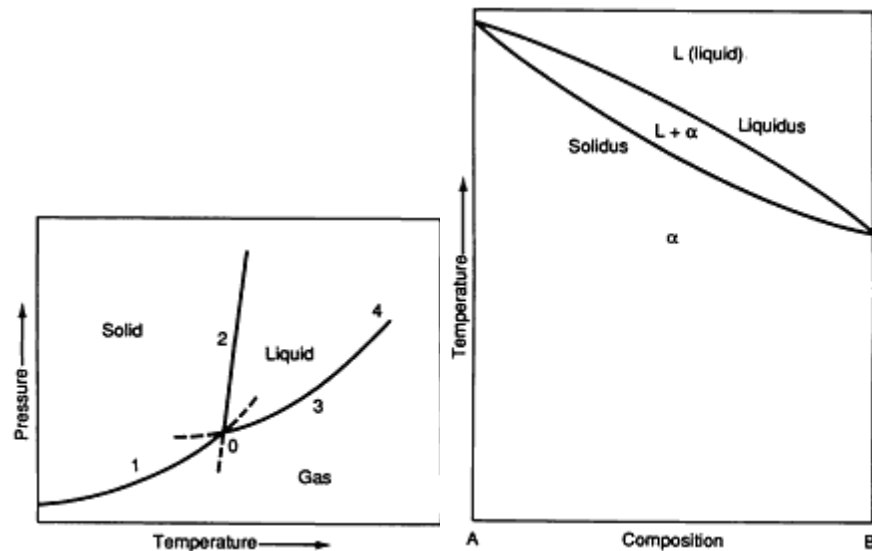
Figure 2-1 Schematic pressure-temperature phase diagram (left) and binary phase diagram showing miscibility in both the liquid and solid states (right).[104]

In many systems the components have the same crystal structure, and therefore may be completely miscible (completely soluble in each other) in the solid form, forming a continuous solid solution.[104] In this case the diagram consists of two single-phase fields separated by a two-phase field (Figure 2-1 (right)). The phases in equilibrium across the two-phase field (the liquid and solid solutions) are called conjugate phases.[104] It is also possible to have a miscibility gap, where the two components are not completely soluble in each other. This may be due to temperatures not being high enough to favour mixing or a mismatch in crystal structures. Real phase diagrams are often far more complex than those shown in Figure 2-1, containing various phases depending on the miscibility's of the various components at different temperatures and compositions. This is partially determined by the crystal structure an element prefers to adopt at a given temperature and/or pressure.

Most metallic alloys show either cubic or hexagonal crystal structures, only one (a) or two (a and c) lattice constants need to be quoted respectively in order to define the structure. The structure of a particular nanoalloy will depend on both the composition and the synthetic conditions employed.[70]

2.1.2 Nanoparticle Synthesis

There are many methods for synthesising nanoalloys (see chapter 1 section 1.6). Synthesising nanoparticles directly on a support material is often a simple reaction with very few steps, but it can be hard to control size distribution and ensure a uniform composition in all individual nanoparticles.[102] Pulsed laser deposition techniques can give better size control but it is still difficult to ensure the composition in all nanoparticles. In contrast, ligand stabilised alloy nanoparticle synthesis can give good control over both size and composition, as the ligands prevent aggregation of the nanoparticles and also improve their solubility.[105]

A common method for the synthesis of nickel nanoparticles is the reaction of $Ni(acac)_2$ with oleylamine, under inert conditions, at temperatures over 200 °C. The oleylamine generally acts as the solvent, stabilizing ligand and reductant.[42, 101] Carenco and co-workers have studied this reaction in more detail, including investigating the by-products formed, in order to gain further insight into the mechanism and have confirmed that reduction is the rate determining step.[101] They have also shown that no reduction occurs below 200 °C, illustrated by a lack of the expected colour change of the solution from green to black which would signify the presence of polynuclear Ni^0 species (nuclei). At 215 °C reduction is complete within a few minutes. By carrying out equivalent reactions with alkylamines, such as hexadecylamine, they have concluded that the amine moiety and not the alkene one is responsible for reduction.[101]

Reaction proceeds via nucleation followed by particle growth,[70, 100, 105] the relative rates of these two steps determine the final particle size[100] and these rates are dependent on the reaction conditions used, including temperature, pressure, reaction time and the ratio of metal salts, stabiliser and reducing agent used.[70, 100]

Similar synthetic methods have also been used to form bimetallic NiCu[42] nanoalloys. Therefore, this would appear to be a suitable procedure for the synthesis of ligand stabilised nickel nanoalloys.

2.1.3 Aims

Synthesis and characterisation of bi- and trimetallic nickel nanoalloys was undertaken to enable electrocatalytic testing of their reduction activity. To allow for

good control of size and composition, ligand stabilised nanoparticles were produced.

2.2 Nanoalloy Synthesis

Various nanoalloys were synthesised using a method adapted from Zhang and co-workers[42] which involves the co-reduction of metal acetylacetonate precursors, pre-dissolved in ca. 1 mL of oleylamine at 85 °C, in a oleylamine/octadecene solution at elevated temperatures (above 200 °C) for 10 minutes. The oleylamine/octadecene solution was held under vacuum at 120 °C for 20 minutes before further heating to the reaction temperature under an argon atmosphere. The oleylamine acts as the solvent, reductant and stabilising ligand. The temperature is high enough to reduce the acetylacetonate precursors and a fast injection time is required to ensure a small size distribution, while the synthesis time helps determine the average particle size. During reaction the solution changes colour (initial colour depends on the metals present), resulting in a black solution due to reduction and formation of metal nanoparticles. A schematic of the reaction is shown in Figure 2-2.

$$Ni(acac)_2 + M^1(acac)_n + M^2(acac)_n \xrightarrow{240\ °C} Ni_{1-x-y}M^1_x M^2_y$$

$n = 2$: M^1 or M^2 = Fe, Co, Cu
$n = 3$; M^1 or M^2 = Cr, Fe, Mo, Ru
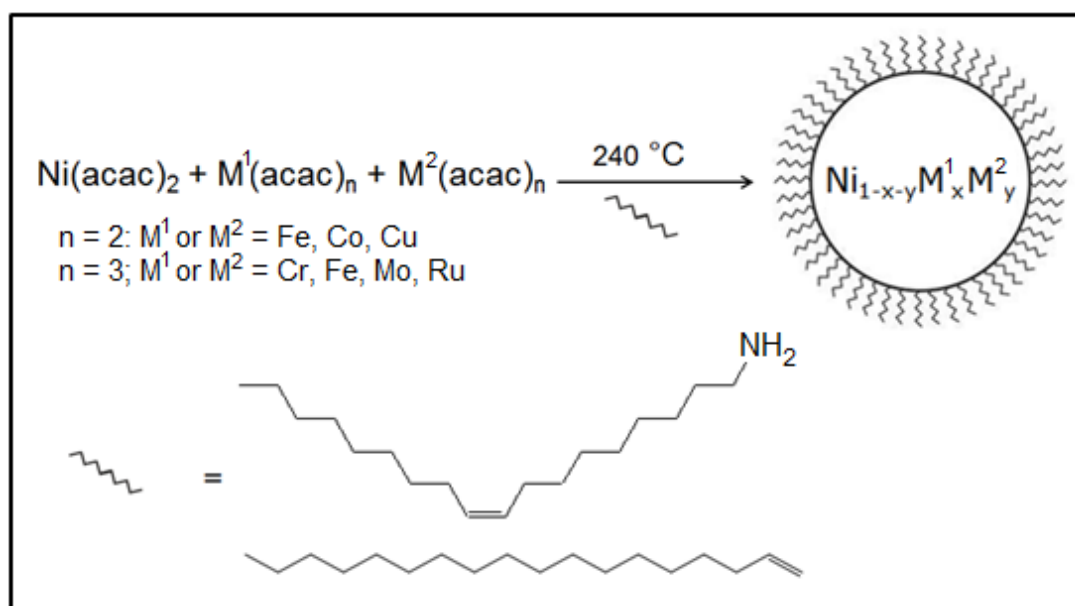
Figure 2-2 Schematic of the nanoparticle synthesis reaction.

A slight change in reaction conditions is known to have a large effect on the particle size and distribution,[42] as observed for $Ni_{0.5}Cu_{0.5}$ nanoalloys synthesised at different reaction temperatures or with different precursor injection rates (Figure 2-3). The

reaction carried out at 220 °C showed a much larger size distribution than that at 240 °C. We observed that the time taken to inject the metal precursors is also important as a slow injection time can result in an overlap between the nucleation and growth processes which results in an increase in the size distribution.[70] The optimum reaction conditions were found to be a temperature of 240 °C and a total inject time of less than 2 seconds.
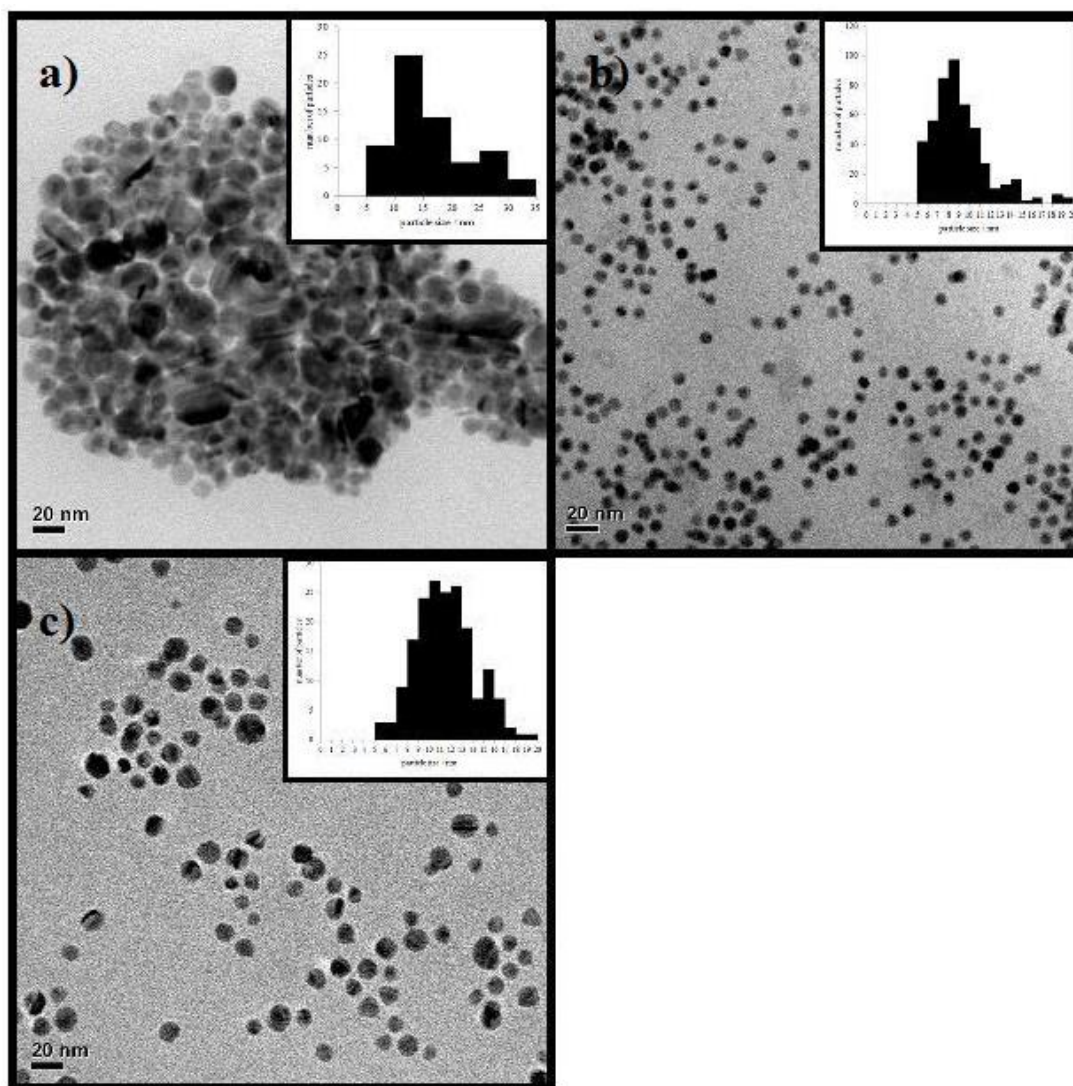
Figure 2-3 TEM images of $Ni_{0.5}Cu_{0.5}$ nanoparticles recorded at 50 kV and histograms of particle size distributions (insets), a) reaction at 220 °C, b) reaction at 240 °C c) reaction at 240 °C but slower injection time.

After synthesis, the solution was allowed to cool to room temperature under an inert atmosphere before adding 100 mL of ethanol and centrifuging at 4000 rpm for 1 hour. Then the liquid was removed and the nanoalloys were washed three times with a hexane/methanol mixture (1:3 ratio). It was noted that the first solution

removed was normally yellow in colour but this varied for certain materials and may suggest the presence of unreduced metal precursors.

The average particle size of the resulting alloy nanoparticles, determined using TEM, varies (from 5 nm to around 20 nm) depending on the metals used. Powder X-ray diffraction (XRD) was used to assess whether alloy formation was successful, to analyse the resulting structure and to determine the minimum crystallite size. This was achieved using the Scherrer equation. An underestimate of the true size is obtained as broadening due to size effects is indistinguishable from peak broadening due to the presence of strain in the crystal lattice and instrumental broadening of the peaks.[7, 106] Where possible, comparisons have been made to the expected structure based on bulk phase diagrams. The composition of the synthesised nanoalloys was determined using EDX and XRF.

2.3 Bimetallic Nanoalloys

2.3.1 Introduction

Many bimetallic alloys have been extensively investigated as electrodeposits for HER, including NiCo,[51, 52] NiCu,[54] NiFe,[26, 51, 71] and NiMo.[26, 72-74] These materials show promising activity however, the exact composition of the active material is not known. Certain elements, including iron and molybdenum are known to leach during electrochemical reduction. This improves surface roughness and therefore the active surface area making it more difficult to determine if an increase in activity is due to the material or just a surface area enhancement.

To allow for greater control over the alloy composition, while still providing a large surface area for electrocatalytic HER to occur on, nanoalloys were synthesised. NiCo, NiCu and NiFe were focussed on because they contain relatively cheap and abundant elements. One of the other main problems that must to be overcome is catalyst longevity. Therefore NiCr was also investigated at it has shown good stability in corrosive environments.[103] Although molybdenum and ruthenium are not as abundant as the first row transition metals, nickel alloys with these materials

have shown good activity in relevant applications.[26, 72-74, 79] Therefore, they provide a good comparison for the activity of the synthesised nickel alloys.

2.3.2   NiCu

Ni_xCu_{1-x} (0 < x < 1) nanoparticles exhibit a range of thermal catalytic activity including BH_4^- reduction,[42] and H_2 production via steam reforming.[80] Electrodeposited NiCu has also previously been investigated for the HER and showed good stability for 120 hours in 1 M KOH. [54]

Synthesis of ligand stabilised NiCu alloy nanoparticles is known.[42] The phase diagram for bulk Ni-Cu (Figure 2-4) consists of solid solutions with cubic structures, with a miscibility gap below 354.5 °C for 65.5 wt % Ni. The temperature below which this immiscibility occurs varies with composition, as seen in Figure 2-4.[104] This is due to the small positive enthalpies of solution of Cu in Ni and Ni in Cu for the bulk.[70] However, in nanoparticles the alloy-formation enthalpies may become negative.[79]
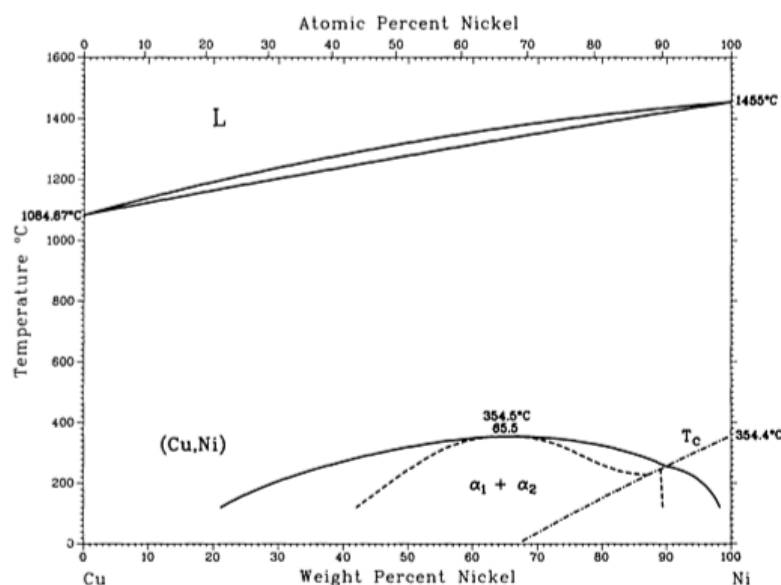
Figure 2-4 Alloy phase diagram for Cu-Ni shown in percent of nickel.[104]

Powder x-ray diffraction (XRD) was used to confirm the formation of alloys (Figure 2-5). The pure nickel nanoparticles exist in two polymorphs (one hexagonal and one cubic phase); however the Ni_xCu_{1-x} alloy nanoparticles solely adopt the cubic phase,

consistent with literature findings.[42] The single set of peaks, present in the alloy XRD spectra, also supports alloy formation as a mixture would result in separate peaks corresponding to nickel and copper. The peaks were also shifted to lower angles compared to the pure nickel and the lattice parameter, a, was calculated by rearranging Braggs law (Equation 2-1 and Equation 2-2). Where; θ is the diffraction angle, λ is the radiation wavelength (0.071073 nm for a Mo Kα radiation source.) and d is the interplannar spacing with indices h, k and l. By taking an average of values calculated for the (111) and (200) peaks, which occur at approximately 2θ = 20 ° and 23 ° respectively (for more precise angels see Table A1 in Appendix 1), for pure nickel nanoparticles, a = 0.35 nm and for both $Ni_{0.7}Cu_{0.3}$ and $Ni_{0.5}Cu_{0.5}$, a = 0.37 nm. For the $Ni_{0.3}Cu_{0.7}$ structure, the peaks were not intense enough to allow for accurate calculation of the lattice parameter.

$$2d\sin\theta = n\lambda \qquad\qquad \text{Equation 2-1}$$

$$d = \frac{a}{\sqrt{h^2 + k^2 + l^2}} \qquad\qquad \text{Equation 2-2}$$
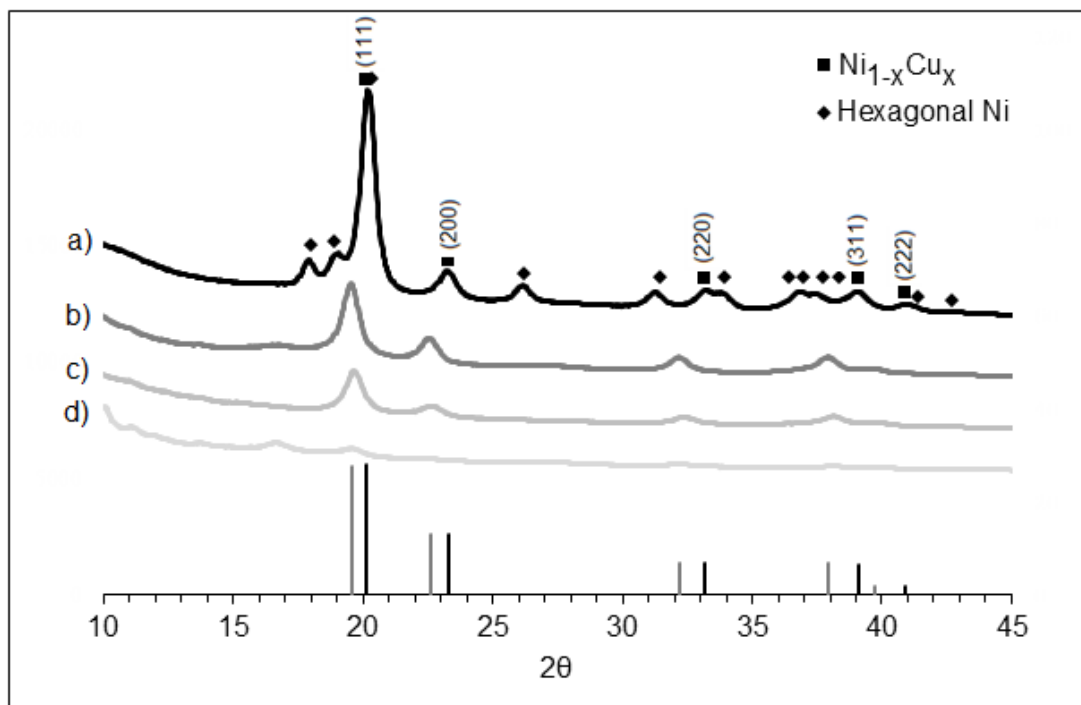
Figure 2-5 Powder XRD diffractogram of $Ni_{1-x}Cu_x$ materials where x = a) 0, b) 0.3, c) 0.5 and d) 0.7, showing formation of single face-centred cubic phase, alloy materials. Standards for the cubic polymorphs of the individual metals, nickel (black) and copper (grey), are given as lines below.

The crystallite size, D, was also estimated from the powder XRD spectra, using Scherrer's formula (Equation 2-3). Where; k is the Scherrer constant (0.89), λ is the wavelength of the x-ray radiation (0.07107 nm), β is the full width at half maximum (FWHM) of the diffraction peak measured at 2θ and θ is the Bragg diffraction angle.

$$D = \frac{k\lambda}{\beta cos(\theta)}$$

Equation 2-3

This method provides a minimum estimation of crystallite size as it cannot separate the contributions from size and strain to the peak broadness. Using transmission electron microscopy (TEM) allows for more accurate determination of the particle size. Particle sizes based on TEM images are around 10 nm for $Ni_{1-x}Cu_x$ (x = 0.3, 0.5 and 0.7) and larger for the pure nickel nanoparticles (Figure A1), at around 15 nm. A summary of average particle sizes can be seen in Table 2-1.

Table 2-1 The size and average composition of synthesised $Ni_{1-x}Cu_x$ nanoalloys.

Alloy Composition	Average Composition from XRF	TEM average particle size / nm	XRD crystallite size (Scherrer's formula) / nm
Ni	Ni	15.0 ± 3.5	4.5
$Ni_{0.7}Cu_{0.3}$	$Ni_{0.64}Cu_{0.36}$	10.0 ± 3.0	2.7
$Ni_{0.5}Cu_{0.5}$	$Ni_{0.46}Cu_{0.54}$	9.0 ± 2.5	2.7
$Ni_{0.3}Cu_{0.7}$	$Ni_{0.18}Cu_{0.82}$	11.0 ± 3.0	-
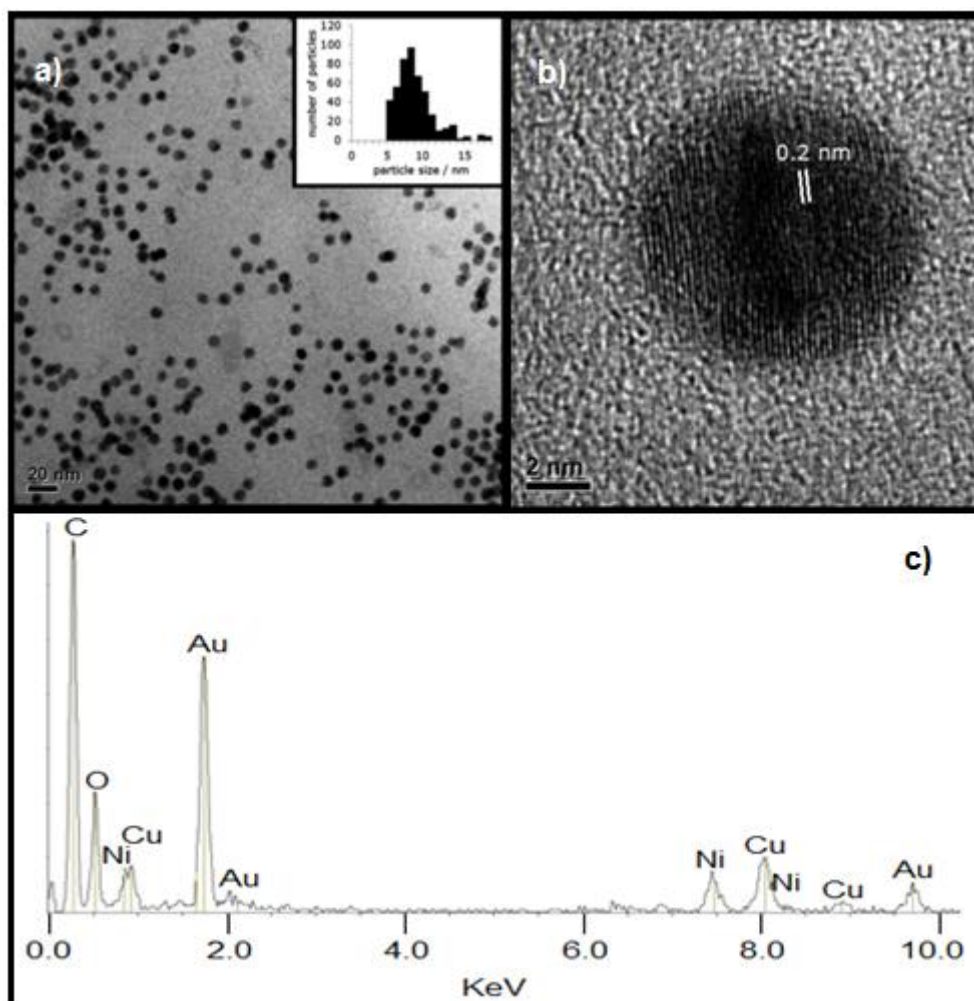
Figure 2-6 $Ni_{0.5}Cu_{0.5}$ nanoalloy TEM at magnifications of a) 50,000 with histogram of size distribution (inset) and b) 800,000 showing the lattice fringes and c) EDX or a single nanoalloy showing the presence of Ni and Cu.

TEM images also indicate the formation of uniformly spherical particles with a reasonably narrow size distribution (Figure 2-6 a)). By using EDX it was possible to determine the composition and confirm the presence of both metals in individual nanoparticles, supporting alloy formation (Figure 2-6 c)). The large signal corresponding to gold is from the TEM grid and the carbon is from the ligands and the TEM grid. Electron diffraction was also carried out and an example is given in Appendix 1, Figure A2. The average composition was confirmed by X-ray fluorescence (XRF, Figure 2-7) and the average compositions for each material can be seen in Table 2-1.
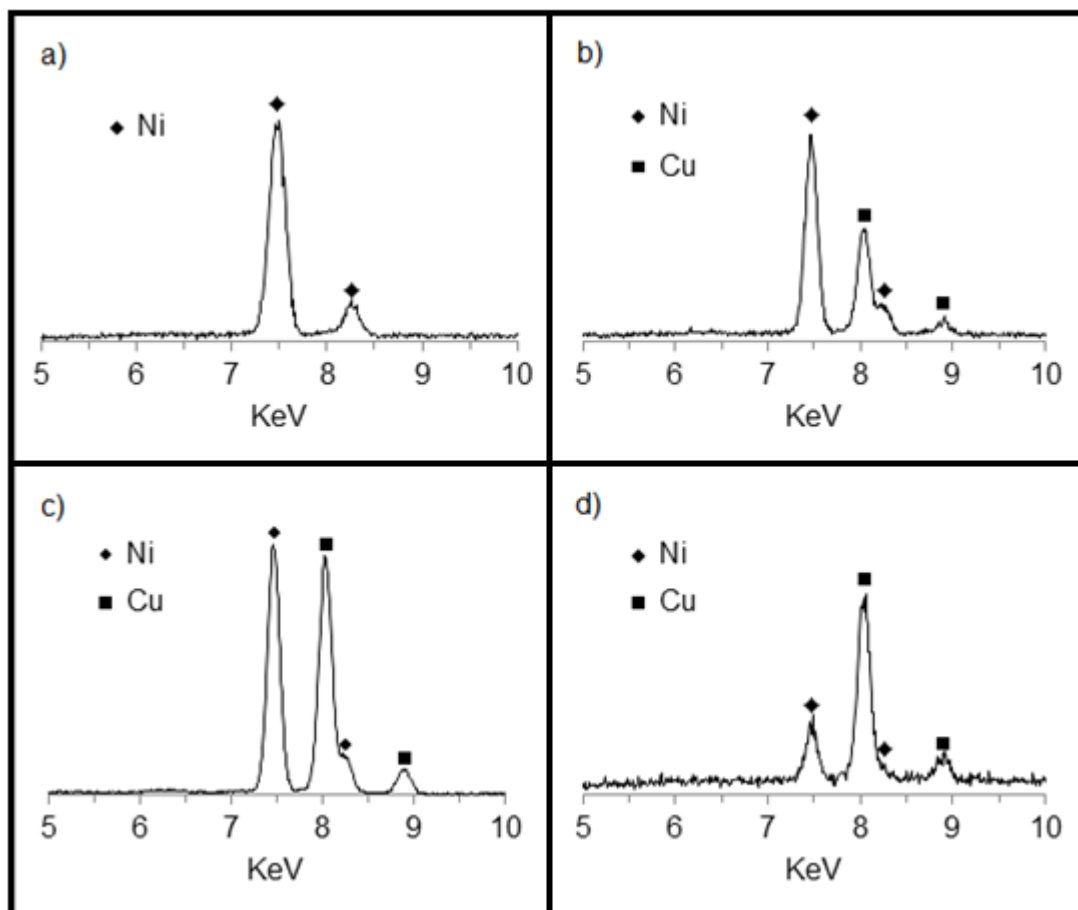
Figure 2-7 XRF spectrum of a) Ni, b) $Ni_{0.7}Cu_{0.3}$, c) $Ni_{0.5}Cu_{0.5}$ and d) $Ni_{0.3}Cu_{0.7}$ nanoalloys.

For the $Ni_{0.7}Cu_{0.3}$ and $Ni_{0.5}Cu_{0.5}$ nanoalloys, the average composition measured by XRF is relatively close to that expected based on the molar ratios used in the synthesis (giving compositions of $Ni_{0.64}Cu_{0.36}$ and $Ni_{0.46}Cu_{0.54}$ respectively). However, the $Ni_{0.3}Cu_{0.7}$ nanoalloy appears to contain a much lower concentration of nickel than expected ($Ni_{0.18}Cu_{0.82}$). This may suggest that this is a particularly stable composition and preferentially forms.[70] Also, in all cases the copper content is higher than expected; this may be due to the relative redox potentials of nickel (-0.257 V) and copper (0.3419 V). Copper has a more positive redox potential and is therefore more easily reduced, resulting in more copper atoms being incorporated in the nanoalloys.

The difference in reducibility of the copper and nickel may also explain why nickel nanoparticles show a mixture of the hexagonal and cubic phases whereas the NiCu nanoalloys only show the cubic phase. As copper is reducing first and forming the nuclei for further particle growth it may also dictate the crystal packing. However,

copper forming the initial nuclei does not necessarily mean that a core-shell, rather than a mixed alloy structure is being formed. The atomic radii and electronegativity of nickel (1.97 Å and 1.91) and copper (1.96 Å and 1.90) are very similar, so once both elements are reduced there may be little difference in preference for the core or surface of the particle. Although Zhang and co-workers carried out an X-ray line scan using annular dark-field scanning transmission electron microscopy (ADF-STEM) which suggested that the core may be more copper rich and the surface more nickel rich, particularly in larger particles (> 20 nm).[42] Nickel is the more active HER catalyst, therefore having a high nickel content in the shell may be beneficial as core-shell alloys with a platinum shell are known to have comparable or even better HER activity than pure platinum.[50]

2.3.3   NiCo

Brayner and co-workers have reported the templated growth of Co-Ni nanoalloys in polysaccharidic alginate biopolymers via formation of gelled capsules, yielding Co-Ni face centred cubic (fcc) solid solution nanoalloys with particle sizes of approximately 10 nm.[107] The synthesis of NiCo nanoparticles with the fcc structure has commonly been reported[108-110] and would be expected based on the phase diagram of bulk Co-Ni[104] (Figure 2-8).
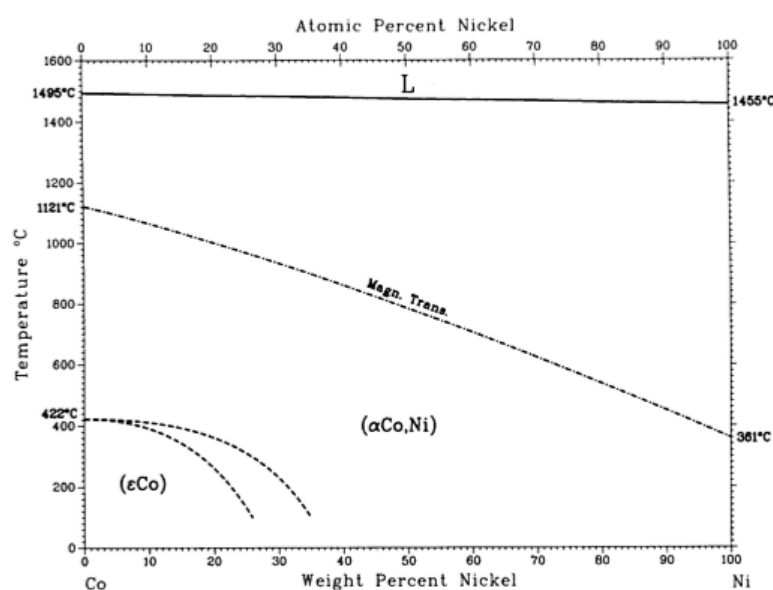
Figure 2-8 Alloy phase diagram for Co-Ni shown in percent of nickel.[104]

Except in the case of high cobalt concentrations (> 70%), a continuous solid solution containing cubic nickel and cobalt is expected, based on the bulk phase diagram. However, XRD suggests the NiCo nanoparticles obtained for the $Ni_{0.5}Co_{0.5}$ and $Ni_{0.7}Co_{0.3}$ compositions are hexagonal, with no evidence for the presence of a cubic phase (Figure 2-9). The hexagonal phase structure has been observed previously by Wu and co-workers for dendritic $Ni_{33.8}Co_{66.2}$ alloy microstructures.[111] These materials were synthesised by the reduction of the corresponding metal chlorides by hydrazine at 55 °C for 30 minutes, with ethanol as the solvent and cetyltrimethyl ammonium bromide (CTAB) as the stabilising ligand.[111] This indicates the importance the conditions have on the structure obtained and supports the observation that only the hexagonal phase is seen under the synthetic conditions used.
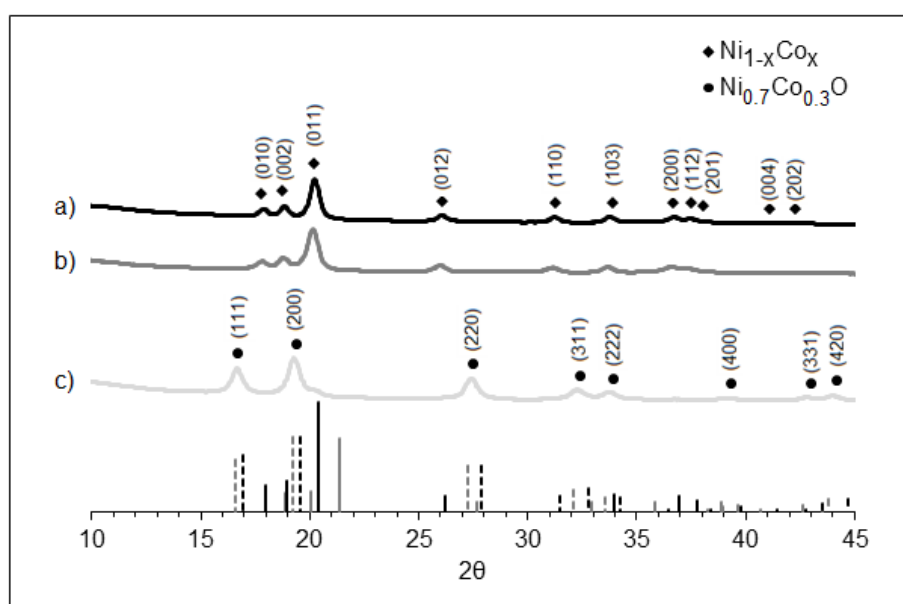
Figure 2-9 Powder XRD diffractogram of $Ni_{1-x}Co_x$ materials where x = a) 0.3, b) 0.5 and c) 0.7. Showing formation of single hexagonal phase, alloy materials. Standards for the hexagonal and metal oxide polymorphs are given for nickel (solid black), cobalt (solid grey), NiO (dashed black) and CoO (dashed grey).

The peaks were also shifted to higher angles compared to the pure nickel, as expected for incorporation of cobalt. The lattice parameters, a and c, were calculated using the lattice spacing equation for hexagonal structures (Equation 2-4) and the (011) peak, which occurred at $2\theta = 20.22°$ and $20.15°$ for $Ni_{0.7}Co_{0.3}$ and

$Ni_{0.5}Co_{0.5}$ respectively. For pure nickel a = 0.262 nm and c = 0.432 nm are expected. For the $Ni_{0.7}Co_{0.3}$ alloy a = 0.286 nm and c = 0.496 nm and for the $Ni_{0.5}Co_{0.5}$ alloy a = 0.287 nm and 0.497 nm were observed, showing an increase in lattice size with increased Co content. This is to be expected, due to the larger atomic radius of Co (2.00 Å) compared to Ni (1.97 Å).

$$d = \sqrt{\frac{3}{4}\left(\frac{a}{\sqrt{h^2 + k^2 + hk}}\right) + \frac{c^2}{l^2}}$$

Equation 2-4

Under the same synthetic conditions, the $Ni_{0.3}Co_{0.7}$ composition resulted in an alloy of nickel and cobalt oxides, as seen from the XRD (Figure 2-9). The lattice parameter, a, was calculated using Equation 2-2 and the (200) peak at 2θ = 19.28°. For NiO and CoO; a = 0.417 nm and a = 0.426 nm respectively; for the $Ni_{0.3}Co_{0.7}$ sample a = 0.424 nm which matches to a Ni:Co ratio of 3:7.

Table 2-2 The crystallite size and average composition of synthesised $Ni_{1-x}Co_x$ nanoalloys

Alloy Composition	Average Composition from XRF	XRD crystallite size (Scherrer's formula) / nm
$Ni_{0.7}Co_{0.3}$	$Ni_{0.71}Co_{0.29}$	7.8
$Ni_{0.5}Co_{0.5}$	$Ni_{0.48}Co_{0.52}$	6.7
$Ni_{0.3}Co_{0.7}$	$Ni_{0.18}Co_{0.82}$	5.9

TEM images show the hexagonal NiCo nanoalloys have an irregular shape and a larger particle diameter (23 ± 3 nm) than the cubic NiCu nanoalloys (Figure 2-10). Electron diffraction was also carried out and an example is given in Appendix 1, Figure A4. EDX confirms the presence of both metals in individual nanoparticles and XRF (Appendix 1, Figure A3) gave average ratios for each composition (Table 2-2).
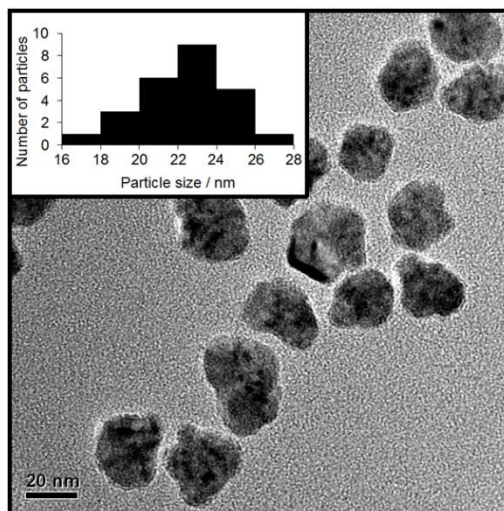
Figure 2-10 TEM of $Ni_{0.5}Co_{0.5}$ alloy nanoparticles, with histogram of size distribution (inset).

As with the NiCu nanoalloys, the average composition measured by XRF for the $Ni_{0.7}Co_{0.3}$ and $Ni_{0.5}Co_{0.5}$ nanoalloys is relatively close to that expected based on the molar ratios used in the synthesis (giving compositions of $Ni_{0.71}Co_{0.29}$ and $Ni_{0.48}Co_{0.52}$ respectively). However, again the $Ni_{0.3}Co_{0.7}$ nanoalloy appears to contain a much lower concentration of nickel than expected ($Ni_{0.18}Co_{0.82}$). This may be partly due to the presence of oxygen, in this material, which was not accounted for in the XRF analysis. Unlike with the NiCu nanoalloys, there does not appear to be one element that is more prevalent than expected. This is likely due to nickel and cobalt having very similar redox potentials (-0.257 V and -0.28 V) and would also make it more likely that a mixed rather than core-shell alloy has been formed.

2.3.4   NiFe

Ni_xFe_{1-x} (0 < x < 1) alloy nanoparticles have been shown to exhibit comparable activity to platinum for the decomposition of ammonia borane (NH_3BH_3) to dihydrogen, in water.[78] However, Fe^{II} is difficult to reduce, with a redox potential of -0.447 V whereas Fe^{III} is theoretically much easier to reduce, with a redox potential of -0.037 V. However, starting with an Fe^{II} or Fe^{III} precursor did not affect the nanoalloy structure formed. In both cases a bimetallic oxide with the inverse spinel structure was obtained (Figure 2-11). The synthetic conditions used were not strong enough to reduce the iron although the iron was still incorporated. Also, the

$Ni_{0.3}Fe_{0.7}$ material did show the hexagonal and cubic metal phases as well as the $NiFe_2O_4$ structure.
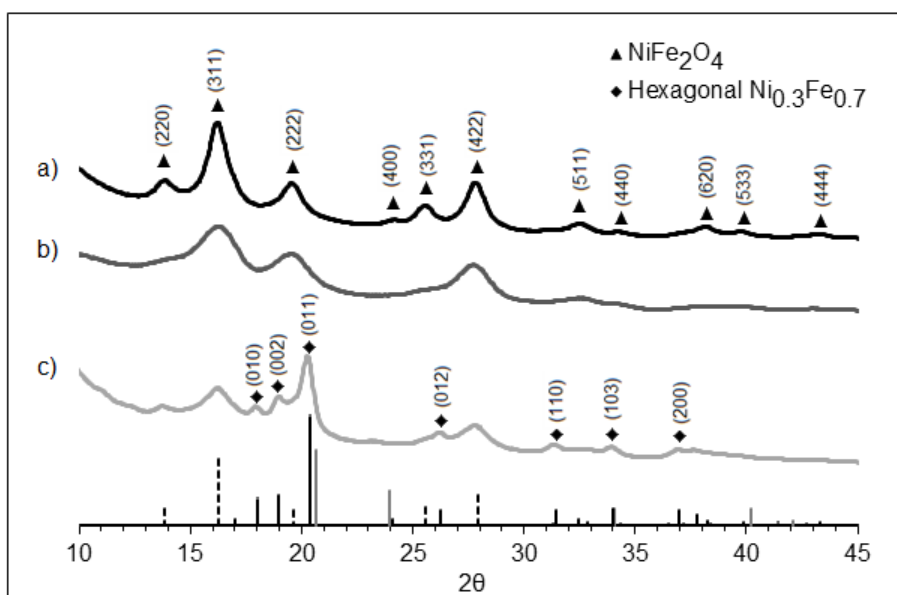
Figure 2-11 Powder XRD spectra for $Ni_{1-x}Fe_x$ materials where x = a) 0.3, b) 0.5 and c) 0.7. Standards for the hexagonal nickel (solid black), cubic iron (solid grey), and $NiFe_2O_4$ (dashed black) are also shown.

It is known that nanoparticles of light transition metals can be difficult to prepare as the ions of these transition metals are difficult to reduce and once zerovalent they are easy to oxidise.[102] Using a stronger reducing agent, such as $LiBEt_3H$ may overcome this issue.[79]

However, it is also possible for the oxide to be reduced during electrochemistry and nickel-iron-oxides have recently been shown to be active HER electrocatalysts.[15] Therefore, these oxide nanoalloys were still tested for HER activity.

2.3.5 NiCr

Ni-Cr alloys have been used extensively in dentistry, due to their corrosion resistance.[103] Aljohani and co-workers have studied the corrosion behaviour of a range of NiCr thin film alloys under acidic conditions and linked the stability to the crystal structure.[112] Ni-Cr alloy nanoparticles synthesised directly onto supports

have also been previously reported although the alloy composition of individual particles was seen to vary greatly from the average.[90] Little has been reported on the synthesis of ligand stabilised NiCr naonalloys. This may be due to the large difference in reduction potentials between nickel (-0.257 V) and chromium (-0.744 V) which makes it difficult to successfully co-reduce the nickel and chromium precursors. Also, the very negative redox potential makes it difficult to reduce the chromium at all.

Initial attempts to synthesise NiCr nanoalloys, employing the same procedure used to synthesise the other Ni_xM_{1-x} alloys, were unsuccessful. The resulting NiCr nanoparticles had an average diameter of 23 ± 4.5 nm and analysis by EDX and XRF revealed that less than 1 % Cr had been incorporated into the particles. Attempts were made to increase the amount of Cr incorporated by increasing the temperature, reaction time, molar ratio of Cr precursor used and by adding the chromium and nickel sequentially rather than combined. In all cases the amount of chromium incorporated was less than 1 % (see Appendix 1, Figure A5).

The XRD indicates that as in the case of pure nickel nanoparticles, the structure is a mixture of hexagonal and cubic phases with the majority being hexagonal (Figure 2-12). This is understandable as the majority of the particle is Ni even though chromium would normally lead to cubic structures. Unfortunately, a phase diagram for NiCr alloys at temperatures below 500 °C could not be found for comparison.
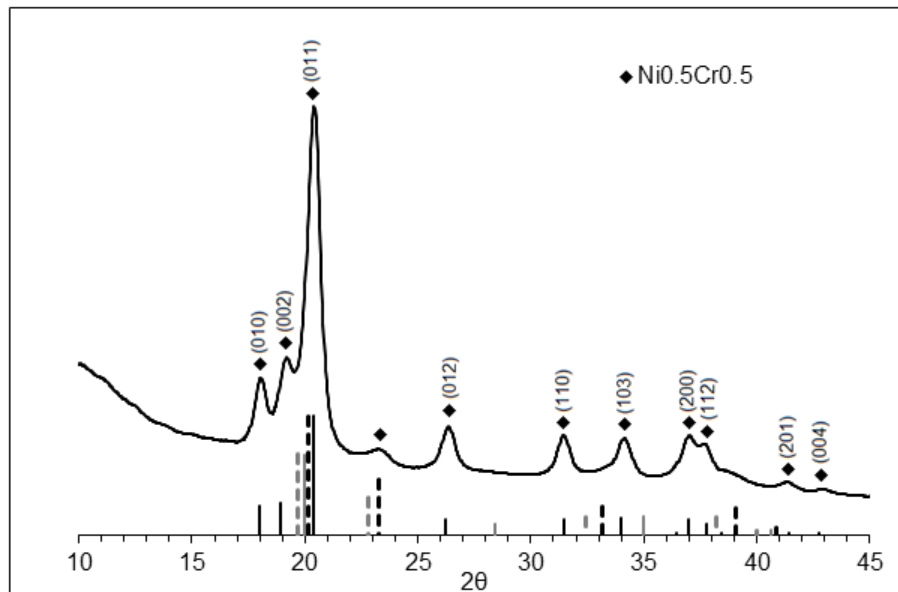
Figure 2-12 Powder XRD of $Ni_{0.5}Cr_{0.5}$ nanoalloys showing mainly hexagonal phase of alloyed material. Standards for the hexagonal (solid black lines) and cubic (dashed black lines) nickel polymorphs and chromium body centred (solid grey lines) and cubic (dashed grey lines) are shown.

As XRF gives an average composition for the bulk sample and the percent of chromium appeared too low to pick up by EDX, it is possible than not all particles have the same composition, those with chromium giving rise to cubic structures and those without forming hexagonal nickel particles. This could also explain the differences in shape and size observed by TEM (Figure 2-13). The TEM revealed the presence of spherical and oval particles as well as some irregular shapes closer to those seen for the NiCo nanoalloy materials.
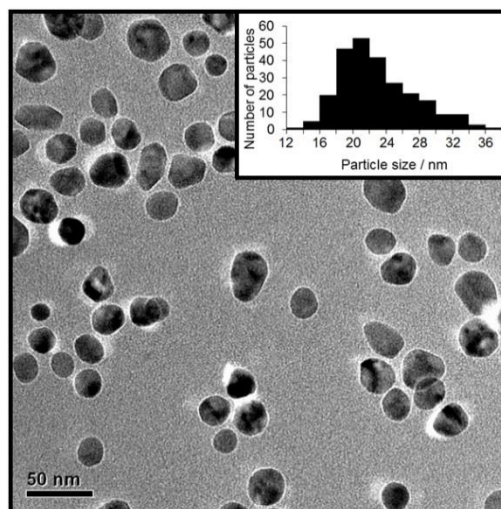
Figure 2-13 TEM of $Ni_{0.5}Cr_{0.5}$ alloy nanoparticles with histogram of size distribution (inset)

Employing different stabilising ligands and stronger reducing agents may allow for the synthesis of ligand stabilised NiCr nanoalloys. Although the larger atomic radius of chromium (2.06 Å compared to 1.97 Å for nickel) and its much more negavtive redox potential make it likely that resulting nanoalloys would have the core-shell structure with the nickel at the core.[70] As the nickel is the more active HER catalyst it appears formation of ligand stabilised NiCr nanoalloys by co-reduction are unlikely to be beneficial to HER activity.

2.3.6   NiMo

NiMo has been studied extensively for the HER in both acidic[26, 74] and basic[27, 58] conditions. It has shown good activity, however, as in the case of pure nickel catalysts, there are stability issues with this material. A NiMo nanoalloy was synthesised in order to compare the activity and stability of this known HER material to the other nanoalloys under investigation. Molybdenum is in the same group as chromium but as a second row transition metal it is much easier to reduce (MoO_2 has a redox potential of -0.152 V and Mo^{3+} has a redox potential of -0.2 V). Unlike the other metals investigated, the Mo was synthesised from an $MoO_2(acac)_2$ complex as the $Mo(acac)_3$ is relatively unstable.[25] Otherwise, the same synthetic conditions were used.

As for NiCo and NiCr materials, the hexagonal structure was observed by XRD (Figure 2-14), although a small amount of the cubic phase also appears to exist. The lattice parameter(s) were not calculated due to the presence of both phases and the resulting overlap of peaks in the XRD. XRF gave a NiMo composition of $Ni_{74}Mo_{26}$ which is different to the expected $Ni_{0.5}Mo_{0.5}$ composition. This may be due to the different molybdenum precursor used.
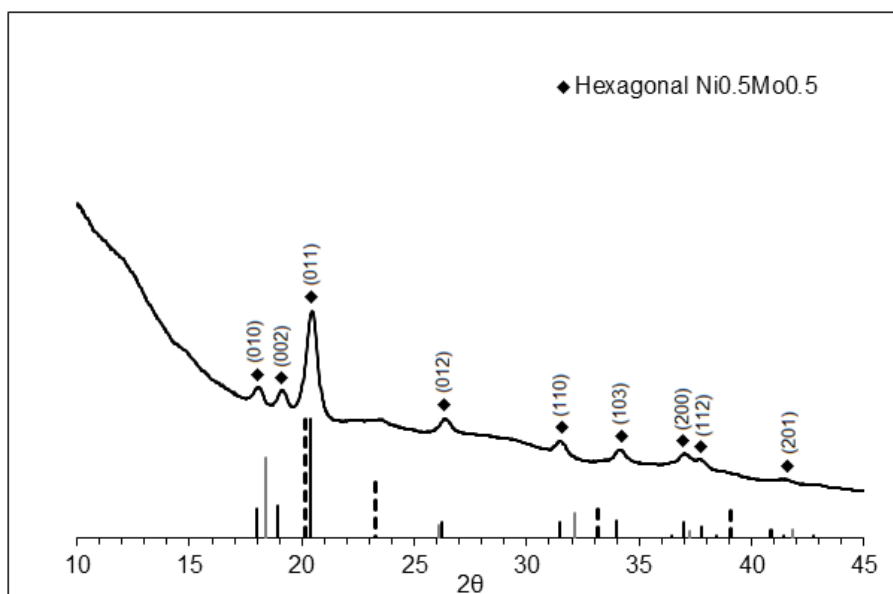
Figure 2-14 Powder XRD of $Ni_{0.5}Mo_{0.5}$ nanoalloys showing mainly hexagonal phase of alloyed material. Standards for the hexagonal (solid black lines) and cubic (dashed black lines) nickel polymorphs and body centred molybdenum (solid grey lines are shown.

2.3.7 NiRu

NiRu nanoalloys have also been synthesised, as in the case of NiFe nanoalloys, they show good activity for hydrogen production via ammonia borane reduction.[79] Ruthenium also has a higher redox potential than that of iron (0.455 V compared to -0.037 V) and therefore, it should be easier to prepare alloy nanoparticles using ruthenium.[102]

As with NiCu alloys, although nickel and ruthenium are immiscible in the bulk, alloy formation at the nanoscale is possible.[79] In order to synthesise the NiRu nanoparticles, first the $Ru(acac)_3$ precursor was synthesised following literature methods.[113]

The TEM images show uniform spherical particles with a much smaller average particle size than that obtained for the nickel nanoalloys with first row transition metals (Figure 2-15). The average particle size is 6.5 ± 1.0 nm.
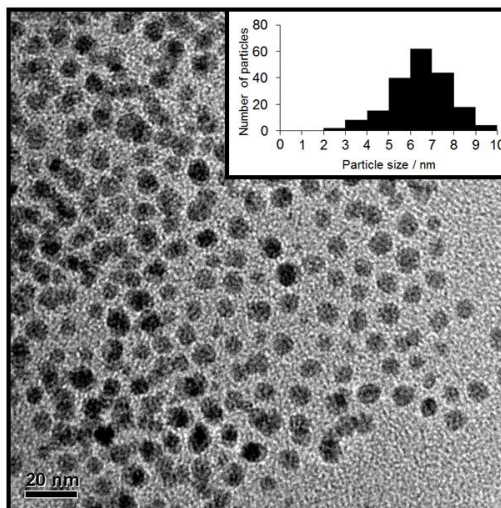
Figure 2-15 TEM of $Ni_{0.5}Ru_{0.5}$ alloy nanoparticles with histogram of size distribution (inset).

The smaller size of these nanoalloys may explain why XRD analysis was unsuccessful, with no diffraction peaks being visible. Therefore, the structure of these nanoalloys cannot be confirmed. Also no NiRu phase diagram exists for comparison (due to the immiscibility of these components in the bulk). However, ruthenium normally exists in a hexagonal phase and therefore it is likely that the NiRu nanoalloy exists in a hexagonal phase, similar to the NiCo nanoalloys.

2.3.8   Summary of Bimetallic Nanoalloys Synthesised

An adapted literature nanoalloy synthesis method[42] has been used to successfully synthesise a variety of bimetallic nickel nanoalloys with various compositions. However, due to their very negative redox potentials, it was not possible to synthesise NiFe or NiCr nanoalloys using this method. Although a NiFe-oxide nanoalloy was formed and may still be active for HER.

The structure formed is very material dependent and appears to be related to how easily the different elements are reduced. Whereas both cubic and hexagonal phases were observed for pure nickel nanoparticles, only a cubic phase was

observed for NiCu nanoalloys and only the hexagonal phase was observed for NiCo nanoalloys. The arrangement of elements within the particles, to determine if they are core-shell or mixed nanoalloys has not been established as line scans with very small nanoparticles, such as those synthesised, is difficult and often inconclusive (as the core is much smaller than in larger particles and so less of a difference is seen across the sample).

2.4 Trimetallic Nanoalloys

The nanoalloy synthesis method can successfully produce a range of bimetallic nanoalloy materials therefore, it was also used to attempt to synthesise trimetallic materials. Being able to consistently control the atomic ratios becomes more difficult the more complex the alloy becomes. However, trimetallic nickel alloys have been shown to be active HER electrocatalysts.[76, 114, 115] Also it is more likely that a more complex alloy will have the needed combination of stability and activity. As an ideal catalyst should be made of abundant and relatively cheap materials, synthesis of trimetallic nickel alloys with first row transition metals (specifically chromium, cobalt, copper and iron) was focussed upon. Even though NiMoM alloys have been shown to be active electrocatalysts for HER; these compositions were not focussed on as molybdenum is much less abundant than the first row transition metals[46] and most of the NiMoM alloys tested still have long term stability issues.[11]

2.4.1 NiCuCo

NiCuCo has been investigated for the HER as a 3D nano-network structure.[114] Also, nanocrystalline cobalt-nickel-copper particles have previously been synthesised, however these particles formed large aggregates and the XRD data showed alloying did not occur.[116] To the best of our knowledge, this is the first reported synthesis of NiCuCo nanoalloys. The XRD shows one set of peaks, with a lattice parameter of a = 0.36 nm. The cubic polymorph is observed and the single set of peaks confirms alloying has occurred (Figure 2-16).
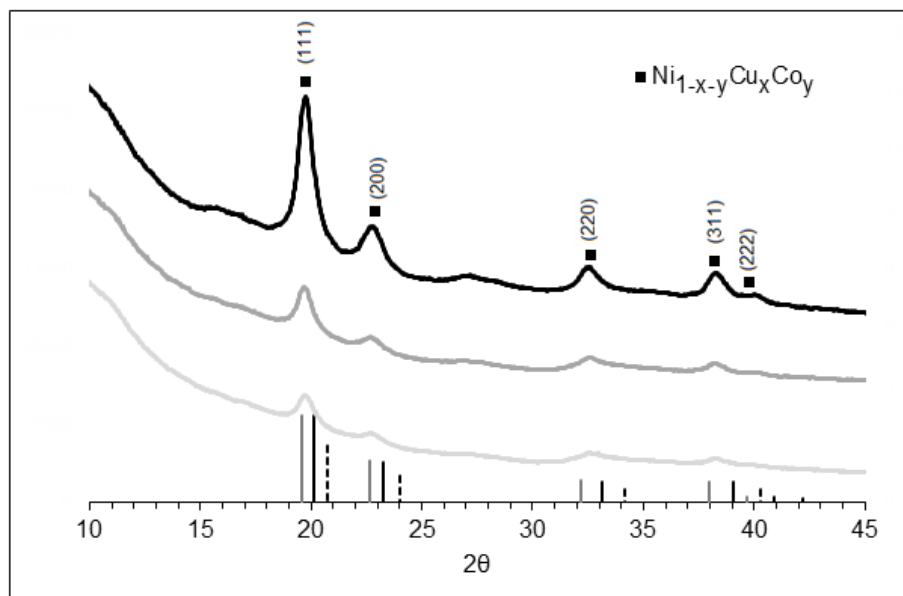
Figure 2-16 Powder XRD spectra for $Ni_{1-x}Cu_xCo_y$ materials where a) x = 0.3, y = 0.2, b) x = 0.3, y = 0.3 and c) x= 0.27, y = 0.27; showing formation of cubic phase, alloy materials. Standards for cubic nickel (solid black lines), copper (solid grey lines) and cobalt (dashed black lines) are shown.

It is also interesting to note that the hexagonal phase was not observed although bulk Co usually exhibits the hexagonal phase below 417 °C.[116] As previously noted, the hexagonal phase was observed for the bimetallic NiCo nanoalloy (see section 2.3.3) and the pure nickel nanoparticles gave a mixture of the cubic and hexagonal phases (see section 2.3.2), whereas the NiCu nanoalloys showed just the cubic phase. This again suggests the Cu has a large influence on the nanoalloy structure, as copper has a much more positive redox potential (0.3419 V) compared to both nickel (-0.257 V) and cobalt (-0.28 V). Therefore, it is likely that the copper is the first element reduced during the co-reduction and forms cubic phase nuclei that direct further nanoparticle growth giving purely cubic phase nanoalloys. It may also mean that, as in the case of the NiCu nanoalloys, the copper is more likely to be in the core of the particle rather than at the surface.

Attempts were made to synthesise NiCuCo nanoalloys with marginally different atomic ratios to determine how much control over the composition this synthesis method provided. This was reasonably successful although XRF showed that less cobalt than expected was present in all cases (Table 2-3). As with the NiCu nanoalloys, it is copper that is more prevalent than expected. Again this can be

explained by the relative redox potentials of the three elements, with copper being the most easily reduced and cobalt the least.

Table 2-3 The crystallite size and average composition of synthesised $Ni_{1-x-y}Cu_xCo_y$ nanoalloys

Alloy Composition	Average Composition from XRF	XRD crystallite size (Scherrer's formula) / nm
$Ni_{0.5}Cu_{0.3}Co_{0.2}$	$Ni_{0.52}Cu_{0.32}Co_{0.16}$	4.8
$Ni_{0.4}Cu_{0.3}Co_{0.3}$	$Ni_{0.41}Cu_{0.36}Co_{0.23}$	5.6
$Ni_{0.46}Cu_{0.27}Co_{0.27}$	$Ni_{0.45}Cu_{0.33}Co_{0.22}$	5.1

TEM showed spherical particles with a relatively small size distribution (Figure 2-17). Average particle size is 11.5 ± 2.5 nm, similar to the sizes obtained for the NiCu nanoalloys and substantially smaller than those obtained for the NiCo nanoalloys. Electron diffraction and EDX were also carried out and example data is given in Appendix 1, Figure A8.
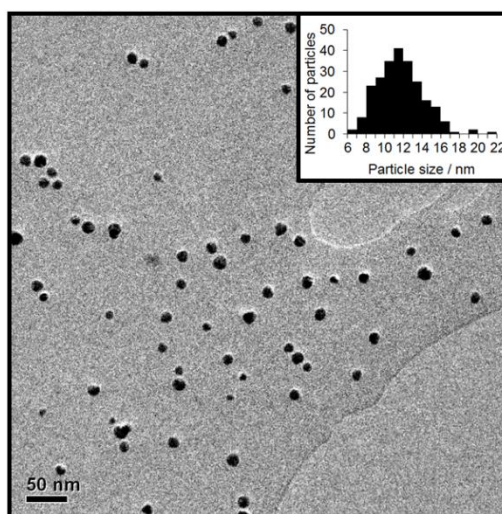
Figure 2-17 TEM of $Ni_{0.5}Cu_{0.3}Co_{0.2}$ alloy nanoparticles with histogram of size distribution (inset)

2.4.2 NiCuFe

Ni-Cu-Fe materials have been investigated as electrocataysts for the HER in alkaline solutions,[115] hydrogen production from methanol[117] and decomposition of hydrous hydrazine.[118] However, as seen with the NiFe nanoalloys, the resulting materials often contained oxidised iron rather than $Fe^{(0)}$ and trimetallic alloys were not always formed.[117, 118]

The powder XRD shows the presence of a cubic phase that is shifted to lower angles than that of the pure nickel cubic phase (Figure 2-18), with a lattice parameter of a = 0.360 nm, again suggesting the copper has a large influence on the structure. However, there is also the presence of $NiFe_2O_4$ spinel structure as seen for the bimetallic NiFe samples. The $NiFe_2O_4$ spinel structure was also observed by Srivastava and co-workers when attempting to synthesise Cu-Ni-Fe metal oxide nanocomposites by a sol-gel combustion method.[119] However, they also observed CuO and FeO phases which we do not observe here. Although, due to the values at which peaks corresponding to CuO would be expected it is possible that this phase is present but just cannot be observed in the XRD.
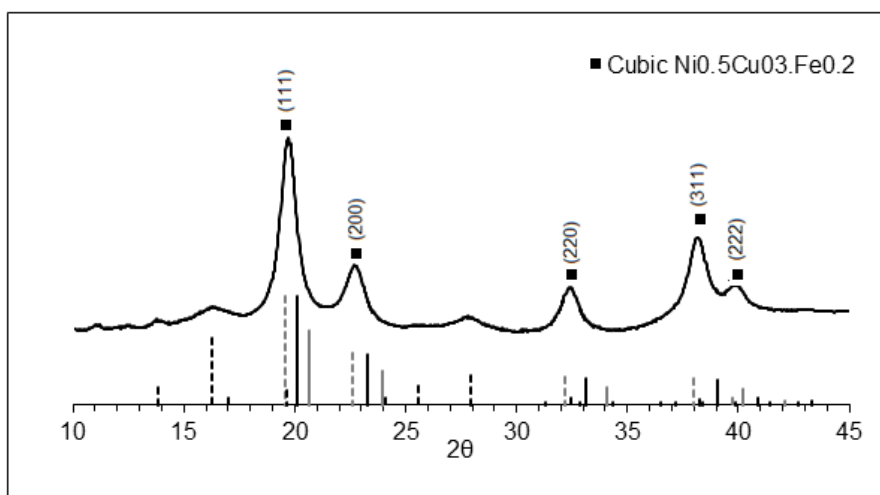
Figure 2-18 Powder XRD of $Ni_{0.5}Cu_{0.3}Fe_{0.2}$ nanoalloys showing spinel and metallic cubic phases. Standards for cubic nickel (solid black lines), copper (dashed grey lines), iron (solid grey lines) and $NiFe_2O_4$ (dashed black lines) are shown.

The TEM images show spherical particles and a wide range of particle sizes, although interestingly there appear to be two size distributions present (Figure

2-19). One particle size is centred around 8 nm and the other around 22 nm. This may suggest that the different sized particles are different materials, with one being the NiCuFe and the other being the $NiFe_2O_4$. EDX of one of the smaller particles shows the presence of all three elements. Electron diffraction was also carried out and is shown in Appendix 1, Figure A10.
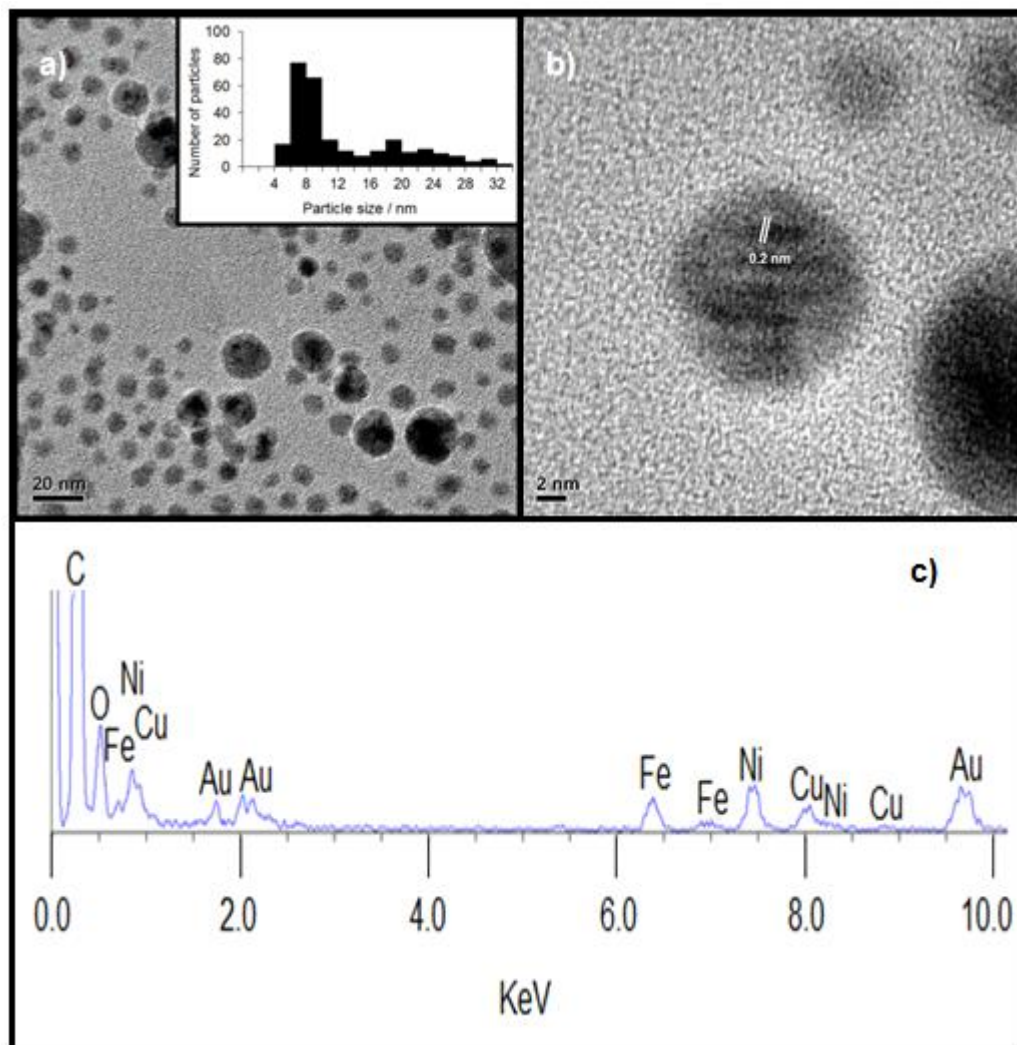
Figure 2-19 $Ni_{0.5}Cu_{0.3}Fe_{0.2}$ nanoalloy TEM at magnifications of a) 50,000 with histogram of size distribution (inset) and b) 800,000 showing the lattice fringes and c) EDX or a single nanoalloy showing the presence of Ni, Cu and Fe.

XRF gave a composition of $Ni_{0.49}Cu_{0.30}Fe_{0.21}$. Although not all the nanoalloys are the desired material, it is possible that reduction will occur during electrochemistry.

2.4.3 NiCoFe

NiCoFe has been used as an electrodeposit for HER in alkali solutions and showed higher activity than pure nickel,[76] although being an electrodeposit means the exact composition is unknown, and it was also uncertain whether the increase in activity was due to the composition or just an increase in surface roughness.[76] Therefore, this material is worth investigating to determine the source of the activity observed.

The XRD shows the hexagonal nickel phase as well as peaks corresponding to a NiO phase (Figure 2-20). This may indicate an oxide layer has formed on the surface and as with Ni/NiO core/shell nanaparticles may result in long term stability issues with this material.[45]
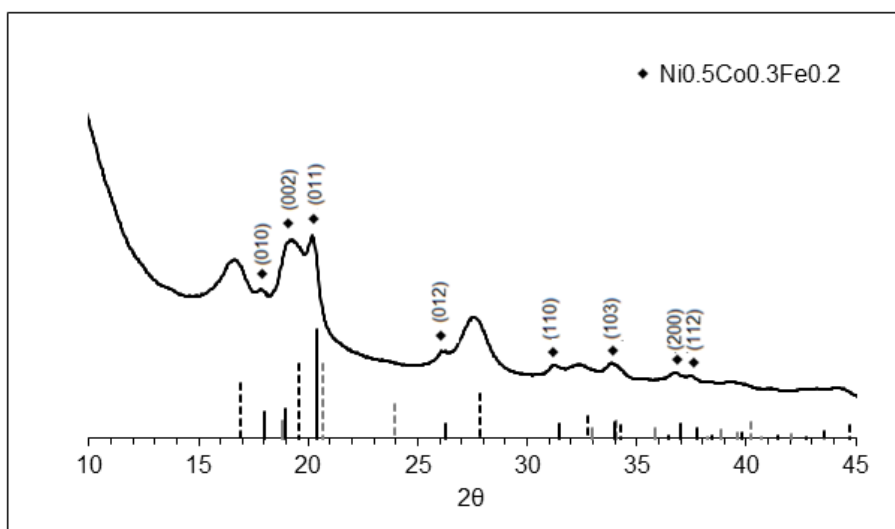
Figure 2-20 Powder XRD of $Ni_{0.5}Co_{0.3}Fe_{0.2}$ nanoalloys showing the presence of NiO and metallic hexagonal phases. Standards for hexagonal nickel (solid black lines), hexagonal cobalt (solid grey lines), cubic iron (dashed grey lines) and NiO (dashed black lines) are shown.

Unlike the other trimetallic nanoalloys synthesised, the $Ni_{0.5}Co_{0.3}Fe_{0.2}$ nanoalloy shows a hexagonal rather than cubic phase structure. This is consistent with observations of the bimetallic particles where the absence of copper lead to hexagonal or mixed phases being present. This is also the only nanoallloy containing iron that does not appear to contain the $NiFe_2O_4$ spinel phase.

The synthesis was repeated under identical conditions to assess how well the composition could be controlled and XRF analysis gave compositions of

$Ni_{0.56}Co_{0.26}Fe_{0.18}$ and $Ni_{0.58}Co_{0.24}Fe_{0.18}$, confirming good control over nanoalloy composition is possible. Electron diffraction and EDX were also carried out and example data is given in Appendix 1, Figure A12.

2.4.4 NiCuCr

Cu-Ni alloys, used for various applications, often contain small amounts of chromium as well as other metals in order to improve longevity.[103] Therefore attempts were made to synthesise a NiCuCr alloy. However, as with the NiCr material, little chromium was detected in the structure by XRF. A composition of $Ni_{0.63}Cu_{0.36}Cr_{0.01}$ was determined, although the XRD indicates an oxide phase may be present making the analysis less accurate. As with all copper containing nanoalloys synthesised, the $Ni_{0.5}Cu_{0.3}Cr_{0.2}$ nanoalloy displays the cubic phase (Figure 2-21) with a lattice parameter of a = 0.36 nm.
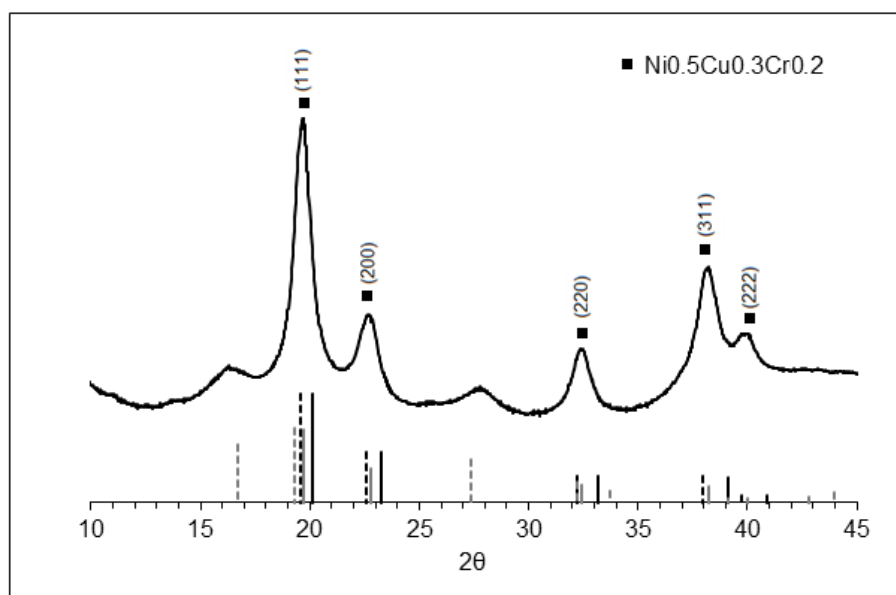
Figure 2-21 Powder XRD of $Ni_{0.5}Cu_{0.3}Cr_{0.2}$ nanoalloys showing the presence of metallic cubic and CuO phases. Standards for cubic nickel (solid black lines), cubic cobalt (dashed black lines), cubic chromium (solid grey lines) and CuO (dashed grey lines) are shown.

TEM images show an average particle size of 12.5 ±2.0 nm which is much smaller than that seen for the NiCr nanoalloy and only slightly larger than observed for the NiCu nanoalloys.
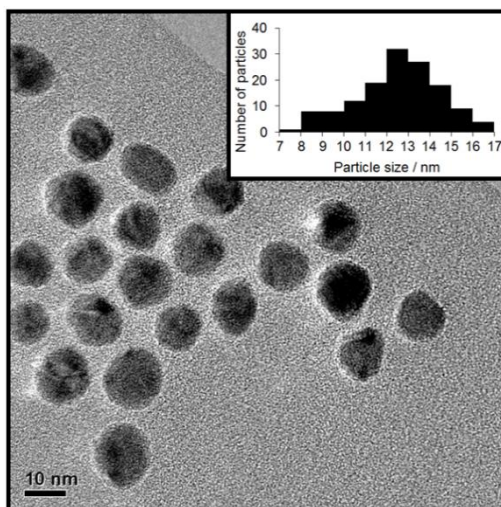
Figure 2-22 TEM of $Ni_{0.5}Cu_{0.3}Cr_{0.2}$ alloy nanoparticles with histogram of size distribution (inset)

In general, it appears this synthesis method is not suitable for the production of chromium containing nanoalloys. Although synthesis of trimetallic nickel nanoalloy combinations with copper, chromium and iron were possible.

2.5 Conclusions

Various bi- and trimetallic nickel nanoalloys with Cu, Co, Fe, Cr, Ru and Mo have been synthesised. Control over the composition is possible, even for trimetallic materials. Particle sizes range from around 5 to 20 nm depending on the alloy composition. The polymorphs observed are also structure dependent.

All copper containing nanoalloys show only the cubic phase. This has been attributed to the positive redox potential of copper, resulting in copper nuclei being formed and controlling particle growth. Conversely, all materials containing cobalt without copper show only a hexagonal phase. This is likely due to the similar redox potentials of cobalt and nickel and the ability of nickel to exist in both the cubic and hexagonal polymorphs. Therefore, in the absence of copper, cobalt appears to direct particle growth.

It was also noted that trimetallic nanoalloys containing iron were more successfully synthesised than the bimetallic NiFe nanoalloy. Iron can exist in various polymorphs and seems to be less likely to form oxide species when structure growth is strongly directed. Although some materials contain oxides, it is still possible for them to show HER activity. Therefore, the HER activity of synthesised nanoalloys will be discussed in Chapter 3.

3   Proton Reduction

3.1   Introduction

Hydrogen is an important clean energy alternative to fossil fuels as a chemical feed stock and possible transport fuel. Production of hydrogen from solar energy allows for the storage of this energy in chemical bonds. This energy can then be released when required. The production of hydrogen can be achieved electrochemically and often employs a proton reduction electrocatalyst to increase activity and decrease overpotentials.

The literature contains many examples of electrocatalytic systems for HER using a wide range of elemental compositions and microstructures and prepared in a variety of ways,[19] as previously discussed in chapter 1, section 1.4. However, direct comparison between different studies is rarely possible as no standard conditions exist for the testing of HER electrocatalysts. High-throughput combinatorial techniques are useful in identifying new materials active compositions of ternary and quaternary compositions although the synthesis techniques used in these cases can be unreliable.

 Recently McCrory and co-workers assessed a range of electrocatalysts for water splitting under identical conditions in order to directly compare activities for the HER in both acidic and basic conditions. However, as with many other examples, they have used electrodeposition to synthesise their electrocatalysts and have made no attempt to analyse the quantitative composition before or after electrochemical testing. It is known that the exact composition can have a large effect on activity in bimetallic electrocatalysts and it is expected that this would be even more important in trimetallic materials. Therefore, although this study may help identify materials for further investigation it may also overlook potentially active materials due to the elemental ratio in the composition tested.

To improve control over composition and also to increase the surface area of the electrocatalyst, nanoparticles can be synthesised. Another advantage of nanoparticles is that elements that would not form alloys in the bulk can be created at the nanoscale. This results in a wider range of potential materials that can be tested for HER activity.[42, 70, 79]

Various nanoparticles have been tested for electrocatalytic activity however, again, there is no standard procedure employed.[25-28, 55, 57, 58, 96, 120, 121] Often nanoparticles are loaded onto the end of the electrode by first supporting onto high surface area carbon. This may then be

mixed with Nafion (a proton transfer membrane material) to increase stability. However, catalyst loadings vary widely and the presence of stabilising ligands used in nanoparticle synthesis can affect electrocatalytic activity. Being able to support the electrocatalytic nanoparticles directly on the electrode would allow for a much simpler procedure. Also, if the catalyst is to be incorporated into a solar device it is highly likely that it would be deposited directly onto a semiconductor and therefore measurements of HER activity where the catalyst has been directly deposited onto the electrode will be the most representative. Development of a quick and straightforward method for testing HER activity of nanoparticle proton reduction catalysts would be beneficial.

3.1.1   Electrochemical Techniques

Proton reduction catalysts are often tested electrochemically to assess their activity and stability. Common techniques used include cyclic voltammetry (CV), linear sweep voltammetry (LSV), controlled potential electrolysis (CPE) and electrochemical impedance spectroscopy (EIS).

3.1.1.1   Electrochemical theory

The current density, i, is measured vs. potential. For a cathodic process the current density will be negative, as the electroactive species is being reduced and so gaining electrons from the electrode. Whereas an anodic process would give a positive current density (species is oxidised and loses electrons to the electrode). The electrode potential, E for a reaction is derived directly from the free energy change for that reaction (Equation 3-1).

$$\Delta G = -nFE \hspace{4cm} \text{Equation 3-1}$$

Where n is the number of electrons transferred and F is the Fraraday constant (96485 C mol^{-1}). The cell reaction will only be spontaneous if the free energy change associated with the net cell reaction is negative, otherwise a potential must be applied between the two electrodes. Even if the reaction is thermodynamically favourable, the rate of electrolysis (e.g. the current density, i) will depend on the kinetics of the two electrode reactions.

The total cell voltage is given by Equation 3-2; where E_e^C and E_e^A are the reversible potentials of the cathode and anode cell respectively, η_A and η_C are the overpotentials of the anode and cathode cells and iR is the potential drop due to resistance of electrolyte solution between the electrodes.

$$V = E_e^C - E_e^A - |\eta_A| - |\eta_C| - iR$$

Equation 3-2

In order to measure the current-potential (I-E) response characteristic of processes at only one electrode (i.e. the working electrode), a three-electrode cell is used. This incorporates a working electrode and counter or axillary electrode, which pass current. As well as a reference electrode, this controls the potential of the working electrode, using a potentiostat, but does not pass current itself. This also minimises the contribution of the iR drop to the measured potential.

The variation of the cell potential, E_e can be related to the thermodynamic standard potential, E_e^s and the activities of surface active species (obtained from the reaction quotient, Q). This is known as the Nernst equation (Equation 3-3); where R is the gas constant (8.314 J K^{-1} mol^{-1}) and T is the temperature, in Kelvin. It can also be written in base -10 log form, assuming T to be 298 K (Equation 3-4).

$$E_e = E_e^s - \frac{RT}{nF} \ln Q$$

Equation 3-3

$$E_e = E_e^s - \frac{0.059}{n} \log Q$$

Equation 3-4

The deviation of the measured potential, E for a redox reaction from the expected thermodynamic potential, E_e is known as the overpotential, η (Equation 3-5).

$$\eta = E - E_e$$

Equation 3-5

The relationship between electrical current produced at an electrode and the electrode potential can be defined using the Butler-Volmer eqution (Equation 3-6). Where η (V) is the

applied overpotential, i (mA cm-2) is the resulting current density, i0 (mA cm-2) is the exchange current density and $\propto A$ and $\propto c$ are the transfer coefficients for anodic and cathodic reactions respectively. The transfer coefficients for a multistep electron transfer process are defined in Equation 3-7 to Equation 3-9.

$$i = i_0 \left[\exp^{\left(\frac{\propto_A nF}{RT} \eta \right)} - \exp^{\left(\frac{\propto_C nF}{RT} \eta \right)} \right] \qquad \text{Equation 3-6}$$

$$\alpha_a = n_b + n_r(1\text{-}\beta) \qquad \text{Equation 3-7}$$

$$\alpha_c = \frac{n_f}{v + n_r \beta} \qquad \text{Equation 3-8}$$

$$\alpha_{a} + \alpha_c = \frac{n}{v} \qquad \text{Equation 3-9}$$

Here n_f is the number of electrons released by the electrode before the rate determining step (rds), v is the number of occurrences of the rds in the electrode reaction as written, n_r is the number of electrons involved in the rds, and β is the symmetry factor, which is usually assumed to take values close to 0.5.[122]

The exchange current density is the current density when the system is at dynamic equilibrium; processes occur at equal rate and there is not net current. This cannot be directly measured experimentally. At high positive or negative overpotentials, the Butler-Volmer equation can be simplified to give the Tafel equations which can be used to derive the exchange current density and gain insight into the HER mechanism (see section 3.7).

3.1.1.2 *Electrochemical testing of electrocatalysts*

Normally the current density is limited by the concentration of the electroactive species in solution however, for a catalytic reaction once the overpotential has been reached; the current density continues to increase with current. This can be seen using CV or LSV techniques.

To be active enough for use in a complete water splitting device, an electrocatalyst needs to yield a high current density at a low overpotential. As a current density of -10 mA cm^{-2} is expected to give a 12.3% efficient solar water-splitting device,[46] the overpotential required to achieve this current density is a good measure of the activity of an electrocatalyst. Ideally an active HER catalyst will have a less negative overpotential than -0.2 V.

However, in the literature the parameters used to assess the HER activity of the electrocatalysts varies from study to study. Often the overpotential for a particular current density is quoted but -10 mA cm^{-2} is not always the current density used. Alternatively, the potential at which proton reduction begins to occur, known as the onset potential may be quoted. However, determination of the onset potential is not trivial and a low onset potential does not guarantee a low overpotential at -10 mA cm^{-2}.

Also, it should be noted that the actual surface area of the catalyst is rarely reported due to the difficulty in determination. This is especially difficult for small nanoparticles and as a consequence the geometric surface area of the electrode is used. For electrodeposited materials with a high roughness factor this would result in an underestimation of the actual surface area and therefore and overestimation of activity based on current density. Whereas, for nanoparticles the geometric surface area is likely to be a large overestimation of the actual surface area and therefore may result in an underestimation of the activity. Therefore, techniques to attempt to analyse the electrode, such as HR-SEM are important.

When testing HER activity of electrocatalysts it is also important to test their stability although this is not always done. In order to test electrode stability EIS can be used, alternatively the current produced at a fixed potential can be measured overtime (using CPE) or the resulting polarisation after multiple cycles (> 100) can be measured (using CV). The fixed potential used should be larger than that required to produce -10 mA cm^{-2} and should be held for longer than 10 hours in order to effectively assess the variation of current density with time.[46] A better option would be to use a galvanostatic test, by fixing the current and measuring the potential as a function of time. However, this is not possible with all potentiostats.

3.1.2   Known Electrocatalysts

Many electrocatalysts have been studied for the HER. Although the majority are alloy materials, work has also investigated molecular catalysts however much lower current densities are observed with these materials. Some examples of alloy electroctalysts for HER can be seen in Table 3-1. Many other materials have been investigated however not all studies use the same parameters to assess activity and therefore comparison is difficult. As mentioned previously, one of the main difficulties is comparing between studies due to the lack of standard conditions for HER analysis. However, more recently it has become common to quote the potential required to reach a current density of -10 mA cm^{-2} as this is the current density that would be required in a working device to give reasonable efficiency. This potential should be as low as possible and generally values less negative than -200 mV are considered promising.

In attempts to move away from platinum due to poisoning and stability issues, as well as the expense of platinum, a lot of work has focussed on molybdenum based materials as these often show good activity. However, molybdenum is still reasonably expensive, not that abundant and has stability issues.[121] Whereas first row transition metals are much cheaper, more abundant and relatively stable. In particular, nickel alloys have shown promising HER activity although stability is often still an issue depending on the exact composition and electrochemical conditions used. For example Ni_2P nanoparticles show good HER activity and reasonable stability in acidic solutions but quickly degrade in basic conditions.[28] On the other hand, many bi- and trimetallic nickel alloys are not very stable in acid but show good stability in base.

As electrolysers for HER operate under acidic or basic conditions, a material with good stability and activity in only one environment can still be beneficial. However, it is still important to assess the stability and activity under different conditions, especially if the electrocatalysts will be incorporated into a solar device that utilises photocatalytic semiconductors. The operating pH range of some semiconductors is very limited and is often best around pH 7 but electrocatalysts are rarely studied and often show lower activity under these conditions.

Table 3-1 Examples of electrocatalysts for HER, giving the overpotential required to reach a particular current density and the electrolyte solution used. Current densities are quoted with respect to geometric surface area.

Catalyst	Current Density / mA cm^{-2}	Overpotential / mV	Electrolyte Solution	Reference (from main text)
Ni$_2$P (1 mg cm^{-2})	-20	-130	0.5 M H$_2$SO$_4$	[28]
Bulk Mo$_2$C	-20	-240	0.5 M H$_2$SO$_4$	[55]
Bulk MoB	-20	-240	0.5 M H$_2$SO$_4$	[55]
Ni-Mo nanopowder (3 mg cm^{-2})	-10	-80	0.5 M H$_2$SO$_4$	[58]
MoS$_2$/RGO (0.28 mg cm^{-2})	-10	-150	0.5 M H$_2$SO$_4$	[120]
Ni$_{43}$Au$_{57}$	-10	-230	0.5 M H$_2$SO$_4$	[96]
Ni$_{34}$Au$_{66}$	-10	-260	0.5 M H$_2$SO$_4$	[96]
Ni$_{59}$Au$_{41}$	-10	-260	0.5 M H$_2$SO$_4$	[96]
Au nanoparticles	-10	-300	0.5 M H$_2$SO$_4$	[96]
Ni nanoparticles	-10	-400	0.5 M H$_2$SO$_4$	[96]
W$_2$N	-10	-750	0.5 M H$_2$SO$_4$	[121]
Ni7.3Mo	-1	-65	0.5 M H$_2$SO$_4$	[26]
Ni3Mo	-1	-75	0.5 M H$_2$SO$_4$	[26]
Ni3.4W	-1	-85	0.5 M H$_2$SO$_4$	[26]
Ni4Fe	-1	-257	0.5 M H$_2$SO$_4$	[26]
NiFe5.6	-1	-284	0.5 M H$_2$SO$_4$	[26]
Mo$_2$C/CNT (2 mg cm^{-2})	-10	-150	0.1 M HClO$_4$	[57]
NiMoNx/C (0.25 mg cm^{-2})	-5	-225	0.1 M HClO$_4$	[25]
MoN/C	-5	-375	0.1 M HClO$_4$	[25]
Ni-Mo-N nanosheets (0.25 mg cm^{-2})	-3.5	-200	0.1 M HClO$_4$	[25]
Mo$_2$C/CNT	-2	-150	0.1 M HClO$_4$	[121]
Mo$_2$C/XC	-2	-175	0.1 M HClO$_4$	[121]
Mo$_2$C	-2	-300	0.1 M HClO$_4$	[121]
Pt/C	-1	-14	H$_2$-saturated 0.1 M HClO$_4$	[57]
Ni$_{0.6}$Mo$_{0.4}$	-1000	-89	30 % KOH	[27]
Ni$_{0.75}$V$_{0.25}$	-1000	-120	30 % KOH	[27]
Co$_{0.8}$Mo$_{0.2}$	--1000	-120	30 % KOH	[27]
Ni$_{0.73}$W$_{0.27}$	-1000	-134	30 % KOH	[27]
Fe$_{0.54}$Mo$_{0.46}$	-1000	-181	30 % KOH	[27]

3.1.3   Aims

As highlighted, the main difficulty with developing new electrocatalysts for the HER is the comparability between studies. In order to test the HER activity of new nanoalloy catalaysts a simple electrode preparation method needs to be developed. Materials will then be analysed in both acidic and basic conditions to assess both HER activity and stability.

3.2   Electrocatalytic Setup

3.2.1   Developing Setup

The literature contains many examples of hydrogen evolution electrocatalysts[46] however; there are no standard conditions for testing. Coupled with the difficulty of characterising the electrocatalysts (especially if synthesised by electrodeposition) explains why it is often difficult to directly compare the activity of materials between different studies. Recently, McCrory and co-workers have reported the HER and OER activities of a number of electrodeposited electrocatalysts.[19] Showing that electrochemistry can be a useful tool for comparing the activity of materials. Similarly, in our work, a quick and simple method for electrochemically assessing the catalytic activity of the synthesised nanoalloys has been developed.

3.2.1.1   Electrode Development

To electrochemically test nanoparticle materials, such as for applications in fuel cells, the commonly used method involves initially depositing nanoparticles on a high surface area carbon support and this is then deposited onto the electrode (often glassy carbon).[36-43] Ideally nanoparticles should be deposited directly onto the electrode, rather than onto a carbon support first. Therefore, the electrode material needs to be able to withstand the temperatures used to remove the ligands (450 °C). Indium or fluorine doped tin oxide coated transparent conducting glass electrodes (ITO or FTO), covered with a TiO_2 film have been used for investigating molecular and biological catalysts for the HER[99, 123-125] as well as photodeposited platinum nanoparticles.[54] These materials can survive temperatures of 450 °C. Another advantage of this method is the use of TiO_2, a common photocatalytic

semiconductor for water splitting, which would enable easy adaptation of the set-up in order to run photoelectrocatalytic experiments as well.

However, as well as being very time consuming to synthesise, it was found that the reduction potentials required for the alloys to give high enough HER activity, were below the reduction potential for TiO_2. Resulting in the TiO_2 film being stripped off the surface of the electrode. Although, stripping of the TiO_2 did not occur when platinum nanoparticles were deposited on the surface. This is most likely due to the high activity of platinum for the HER leading to good electron transfer from the electrode to the platinum and so preventing a build-up of electrons on the TiO_2 and consequently preventing reduction of the TiO_2. This suggests this method may still be useful for future photoelectrochemical measurements once an active material has been identified.

Carbon electrodes were used to allow the reduction potential to be probed over a larger potential window. Carbon veils were considered as they provided a large surface area for nanoalloy deposition. However, the binding agents in the veils could not survive the calcination temperatures resulting in the electrodes falling apart in solution. Instead, carbon rods were used and provided a cheap and quick method for testing materials, as nanoparticles can be quantitatively deposited directly from a hexane solution onto the end of the rod, heated to 450 °C for 30 minutes to remove the ligands and then tested for electrocatalytic activity for the HER. The electrodes can also be stored or soaked in solution to test for longevity and stability. To insulate the sides of the electrodes and ensure the same geometric area in all cases, nail polish was used as a quick and inexpensive method. Epoxy resin had also been considered but could not be applied until after the calcination step and was found to be more time consuming. There was also a higher risk of damaging the electrode in the process and no extra benefit was obtained when compared to the much simpler nail polish method.

However, using a carbon rod meant the active surface was pointing down into the solution and this led to an inaccurate measurement of the electrochemical activity. This was due to a build-up of hydrogen gas on the electrode during the CV measurement, which prevented more of the reactant from reaching the surface of the electrode and so limited activity. By rotating the electrode, it is possible to reduce the build-up of product, on the electrode surface, leading to a more representative indication of the reduction ability of the electrode. The rotating electrode acts like a pump, pushing the product away from the surface while at the same time drawing more of the reactant in. An increase in overall current was clearly seen with increasing rotation rate. A rotation rate of 4000 rpm was selected for

electrochemical testing of the HER activity of the nanoalloys as higher rotation rates resulted in little difference in activity.
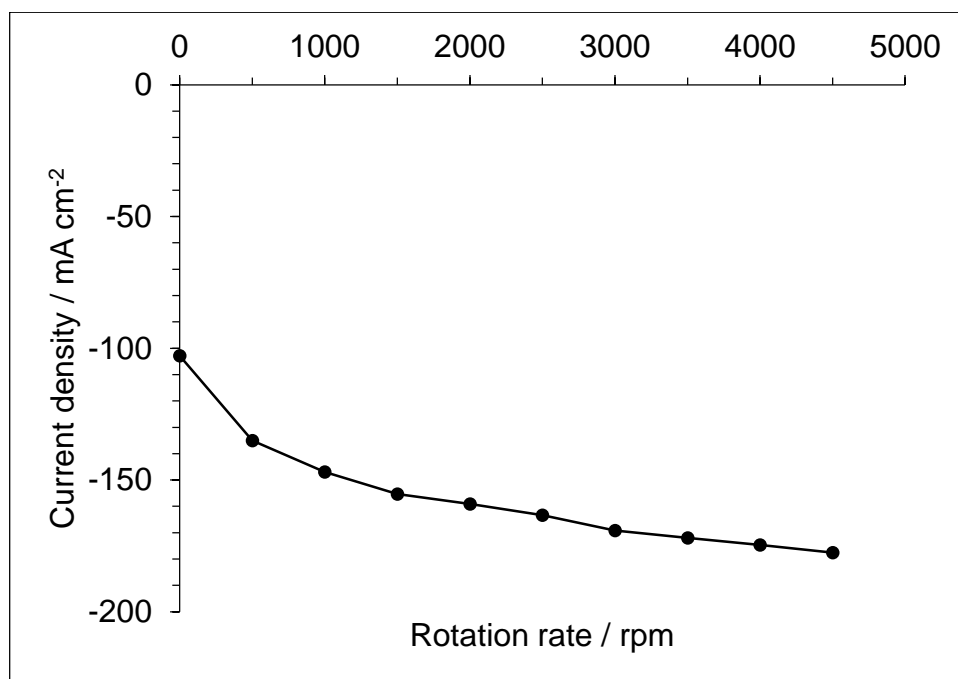
Figure 3-1 Variation of current density with rotation rate.

3.2.1.2   *Electrochemical Conditions*

All measurements were carried out in a three-electrode electrochemical cell (Figure 3-2), using an Ag/AgCl reference electrode and a Pt mesh (1 cm × 5 cm) counter electrode to ensure a much larger surface area of the counter electrode than working electrode, to prevent serious polarisation of the former.

HER activity is often tested in strongly acidic (pH 1) or alkaline (pH 13) conditions. In all proceeding measurements, a solution of 0.1 M H_2SO_4 or 0.1 M NaOH was used. However, concentrations of 0.5 M and 1 M are also commonly seen in the literature[38, 91, 97, 126-128] which again makes direct comparisons between studies difficult. To increase electrolyte conductivity and reduce iR effects, 0.1 M Na_2SO_4 was also present in the solution.

All solutions were purged for 20 minutes with argon and an argon atmosphere was maintained during measurements, in order to exclude oxygen and the chance of oxygen reduction occurring on the electrode.
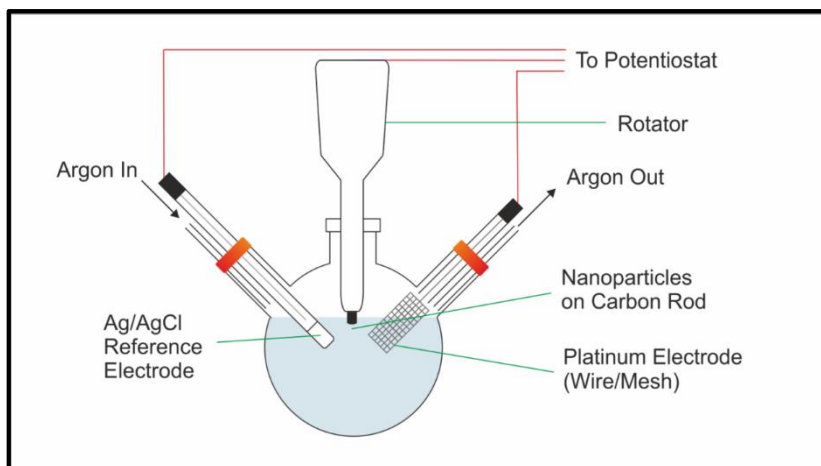
Figure 3-2 Electrochemical setup showing a one-compartment three-electrode electrochemical cell. Employing a Pt mesh counter electrode and Ag/AgCl reference electrode.

Conversion of the electrode potential from Ag/AgCl ($E_{Ag/AgCl}$) to the reversible hydrogen electrode (RHE, E_{RHE}) used.

$$E_{RHE} = E_{Ag/AgCl} + 0.21 + (0.059 \times pH)$$ Equation 3-10

Activities were compared by reporting the potential required to reach a current density of -10 mA cm^{-2}. To gain a better idea of the actual surface area of the sample the surface roughness factor can be calculated by measuring the capacitance of the electrode in the non-faradaic region at different scan rates. However, although the carbon rods are polished before the nanoalloys are deposited, they are not completely smooth and any differences in roughness seen would be due to the surface of the carbon rods not the small nanoalloys deposited on them. Therefore, the current densities reported use the geometric surface area which may be a large overestimation of the actual catalytic surface area.

3.2.2 Effect of the Ligands on Electron Transfer and Catalytic Activity

Removal of the stabilising ligands results in agglomeration of the nanoparticles (see section 3.2.4), which may be detrimental to activity. It has previously been shown that it is possible for the electrocatalysts to function with the ligands still attached without inhibition of the

electron transfer by the stabilising ligands.[50] Therefore, for comparison, the nanoalloys were electrocatalytically tested with the ligands present and removed (Figure 3-3).
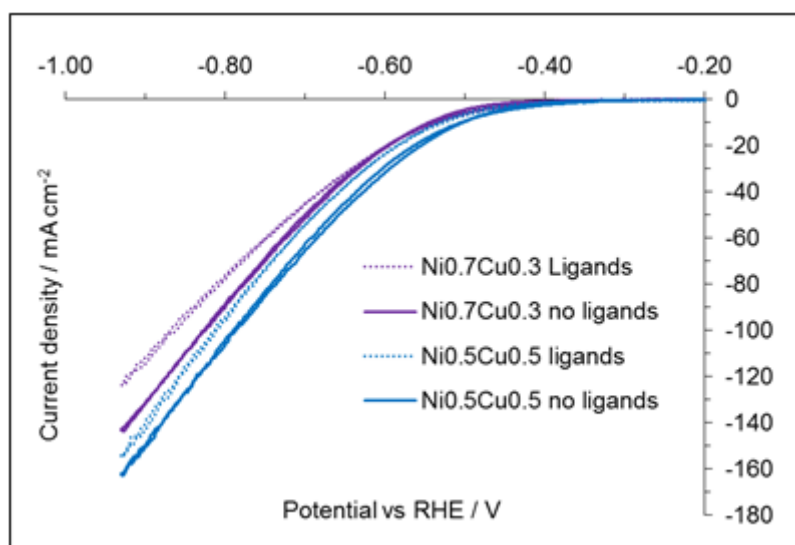
Figure 3-3 Comparison of HER activity with and without ligands present for $Ni_{1-x}Cu_x$ nanoalloys in pH 1, 0.1 M H_2SO_4 and 0.1 M Na_2SO_4. Under Ar with a rotation rate of 4000 rpm.

Higher overpotentials for HER were observed with the ligands present suggesting that the long non-conjugated hydrocarbon chains are inhibiting charge transfer, to and from the surface of the electrocatalyst. However, the extent to which this occurred was not consistent for different compositions (Figure 3-3). Dominguez-Crespo and co-workers have shown that the concentration of stabilising ligands can affect the redox activity of nickel nanoparticles.[91] Therefore the differences seen may be due to different amounts of ligand surrounding the various nanoalloys. It is also possible that the different electronic structures of the various compositions will affect the interaction between the nanoalloys and the stabilising ligands and ultimately the redox activity observed.

Consequently, analysing HER activity in the presence of the stabilising ligands may not yield comparable results for materials. Therefore, after deposition onto the carbon electrode, the ligands were removed by calcination before electrochemical testing occurred.

3.2.3 Loading Tests

In the literature, deposition of nanoparticles onto electrode surfaces often involves dropping a 1 mg mL^{-1} aliquot onto the end of the electrode.[28, 43, 91, 98, 128-130] Therefore initial measurements of the NiCu nanoalloys (section 3.3.1) and the Ni$_{0.5}$M$_{0.5}$ nanoalloys (section 3.3.2) used this method. This produced a catalyst loading of approximately 0.3 mg cm^{-2}. Although, other loadings have also been reported and no standard appears to exist.[37, 38, 97, 126, 127, 131-133]

To get the best activity a monolayer of the nanoparticles was required, as this would provide the largest catalytic surface area. The average size of the particles and molecular mass of nickel were used to roughly calculate the mass required to give a monolayer coverage (Equation 3-11, see Appendix 2 for more details). Where SA$_{cr}$ is the surface area of the carbon rod, CSA$_{np}$ is the cross sectional area of a 10 nm nanoparticle, V$_{np}$ is the volume of a nanoparticle (assuming a cube of space is occupied) and ρ is the density of nickel. It was predicted that to acquire a monolayer coverage, a catalyst loading of 6 μg cm^{-2} would be required. This is clearly a lot lower than the original loading, suggesting surface area utilisation may not be at its optimum in these measurements.

$$m = \frac{SA_{cr}}{CSA_{np}} \times V_{np} \times \rho \qquad\qquad \text{Equation 3-11}$$

To estabilish the optimum loading, the steady state current produced by different nanoalloy loadings, at a potential of -500 mV vs Ag/AgCl electrode was measured using CPE. A loading ten times higher than predicted (56 μg cm^{-2}) was required to give the highest activity. This may have been due to the assumptions made in the calculation. For example, the volume of the particles was equated to that of a cube although it may actually be possible for the spheres to pack more closely. Also the mass used includes the ligands so will be lower than reported. Although elemental analysis showed that the majority of the mass is due to the metal nanoalloys rather than the ligands, with the organic ligands accounting for less than 20% of the total mass.

Above 56 μg cm^{-2} the current density decreases again and there is a sharp decrease in activity at a loading of 85 μg cm^{-2} which may suggest agglomeration of particles is most limiting at this loading. Higher loadings will also contain agglomerated particles but also a higher amount of catalyst and therefore a higher activity is seen. Above 141 μg cm^{-2} there is little change to activity upon further increasing the loading.
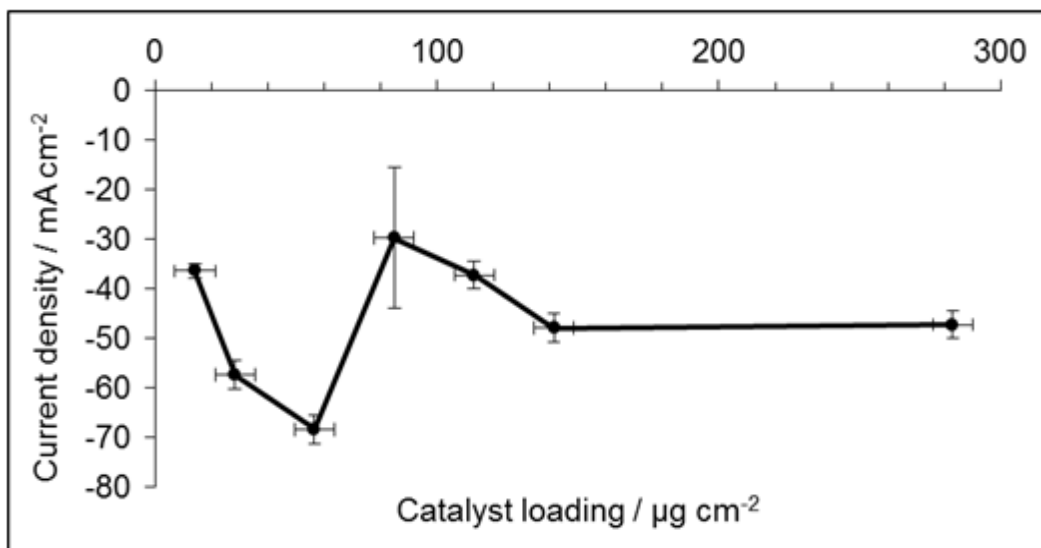
Figure 3-4 Current density recorded at -500 mV vs Ag/AgCl for various catalyst loadings.

Deposition of 56 μg cm^{-2} onto a TEM grid was used to corroborate the coverage as the TEM grids are a similar diameter to the carbon rods (both approximately 0.3 cm). An even coverage was observed across the sample, showing lower than a monolayer loading.
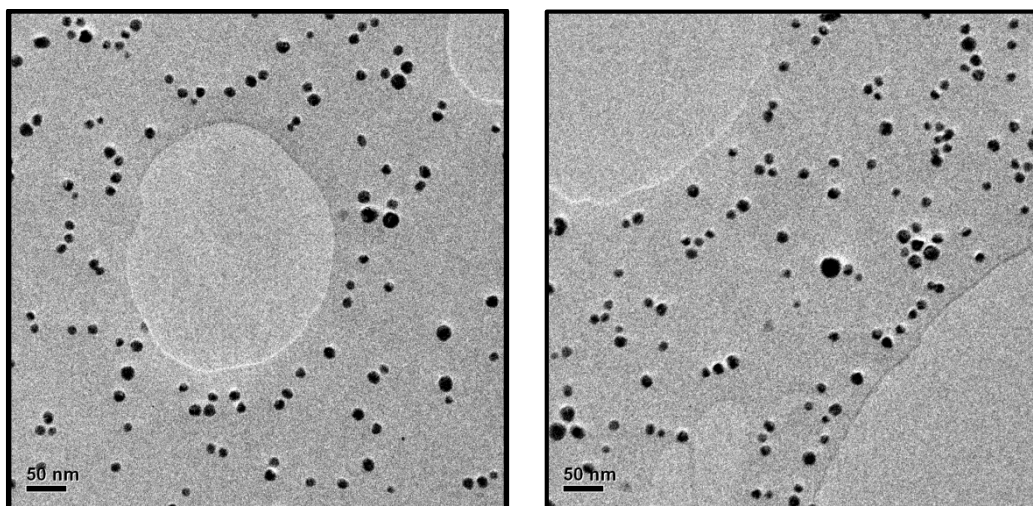
Figure 3-5 TEM images of NICuCo nanoalloys showing less than a monolayer of coverage for a loading of 56 μg cm^{-2}.

However, the TEM only shows the nanoparticles before calcination so may not give an accurate indication of distribution on the electrode surface. It is possible that more closely packed particles would result in more agglomeration upon calcination and lead to lower activity. To observe any changes that occur upon calcination, nanoparticles deposited on a

TEM grid were calcined in the same way as the carbon rod electrodes. Unfortunately, the conductive carbon layer in the grid was not stable at the temperatures used and the grid degraded. Therefore, it was not possible to observe the effect of calcination using TEM.

3.2.4 High Resolution – Scanning Electron Microscopy (HR-SEM)

All characterisation reported in chapter 2 was carried out on the as-formed ligand stabilised nanoalloys, before deposition on the electrodes and calcination. However, this may not give an accurate representation of the nanoalloys after calcination or electrochemical testing as agglomeration of particles and leaching of atoms may occur in these processes respectively. Attempts to replicate the conditions on a TEM grid were unsuccessful; as were attempts to remove the nanoalloys from the carbon electrodes, for analysis, after electrochemical measurements.

3.2.4.1 Limitations of analysis by TEM

TEM analysis of the material scraped off of the end of the electrode was attempted. However, it was not possible to detect the nanoparticles. Originally this was due to the presence of too much carbon, from the electrode, making transmission though the sample and consequently the production of an image difficult. Therefore, attempts were made to remove as little carbon as possible but this made it very difficult to determine if the nanoparticles were collected in the sample vial. The very low concentration also made the chance of seeing the nanoparticles very unlikely and they were not observed using TEM.

3.2.4.2 HR-SEM loading analysis

In order to get a more accurate idea of the active materials, the trimetallic samples were submitted to LENNF in Leeds, for high resolution scanning electron microscopy (HR-SEM) analysis. The contrast between the carbon background and the metallic nanoparticles is high enough to give an image of the surface, although the size of the nanoalloys (around 10 nm) still makes them difficult to see (Figure 3-6).

Upon calcination of the electrodes the nanoalloys appear to undergo sintering, leading to agglomeration of the particles on the electrode surface. The resulting particles are closer to 20 nm in diameter rather than around 10 nm as seen by TEM for the ligand stabilised nanoalloys. This may explain why the optimal loading is ten times higher than the theoretical monolayer coverage. It would also suggest a further increase in loading decreases activity due to the formation of larger agglomerates. It may be possible to create a more homogeneous coverage by using different solvents or making a film with Nafion. Although using different solvents did not affect the coverage seen by TEM and is therefore unlikely to affect initial coverage on the electrode surface and therefore unlikely to effect the coverage after calcination. If Nafion was used the electrodes would not be able to be calcined and the presence of the ligands has already been shown to interfere with HER activity (see section 3.2.2).
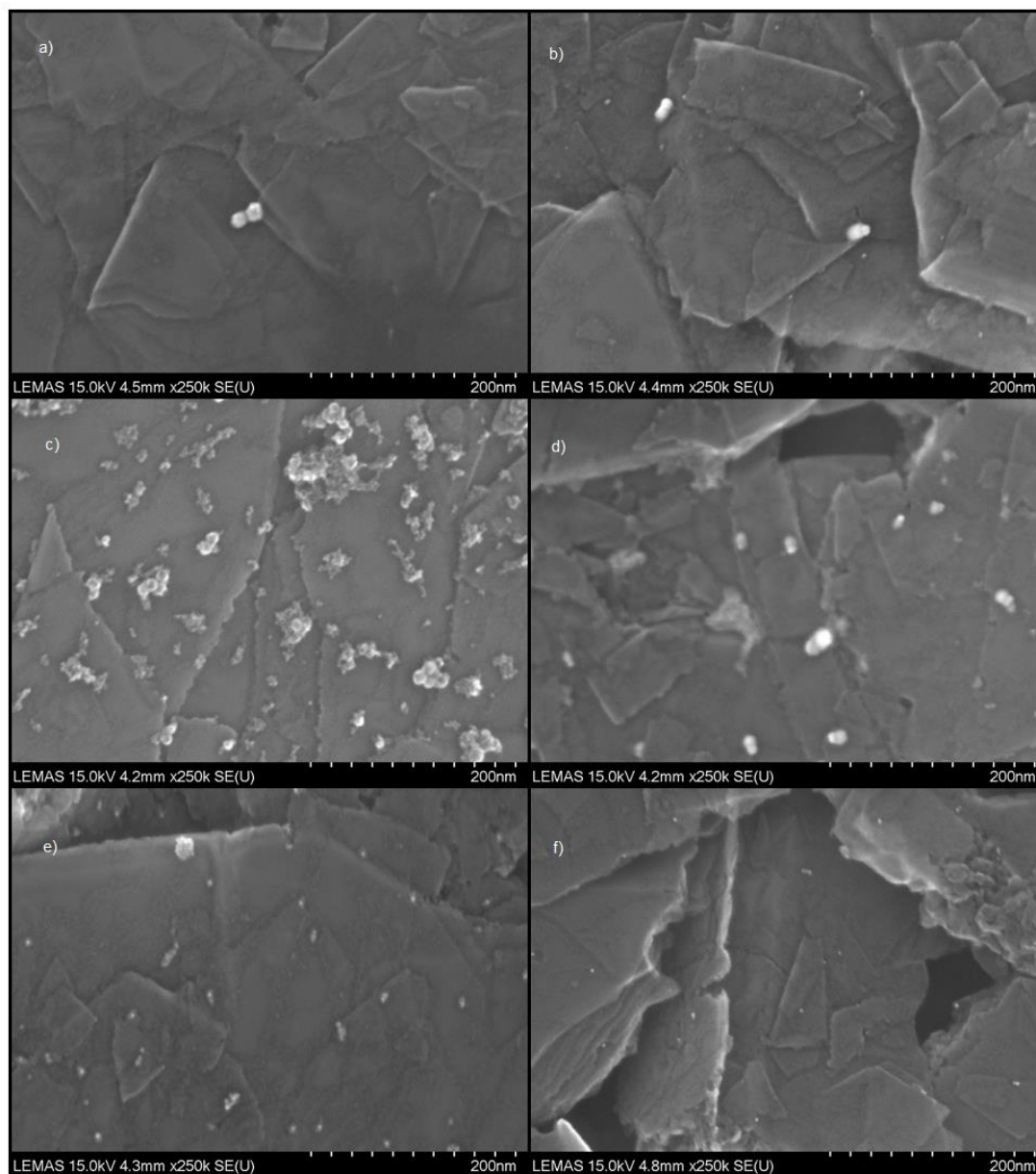
Figure 3-6 HR-SEM of a), b) $Ni_{0.5}Cu_{0.3}Co_{0.2}$, c), d) $Ni_{0.5}Cu_{0.3}Fe_{0.2}$ and e), f) $Ni_{0.5}Co_{0.3}Fe_{0.2}$ nanoalloys on carbon electrodes, before and after electrochemistry respectively. Electrochemical experiments consisted of 20 CV cycles between 0.0 and -1.2 V vs Ag/AgCl in pH 1 0.1 M H_2SO_4 / 0.1 M H_2SO_4.

3.2.4.3 HR-SEM comparison of structure before and after electrochemical analysis

The different trimetallic nanoalloys show varying amounts of agglomeration after calcination. The $Ni_{0.5}Co_{0.3}Fe_{0.2}$ nanoalloy still contains many particles around 10 nm in size as well as some larger agglomerates whereas; the $Ni_{0.5}Cu_{0.3}Co_{0.2}$ nanoalloy shows particles around 20 nm and the $Ni_{0.5}Cu_{0.3}Fe_{0.2}$ nanoalloy shows extensive agglomeration with a wide size distribution.

After 20 CV cycles in pH 1, the particles appear smaller and more dispersed than before. This may be due to the electrochemical processes happening at the nanoalloy surface, it may also suggest that dissolution and re-deposition is occurring during the electrochemical experiment. However, this would normally lead to an agglomeration (Ostwald ripening) of the particles rather than redistribution.[50]

EDX was also attempted to analyse the composition of the nanoalloys, before and after electrochemistry as elemental leaching is known to occur during HER and may explain changes in electrocatalytic activity over time. However, the small size of the particles and the large background signal from the carbon electrode prevented the collection of quantitative data.

3.2.5   Conclusions

A quick and simple procedure for electrode synthesis was developed. Nanoalloys are deposited onto carbon rods and rotated during measurements to prevent diffusion limitations. It allows the ligands to be removed after deposition of the nanoalloys which is necessary to acquire the best HER activity possible from a given material as the hydrocarbon chains of the ligands appear to be inhibiting electron transfer and reducing activity.

The catalyst loading was also investigated to discover the maximum activity possible. A loading of 56 μg cm^{-2} was found to be optimal and appeared to give less than a monolayer loading base on TEM analysis. However, HR-SEM analysis shows that the nanoalloys agglomerated during calcination with a very low surface coverage detected. Although higher loadings did not improve activity suggesting that more agglomeration occurred, reducing the active surface area.

3.3 Nanoalloy Activity in pH 1

Due to the high concentration of protons present, low pH conditions often give higher activities for the HER. However, the acidic environment often results in corrosion of the catalysts and this lack of stability can lead to lower overall efficiencies. However, as a lot of

electrolysers operate at low pH; this is a good way to test the activity and stability of the reduction catalysts.

Activity was analysed by comparing the overpotential required to produce a current density of 10 mA cm^{-2} as this is widely accepted to be the current density required for a high efficiency photoelectrolytic cell operating at one sun illumination.[46] However, as some nanoalloy compositions had very similar overpotentials, the current density produced at an overpotential of -500 mV (vs. RHE) is also reported.

3.3.1   Comparison of NiCu Compositions

NiCu nanoalloys have previously been investigated for the reduction of hydrazine.[42] NiCu has also been tested as an electrodeposit for HER and shows better activity and stability than bulk nickel. To gain more insight into the effect of composition on HER activity, NiCu nanoalloys with different compositions were tested for their electrocatalytic activity for hydrogen production in water.

3.3.1.1   Electrochemical Setup

CV measurements were carried out in a 0.1 M H$_2$SO$_4$ / 0.1 M Na$_2$SO$_4$ (pH 1) solution with a scan rate of 20 mV s^{-1}, in order to assess the activity of the NiCu nanoalloys for HER. As these measurements were carried out before the electrocatalyst loading had been optimised a loading of 0.3 mg was used, these results are not directly comparable with those discussed later. Although comparison between the different NiCu nanoalloys is possible.

3.3.1.2   HER Activity of Ni$_{1-x}$Cu$_x$ Nanoalloys

Comparing the CVs; all compositions show higher activity than the pure nickel nanoparticles. This confirms that alloying nickel with other transition metals could improve activity as well as stability. Of the various NiCu compositions, the Ni$_{0.5}$Cu$_{0.5}$ gave the highest activity,

requiring 0.14 V less than pure nickel nanoparticles to reach a current density of -10 mA cm^{-2}.

The Ni$_{0.7}$Cu$_{0.3}$ nanoalloy required 0.10 V more than the Ni$_{0.5}$Cu$_{0.5}$ nanoalloy to reach the same current density suggesting that a higher copper content is beneficial for HER activity. Whereas the Ni$_{0.3}$Cu$_{0.7}$ nanoalloy initially appears to show good activity but it has a very different profile to the other materials and becomes less active than the Ni$_{0.7}$Cu$_{0.3}$ nanoalloy at higher overpotentials (above -0.8 V). It is believed the initial reduction observed is a surface oxide layer[26] and hydrogen reduction does not begin until higher overpotentials. Therefore, the most HER active material is the Ni$_{0.5}$Cu$_{0.5}$ nanoalloy.
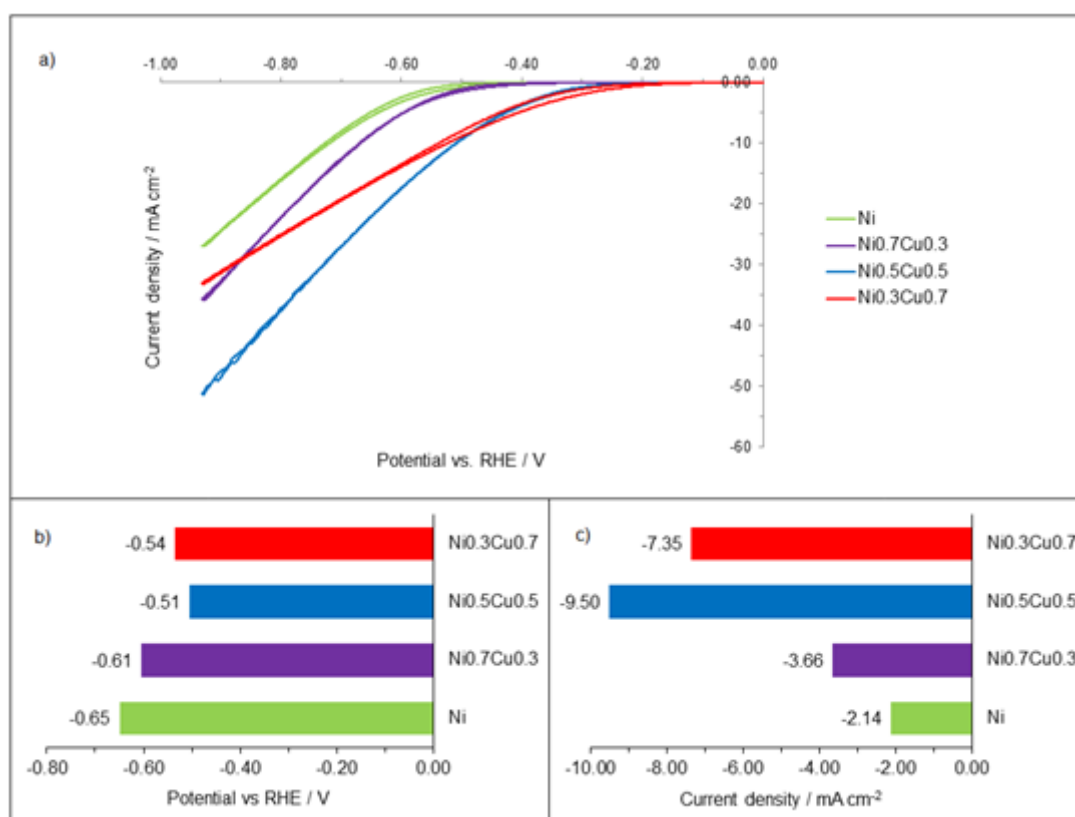
Figure 3-7 Comparison of the HER activity of Ni$_{1-x}$Cu$_x$ nanoalloys (where x = 0.0, 0.3, 0.5 or 0.7) in pH 1 0.1 M H$_2$SO$_4$ / 0.1 M Na$_2$SO$_4$. Under Ar and with a rotation rate of 4000 rpm. a) CV data, b) overpotential required to reach a current density of -10 mA cm^{-2} and c) current density at an overpotential of -0.5 V.

Ni$_{0.5}$Cu$_{0.5}$ had also been observed to be the most active composition, for the reduction of hydrazine.[42] The higher activity of Ni$_{0.5}$Cu$_{0.5}$ could be due to a number of factors including a synergy between the two elements. As nickel is known to bind hydrogen relatively strongly and copper binds it relatively weakly, a combination of the two may lead to an overall binding

strength for the alloy between the two pure metals and consequently similar to platinum. The $Ni_{0.5}Cu_{0.5}$ having higher activity than the other compositions may suggest this is the best balance of the two elements. However, the stability of the alloy structure may also play a part in the higher activity seen for this composition.[42, 70] Therefore it is not surprising that the $Ni_{0.5}Cu_{0.5}$ was also the most active NiCu alloy for proton reduction in water.

3.3.2 Comparison of $Ni_{0.5}M_{0.5}$ Alloys

The $Ni_{0.5}M_{0.5}$ compositions gave the best structured alloys in all cases and the literature suggests $Ni_{0.5}M_{0.5}$ compositions often show better activity than other ratios for the same alloy.[42, 70] This is supported by the observations made for the $Ni_{1-x}Cu_x$ nanoalloys (section 3.3.1) and also $Ni_{1-x}M_x$ materials (where M = Fe or Co, see Appendix 2, Figure A5). Therefore, the $Ni_{0.5}M_{0.5}$ nanoalloys were focussed on in order to test and compare the HER activity of different alloys.

3.3.2.1 *Electrochemical Setup*

Measurements were carried out in a 0.1 M H_2SO_4 / 0.1 M Na_2SO_4 (pH 1) solution with a scan rate of 20 mV s^{-1}. Catalyst loading was 0.3 mg, as measurements were taken before loading was optimised. The activities of the carbon rod without nanoparticles deposited and with Pt nanoparticles, deposited in the same way as the $Ni_{0.5}M_{0.5}$ nanoalloys, were also tested for comparison. No discernible HER activity is seen for the carbon rod and the Pt nanoparticles show comparable activity to that reported for this material in the literature.[57, 121]
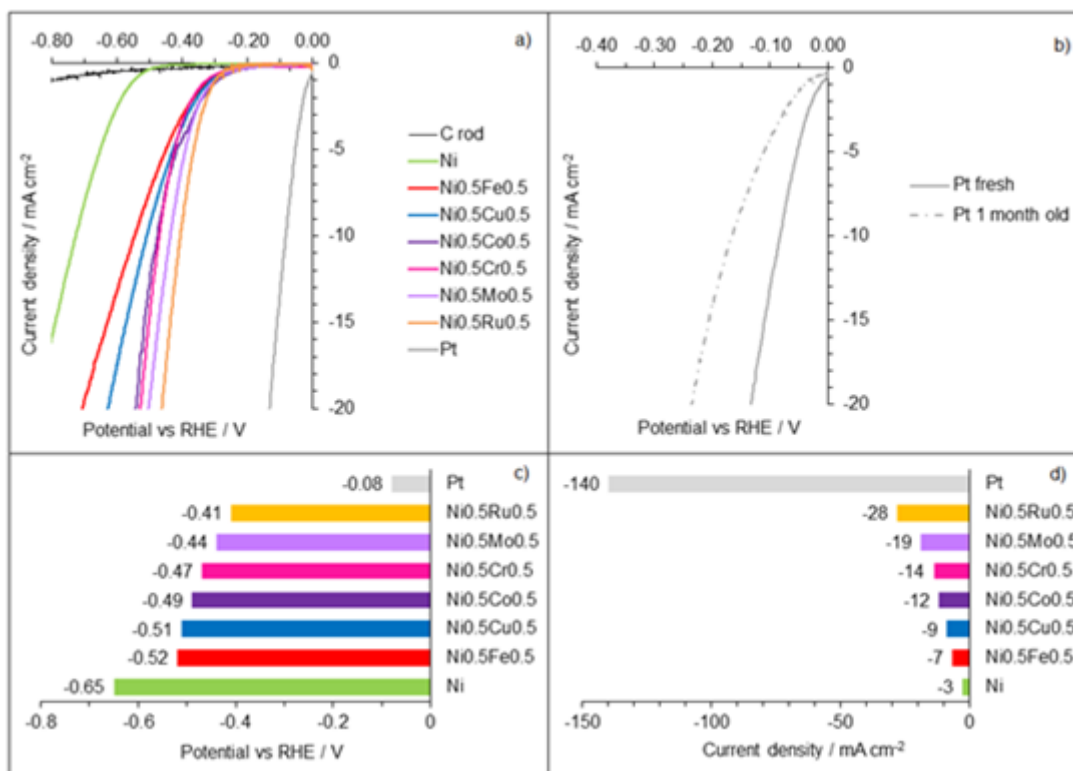
Figure 3-8 Comparison of the HER activity of $Ni_{0.5}M_{0.5}$ nanoalloys (where M = Ru, Mo, Co, Cu and Fe) in pH 1 0.1 M H_2SO_4 / 0.1 M Na_2SO_4. Under Ar and with a rotation rate of 4000 rpm. a) CV data, b) comparison of polarisation data for Pt electrodes freshly prepared and after 1 month c) overpotential required to reach a current density of -10 mA cm^{-2} and d) current density at an overpotential of -0.5 V.

3.3.2.2   HER Activity of $Ni_{0.5}M_{0.5}$ Nanoalloys

The results show there is not a large difference between the activities of the different nanoalloys though all show higher activity than pure nickel. This higher HER activity was expected and has been reported previously for many bimetallic nickel electrodeposits including NiCo[51, 52] and NiFe[26]. The most active bimetallic nanoalloys appear to be the $Ni_{0.5}Ru_{0.5}$ and $Ni_{0.5}Mo_{0.5}$.

As NiRu nanoalloys have been known to show good activity for dehydrogenation of ammonia borane;[79] their electrocatalytic HER activity is not unexpected. NiMo is also known to be a good HER electrocatalyst although the activity observed here is lower than that reported in the literature. The structure of NiMo is often not investigated although Chialvo and Chialvo reported the exclusive formation of the cubic polymorph[134] as would be expected for the bulk alloy. Whereas, the $Ni_{0.5}Mo_{0.5}$ nanoalloys tested here adopted the hexagonal polymorph and this change in structure and surface facets may have an effect on the observed activity. Another factor effecting the HER activity may be the degradation of the

sample in acidic solutions, as a decrease in activity was observed for successive runs and stability is a known issue with this material.[25]

Stability is also one of the problems with Pt electrodes and this is clearly shown in Figure 3-8, by comparing the HER activity of a freshly prepared Pt electrode to one after a month. The overpotential required for the Pt electrode after one month is double that of the fresh sample. Whereas, with the exception of the $Ni_{0.5}Mo_{0.5}$ material, the bimetallic nanoalloys showed negligible difference in activity overtime.

Although the bimetallic nanoalloys comprising solely of first row transition metals were not as active for HER as the other bimetallic nanoalloys, they do still show a significant improvement over pure nickel nanoparticles. The $Ni_{0.5}Cu_{0.5}$, $Ni_{0.5}Co_{0.5}$ and $Ni_{0.5}Fe_{0.5}$ all show very similar activities, with overpotentials to achieve -10 mA cm^{-2} of -0.51 ± 0.02 V, -0.49 ± 0.02 V and -0.52 ± 0.5 V respectively. The larger variation seen in the activity of $Ni_{0.5}Fe_{0.5}$ electrodes may be due to leaching of the iron overtime. Although the XRD showed that the $Ni_{0.5}Fe_{0.5}$ material is actually $NiFe_2O_4$, it still showed more activity for HER than pure nickel but not the other nanoalloy compositions.

Interestingly the $Ni_{0.5}Cr_{0.5}$ nanoalloy shows a marked difference in HER activity compared to pure nickel nanoparticles, even though XRF analysis revealed only 1% Cr content present in the $Ni_{0.5}Cr_{0.5}$ nanoalloy, meaning the actual composition was $Ni_{0.99}Cr_{0.01}$. The overpotential required to reach a current density of -10 mA cm^{-2} is 0.18 V less for the $Ni_{0.5}Cr_{0.5}$ nanoalloys than pure nickel nanoparticles. Although analysis was unable to confirm if Cr is present in all nanoparticles, it did show a much larger preference for the hexagonal structure than the pure nickel nanoparticles. The structure affects the surface facets of the nanomaterial and it is well documented that different activity is often observed on different facets. Therefore, this large difference in HER activity may have more to do with the difference in structure observed rather than any direct effect on catalysis from the chromium.

3.3.2.3 Intrinsic Activity

The HER catalytic activity is believed to be related to the electronic structure of metals although no comprehensive explanation currently exists. Several theories for the HER activity of alloys have been proposed. One is the Engel-Brewer valence-bond theory, as a generalised Lewis acid-base reaction model.[26, 135, 136] Jaksic and co-workers have postulated

that alloying metals with empty or half-filled vacant d-orbitals (hypo-d-electronic elements, e.g. Mo, V or W) with metals with internally paired d-electrons not available for bonding in the pure metal (hyper-d-electronic elements, e.g. Ni, Pt, Pt or Co) results in a change to their bonding strength and increased intermetallic stability. In such hypo-hyper-d-electronic interactions, transfer of paired d-electrons from the hyper-d-electronic element to the empty or half-filled semi-d-shells of the hypo-d-electronic element occurs. The resulting change of bonding strength and increased intermetallic stability has a maximum that generally coincides with d^8-electrons for the synergism and optimal HER activity.[26, 135, 136]

The d-band is claimed to be important for electrocatalytic hydrogen reactions although overall kinetics for the HER have been related to the electron density.[26] The direction of electron transfer in the Engel-Brewer theory is opposed to Pauling rule of electronegativity. Other theories including the Miedema model[136] suggest electron transfer occurs from more to less electronegative elements,[137, 138] as generally expected.[26, 136]

Although determining the direction of electron transfer is beyond the scope of this work; a correlation between the electronegatives of the second element and HER activity was noted. With the more electronegative elements (Mo and Ru) giving higher activity. The main exception to this order was chromium, which has the lowest electronegativity but higher activity than that of nanoalloys containing other first row transition metals. Chromium is a hypo-d-electronic element and as such the activity seen may be a result of the improved stability of the nickel material produced by alloying with chromium. Although as previously mentioned there is very little chromium present in the sample and so this increase in activity may be a structure effect.

3.3.3   Activity of Trimetallic Alloys

Although an improvement in HER activity, compared to pure nickel, is observed for the bimetallic nanoalloys it appears the use of just two elements does not provide enough variation to further improve efficiency. Also, even though the nickel bimetallic alloys with first row transition metals did not give the highest HER activity, an improvement over pure nickel nanoparticles was observed. Furthermore, materials employing only first row transition metals would be less expensive and therefore more desirable for a commercial device. Therefore, the HER activities of first row transition metal trimetallic alloys were investigated.

3.3.3.1   Electrochemical Setup

LSV measurements were carried out in a 0.1 M H_2SO_4 / 0.1 M Na_2SO_4 (pH 1) solution with a scan rate of 1 mV s^{-1}, in order to assess the activity of the NiCu nanoalloys for HER. These measurements were carried out after the electrocatalyst loading had been optimised, and therefore use a catalyst loading of 56 μg cm^{-2}.

3.3.3.2   HER Activity of Trimetallic Nanoalloys

The HER activities of the trimetallic nanoalloys show much more variation than those of the various bimetallic nanoalloy compositions. In pH 1 the two trimetallic alloys containing iron require higher overpotentials to achieve a current density of -10 mA cm^{-2} than the pure nickel nanoparticles. The $Ni_{0.5}Cu_{0.3}Fe_{0.2}$ nanoalloy also showed much higher deviation between samples tested than the other materials, with a difference in potential required to produce - 10 mA cm^{-2} of ± 0.06 V whereas different samples of other materials deviated by ± 0.01 V. The XRD showed that this material contained some $NiFe_2O_4$ as well as the trimetallic alloy. The deviation between samples may be due to differing amounts of this material being present. It is also expected that leaching of the elements, especially iron, will occur during electrolysis. A large increase in activity was observed over the 20 cycles and suggests this material had not stabilised (see section 3.5)

Figure 3-9 Comparison of the HER activity of trimetallic nanoalloys in pH 1 0.1 M H_2SO_4 / 0.1 M Na_2SO_4. Under Ar and with a rotation rate of 4000 rpm. a) CV data, b) overpotential required to reach a current density of -10 mA cm^{-2} and c) current density at an overpotential of -0.5 V.

The $Ni_{0.5}Cu_{0.3}Co_{0.2}$ nanoalloy, was expected to show reasonable activity as a CoNiCu alloy has been investigated for the HER as a 3D nano-network structure.[114] The $Ni_{0.5}Cu_{0.3}Co_{0.2}$ nanoalloy showed similar activity (-0.41 V for -10 mA cm^{-2}) to both the $Ni_{0.5}Cu_{0.5}$ and $Ni_{0.5}Co_{0.5}$ nanoalloys (-0.40 V and -0.42 V respectively for -10 mA cm^{-2}).

Although direct comparison to other studies is difficult, it is generally believed that an overpotential of less than 0.2 V for a current density of -10 mA cm^{-2} is required for application in a complete water splitting device. Therefore, under the conditions employed, the nanoalloys are not active enough to be used in an efficient water splitting device. However, although NiMo has been known to show reasonable activity for HER it is also unstable in acidic solutions leading to a sharp decrease in activity over a short period of time.[25, 58] Whereas, the nickel nanoalloys investigated here may show less activity but they show much greater stability (see section 3.5).

Proton reduction activity of the different nanoalloys decreases in the order: $Ni_{0.5}Cu_{0.5}$ > $Ni_{0.5}Cu_{0.3}Co_{0.2}$ > $Ni_{0.5}Co_{0.5}$ > Ni > $Ni_{0.5}Cu_{0.3}Fe_{0.2}$ > $Ni_{0.5}Co_{0.3}Fe_{0.2}$. This suggests that the more electronegative the second element the higher the activity, as generally seen for the bimetallic alloys as well.

3.3.4 Summary of Nanoalloy Activity in pH 1

Better activity is seen for bimetallic alloy compositions of $Ni_{0.5}M_{0.5}$ compared to other atomic ratios, which may be a result of better alloying in this material. All bimetallic nanoalloys showed higher HER activity than the pure nickel nanoparticles and the $Ni_{0.5}Cu_{0.5}$ and $Ni_{0.5}Co_{0.5}$ nanoalloys use abunadant and cheap materials and appeared to be both active and stable. The trimetallic nanoalloys did not show better activity under these conditions and the compositions containing iron showed worse activity than the pure nickel nanoparticles.

From these measurements, it would appear the nanoalloys containing copper and/or cobalt, but not iron, are better for the HER in pH 1. However, many electrolysers use alkali, rather than acidic, conditions and if these reduction catalysts are to be used as part of a photoelectrolytic cell for water splitting they need to be active around neutral pH, as operating around pH 7 is required for the majority of the photocatalytic semiconductors being developed. It is known that materials often show different activities for HER at different pH and so it is necessary to assess the activity of the nanoalloys under these conditions.

3.4 Nanoalloy Activity in pH 7 and pH 13

Changing the pH can make a large difference to the activity as the mechanism of hydrogen production is different in acid and base (see section 3.7). Also most nickel based materials are much more stable in base than acid[26, 27] therefore the nanoalloys may show higher activity in basic conditions.

Although the nanoalloys have been tested as electrocatalysts there is potential to deposit them on semiconductor photocatalysts to use both photocatalytically and photoelectrocatalytically. Therefore, the working range of the semiconductor becomes relevant and a lot of phtotocatalytic semiconductors are most stable at pH 7. Being able to operate at good efficiency in neutral pH would also be ideal for a working solar fuel device. Hence the nanoalloys have been tested at pH 7 and 13 and the activities compared to those in pH 1.

3.4.1   Nanoalloy Activity in pH 13

Under basic conditions, all nanoalloys showed higher activity than the pure nickel nanoparticles. Again there is little difference between the $Ni_{0.5}Cu_{0.5}$ and $Ni_{0.5}Co_{0.5}$ nanoalloys (-0.53 V and -0.55 V respectively for -10 mA cm^{-2}) and both perform better than the $Ni_{0.5}Cu_{0.3}Co_{0.2}$ nanoalloy (-0.59 V for -10 mA cm^{-2}). Interestingly, unlike in pH 1, the iron containing trimetallic alloys have the best activities and the $Ni_{0.5}Co_{0.3}Fe_{0.2}$ nanoalloy is more active (-0.44 V for -10 mA cm^{-2}) than the $Ni_{0.5}Cu_{0.3}Fe_{0.2}$ nanoalloy (-0.51 V for -10 mA cm^{-2}). Activity of the different nanoalloys decreases in the order: $Ni_{0.5}Co_{0.3}Fe_{0.2}$ > $Ni_{0.5}Cu_{0.3}Fe_{0.2}$ > $Ni_{0.5}Cu_{0.5}$ > $Ni_{0.5}Co_{0.5}$ > $Ni_{0.5}Cu_{0.3}Co_{0.2}$ > Ni.

This may be due to less leaching occuring under these conditions. However, it may also be due to the presence of oxides in these materials, as metal oxides are known to have good HER activity under basic conditions.[19] The common problem often encountered with these materials is that overtime they convert to the hydroxide and lose activity.[45]
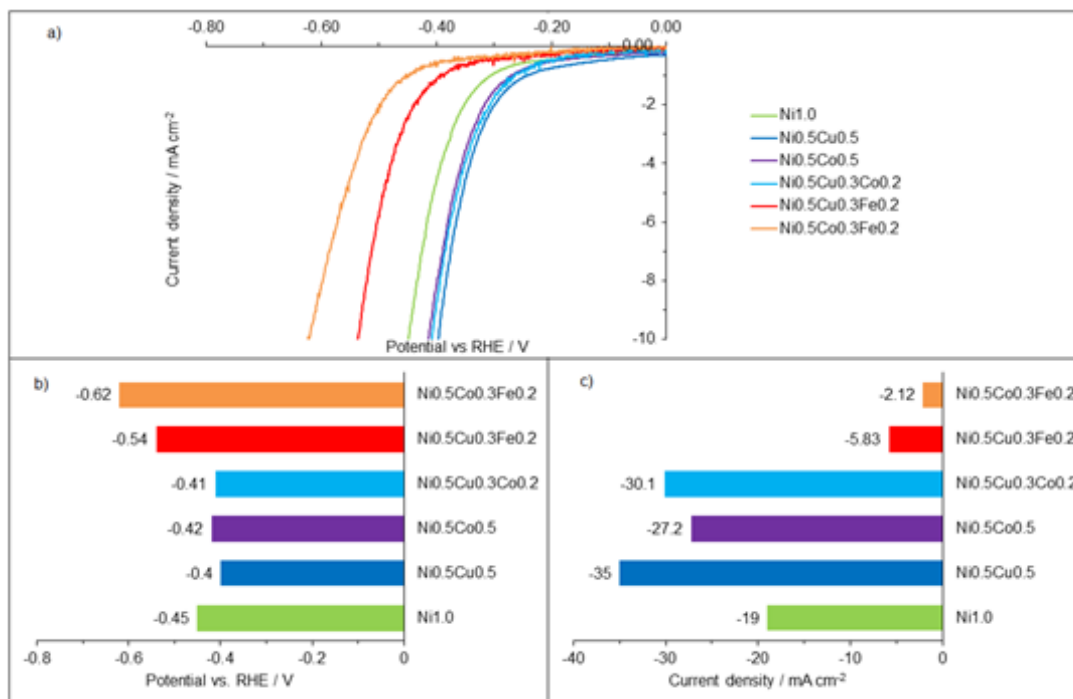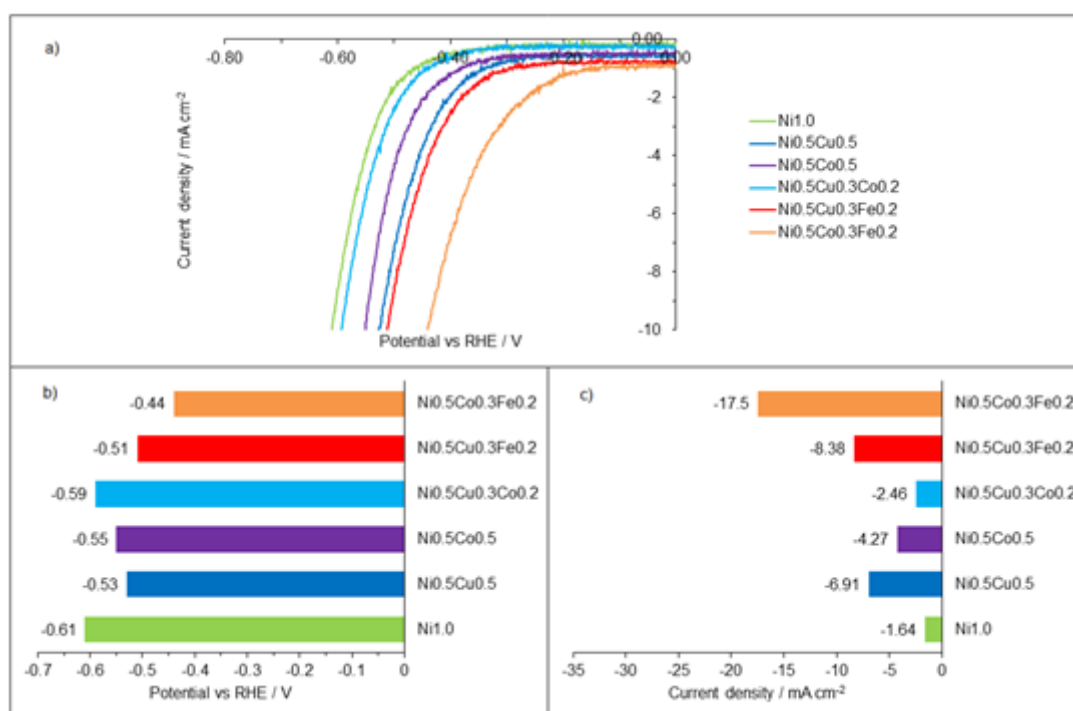

Figure 3-10 Comparison of the HER activity of trimetallic nanoalloys in pH 13 0.1 M NaOH / 0.1 M Na_2SO_4. Under Ar and with a rotation rate of 4000 rpm. a) CV data, b) overpotential required to reach a current density of -10 mA cm^{-2} and c) current density at an overpotential of -0.5 V.

3.4.2 Nanoalloy Activity in pH 7

In pH 7, very little difference is observed between all materials; all nanoalloys require an overpotential between -0.51 and -0.53 V for a current density of -10 mV cm^{-2} to be obtained. Based on the large differences seen between materials under very acidic or basic conditions, this very limited variation at neutral pH may seem strange. However, if the activities of a nanoalloy composition at various pH values are compared the limited variation between compositions under neutral conditions can be explained.
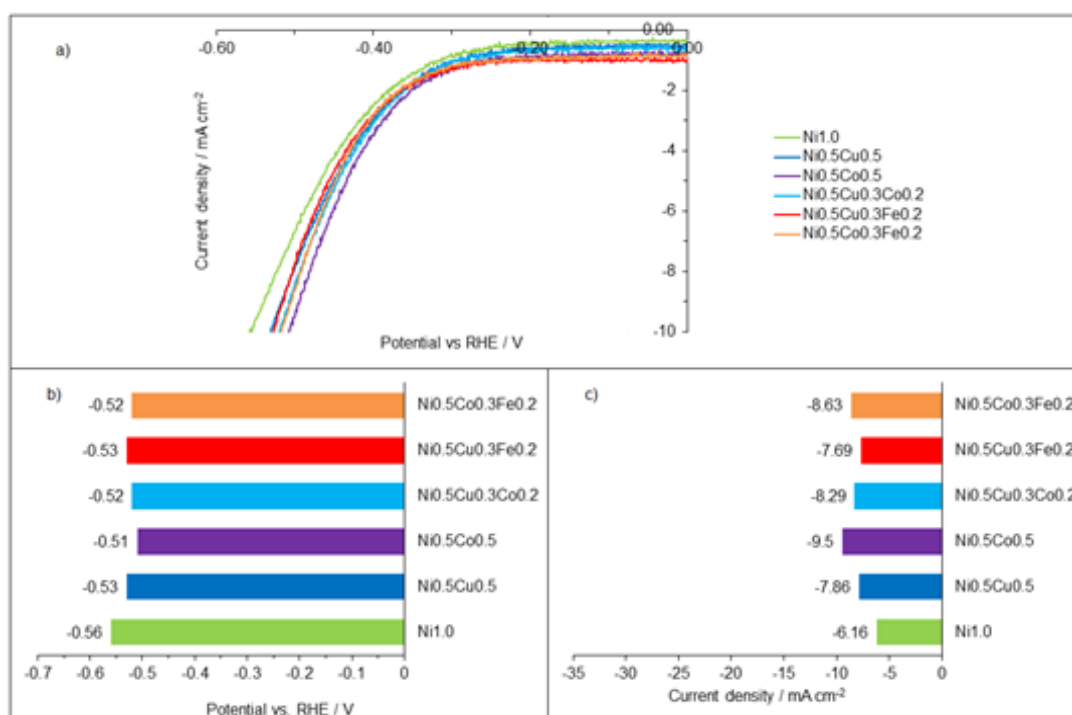
Figure 3-11 Comparison of the HER activity of trimetallic nanoalloys in pH 7 0.1 M phosphate buffer / 0.1 M Na$_2$SO$_4$. Under Ar and with a rotation rate of 4000 rpm. a) CV data, b) overpotential required to reach a current density of -10 mA cm^{-2} and c) current density at an overpotential of -0.5 V.

For example, the Ni$_{0.5}$Co$_{0.3}$Fe$_{0.2}$ nanoalloy shows little activity in pH 1 (-2.12 mA cm^{-2} at an overpotential of -0.5 V) and good activity in pH 13 (-17.5 mA cm^{-2} at an overpotential of -0.5 V). The value observed at pH 7, an intermediate pH is an intermediate value (-8.63 mA cm^{-2} at an overpotential of -0.5 V). A similar situation occurs with the Ni$_{0.5}$Cu$_{0.3}$Co$_{0.2}$ nanoalloy, which shows reasonable activity in pH 1 (-30.1 mA cm^{-2} at an overpotential of -0.5 V), poor activity at pH 13 (-2.46 mA cm^{-2} at an overpotential of -0.5 V) and intermediate activity at pH 7 (-8.29 mA cm^{-2} at an overpotential of -0.5 V).
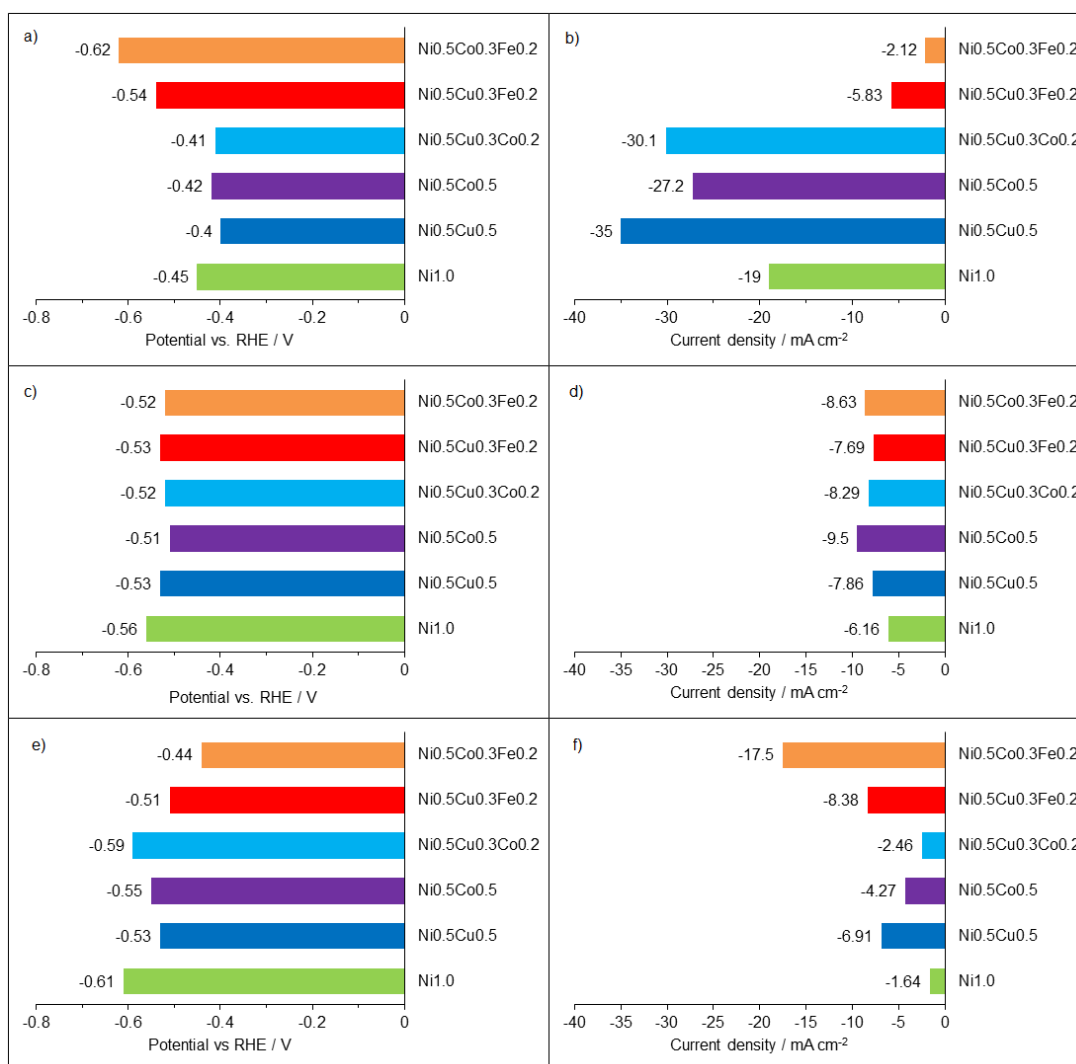
Figure 3-12 Comparison of HER activity of selected nanoalloys at various a), b) pH 1, c), d) pH 7 and e), f) pH 13. Respectively showing the overpotential required to reach a current density of 10 mA cm^{-2} and the current density obtained at an overpotential of 0.5 V vs RHE.

3.4.3 Conclusions

The HER activity of the trimetallic nanoalloys was tested in various conditions. The iron containing materials were far more active under basic conditions whereas the $Ni_{0.5}Cu_{0.3}Co_{0.2}$ material showed much greater activity in acidic solutions. Also, in acidic solutions a general trend between activity and electronegativity of the elements was observed, with the nanoalloys containing elements with higher electronegativity giving greater HER activity. Although the same trend was not seen under neutral or basic conditions. The reasons for the observed activities are still unclear although it is interesting to note that all nanoalloys gave very similar activities at pH 7.

If these catalysts were to be deposited on semiconductors, to use as part of a solar device, it is highly likely operation would occur at pH 7. Therefore, all nanoalloys are an option based on activity and the stability should be used as a way to differentiate between materials.

3.5 Stability Tests

One of the main limitations of the nickel catalyst previously investigated for hydrogen production was its stability.[45] From the measurements recorded over 20 cycles it is clear that the nanoalloys appear to be reasonably stable. There is no decrease in activity seen, instead a slight increase was observed for bimetallic samples with around -0.02 V less overpotential required to reach a current density of -10 mA cm^{-2} after 20 cycles. This variation is on the same scale as that seen between different samples of the same material and suggests the nanoalloys are stable under these conditions.

A much larger increase in activity was observed for the trimetaliic nanoalloys and especially the $Ni_{0.5}Cu_{0.3}Fe_{0.2}$ material. In this case the overpotential required to reach a current density of -10 mA cm^{-2} decreased by -0.1 V after 20 cycles. This is a large change in activity and was observed for all $Ni_{0.5}Cu_{0.3}Fe_{0.2}$ electrodes tested. As leaching is expected to occur it is possible this is leading to a more active material over time. Lv and co-workers have recently reported the same effect for core/shell NiAu/Au nanoparticles and have attributed it to the leaching of nickel from the nanoparticles over time.[96] Sweeping to more negative potentials is also known to result in improved activity. Therefore, cycling between 0 and -1 V vs Ag/AgCl may be responsible for the increased activity seen.
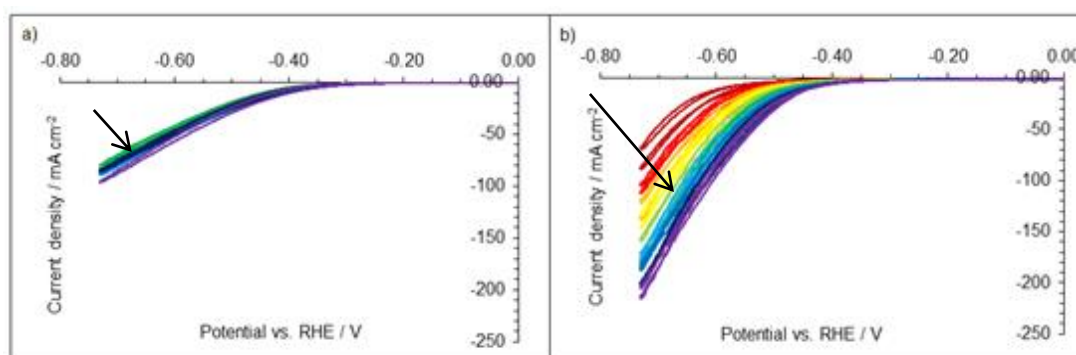
Figure 3-13 CV measurements for a) $Ni_{0.5}Cr_{0.5}$ and b) $Ni_{0.5}Cu_{0.3}Fe_{0.2}$ nanoalloys, showing the change in HER activity over 20 scans between 0.0 and -1.0 V vs Ag/AgCl. Measurements taken in pH 1 0.1 M H_2SO_4 / 0.1 M Na_2SO_4. Under Ar and with a rotation rate of 4000 rpm.

Attempts to analyse the composition of the nanoalloy before and after electrochemical measurements using TEM/EDX were made. However, it was not possible to observe the small amount of material from the end of the carbon rod, as described in section 3.2.4. It was possible to observe the nanoparticles on the carbon rods by HR-SEM. Unfortunately, the small size of the nanoparticles and the large carbon background signal prevented quantitative analysis of the nanoalloy compositions using EDX (see Appendix 2 Figure A14). After electrochemical measurements were carried out, the solution volume was reduced using a rotary evaporator to allow for analysis by ICP-MS to determine the presence of metals in the solution due to leaching from the sample. The results of this are still pending.

Nevertheless, this initial increase in activity suggests a potentially promising electrocatalyst. Therefore, establishing the stability of the electrodes over a longer timescale is important for applications' in a commercial device.

3.5.1   CV Sweeps

In order to test the stability of the trimetallic nanoalloys, 500 scans were measured for the trimetallic nanoalloy materials. Measurements were carried out at pH 1 and pH 13, as the HER activities of the various trimetallic nanoalloys varied depending on the pH.

As with the 20 scan runs, a large change in activity is observed for the $Ni_{0.5}Cu_{0.3}Fe_{0.2}$ material, with an increase in HER activity overtime. This increase in activity with consecutive scans is observed for all three trimetallic compositions. The HR-SEM data showed the particles on the electrode surface appear less agglomerated after 20 scans (section 3.2.4). Therefore, although effects due to elemental leaching cannot be ruled out, it is not clear exactly what is happening to the nanoalloy materials on the electrode surface during electrochemistry.
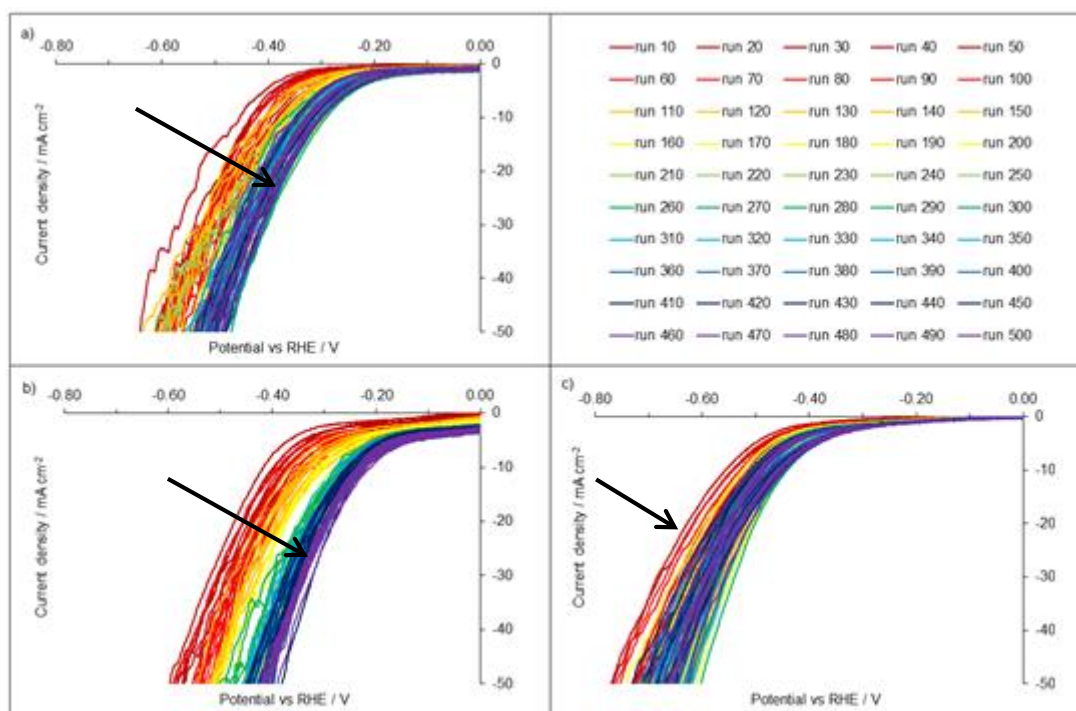
Figure 3-14 CV measurements of a) $Ni_{0.5}Cu_{0.3}Co_{0.2}$, b) $Ni_{0.5}Cu_{0.3}Fe_{0.2}$ and c) $Ni_{0.5}Co_{0.3}Fe_{0.2}$ nanoalloys, showing the change in HER activity over 500 scans between -0.2 and -1.2 V vs Ag/AgCl. Measurements taken in pH 1 0.1 M H_2SO_4 / 0.1 M Na_2SO_4. Under Ar and with a rotation rate of 4000 rpm.

In pH 1, The $Ni_{0.5}Cu_{0.3}Co_{0.2}$ and $Ni_{0.5}Co_{0.3}Fe_{0.2}$ nanoalloys initially show an increase in activity although this appears to have stabilised after 250 scans. Whereas for the $Ni_{0.5}Cu_{0.3}Fe_{0.2}$ nanoalloy a much larger increase is observed and the activity has only just stabilised after 500 scans. After 500 scans, the $Ni_{0.5}Cu_{0.3}Fe_{0.2}$ nanoalloy appears to show higher activity than the $Ni_{0.5}Cu_{0.3}Co_{0.2}$ nanoalloy. Unfortunately, as previously discussed, the exact composition of the active material has not been established as measuring the composition of the nanoalloys on the electrode has not been possible.

Many electrocatalysts show better stability in alkaline solutions and the trimetallic nanoalloys do not show a decrease in activity upon potential cycling under these conditions. However, as in the acidic solutions, an increase in activity is observed.
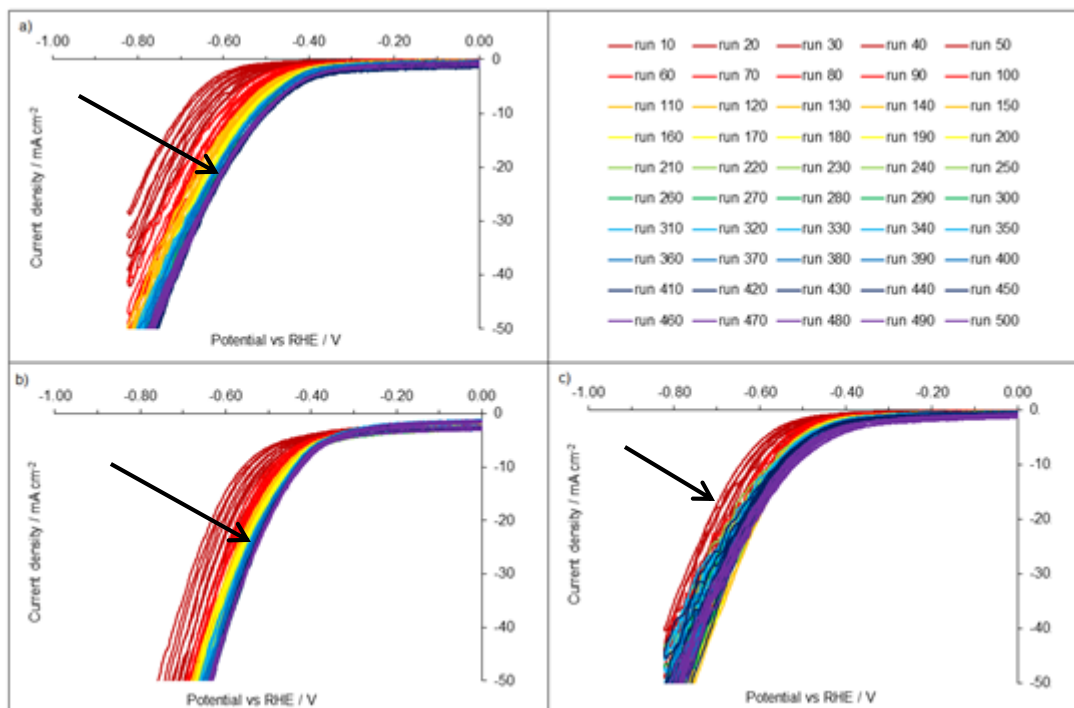
Figure 3-15 CV measurements of a) $Ni_{0.5}Cu_{0.3}Co_{0.2}$, b) $Ni_{0.5}Cu_{0.3}Fe_{0.2}$ and c) $Ni_{0.5}Co_{0.3}Fe_{0.2}$ nanoalloys, showing the change in HER activity over 500 scans between -0.8 and -1.8 V vs Ag/AgCl. Measurements taken in pH 13 0.1 M NaOH / 0.1 M Na_2SO_4. Under Ar and with a rotation rate of 4000 rpm.

Similar to the behaviour observed under acidic conditions, the activity of the $Ni_{0.5}Co_{0.3}Fe_{0.2}$ nanoalloy appears to have stabilised after 250 scans. Although in pH 13 both the $Ni_{0.5}Cu_{0.3}Fe_{0.2}$ and $Ni_{0.5}Cu_{0.3}Co_{0.2}$ nanoalloys show a dramatic increase in activity over the first 50 scans and do not stabilise until after 400 scans. The final activity of the $Ni_{0.5}Co_{0.3}Fe_{0.2}$ and $Ni_{0.5}Cu_{0.3}Co_{0.2}$ nanoalloys are similar although again it is the $Ni_{0.5}Cu_{0.3}Fe_{0.2}$ that appears most active after 500 scans.

Previous studies suggest that leaching of Ni, Co and Cu would not be expected to occur to any great extent in alkaline solutions.[139] Although the exact cause of the increased activity cannot be determined.

3.5.2   Held Potential Long Runs

The trimetallic nanoalloys were also tested for their stability over long runs at an overpotential of -0.5 V vs RHE at pH 1. Unfortunately, interference from the mains electrical

supply has resulted in very noisy data. Never the less, all three samples appear relatively stable over the 12 hours of testing. As observed for the repetitive cycling scans, the current density for the $Ni_{0.5}Co_{0.3}Fe_{0.2}$ and $Ni_{0.5}Cu_{0.3}Co_{0.2}$ nanoalloys increases overtime. The reason for the initial large current density for the $Ni_{0.5}Cu_{0.3}Fe_{0.2}$ is unknown and had not been seen previously, unfortunately due to time and equipment constraints it was not possible to run more samples.
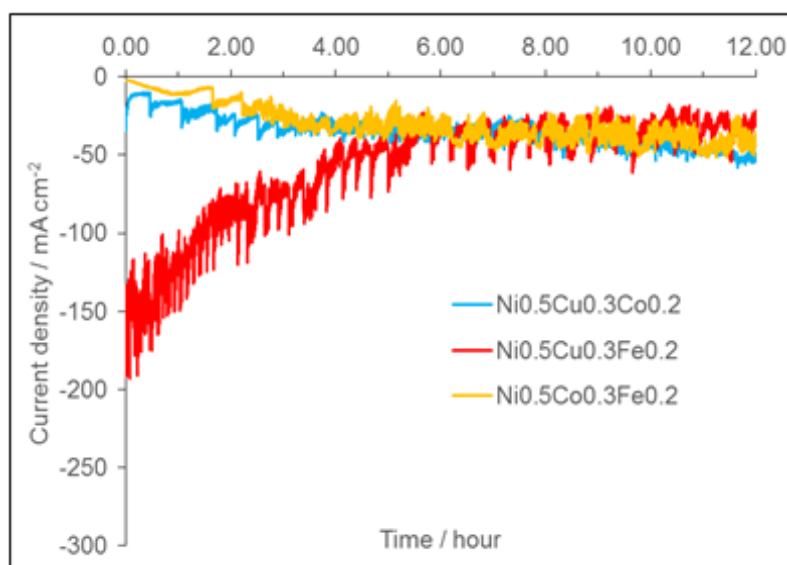
Figure 3-16 CPE measurements of trimetallic nanoalloys at -0.5 V vs RHE for 12 hours.

After 12 hours, the $Ni_{0.5}Cu_{0.3}Co_{0.2}$ material had the highest current density of around -50 mA cm^{-2}, followed by the $Ni_{0.5}Co_{0.3}Fe_{0.2}$ material (around -40 mA cm^{-2}) and the $Ni_{0.5}Cu_{0.3}Fe_{0.2}$ material had the lowest current density (around -30 mV cm^{-2}). Apart from the $Ni_{0.5}Cu_{0.3}Fe_{0.2}$ material, these results are in line with the other electrochemical experiments. They also show that the nanoalloys are reasonably stable in very acidic conditions over extended periods of time which has rarely been observed for nickel based catalysts. The notable exception being Ni_2P which shows reasonable stability in acidic environments but low stability in alkaline conditions.

3.6 Electrochemical Impedance Spectroscopy (EIS)

Impedance is a measure of the ability of a circuit to resist the flow of electrical current, similar to resistance. However, resistance is independent of frequency and follows Ohm's law (Equation 3-12) at all current and voltage levels. Also, AC current and voltage signals through a resistor are in phase with each other.[140]

$$R \equiv \frac{E}{I}$$
Equation 3-12

Impedance is not restricted by the same rules as resistance and so is a more realistic parameter for describing the behaviour of more complex circuits. Impedance is normally measured by applying a small excitation signal, to give a pseudo-linear response. The current response to a sinusoidal potential will be a sinusoid of the same frequency but shifted in phase. This allows the impedance of the system to be calculated, using an equation analogous to Ohm's law.[140]

$$Z = \frac{E_t}{I_t} = \frac{E_0 \sin(2\pi f\, t)}{I_0 \sin(2\pi f\, t + \phi)} = Z_0 \frac{\sin(2\pi f\, t)}{\sin(2\pi f\, t + \phi)}$$
Equation 3-13

Where E_t is the potential at time t, E_0 is the amplitude of the signal, f is the frequency (in hertz), Z_0 is a magnitude and $\emptyset$ a phase shift. The impedance can also be represented as a complex number (Equation 3-14). If the real part is plotted against the imaginary part, a Nyquist plot is obtained.[140]

$$Z_{(2\pi f)} = Z_0 e^{(j\phi)} = Z_0 (\cos\phi + j\sin\phi)$$
Equation 3-14

The problem with Nyquist plots is that you cannot tell just from looking at the graph what frequency was used to record any of the points. An alternative is to use Bode plots; in this case the log of the frequency is plotted against both the absolute impedance ($|Z| = Z_0$) and the phase shift.[140]

In order to analyse EIS data, it is fitted to an equivalent electrical circuit that may contain some or all of the following electrical elements: resistor, capacitor and inductor. These

elements all have different current versus voltage relationships and impedances (summarised in Table 3-2).[140]

Table 3-2 Common electrical elements, their current vs. voltage relationship and impedance

Component	Current Vs. Voltage	Impedance
resistor	$E = IR$	$Z = R$
inductor	$E = L \, di/dt$	$Z = j2\pi fL$
capacitor	$I = C \, dE/dt$	$Z = 1/j2\pi fC$

The simplified Randles Cell, which most circuits are based off of, includes a solution resistance, a double layer capacitor and a charge transfer resistance (Figure 3-17 a)). Although often a more complex circuit is required to model experimental data. Combinations of elements can occur in series or parallel (Figure 3-17 b) and c)).
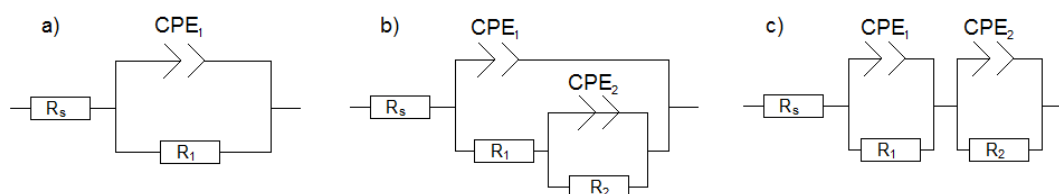
Figure 3-17 Examples of model electrochemical circuits: a) Circuit containing solution resistance (R_s), constant phase element (an imperfect capacitor, CPE_1) and a single variable resistor (R_1), b) Circuit containing solution resistance and two variable resistors in parallel, c) Circuit containing solution resistance and two variable resistors in series.

The solution resistance is often a significant factor in the impedance of an electrochemical cell and therefore, is always modelled in the equivalent circuit. A modern three-electrode potentiostat compensates for the solution between the counter and reference electrodes but any solution resistance between the reference electrode and the working electrode must be considered.[140]

The double layer capacitance, polarisation resistance (which results from the amount of current produced due to electrochemical reactions occurring at the electrode surface), charge transfer resistance and impedance caused by diffusion may also need to be considered.[140]

However, capacitors often do not show ideal behaviour and instead act like a constant phase element (CPE) due to a distribution of the relaxation times.[26, 140] This may be caused by adsorption[26, 141] or diffusion[26, 142] over the electrode surface.

3.6.1   EIS Measurements

As the materials have shown markedly different activities and stabilities in acidic and basic conditions, EIS spectra were recorded at both pH 1 and pH 13. The ESI measurements were carried out in the frequency region from 100 kHz to 10 mHz (6 points per decade) with an amplitude of 10 mV root mean square. In order to characterise the electrocatalytic activity of the electrodes, EIS was carried out at various overpotentials (η = -100, -300 and -500 mV).

The EIS setup differed from the electrochemical setup in the use of nitrogen instead of argon to purge the solution. This may result in some oxygen still being present but unfortunately this was the only gas available. Otherwise, initial measurements were attempted using exactly the same electrochemical setup as that used for all previously mentioned electrochemical experiments, as this would give the most comparable data. However, the motion of the rotator appeared to interfere with the EIS measurements, preventing the collection of meaningful data (Figure 3-18), even when the rotation rate was reduced.
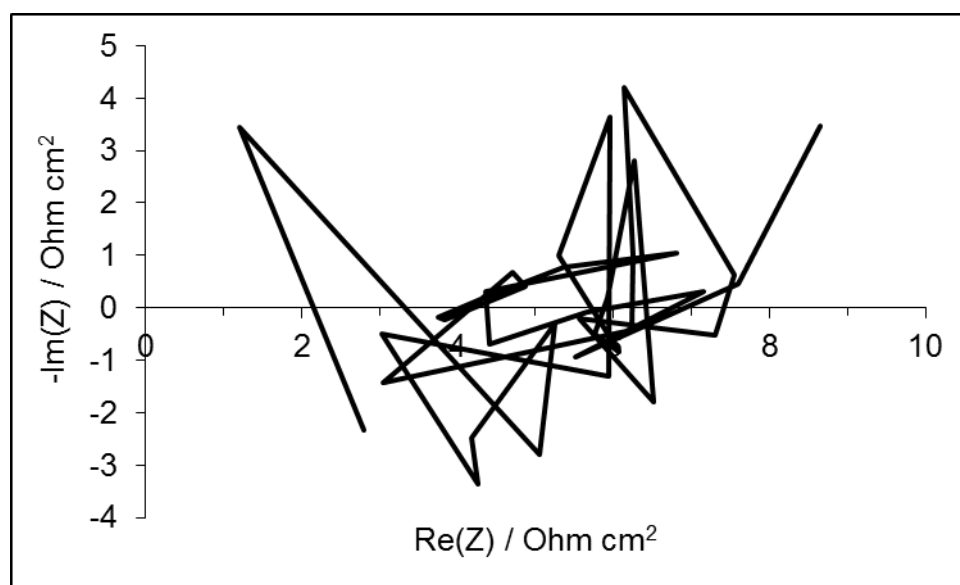
Figure 3-18 EIS spectra for Ni nanoparticles on a carbon rod recorded at -500 mV vs RHE in 0.1 M H_2SO_4 / 0.1 M Na_2SO_4, pH 1 with a rotation rate of 4000 rpm.

Attempts to measure the impedance without rotating the electrode encountered the same diffusion problems discussed in section 3.2.1 and consequently were also unsuccessful. In order to reduce the diffusion issues without rotating the electrode; a flat surface was carved into the side of a carbon rod (Figure 3-19). The nanoparticles were deposited onto the very end of the flat surface, covering a 0.06 cm^2 area. This enabled the working surface to be orientated vertically and therefore the hydrogen gas formed could more easily escape from the electrode surface.
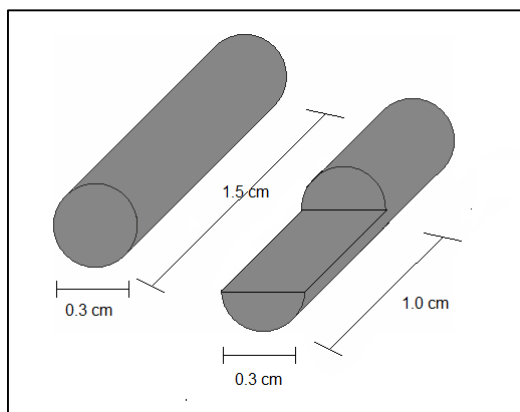
Figure 3-19 Schematic depiction of the carbon rod electrode used and the adaption made reduced diffusion problems occurred due to the build-up of hydrogen on the electrode surface during electrolysis.

Although this setup helped to reduce diffusion problems, to an extent, at low frequencies results were still often unreliable. This may have been due to variations in hydrogen gas coverage at the electrode over the larger lengths of time required for the lower frequency measurements. As this will have inconsistently affected the impedance of the system and a diffusion component would explain the apparent inductor behaviour (negative imaginary impedance) seen at lower frequencies (Figure 3-19). Therefore, data was only used to a frequency of 100 mHZ rather than 10 mHz.
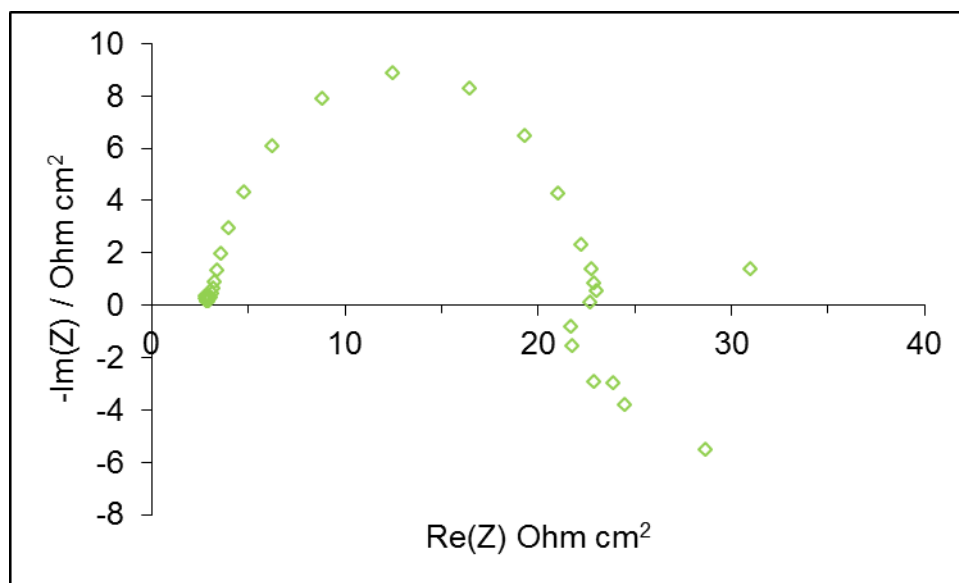
Figure 3-20 EIS spectra of nickel nanoparticles on an adapted carbon rod, recorded at -500 mV vs RHE in 0.1 M H_2SO_4 / 0.1 M Na_2SO_4, pH 1. Showing unexpected induction behaviour at low frequencies that may be due to diffusion problems.

3.6.2 EIS at pH 1, Comparison at Various Overpotentials

The impedance spectra, for all compositions measured, show the presence of two time constants at all overpotentials measured. The results for pure nickel nanoparticles are in line with those previously reported and recorded under similar conditions.[50] However, our results show a much lower impedance for this material at high overpotentials (-500 mV). Upon increasing the overpotential, a decrease in the semicircle size indicates enhancement of HER kinetics, as expected. Unexpectedly, the $Ni_{0.5}Cu_{0.3}Co_{0.2}$ nanoalloy appears to show the largest impedance although from the CV and LSV measurements this appeared to be one of the most active compositions. In fact, the least active compositions appear to show the lowest impedance.
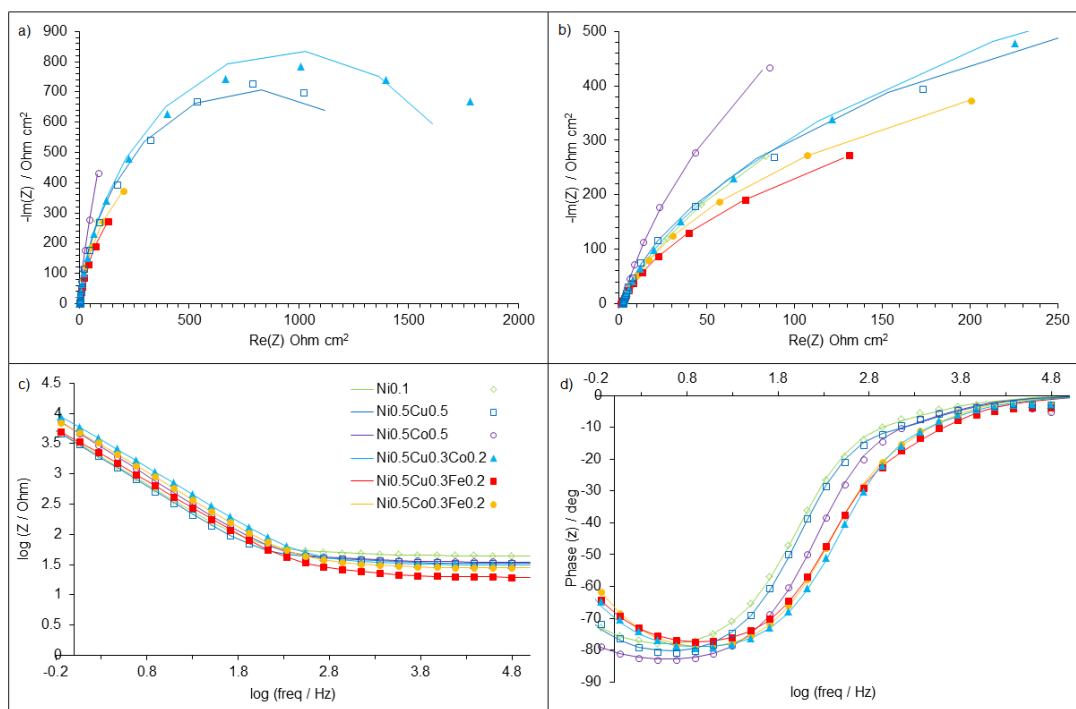
Figure 3-21 EIS data at an overpotential of -100 mV in 0.1 M H2SO4 pH 1. The symbols are the experimental data and the lines are the fits a) Nyquist plot for all frequencies, b) zoomed in image of Nyquist plot at high frequencies, c) Bode impedance plot and d) Bode phase plot.
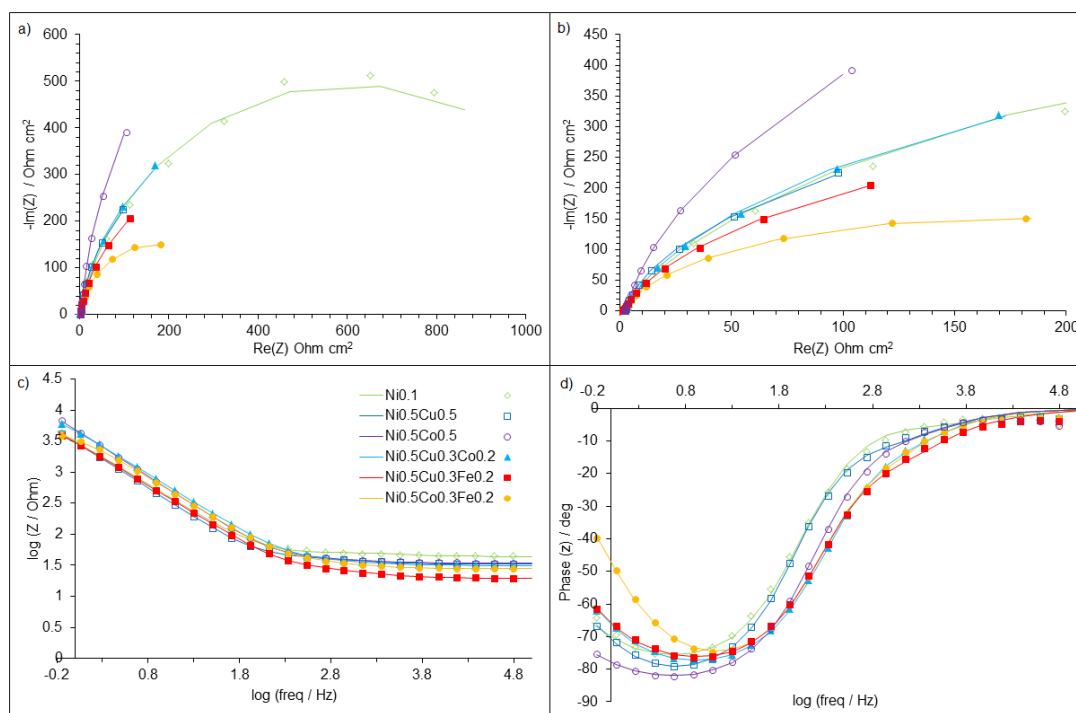
Figure 3-22 EIS data at an overpotential of -300 mV in 0.1 M H2SO4 pH 1. The symbols are the experimental data and the lines are the fits a) Nyquist plot for all frequencies, b) zoomed in image of Nyquist plot at high frequencies, c) Bode impedance plot and d) Bode phase plot.
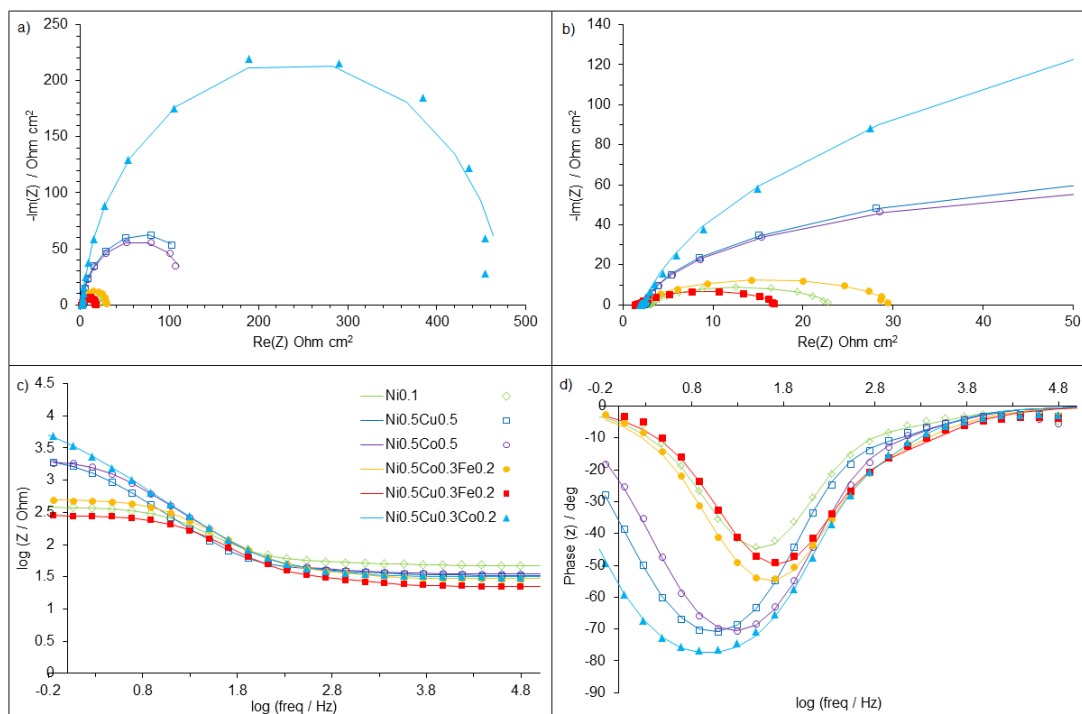
Figure 3-23 EIS data at an overpotential of -500 mV in 0.1 M H2SO4 pH 1. The symbols are the experimental data and the lines are the fits a) Nyquist plot for all frequencies, b) zoomed in image of Nyquist plot at high frequencies, c) Bode impedance plot and d) Bode phase plot.

Little difference between the various materials is observed at more positive potentials than -300 mV. However, at -500 mV lower impedance is observed for the electrocatalytically least active materials, although little difference is observed between these materials. It is possible that oxygen was not completely removed before analysis and oxygen reduction is occurring and complicating the results. It is also possible that the measurements are recording an effect due to the carbon rod rather than just the nanoparticles.

3.6.2.1   Modelling the EIS Experimental Data

The experimental data was modelled using non-linear least squares fit analysis software and an electrical equivalent circuit. The three most commonly used circuits to describe the AC impedance for HER on nickel based electrodes were discussed in section 3.6 (Figure 3-17). The Randles cell (Figure 3-17 a)) has been used to describe the HER response on relatively smooth surfaces[143] when there is no obvious response related to hydrogen adsorption.[26] The other two circuits possess two time constants, one or both may be related to the HER

kinetics and so change with overpotential.[26] If a time constant does not change with overpotential it is related to the porosity of the electrode surface.[50]

All three circuits were tested and a better fit was seen for the two time constant, parallel circuit model (Figure 3-17 b)).

Table 3-3 Modelling of equivalent circuits for the EIS data for various nanoalloys in pH 1.

η = -100 mV	Randles cell	Parallel circuit	Series circuit
R_s / Ohm cm^2	2.74	2.64	2.68
CPE_1 / Fs$^{(a-1)}$		3.80E-05	6.61E-04
a_1		0.86	0.66
R_1 / Ohm cm^2		1.20	53.23
CPE_2 / F s$^{(a-1)}$	5.32 E-05	1.55E-05	4.70E-05
a_2	0.91	1.00	1.00
R_2 / Ohm cm^2	1931.22	1923.84	1037.96
χ^2	5.76 E-02	2.77E-02	3.87E-02
η = -300 mV			
Rs / Ohm cm2	2.75	2.08	1.55
CPE1 / Fs(a-1)		8.57E-06	2.83E-07
a1		0.67	0.83
R1 / Ohm cm2		0.8	1.25
CPE2 / F s(a-1)	5.92 E-05	3.35E-05	5.88E-05
a2	0.90	0.91	0.90
R2 / Ohm cm2	1149.84	1190.16	1144.98
χ2	9.39 E-02	4.55E-02	5.19E-02
η = -500 mV			
Rs / Ohm cm2	2.93	2.83	1.95
CPE1 / Fs(a-1)		3.93E-05	6.49E-05
a1		0.85	0.46
R1 / Ohm cm2		0.94	1.19
CPE2 / F s(a-1)	6.53 E-05	2.16E-05	55.55E-06
a2	0.90	1.00	0.93
R2 / Ohm cm2	20.29	19.18	19.49
χ2	5.76 E-02	3.45E-02	4.81E-02

When the high frequency (HF, smaller) semicircle is potential independent, it is related to the porosity of the electrode surface[26, 50] or hydrogen adsorbed[50] while the larger and potential dependent low frequency (LF, larger) semicircle can be related to the charge transfer resistance.[26, 50, 140] However, the EIS results do not appear to be in agreement with the other electrochemical data. It is possible that the high sensitivity of this technique is actually measuring an effect from the carbon rod rather than the nanoparticles or that oxygen reduction is occurring and complicating the results. Therefore, the data will not be discussed further here although the circuit fits for the pH 1 data and all data for pH 13 can be seen in Appendix 2.

3.7 Mechanistic Investigations (Tafel plots)

As previously stated, the hydrogen evolution reaction (HER) involves two of three steps which are shown in Equation 3-15 to Equation 3-19, the mechanism of steps 1 and 3 depends on whether the solution is acidic ((1A) and (3A)) or basic/neutral (3A and 3B). The first step involves hydrogen adsorption onto the metal surface (Volmer step, Equation 3-15 or Equation 3-16, this adsorbed species can then either combine with another adsorbed hydrogen (Tafel Equation 3-17) or with a species in solution (Heyrovsky step, Equation 3-18 and Equation 3-19) to produce dihydrogen.

Step 1A:	$M + H^+ + e^- \rightarrow M\text{-}H_{ads}$	Equation 3-15
Step 1B:	$H_2O + M + e^- \rightarrow M\text{-}H_{ads} + OH^-$	Equation 3-16
Step 2:	$2M\text{-}H_{ads} \rightarrow H_2 + 2M$	Equation 3-17
Step 3A:	$M\text{-}H_{ads} + H^+ + e^- \rightarrow H_2 + M$	Equation 3-18
Step 3B:	$M\text{-}H_{ads} + H_2O + e^- \rightarrow H_2 + M + OH^-$	Equation 3-19
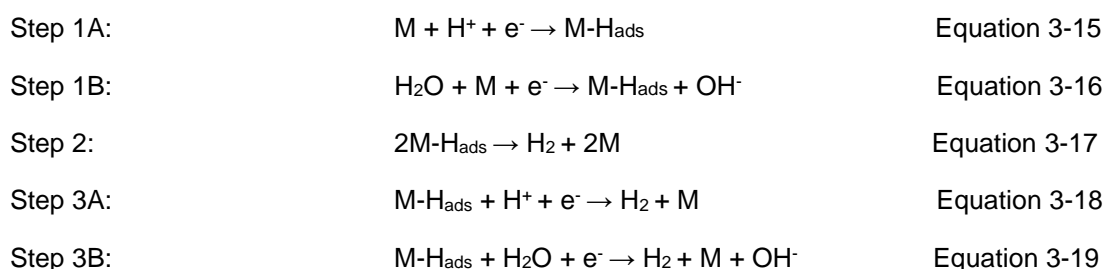
Both the Volmer–Heyrovsky or Volmer–Tafel mechanisms involve the formation and cleavage of $M\text{-}H_{ads}$ bonds which is why metals with intermediate M-H bond strengths, such as platinum, give the highest activity for the HER.

At high negative overpotentials, the Butler-Volmer equation (Equation 3-6) can be simplified to give the cathodic current density (Equation 3-20). This can be rearranged to give the Tafel equation (Equation 3-21).

$$\log\text{-}i = \log i_o - \frac{\alpha_C nF}{2.3RT}\eta \qquad\qquad \text{Equation 3-20}$$

$$\eta = a + b\log i \qquad\qquad \text{Equation 3-21}$$

Where η (V) is the applied overpotential, i (mA cm^{-2}) is the resulting current density, b is the Tafel slope and a is the intercept and is related to the exchange current density, i_0 (mA cm^{-2}), by Equation 3-22. Where R is the gas constant (8.314 J K^{-1} mol^{-1}), T (K) is the temperature,

n is the number of electrons transferred, F is the Faraday constant (96485 C mol^{-1}) and β is the symmetry factor which can be calculated from the Tafel slope using Equation 3-23.

$$a = \frac{2.3RT}{\beta nF} \times \log i_0 \qquad\qquad \text{Equation 3-22}$$

$$b = \frac{2.3RT}{\beta nF} \qquad\qquad \text{Equation 3-23}$$

Plotting the overpotential against the log of the current density can give insight into electrode activity and the reaction mechanism the exchange current density, Tafel slope and transfer coefficient can then be derived.[26]

The value for the Tafel slope gives an indication of the rate determining step and potentially the reaction pathway.[18] If step 1, the Volmer reaction step, is the rate determining step then a Tafel slope of around 120 mV decade^{-1} would be expected. Whereas, a Tafel slope of 30 mV decade^{-1} or 40 mV decade^{-1} would be expected for the Tafel (step 2) and Heyrovsky (step 3) steps respectively. The Tafel slope also suggests the overpotential increment that is required to increase the current density ten-fold. Therefore, a small Tafel slope denotes a steep rise of the electrocatalytic current density and a more active material for proton reduction.[18]

3.7.1   Tafel Plots in Acidic Conditions (pH = 1)

Tafel plots were recorded in pH 1 0.1 M H_2SO_4 / 0.1 M Na_2SO_4 solution, with a scan rate of 1 mV s^{-1}. Electrodes were rotated at 4000 rpm and the solution was purged with argon for 20 minutes prior to measurement.

Figure 3-24 Tafel plot of nanoalloys in pH 1 0.1 M H_2SO_4 / 0.1 M Na_2SO_4. Under Ar and with a rotation rate of 4000 rpm.

Table 3-4 Tafel slope, exchange current density and transfer coefficient for nanoalloys in pH 1 0.1 M H_2SO_4 / 0.1 M Na_2SO_4.

Catalyst	b / mV decade^{-1}	i_0 / A cm^{-2}	Log(i_0 / A cm^{-2})	$\propto$
Ni	-145	-7.9×10^{-6}	-5.1	-0.40
$Ni_{0.5}Cu_{0.5}$	-147	-2.0×10^{-5}	-4.7	-0.39
$Ni_{0.5}Co_{0.5}$	-145	-1.3×10^{-5}	-4.9	-0.40
$Ni_{0.5}Cu_{0.3}Co_{0.2}$	-146	-1.6×10^{-5}	-4.8	-0.40
$Ni_{0.5}Cu_{0.3}Fe_{0.2}$	-147	-2.0×10^{-6}	-5.7	-0.39
$Ni_{0.5}Co_{0.3}Fe_{0.2}$	-161	-1.6×10^{-6}	-5.8	-0.36

All materials show larger Tafel slopes than the theoretical value of -118 mV decade^{-1} suggesting the hydrogen adsorption (Volmer) step is the rate determining step and that HER proceeds via a Volmer-Tafel mechanism.[144] This is in agreement with high overpotential measurements for nickel alloy electrodeposits.[26] Therefore the rate of hydrogen adsorption is rate determining as the coverage of adsorbed hydrogen atoms approaches saturation at high enough overpotentials leading to accelerated atom–atom recombination.[18]

The larger than theoretical values obtained may be due to the presence of an oxide film on the electrode surface, which would inhibit electron transfer and therefore larger overpotentials would be required for the HER.[26]

XRD data clearly showed the presence of NiO in the $Ni_{0.5}Co_{0.3}Fe_{0.2}$ nanoalloy which may account for the much larger Tafel slope, of -161 mV decade^{-1}, observed for this material. All other nanoalloys have Tafel slopes of around -146 mV decade^{-1}. This suggests on $Ni_{0.5}Co_{0.3}Fe_{0.2}$ the hydrogen adsorption step is relatively difficult under these conditions and is consistent with the low activity and requirement of a high overpotential observed for HER. All of this suggests that the $Ni_{0.5}Co_{0.3}Fe_{0.2}$ nanoalloy has a lower hydrogen adsorption strength than the other compositions which results in lower activity for HER on this material, under these conditions.

The similarity between the Tafel slope values for the majority of nanoalloys indicates that the same mechanism is responsible for HER on all materials. However, differences are observed in the exchange current densities and this is often used as an indicator of HER activity, although the Tafel slope is the more useful parameter (as the exchange current density gives information for equilibrium rather than operating conditions).

The value obtained for the pure nickel nanoparticles of -7.9×10^{-6} A cm^{-2} to the value obtained for bulk nickel in 1 M H_2SO_4 of -6.3×10^{-6} A cm^{-2}. Whereas, much larger exchange current densities of -2.0×10^{-5} A, -1.3×10^{-5} A and -1.6×10^{-5} A are observed for the $Ni_{0.5}Cu_{0.5}$, $Ni_{0.5}Co_{0.5}$ and $Ni_{0.5}Cu_{0.3}Co_{0.2}$ materials respectively. These values would not be expected based purely on the exchange current densities of the individual metal elements present in the nanoalloys. This suggests a synergistic effect occuring in the alloy material, resulting in a higher exchange current density and HER activity than that observed for the pure nickel nanoparticles. These values are still not quite as high as those observed for Ni_2P nanoparticles (3.2×10^{-5} A) although they are of a similar magnitude.[28]

Both iron containing nanoalloys gave exchange current densities an order of magnitude lower than the values obtained for the other nanoalloy materials. Again confirming the poor activity of these materials in acidic solutions.

3.7.2 Tafel Plots in Basic Conditions (pH = 13)

Tafel plots were recorded in pH 13 0.1 M NaOH / 0.1 M Na$_2$SO$_4$ solution, with a scan rate of 1 mV s^{-1}. Electrodes were rotated at 4000 rpm and the solution was purged with argon for 20 minutes prior to measurement.
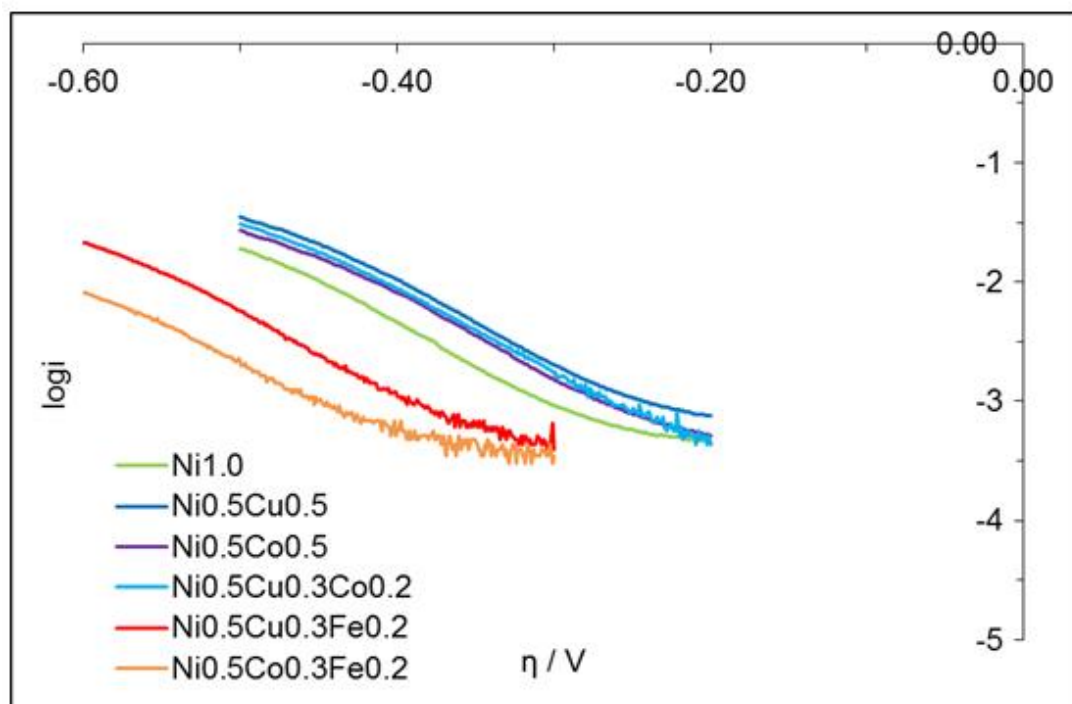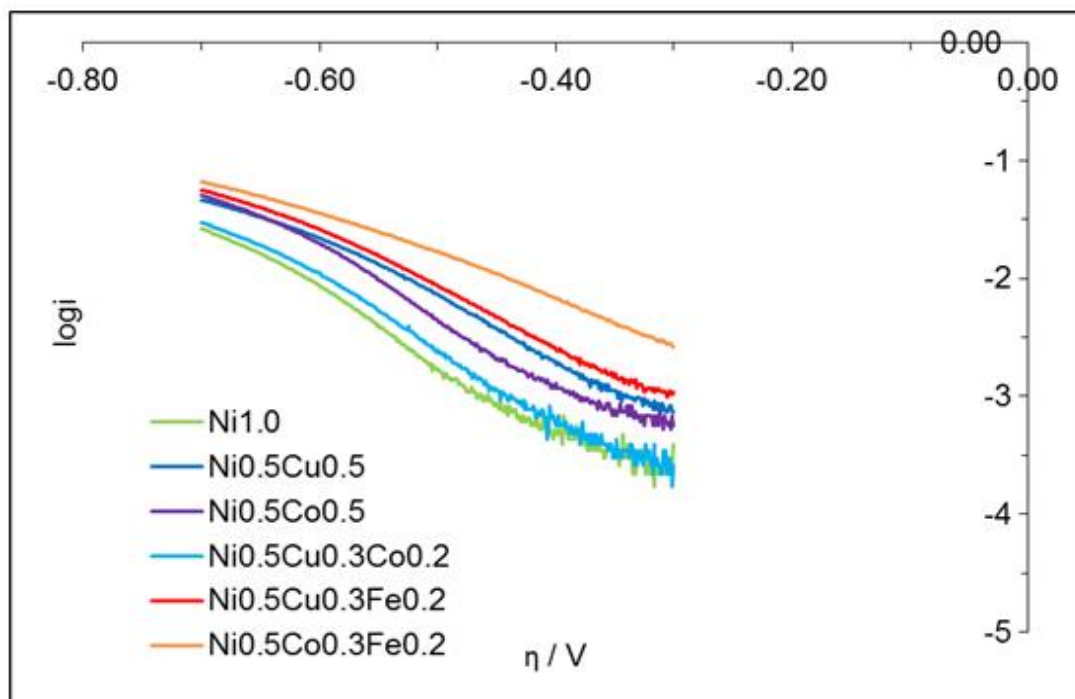

Figure 3-25 Tafel plot of nanoalloys in pH 13 0.1 NaOH / 0.1 M Na$_2$SO$_4$. Under Ar and with a rotation rate of 4000 rpm.

Table 3-5 Tafel slope, exchange current density and transfer coefficient for nanoalloys in pH 13 0.1 M NaOH/ 0.1 M Na$_2$SO$_4$.

Catalyst	b / mV decade^{-1}	i$_0$ / A cm^{-2}	Log(i_0 / A cm^{-2})	$\propto$
Ni	-154	-1.0×10^{-6}	-6.0	-0.38
Ni$_{0.5}$Cu$_{0.5}$	-192	-1.6×10^{-5}	-4.8	-0.30
Ni$_{0.5}$Co$_{0.5}$	-168	-5.0×10^{-6}	-5.3	-0.35
Ni$_{0.5}$Cu$_{0.3}$Co$_{0.2}$	-157	-1.6×10^{-6}	-5.8	-0.37
Ni$_{0.5}$Cu$_{0.3}$Fe$_{0.2}$	-201	-1.6×10^{-5}	-4.8	-0.29
Ni$_{0.5}$Co$_{0.3}$Fe$_{0.2}$	-259	-2.0×10^{-4}	-3.7	-0.22

As seen in pH 1, the hydrogen adsorption (Volmer) step is the rate determining step and HER appears to proceed via a Volmer-Tafel mechanism. Although larger Tafel slopes are observed for all materials in alkaline compared to acidic conditions, there are some large differences in the exchange current densities seen for most materials. The pure nickel nanoparticles and the $Ni_{0.5}Co_{0.5}$ nanoalloy both show lower exchange current densities at pH 13 however; the differences are not as large as those observed for the trimetallic materials. For the $Ni_{0.5}Cu_{0.3}Co_{0.2}$ nanoalloy the exchange current density observed at pH 13 was an order of magnitude smaller than that observed at pH 1, with values of -1.6×10^{-6} A and -1.6×10^{-5} A respectively. This is consistent with the lower activity seen for this material in alkaline solutions. Although NiCuCo alloys with higher copper contents have shown reasonable activity in alkaline solutions.[114]

Conversely, the iron containing trimetallic nanoalloys show exchange current densities one or two orders of magnitude larger in alkaline solutions. The greatest exchange current density was observed for the $Ni_{0.5}Co_{0.3}Fe_{0.2}$ nanoalloy, with a value of -2.0×10^{-4} A and is consistent with this being the most active material for HER in alkaline solutions. A NiCuFe electrodeposit studied by Jafarian and co-workers was also found to be active in alkaline solutions although the exchange current density of this material was -4.4×10^{-5} A,[76] an order of magnitude lower than the value observed for the $Ni_{0.5}Co_{0.3}Fe_{0.2}$ nanoalloy studied here.

3.8 Conclusions

A quick and simple electrode synthesis method has been developed to test the synthesised nanoalloys. HR-SEM images suggest the nanoalloy loading was a lot lower than expected and therefore improving this could lead to the observation of higher HER activities.

Testing of various atomic ratios of the same alloy composition revealed that the $Ni_{0.5}M_{0.5}$ material is the most active. This may be a result of this ratio forming the most stable nanoallloy materials although it may also suggest a synergistic effect occurring between the elements that is most prevalent at this ratio. Of the various $Ni_{0.5}M_{0.5}$ compositions tested; the $Ni_{0.5}Mo_{0.5}$ and $Ni_{0.5}Ru_{0.5}$ materials showed the highest activity. Although, all bimetallic nanoalloys showed significantly higher activity than pure nickel. However, in pH 1 only the $Ni_{0.5}Cu_{0.3}Co_{0.2}$ nanoalloy showed reasonable activity. The iron containing materials showed lower activity than pure nickel. Although their activity continued to increase with successive cycles and eventually very little difference was seen between all three alloy materials. For all

materials tested at pH 1, a correlation between HER activity and electronegativity of the elements in the nanoalloy was observed. More electronegative elements resulted in higher activity. This suggests the electronic structure of the active sites on the catalyst are altered by the presence of the other elements in the alloy although exactly how this aids proton reduction is still unclear. Whereas in basic conditions the $Ni_{0.5}Co_{0.3}Fe_{0.2}$ material gave the highest HER activity and the $Ni_{0.5}Cu_{0.3}Co_{0.2}$ nanoalloy had one of the lowest. Also, no trend between electronegativity and HER activity was observed. At pH 7 all nanoalloys had very similar activities. This can be understood based on the difference in activity of a particular nanoalloy in pH 1 and pH 13; resulting in an activity between the two at pH 7. The exchange current densities calculated for each material agree with the activities observed. Although the Tafel slopes are relatively high and clearly indicate that the Volmer step is the rate determining step in all cases, as previously seen for nickel electrocatalysts.

The stability of the nanoalloys was also tested and as well as showing higher stability than platinum, the trimetallic materials appear stable over 12 hours at a reasonable overpotential (-0.5 V vs RHE). Also, sweeping potentials between 0.0 and -1.0 V (vs RHE) appears to result in an increase in electrocatalytic HER activity and the materials were still stable after 500 cycles. To further test stability, EIS was carried out.

Unfortunately, the EIS data was inconclusive and further experiments would be necessary to confirm the reliability of the data. More experiments are also required to try to establish the exact composition of the active nanoalloy catalyst as leaching is a large possibility. The change in nanoalloy dispersion on the electrode after electrochemistry and the increased HER activity seen over time support the theory that the nanoalloy structure and/or composition is altered during measurements. To further develop materials it is important to understand how they are changing during electrolysis and to identify the active species.

4 CO$_2$ Reduction

4.1 Introduction

Extensive use of fossil fuels has led to an increase in levels of atmospheric CO$_2$ and this has been linked to the rise in global temperature.[83, 145] The dwindling levels of fossil fuel reserves necessitate the development of alternative hydrocarbon feedstocks. Being able to efficiently turn CO$_2$ into fuels would both provide an alternative to fossil fuels and be highly beneficial in helping to prevent an increase in CO$_2$ emissions.[83] Burning fuels produced from reduction of CO$_2$ would release the same amount of CO$_2$ as that originally converted into fuels. Therefore, if a renewable energy source is used to reduce CO$_2$, the process would effectively be CO$_2$ neutral.[145] Compared to thermocatalytic CO$_2$ reduction, (photo)electrocatalytic CO$_2$ reduction has the advantage of operating at ambient temperature and lower partial pressures of reactant gases.[87]

Over the last few decades, several materials capable of electrochemically reducing CO$_2$ in aqueous solutions have been identified.[89 146] However, these materials often have poor stability and efficiency.[89] For example tin has been shown to be selective for formic acid production and gold can give high CO selectivity. However, for the production of hydrocarbons, copper has been the most promising material investigated. A range of hydrocarbon products have been reported for copper electrodes including methane,[24, 146-148] ethylene, [24, 146-148] ethanol[24, 148] and propanol.[24, 148] This is due to the medium hydrogen overvoltage and a relatively weak CO adsorption, of copper, which allows the breaking of the carbon-oxygen bond in CO$_2$ followed by reduction of the CO.[24, 149] One of the main drawbacks of copper electrodes is that they rapidly lose CO$_2$ reduction activity if impurities are present in the electrolyte solution.[89]

Li and Kanan have shown that electrochemically reduced Cu$_2$O layers on Cu^0 electrodes, creates active CO$_2$ reduction catalysts that are stable in solution.[89] Unlike, polycrystalline Cu electrodes, this material has a high FE for CO and HCOOH production and these products start to form at much lower overpotentials. However, a much lower concentration of other hydrocarbons was observed.[89]

As the hydrogen and CO adsorption strengths affect the products formed, alloying copper with other metals may provide a way to tailor product formation and increase stability. Calculations by Peterson and Norskov suggest that for higher hydrocarbon product formation at low overpotentials a slightly weaker CO binding than Cu is optimum.[150]
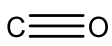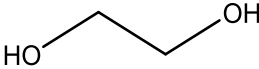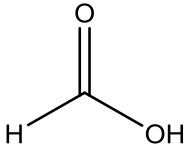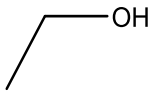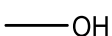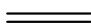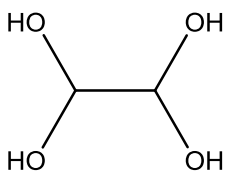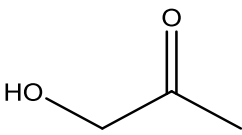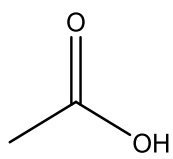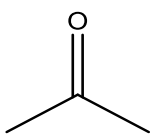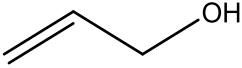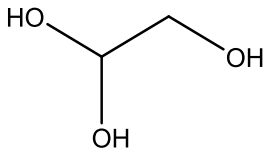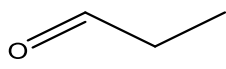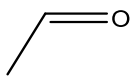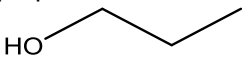
Nickel has recently become the focus of solid oxide fuel cells as a replacement for platinum and can reduce a mixture of CO_2 and H_2 to methane, whereas a copper catalyst resulted in CO formation. Molecular electrocatalysts have also been investigated and nickel cyclams have been shown to be highly selective for CO production.[145] Also, Ali and co-workers have investigated a nickel-nanoparticle electrodeposit and have found it favours ethanol production although there may be a catalytic as well as electrocatalytic process occurring. Whereas, Steinmann and co-workers have shown a Ni(111) to be active for formic acid production, again highlighting the importance of the catalyst surface for product selectivity.

4.1.1   Possible products

The most common products reported from CO_2 reduction are carbon monoxide, formic acid and/or hydrogen. Of the many metal catalysts investigated for CO_2 reduction, only copper has shown significant activity for various hydrocarbon products especially methane and ethylene,[24, 146, 147] low concentrations of other hydrocarbon products have also been detected.[89, 151]

Kuhl and co-workers used a small, custom made electrochemical cell with a total electrolyte volume of 8 mL to investigate the various products produced by a copper electrode at various overpotentials. Using GC and NMR analysis, they identified sixteen CO_2 reduction products.[17] These products are shown in Table 4-1 along with the number of electrons required and the standard reduction potential at pH 6.8 vs. RHE.[17] The major products they detected where hydrogen, methane, formate, CO and ethylene. This is in agreement with previous CO_2 reduction studies on copper electrodes.[151] However, a range of other hydrocarbon products, with various faradaic efficiencies, were also detected.

Table 4-1 Possible carbon based products of CO_2 reduction, the number of electrons required and the standard reduction potential for the reaction at pH 6.8 vs RHE.

Product	e⁻	E / V	Product	e⁻	E / V
Carbon monoxide C≡O	2	-0.10	Ethylene glycol	10	0.20
Formic acid	2	-0.02	Ethanol	12	0.09
Methanol —OH	6	0.03	Ethylene	12	0.08
Glyoxal	6	-0.16	Hydroxyacetone	14	0.46
Acetic acid	8	-0.26	Acetone	16	-0.14
Methane CH_4	8	0.17	Allyl alcolhol	16	0.11
Glycolaldehyde	8	-0.03	Propionaldehyde	16	0.14
Acetaldehyde	10	0.05	1-propanol	18	0.21

The product distribution is very potential dependent and Kuhl and co-workers noted that at potentials more positive than -0.75 V only hydrogen, formate and carbon monoxide were observed.[17] The high overpotentials required for hydrocarbon production on copper electrodes are one of the main limitations of this material,

partly due to the tendency of the competing HER to become more dominant at higher overpotentials.[17] Although it has been shown that increased hydrocarbon production at potentials between -0.9 V and -1.1 V can limit HER efficiency on copper electrodes.[17] Modified copper electrodes have also resulted in hydrocarbon product formation from CO_2 reduction at lower overpotentials with a different product distribution.[89] In this case, much higher CO efficiencies were observed, with ethanol and formate being the main solution based products detected.

4.1.2 Aims

The CO_2 reduction activity of various trimetallic nickel nanoalloys was investigated. To investigate selectivity, GC and NMR analysis were used to identify and quantify the products formed.

4.2 Electrocatalytic Setup

The electrochemical set-up is crucial for analysis of CO_2 reduction products. The cell must allow for analysis of both the gas and solution products; in order to maximise product concentration, it is advantageous to minimise the volume of solution. Generally volumes of 20 mL or less are used with Kuhl and co-workers identifying far more products than previous studies by using a volume of only 8 mL.[17]

4.2.1 Electrochemical Cell Design

Due to the small volume requirements, the electrochemical cell used for the HER experiments was not suitable for the CO_2 reduction experiments. A much smaller cell was designed with a solution volume of 12 mL and a headspace of 5 mL in the working electrode side. In addition to the smaller volume, this cell consists of two compartments separated by a glass frit coated with a Nafion cation exchange membrane. This was to separate the working and counter electrodes, as certain CO_2 reduction products, including formic acid, are known to re-oxidise at platinum anodes.[22] Initial experiments used a single compartment cell, the loss of formic acid during electrolysis was confirmed by addition of a known amount of formic acid before electrolysis and analysis of the solution after 4 hours holding at a potential of – 0.689 V. NMR analysis showed the formic acid concentration decreased a hundredfold. This highlighted the need to separate the working and counter

electrodes to prevent reoxidation of the CO_2 reduction products formed. A photo of the designed two-compartment cell is shown in Figure 4-1.
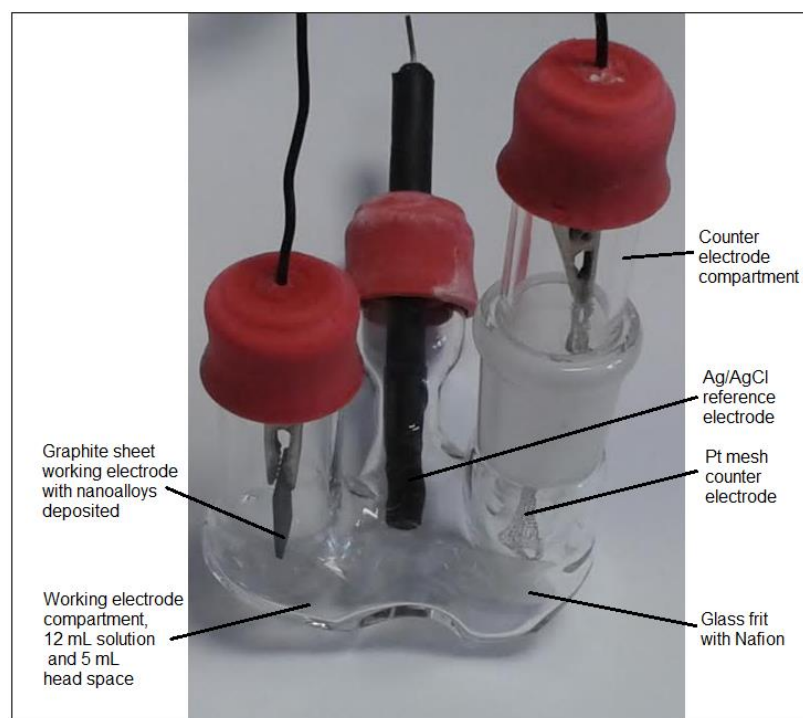
Figure 4-1 Annotated photograph of the two compartment electrochemical cell used. Which has a solution volume of 12 mL and head space of 5 mL.

However, the small size of this cell, coupled with the desire to measure gas products prevented the use of a rotator. Therefore, to overcome the diffusion problems previously observed with the carbon rods (see chapter 3 section 3.2), graphite sheets were used instead.

4.2.2   Effect of Solution on Electrochemical CO_2 Reduction Activity

The composition of the electrochemical electrochemical solution can have a large effect on catalytic activity and the CO_2 reduction products produced. Hori and co-workers have shown that the concentration of bicarbonate can effect whether alcohols and ethylene or methane are the favoured product, with more concentrated solutions resulting in preferential methane formation.[149]

Reduction experiments were carried out under various conditions to assess the source of the CO_2 and current seen. Reduction was run in 0.1 M phosphate buffer (pH 7) with and without the presence of 0.5 M $NaHCO_3$, under argon and CO_2. More current was observed in the presence of CO_2 although materials have been shown to be more active for HER under CO_2 atmospheres therefore without analysis of the products formed, CO_2 reduction is not confirmed (see section 4.4). The presence of the bicarbonate in solution also increased activity and similar current densities were reached under CO_2 or argon. This is in contrast to previous reports that have shown much lower current densities without a CO_2 atmosphere, even with bicarbonate present in solution.[148, 152]
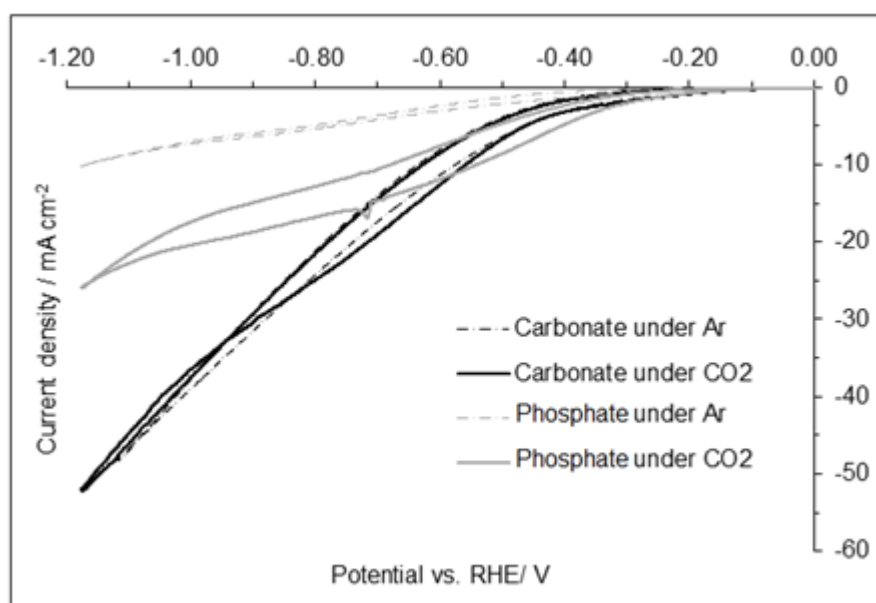
Figure 4-2 CV of $Ni_{0.5}Cu_{0.3}Co_{0.2}$ in carbonate or phosphate solution, under argon or CO_2 (corrected for differences in pH).

4.3 CO₂ Activity of Nanoalloys (CV Studies)

As copper is the only elemental catalyst that shows appreciable activity for the production of solution based hydrocarbons via CO_2 reduction, the nanoalloys containing copper were focussed on. The trimetallic $Ni_{0.5}Co_{0.3}Fe_{0.2}$ material was also analysed for comparison, as this material had shown similar activity to the $Ni_{0.5}Cu_{0.3}Fe_{0.2}$ for hydrogen production.

The CO_2 reduction ability of various nanoalloys was tested in a solution of 0.5 M $NaHCO_3$ and 0.1 M phosphate buffer, pH 6.8. A CO_2/methane gas mixture (5 %) was bubbled through the solution for 40 minutes, prior to measurements, in order to saturate the solution with CO_2. The methane was used as an internal standard for GC measurements. CV sweeps between 0 and -1.2 V vs RHE were recorded (Figure 4-3).
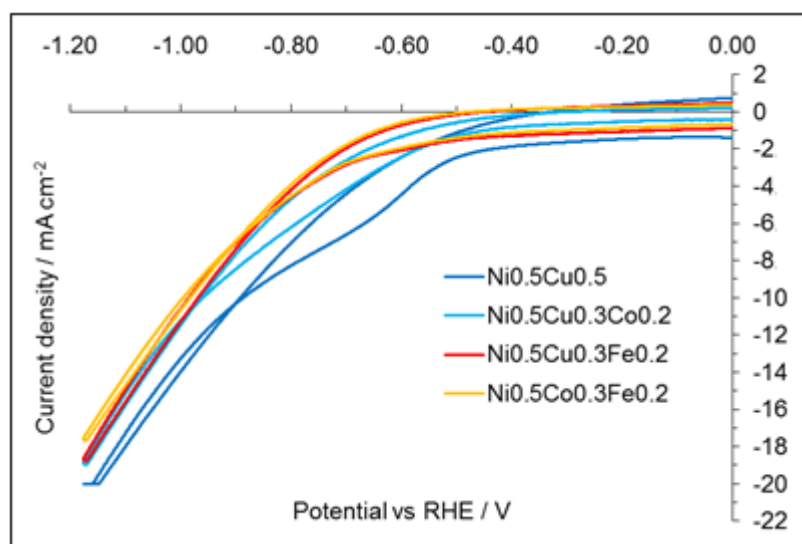
Figure 4-3 CO_2 reduction CV measurements of various nanoalloys in 0.5 M $NaHCO_3$ and 0.1 M phosphate, pH 6.8 between 0.0 V and -1.2 V vs RHE, at a scan rate of 20 mV s^{-1}.

The current densities observed are consistent with those seen for bulk metallic electrodes[145] and much larger than those observed for molecular CO_2 reduction catalysts.[145]

The results show that the $Ni_{0.5}Cu_{0.5}$ nanoalloy had the highest activity for CO_2 reduction, followed by the $Ni_{0.5}Cu_{0.3}Co_{0.2}$ composition. The $Ni_{0.5}Cu_{0.3}Fe_{0.2}$ and $Ni_{0.5}Co_{0.3}Fe_{0.2}$ nanoalloys have more negative onset potentials although at high enough overpotentials (above -0.9 V) they reach a similar current density to the $Ni_{0.5}Cu_{0.3}Co_{0.2}$. Very little difference was observed between the activity of the $Ni_{0.5}Cu_{0.3}Fe_{0.2}$ and $Ni_{0.5}Co_{0.3}Fe_{0.2}$ compositions.

4.3.1   Analysis of CO$_2$ Reduction Products

All materials appear to show reasonable activity for CO$_2$ reduction. However, as a range of products are possible and selectivity can be low, it was necessary to analyse the products produced. Therefore, electrodes were held at a potential of - 0.589 V for 5 hours. In all cases, the current remains constant or increases during the experiment, showing no decomposition occurs. This is in contrast to copper electrodes which often show a decrease in electrochemical CO$_2$ reduction with time. This may suggest that the nanoparticle distribution and/or nanoalloy structure are modified during the experiment, in a similar way to that observed for HER (see chapter 3 section 1.5), resulting in a more active material overtime.[21]
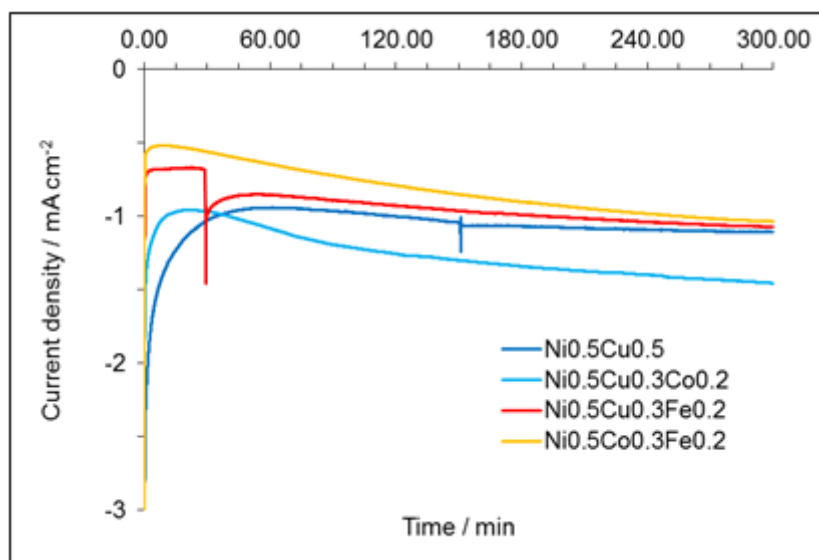
Figure 4-4 Current density observed for nickel nanoalloys over 5 hours of electrolysis in 0.5 M NaHCO$_3$ and 0.1 M phosphate, pH 6.8 at -0.589 V vs RHE.

As expected, poisoning of the pure copper electrode by carbon deposition was observed. However, due to the graphite sheets the nanoalloys were deposited on, it was not possible to tell if similar deactivation of the nanoalloys was occurring. The CPE measurements show stable current densities suggesting this is not the case. Although it is possible some of the current is contributing to deactivation reactions rather than product formation.

The CO_2 reduction products were analysed by GC (of the headspace) and NMR (of the solution). Unfortunately, due to a mixture of difficulties with the GC instrument and leak problems with the cell, full analysis of the gas products was not possible. As these products often account for the majority of FE, it is clear further experiments will need to be conducted to fully analyse all CO_2 reduction products. Linking the cell directly to the GC would solve a lot of the issues.

4.3.1.1   Analysis of HER Activity Under CO_2 Reduction Conditions

It was possible to analyse the hydrogen produced. Although only a semi-quantitative analysis was possible as the possibility of leaks in the system cannot be completely ruled out. Nonetheless, these results still suggest there are large differences between the hydrogen production ability of the different materials under the experimental conditions (Figure 4-5).
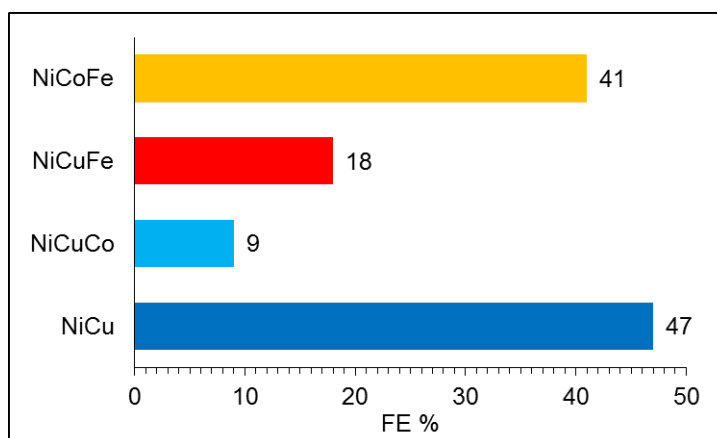
Figure 4-5 FE for HER of the nanoalloys, in 0.5 M $NaHCO_3$ and 0.1 M phosphate, pH 6.8 after 5 hours at –0.589 V.

It is clear that the $Ni_{0.5}Cu_{0.5}$ and $Ni_{0.5}Co_{0.3}Fe_{0.2}$ nanoalloys have the highest HER contributions to current. Whereas the $Ni_{0.5}Cu_{0.3}Co_{0.2}$ shows around five times less FE for the HER. The differences in FE for HER observed are likely due to the competing CO_2 reduction reactions.

4.3.1.2 NMR Analysis of Solution CO_2 Reduction Products

To investigate the solution based CO_2 reduction products, the solution was analysed by proton NMR at the end of the 5 hour electrolysis experiment. The minimum amount of D_2O required (0.06 mL) was added to an aliquot of the electrolysis solution (0.54 mL), along with a small quantity of DMSO (1.87 ppm) as an internal standard. DMSO was used because it does not interfere with peaks arising from CO_2 reduction products and because its non-volatility allowed for use and storage of the same internal standard solution for all measurements.

NMR has rarely been used quantitatively for CO_2 reduction product analysis as the peak area can be sensitive to the measurement conditions, such as number of scans used, shimming, phasing and solution composition.[17] However, it is a very useful way to analyse the solution directly. To minimise possible differences between measurements, the same acquisition parameters were used for all spectra. Also, solvent suppression was used to decrease the size of the large water peak and hence allow analysis of the small quantities of CO_2 reduction products present. Unfortunately, the CO_2 reduction product concentrations were too low to observe in ^{13}C NMR experiments therefore, product assignment could only be carried out based on the ^{1}H NMR spectra.

The water peak was centred at 4.79 ppm, DMSO was observed at 2.71 ppm and product peaks were compared to the expected standard positions.[153] Formic acid was observed in all experiments, giving a singlet at 8.44 pmm. The other main products observed were ethanol, acetic acid, hydroxyacetone, acetone and methanol (see table), not all products were observed in all experiments and in some cases the peaks were too small to quantify.

Table 4-2 ^{1}H NMR Chemical Shifts for various CO_2 Reduction Products

Expected Chemical shift	Observed Chemical shift	Product	Nucleus	Splitting/ Expected J coupling (Hz)	Observed J coupling
8.25	8.44	Formic acid	H**C**OOH	s	s
4.35	Not seen	Hydroxyacetone	CH$_3$COC**H**$_2$OH	s	
3.65	3.65	Ethanol	CH$_3$C**H**$_2$OH	q, 7	
3.34	3.33	Methanol	**C**H$_3$OH	s	s
2.22	2.21	Acetone	**C**H$_3$COCH$_3$	s	s
2.12	2.06	Hydroxyacetone	**C**H$_3$COCH$_2$OH	s	s
2.08	1.90	Acetic acid	**C**H$_3$COOH	s	s
1.17	1.16	Ethanol	**C**H$_3$CH$_2$OH	t, 7	t, 7.3

Copper is known to catalyse CO_2 reduction to methane, unfortunately this could not be confirmed by GC analysis, however, dissolved methane was observed by NMR in the solution in higher concentrations than that observed for the saturated solution before electrolysis. This suggests methane may be being produced, although this cannot be quantified without further experiments and GC analysis.
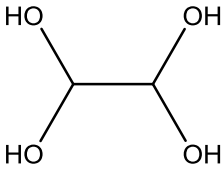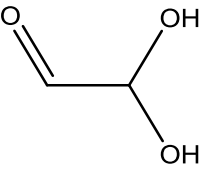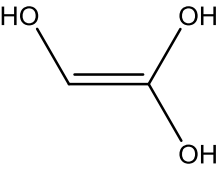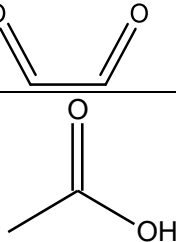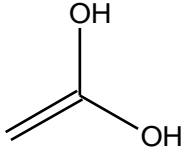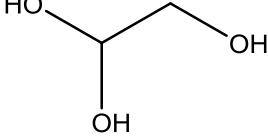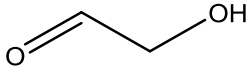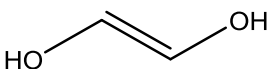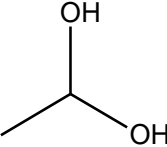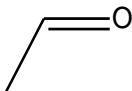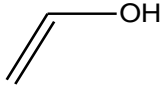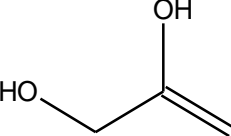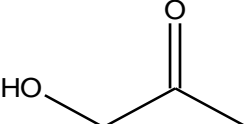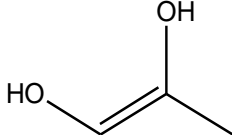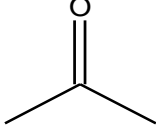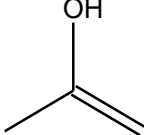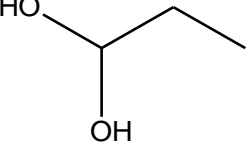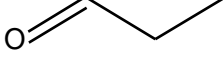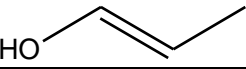
4.3.1.3 CO_2 Solution Reduction Products

Of the 13 solution based CO_2 reduction products that have previously been reported (see Table 4-1), only six were observed in this study. The observed solution products were formic acid, methanol, acetic acid, ethanol, hydroxyacetone and acetone.

The fact that all detected CO_2 reduction products are oxygenates, containing a hydroxyl and/or carbonyl moiety, may suggest the C-C coupling step in C_2 and C_3 products occurs before at least one of the CO_2 carbon-oxygen bonds is broken[17] unlike with the Fischer-Tropsch type mechanism.[154] This may also explain why very different product distributions can be seen on copper electrocatalysts compared to hydrothermal catalysts.

Many of the detected products contain carbonyls which can undergo enol tautomerisation (see table). As the ketone form is more stable in solution it is difficult to determine whether the product detected was produced at the electrode surface or if equilibration to the more stable form occurred in solution. As the enol tautomer is generally thermodynamically unfavourable in aqueous solution,[17] a compound desorbing from the electrode surface in the enol form would be expected to quickly convert to the keto form and therefore explain why this was the only form detected by NMR. Also some known products that were not detected in this study not only tautomerise to form enols but can also undergo hydration in aqueous solution resulting in diol formation. As the diol form is normally as stable as the keto form a 1:1 ratio of these products has previously been observed. As only very small quantities were observed in this study it is possible that these products were formed but in amounts below the detection limit.

Table 4-3 Equilibria of carbon containing products in aqueous solution[17]

Product name	Diol ⇌ Keto ⇌ Enol		
Glyoxal			
Acetic acid			
Glycolaldehyde			
Acetaldehyde			
Hydroxyacetone			
Acetone			
Propionaldehyde			

Also, the volatility of acetaldehyde and propionaldehyde may result in them being undetected by NMR even if they were produced in small quantities. Finally, it is not possible to observe glyoxal in ^{1}H NMR and as products were too weak to detect in ^{13}C NMR, it was not possible to determine whether this product was produced during CO_2 reduction on the nanoalloys.

For the CO_2 reduction products that were detected and quantified, the FE observed on each nanoalloy were calculated. As very small changes in concentration could have quite a large impact on the FE observed, more repeats would be required to confirm the trends observed. The detection limits for NMR analysis were found to be around 1 µmol dm^{-3}.

4.3.1.4   Comparison Faradaic Efficiencies (FE) of Solution Products

For the experiments run at a potential of –0.589 V vs. RHE, NMR analysis revealed formic acid, ethanol, acetic acid and hydroxyacetone were produced by all materials with varying FE. In all cases the FE are around 1 % or lower, however, the production of hydrocarbons at such a low overpotential has rarely been observed.
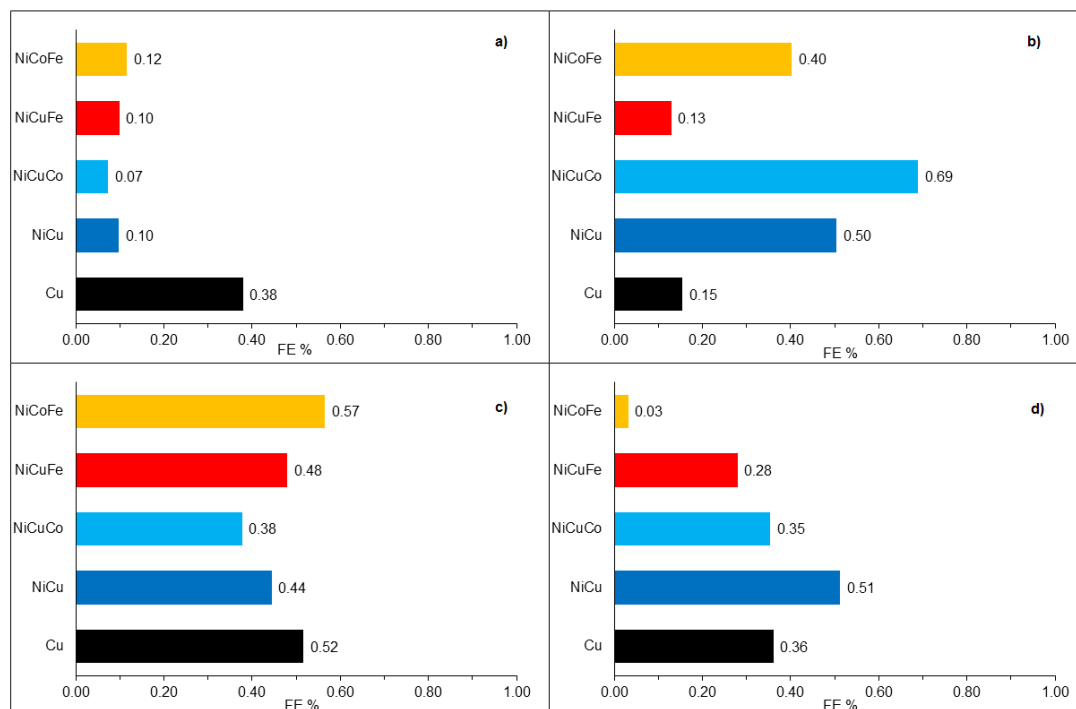
Figure 4-6 The FE of the various nanoalloys for a) formic acid, b) ethanol, c) acetic acid and d) hydroxyacetone in 0.5 M NaHCO$_3$ and 0.1 M phosphate, pH 6.8 after 5 hours at –0.589 V vs RHE.

Interestingly, the FEs observed for formic acid production were much lower than those reported in the literature. With little difference seen between the nanoalloys (around 0.1 % FE) although three to four times higher efficiency was seen for the copper sheet (0.38 % FE). HCO and CO have been proposed as possible initial reduction products on the electrode surface and possible intermediates. The low adsorption ability of most metals tends to result in formic acid and/or CO being the dominant products formed. The common prevalence of formic acid and CO may also be related to the lower number of electrons that need to be transferred in these reactions compared to the production of more complex hydrocabons. Production of formic acid or CO is a two electron process whereas, for example, the production of ethanol requires 12 electrons.

However, all nanoalloys showed higher FEs for ethanol than formic acid with the $Ni_{0.5}Cu_{0.3}Co_{0.2}$ nanoalloy showing almost ten times higher efficiency for ethanol production (0.69 % compared to 0.07 %). It is interesting to note that the $Ni_{0.5}Cu_{0.3}Co_{0.2}$ nanoalloy had the lowest HER efficiency. This may suggest the production of ethanol on the catalyst surface is inhibiting hydrogen production. CO adsorbtion has previously reported to inhibit hydrogen production. However, the $Ni_{0.5}Cu_{0.5}$ and $Ni_{0.5}Co_{0.3}Fe_{0.2}$ nanoalloys show the next highest FE for ethanol and also showed the highest hydrogen FE. As copper electrodes are known to produce different products on different surface sites, this may be responsible for the production of both ethanol and hydrogen seen on these electrodes. It is also possible that different products are produced at different times over the course of the experiment. To assess this, electrolysis should be conducted for various lengths of time and the resulting CO_2 reduction products analysed.

The other quantifiable products observed were acetic acid and hydroxyacetone. These products have rarely been reported in literature experiments. Acetic acid is particularly interesting as it has a reasonably negative thermodynamic reduction potential of -0.26 V, indicating production is occurring at a relatively low overpotential of -0.329 V.

The experimental conditions can play a large part in the observed CO_2 reduction product distribution. It is possible that some products are more prevalent in the initial

stages of electrolysis but may react further overtime. To investigate this, experiments would need to be carried out for shorter lengths of time and the FE of produced products compared. Although the very small concentrations observed make it unlikely that products produced over less time would be above the detection limit.

The potential used can also have a large effect on the product distribution. In order to analyse the selectivity of the nanoalloys, CO_2 reduction was carried out at various potentials, under the same conditions and the products analysed.

4.4 Investigation of Products Formed at Various Potentials and Their FEs.

As the $Ni_{0.5}Cu_{0.5}$ and $Ni_{0.5}Co_{0.3}Fe_{0.2}$ nanoalloys produced the highest current densities and are therefore more likely to give the required efficiencies in an active device, these two materials were investigated further.

In initial studies, potentials more negative than –0.8 V vs RHE resulted in mainly hydrogen production as these materials are very active for the HER at higher overpotentials. Also, from the CV sweeps, little activity is observed below –0.4 V. Therefore, potentials between -0.389 V and –0.789 V were investigated.

4.4.1 Ni$_{0.5}$Cu$_{0.5}$ Nanoalloy
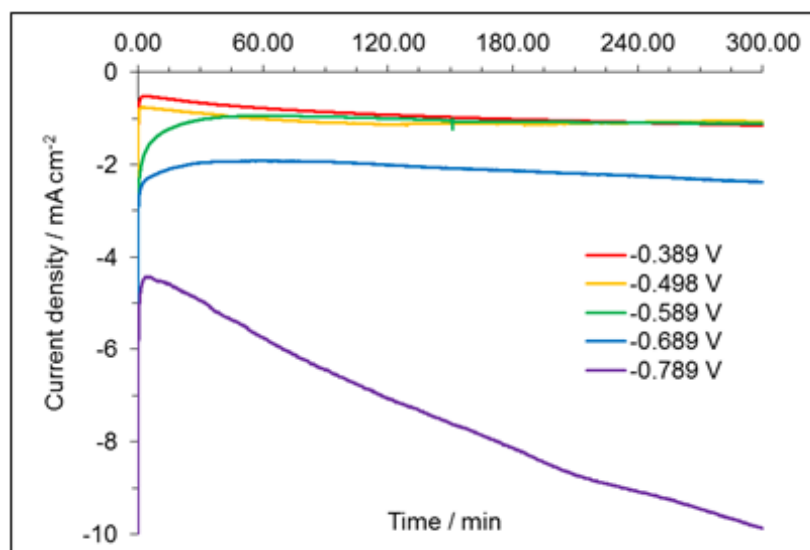
Figure 4-7 Current observed for Ni$_{0.5}$Cu$_{0.5}$ nanoalloys over 5 hours of electrolysis in 0.5 M NaHCO$_3$ and 0.1 M phosphate buffer pH 6.8 at various overpotentials (vs RHE).

As observed in the CV sweep (Figure 4-7), little difference was seen between the current produced at potentials between -0.389 V and -0.589 V inclusively. However, a much larger current was observed at a potential of -0.789 V. At this potential the current appears to increase significantly over the course of the experiment.

4.4.1.1 HER Activity of the Ni$_{0.5}$Cu$_{0.5}$ Nanoalloy Under CO$_2$ Reduction Conditions

The Ni$_{0.5}$Cu$_{0.5}$ nanoalloy showed the highest HER FE of all the nanoalloys tested, at –0.589 V, and reasonable HER activity under acidic and basic conditions (see chapter 3 sections 1.3 and 1.4). Therefore, it is not surprising that this material shows an increase of FE for HER with increased potential. Although, some literature has reported that at intermediate potentials (between -0.9 and -1.1 V vs RHE), the production of hydrocarbons such as ethanol can outcompete hydrogen production and lead to lower HER FE. Further experiments would be required to determine if this was the case, however the lower efficiencies for HER at low potentials suggest that CO$_2$ reduction dominates. CO$_2$ reduction at low overpotentials would be very beneficial. However, it does appear that about half of the observed current is still

unaccounted for. This suggests that the major products may be gases, such as CO, methane and ethylene.
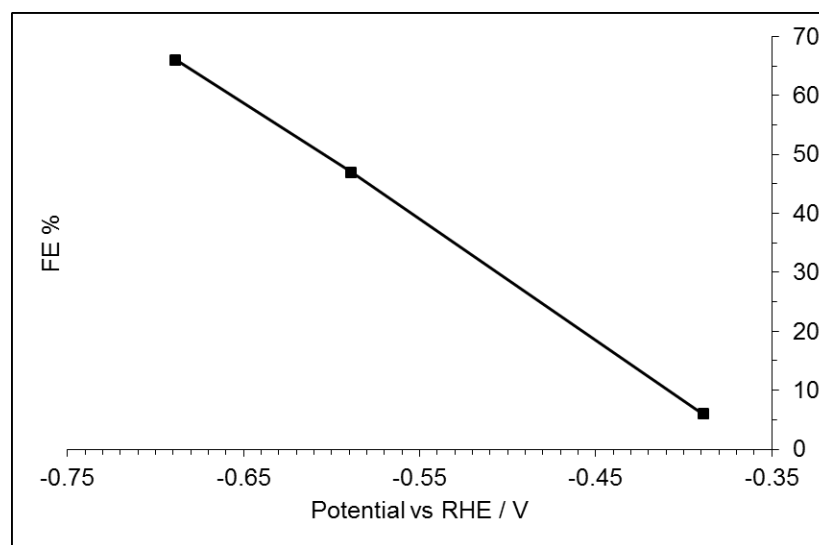
Figure 4-8 FE for hydrogen production on the $Ni_{0.5}Cu_{0.5}$ nanoalloy run in 0.5 M $NaHCO_3$ and 0.1 M phosphate buffer pH 6.8. Measurements taken by injection into a GC after 5 hours of electrolysis.

The Volmer step was found to be rate determining for HER activity on the nanoalloys under inert conditions. Therefore, the rate of hydrogen adsorption is rate determining. The presence of CO_2 will affect the adsorption ability of protons and therefore higher overpotentials will be required to give a high enough coverage of adsorbed hydrogen for atom–atom recombination to occur. This appears to result in higher CO_2 reduction activity at lower potentials.

To confirm the HER FE further experiments need to be carried out as the precision of these measurements is undetermined. Developing a system that allows online GC measurements to be taken during electrolysis would give a clearer indication of the FEs of gaseous products.

4.4.1.2 Solution Based CO₂ Reduction Products Observed Using a Ni₀.₅Cu₀.₅ Nanoalloy Electrocatalyst at Various Potentials

4.4.1.2   Solution Based CO_2 Reduction Products Observed Using a $Ni_{0.5}Cu_{0.5}$
Nanoalloy Electrocatalyst at Various Potentials

Some minor solution based products were identified, these included ethanol and hydroxyacetone which both showed maximum FE (0.49 and 0.51 % respectively) at –0.589 V. Ethanol also showed reasonable product efficiency (0.37 % FE) at -0.389 V, as did acetic acid. Acetic acid is also the only product to show an efficiency greater than 0.15 % at -0.689 V (with an efficiency of 0.53%). Very low efficiencies are seen at the highest potential measured (-0.789 V) which is consistent with the observation that much higher efficiencies are observed for HER as the potential is increased.
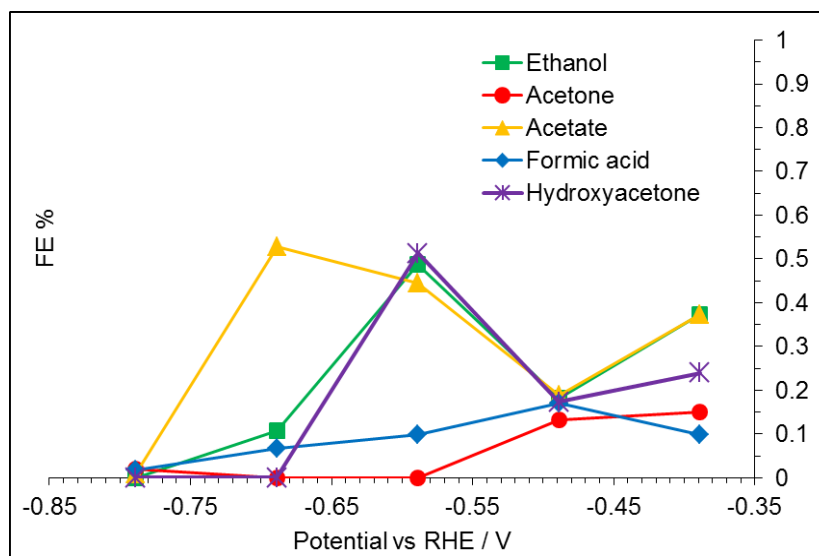
Figure 4-9 FE for hydrocarbon production on the $Ni_{0.5}Cu_{0.5}$ nanoalloy in 0.5 M $NaHCO_3$ and 0.1 M phosphate buffer pH 6.8 at various potentials.

Notably, although some products have reasonable FE at -0.389V and potentials above -0.589 V, products generally showed efficiencies below 0.2 % at -0.489 V. Except methanol, which showed a reasonably high FE of 1.47 % when the potential was held at -0.489 V and a small FE of 0.20 % was seen at a potential of – 0.789 V. However, no significant peak was present for all other potentials tested. Multiple aliquots of the -0.489 V sample solution were analysed by NMR and all gave similar results, the FE quoted is the average.

4.4.2 $Ni_{0.5}Cu_{0.3}Co_{0.2}$ Nanoalloy
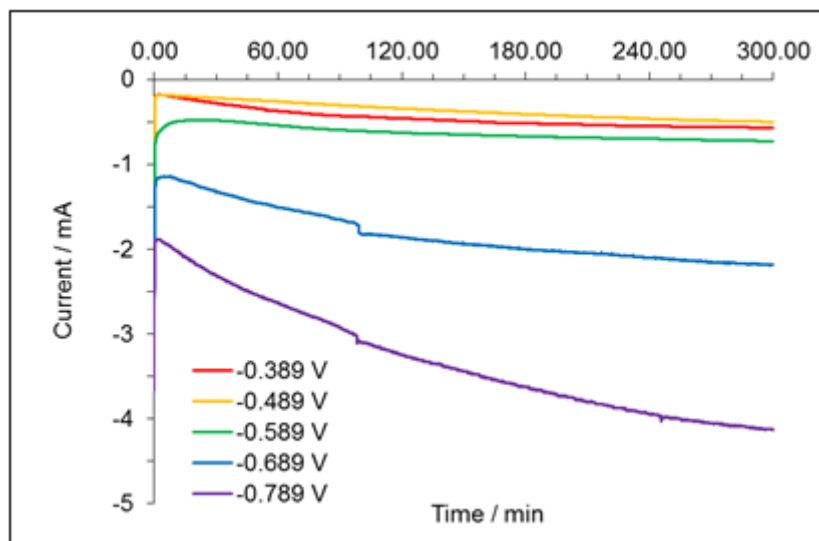
Figure 4-10 Current observed for $Ni_{0.5}Cu_{0.3}Co_{0.2}$ nanoalloys in 0.5 M $NaHCO_3$ and 0.1 M phosphate buffer pH 6.8 over 5 hours of electrolysis at various overpotentials.

As observed for the $Ni_{0.5}Cu_{0.5}$ nanoalloy, very little difference is seen between the current at the first three potentials. However, the current doubles when the voltages is decreased from -0.589 V to -0.689 V and then doubles again when the voltage is decreased to -0.789 V. The two highest potentials show a significant increase of current with time, although the increase is not as large as that seen for the $Ni_{0.5}Cu_{0.5}$ nanoalloy at a potential of -0.789V.

4.4.2.1 *HER Activity of the $Ni_{0.5}Cu_{0.3}Co_{0.2}$ Nanoalloy Under CO_2 Reduction Conditions*

Low efficiencies for hydrogen production were observed with the $Ni_{0.5}Cu_{0.3}Co_{0.2}$ nanoalloy. Although, an increase is still observed at higher potentials, consistent with the expected increase in HER activity at higher overpotentials.
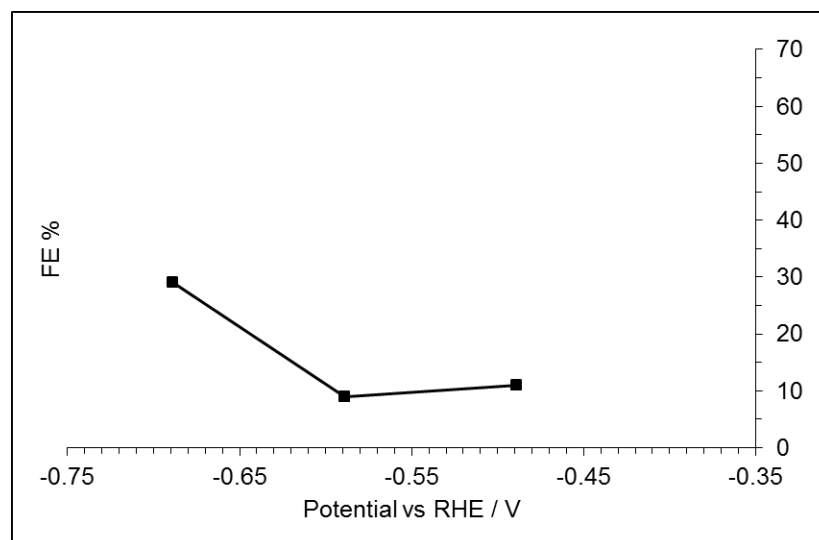
Figure 4-11 FE for hydrogen production on the $Ni_{0.5}Cu_{0.3}Co_{0.2}$ nanoalloy in 0.5 M $NaHCO_3$ and 0.1 M phosphate buffer pH 6.8.

The very low efficiencies seen at low potential again suggests that other products are favoured over hydrogen production. However, the solution based products observed account for very little of the remaining FE. Therefore, it is believed that unidentified gaseous products may be responsible for the remaining current. However, further experiments would need to be carried out to prove this.

4.4.2.2 Solution Based CO_2 Reduction Products Observed Using a $Ni_{0.5}Cu_{0.3}Co_{0.2}$ Nanoalloy Electrocatalyst at Various Potentials

Although low HER efficiency was observed with the $Ni_{0.5}Cu_{0.3}Co_{0.2}$ nanoalloy, only low efficiencies were observed for the CO_2 reduction products analysed by NMR. Reasonable efficiencies between 0.69 and 0.84 % were observed for ethanol production at potentials below -0.589 V. Whereas, at potentials more negative than -0.689 V, less than 0.1 % FE was observed. Other products observed also generally show higher efficiencies at potentials below -0.589 V.
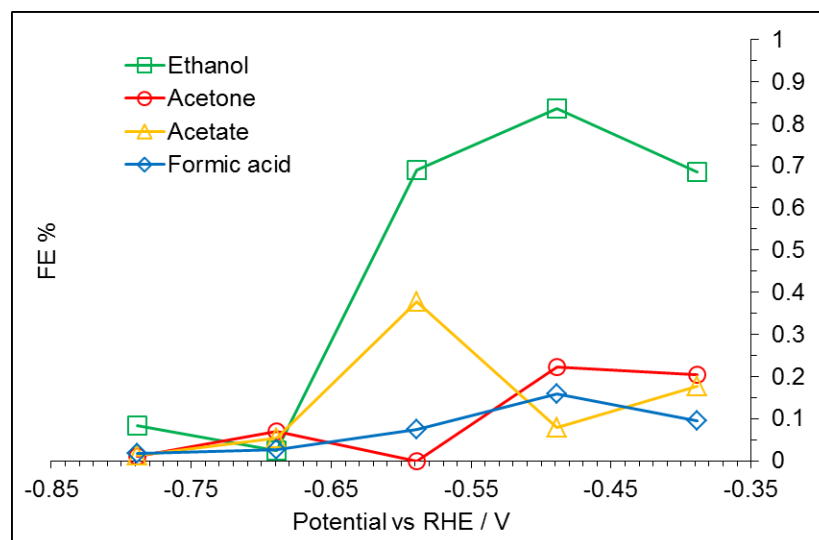
Figure 4-12 FE for hydrocarbon production on the $Ni_{0.5}Cu_{0.3}Co_{0.2}$ nanoalloy in 0.5 M $NaHCO_3$ and 0.1 M phosphate buffer pH 6.8 at various overpotentials.

4.4.3   Comaparison of $Ni_{0.5}Cu_{0.5}$ and $Ni_{0.5}Cu_{0.3}Co_{0.2}$ Nanoalloys for CO_2 Reduction

Unlike the $Ni_{0.5}Cu_{0.5}$ nanoalloy, the $Ni_{0.5}Cu_{0.3}Co_{0.2}$ nanoalloy produced much lower hydrogen efficiencies, suggesting it may be more selective for CO_2 reduction. Both nanoalloys generally show higher efficiencies for CO_2 reduction products at lower potentials (below -0.589 V). The $Ni_{0.5}Cu_{0.3}Co_{0.2}$ nanoalloy shows particular activity for ethanol production under these conditions. Although this is still lower than the 10 % efficiency that has previously been observed for copper electrodes at -1.1 V. Preferential ethanol formation has also been observed by Ali and co-workers on a nickel-nanoparticle electrodeposit.[155] Although in this case the high FE (221±23%) indicated both an electro-catalytic and chemical-catalytic pathway may exist.
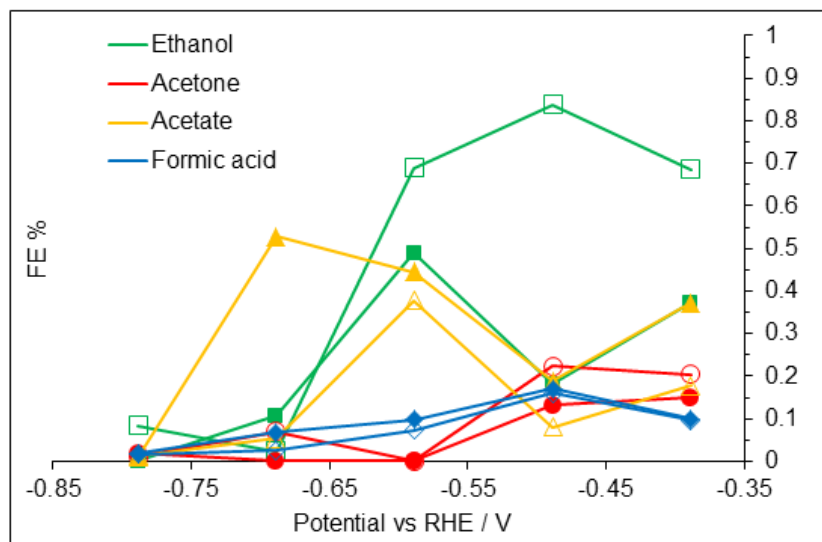
Figure 4-13 FE for hydrocarbon production on the $Ni_{0.5}Cu_{0.5}$ (closed symbols) and $Ni_{0.5}Cu_{0.3}Co_{0.2}$ (open symbols) nanoalloys in 0.5 M $NaHCO_3$ and 0.1 M phosphate buffer pH 6.8 at various overpotentials.

4.5 CO_2 Reduction Mechanism

The low quantity of formic acid observed is interesting as it only requires a two electron reduction whereas, ethanol and acetic acid require 12 and 8 electrons respectively but have shown higher efficiencies. Previous studies have discounted formic acid as a route to other reduction products as running CO_2 reduction experiments with a known quantity of formic acid present did not result in a decrease of formic acid concentration or higher quantities of other products being formed. Although CO has been shown to be an intermediate for other CO_2 reduction products. Chen and Kanan observed the same reduction products when reactions were carried out under CO_2 or CO.[22] Further reduction of CO is kinetically more difficult than the reduction of CO_2 to CO, hence more reduced products often require higher overpotentials.[17, 151, 156]

In order to produce C_2 and C_3 products, C-C coupling must occur. This requires two C-containing adsorbates to be in close proximity and as the electrochemical potential controls the species and their coverage at the electrode surface the C-C coupling rate is expected to be potential-dependent.[17] An initial increase in turnover frequency (TOF) with potential would be expected followed by a decrease at higher potentials, due to proton and electron transfers becoming more favourable at more negative potentials. At more negative potentials surface bound C_1 species, such as

144

CO ad HCO, have a higher chance of being fully reduced to methane and desorb instead of providing a C_1 intermediate for C-C coupling.[17] Also the increase in competing hydrogen production observed at higher potentials will decrease the chance of the necessary C_1 intermediates being in close enough proximity for C-C bond formation to occur. Back and co-workers have carried out DFT calculations that suggest the OH binding energy as well as the CO and H binding energies is important when predicting which products will be favoured. They suggest that the protonation of *OCH_3 is a key step and a catalyst with a weaker OH binding will preferentially produce methanol, whereas a stronger OH binding will favour methane production.[157] Although, the Cu (111) facets and steps are known to produce CH_4 and the (100) facets favour C_2H_4 production; Norskov and co-workers have shown that the (211) facet is more active towards the electroreduction of CO_2 to hydrocarbons.[158]

4.6 Conclusions

Small amounts of solution based CO_2 reduction products were observed at low overpotentials (between -0.389 V and -0.789 V). Unfortunately, the low quantities observed made it difficult to confirm the identities of products, as they were below the detection limit for ^{13}C NMR and difficult to analyse by mass spectroscopy. However, the majority of the FE is still unaccounted for. It is believed that gaseous CO_2 reduction products, which were unable to be analysed due to instrumental issues, are responsible. To confirm this further experiments will be carried out.

Differences in product selectivity were observed for the different nanoalloys with the $Ni_{0.5}Cu_{0.3}Co_{0.2}$ nanoalloy showing the highest activity for ethanol production (0.69% FE) at -0.589 V vs RHE. The $Ni_{0.5}Cu_{0.3}Co_{0.2}$ nanoalloy all had the most current unaccounted for which may suggest selectivity for one or more gas based products. This should be investigated further and if promising, other NiCuCo compositions should also be analysed to investigate the effect of composition on both activity and selectivity. Although the electrodes appear stable over the 5 hours of electrolysis, longer runs would be required to further analyse the stability of the nanoalloys. Also, the CO_2 gas used contained 5% methane (as an internal standard for the GC) and it is possible that this has had an effect on activity and the products formed. To test this, electrochemical measurements should be repeated using pure CO_2 gas.

Overall, the detection of hydrocarbon products at reasonably low overpotentials is promising. However further investigation is required to fully determine the selectivity and activity of the nanoally materials for CO_2 reduction.

5 Conclusions and Future Work

Nickel nanoalloys of around 10 nm with relatively small size distributions, have been synthesised for a variety of compositions utilising first row transition metals (Cr, Fe, Co and Cu). Bi- and trimetallic nanoalloys have been synthesised and good control over composition was demonstrated. The polymorph adopted was dependent on the most stable forms of the different elements present and their redox potentials. Consequently, all copper containing nanoalloys exhibited the cubic structure as copper was more easily reduced than other elements and so dictated overall nanoalloy structure. In the absence of copper, cobalt appears to be significant in controlling the structure and the hexagonal polymorph was formed. The exact arrangement of atoms in the nanoalloys (e.g. core-shell or mixed) is difficult to determine. Although there are some examples in the literature of EDX line scans taken on a TEM image; the small size (~10 nm) of the nanoalloys produced in this work makes this analysis very difficult. Clearly observing any differences between the core and the shell is harder with smaller particles as they will not be as distinct. Knowing more about the type of nanoalloy synthesised and therefore the arrangement of surface atoms, would be useful in understanding catalytic activity.

A clear difference was observed between the HER activity of pure nickel nanoparticles and the NiCr nanoalloy even though XRF analysis suggests only 1% Cr is present. Therefore, alternative synthesis techniques including the use of different stabilising ligands and reductants should be investigated for the synthesis NiCr nanoalloys with various compositions. As NiCr alloys are known to be stable in corrosive environments and the $Ni_{0.5}M_{0.5}$ compositions appear to give the best HER activity; $Ni_{0.5}Cr_{0.5}$ could be a promising material if the difficulties with its synthesis can be overcome.

A quick and easy procedure for testing HER activity was developed, with a loading of 56 μg cm^{-2} proving to be best for optimal activity. The procedure allowed for the direct deposition of nanoalloys onto the supporting electrode without the use of Nafion or other supports that could hinder light absorption if eventually used on photocatalytic semiconductors. Although, HR-SEM analysis revealed that much less than a monolayer coverage was achieved suggesting further increase in activity may be possible if closer to a monolayer coverage can be obtained. Unfortunately,

EDX analysis of the nanoalloys on the electrode was not possible due to the small size of the nanoalloys and the relatively large penetration depth of the X-rays.

$Ni_{0.5}M_{0.5}$ (M = Cr, Fe, Co, Cu, Mo or Ru) nanoalloys were tested for HER activity in pH 1 0.1 M H_2SO_4 and all showed higher activity than the pure nickel nanoparticles (-0.65 V for a current density of -10 mA cm^{-2}). Although only 110 mV separated the overpotentials of all the $Ni_{0.5}M_{0.5}$ nanoalloys, a trend between HER activity and electronegativity was observed. The nanoalloys with the most electronegative elements (i.e. Ru and Mo) showed the highest HER activity. The main exception to this order was the $Ni_{0.5}Cr_{0.5}$ nanoalloy; as chromium has the lowest electronegativity but higher activity that of nanoalloys containing other first row transition metals. Chromium is a hypo-d-electronic element and as such the activity seen may be a result of the improved stability of the nickel material produced by the hypo-hyper alloying with chromium. Although, as previously mentioned, there is very little chromium present in the sample and so this increase in activity may be a structure effect.

HER testing of the trimetallic nanoalloys showed much larger variations in activity. In pH 1 only the $Ni_{0.5}Cu_{0.3}Co_{0.2}$ nanoalloy showed better activity than nickel nanoparticles. This may be due to leaching of elements from the iron containing materials, although an increase in activity was seen with cycling suggesting any alterations to the nanoalloys on the electrode is increasing HER activity.

Conversely, in pH 13 0.1 M NaOH, the iron containing nanoalloys showed the highest activities, although all nanoalloys had higher HER activities than pure nickel. The differences of activity of different materials in acid and base result in very similar activities being observed under neutral conditions (pH 7, phosphate buffer). The larger differences in HER activity between trimetallic samples suggests that tuning of the compositions could lead to variations in activity. Therefore, a larger range of trimetallic nanoalloy compositions should be synthesised and tested for HER activity in acid, base and neutral conditions.

The stability of the trimetallic nanoalloys appears promising, with no decrease in activity seen after 12 hours and an increase observed upon cycling 500 times. The reason for this increase in activity is unclear, although it may be down to leaching of elements from the electrodes. To test this theory, samples of the electrolyte solution

after electrochemical testing are to be tested by ICP-MS to determine the presence of any metals in solution.

To further test the stability EIS measurements were taken however it is unclear whether the results are due to the nanoalloys or just an effect from the supporting carbon rod. The uncertainty is due to little variation being observed between samples and the most active material appearing to give the highest impedance. Also, the high sensitivity of the technique makes it possible that it is measuring an artefact rather than the effect from the nanoalloys. It is also possible that not all oxygen was removed before EIS measurements were taken and this would then complicate the results as both hydrogen and oxygen reduction could be occurring. Further EIS measurements need to be conducted to determine the precision and accuracy of the results.

The HER mechanism was also investigated using Tafel plots. The hydrogen adsorption (Volmer) step was determined to be the rate determining step and HER proceeds via a Volmer-Tafel mechanism. This is in agreement with high overpotential measurements for nickel alloy electrodeposits.

For CO_2 reduction, a two compartment electrochemical cell was used with a solution volume of 12 mL and a headspace of 5 mL in the working electrode compartment. The small size of the electrochemical cell allowed for the identification of very low solution product concentrations.

The products formed on different nanoalloy electrodes at -0.589 V and at different potentials on $Ni_{0.5}Cu_{0.5}$ and $Ni_{0.5}Cu_{0.3}Co_{0.2}$ nanoalloy electrodes were analysed. For solution based products, FEs of less than 1 % were observed for the production of formic acid, ethanol, acetic acid, hydroxyacetone and methanol. The identity and quantity of CO_2 reduction products varied depending on nanoalloy composition and potential used. Higher FEs have been reported at higher overpotentials, therefore further investigation of product formation at higher overpotentials may reveal higher efficiencies. Although, for use in a commercial device the catalyst needs to operate at low overpotentials, therefore higher potentials were not studied in this work.

Unfortunately, analysis of gaseous products after electrolysis, rather than by online monitoring during electrolysis and complications with the GC instruments resulted in most gaseous products being unidentified and the reliability of the hydrogen FE

being uncertain. Further investigations of the nanoalloys for CO_2 reduction should focus on analysis of the gaseous products. Ideally a setup that allows for GC measurements during electrolysis would be developed.

It is also worth noting that the CO_2 gas used contained 5% methane and this may have affected the products formed. To assess the effect of the presence of methane, electrochemical measurements for CO_2 reduction should be carried out using 100% CO_2 gas. Although it is not expected that this will result in any significant differences as methane cannot be reduced further and CO_2 reduction in carbonate solution with and without CO_2 saturation resulted in the same activity.

It is also possible that some products act as intermediates. Therefore, analysis of the solution and headspace over different time intervals is necessary to further assess the CO_2 reduction products.

As nanoalloys with reasonable activity and good stability have been synthesised; the next step would be to test the nanoalloys with the most promising activity and stability, on photocatalytic semiconductors. A good benchmark would be to test the (photo)electrocatalytic activity of the nanoalloys on TiO_2 as this is a well-established photocatalytic semiconductor. Depositing particles on a thin film of TiO_2 on FTO electrodes would allow for (photo)electrocatalytic testing. The same method can then be used to analyse reduction activity on visible light absorbing semiconductors (e.g. $BiVO_4$). Depending on the interaction between semiconductor and nanoalloy electrocatalyst, higher activities may be observed under illumination that those seen for the nanoalloys alone.

Overall, the nickel nanoalloys have shown improvements over pure nickel for both activity and stability. Future work should focus on further characterisation of materials after electrolysis to develop understanding of the reactions occurring and identification of the active material. It should also focus on further analysis of CO_2 reduction products at low overpotentials. The final key area still to be investigated is the use of these nanoalloys on semiconductors as a route to an efficient solar fuels device.

6 Experimental

6.1 Chapter 2 Experimental (Nanoalloy Synthesis)

6.1.1   Materials and Reagents

Ethanol, absolute, analytical grade; Methanol, analytical grade; Hexane, analytical grade; Ethylene glycol, laboratory reagent grade and acetone, analytical grade were purchased from Fisher Scientific. Nickel (II) acetylacetonate, 95 %; Copper (II) acetylacetonate; Iron (II) acetylacetonate; Iron (III) acetylacetonate; Cobalt (II) acetylacetonate; Chromium (III) acetylacetonate; Oleylamine, tech 70 %; 1-Octadecene, 90; Acetylacetone; Ruthenium (III) chloride hydrate; Chloroplatinic acid hydrate (FW: 409.81); Polyvinylpyrrolidone, average molecular weight 40, 000 and Silver nitrate were purchased from Sigma Aldrich.

The Oleylamine and 1-Octadecene were dehydrated using 3 Å molecular sieves, for several days, before use. All other reagents were used as received.

6.1.2   Materials Synthesis

6.1.2.1   Synthesis of Nickel Based Alloy Nanoparticles[42]

Dry oleylamine (10 mL) and dry 1-octadecene (10 mL) were placed into a three-necked 50 mL round bottomed flask and heated to 140 °C, under vacuum, with stirring. The solution was then held at this temperature for 20 min before placing the system under argon and heating to 240 °C at a rate of approximately 10 °C min^{-1}.

Ni(acac)$_2$, M^1(acac)$_n$ and M^2(acac)$_n$, where M^1 and M^2 = Cu, Fe, Co, Cr or Ru and n = 2 or 3; were predissolved in dry oleylamine (1 mL), by heating to 85 ° C, under argon. The exact quantities of metla precursors used and the resulting compositions based on XRF analysis are given in Table 6-1 and Table 6-2. Once the solvent solution had reached 240 °C, the predissolved precursors were injected and the reaction proceeded for 10 min, at 235-340 °C. Then the black solution was cooled to room temperature, under argon, before adding ethanol (~ 100 mL) and centrifuging at 4000 rpm for 60 min. The nanoparticles were then washed in a solution of hexane

(~ 1 mL) and methanol (~ 3 mL) in a 1:3 ratio and centrifuged at 4000 rpm for 30 minutes; this was repeated three times before redispersing the nanoparticles in hexane, to give a density of approximately 1 mg mL^{-1}.

Table 6-1 List of bimetallic nanoalloy compositions synthesised including the actual mass used and the composition obtained by XRF analysis.

Nanoalloy composition expected	Moles of Ni(acac)$_2$ / mmol	Mass of Ni(acac)$_2$ / mg	Moles of M(acac)$_n$ / mmol	Mass of M(acac)$_n$ / mg	Nanoalloy composition obtained (from XRF)
Ni	0.20	51.2	-	-	Ni
Ni$_{0.7}$Cu$_{0.3}$	0.14	36.0	0.06	15.7	Ni$_{0.64}$Cu$_{0.36}$
Ni$_{0.5}$Cu$_{0.5}$	0.10	25.5	0.10	26.2	Ni$_{0.46}$Cu$_{0.54}$
Ni$_{0.3}$Cu$_{0.7}$	0.06	15.4	0.14	36.6	Ni$_{0.18}$Cu$_{0.82}$
Ni$_{0.7}$Co$_{0.3}$	0.14	35.5	0.06	15.6	Ni$_{0.71}$Co$_{0.29}$
Ni$_{0.5}$Co$_{0.5}$	0.10	25.8	0.10	28.0	Ni$_{0.48}$Co$_{0.52}$
Ni$_{0.3}$Co$_{0.7}$	0.06	16.4	0.14	37.6	Ni$_{0.18}$Co$_{0.82}$
Ni$_{0.7}$Fe$_{0.3}$	0.14	36.3	0.06	15.2	-
Ni$_{0.5}$Fe$_{0.5}$[a]	0.10	27.6	0.10	25.4	-
Ni$_{0.5}$Fe$_{0.5}$[b]	0.10	26.0	0.10	41.0	-
Ni$_{0.3}$Fe$_{0.7}$	0.06	15.4	0.14	35.6	-
Ni$_{0.5}$Cr$_{0.5}$	0.10	25.7	0.10	34.9	Ni$_{0.99}$Cr$_{0.01}$
Ni$_{0.5}$Cr$_{0.5}$	0.05	13.1	0.2	70.5	Ni$_{0.99}$Cr$_{0.01}$
Ni$_{0.5}$Cr$_{0.5}$[c]	0.10	25.9	0.10	35.2	Ni$_{0.99}$Cr$_{0.01}$
Ni$_{0.5}$Cr$_{0.5}$[d]	0.10	26.0	0.10	35.0	Ni$_{0.99}$Cr$_{0.01}$
Ni$_{0.5}$Cr$_{0.5}$[e]	0.10	25.9	0.10	34.9	Ni$_{0.99}$Cr$_{0.01}$
Ni$_{0.5}$Ru$_{0.5}$	0.10	25.9	0.10	39.8	-
Ni$_{0.5}$Mo$_{0.5}$	0.10	26.0	0.10	32.5	Ni$_{0.74}$Mo$_{0.26}$
Pt	0.10	78.5	-	-	Pt

a: synthesis using Fe(acac)$_2$, b: synthesis using Fe(acac)$_3$, c: synthesis using a higher reaction temperature (250 °C), d: synthesis using a longer reaction time (20 minutes) and e: synthesis with initial injection of just the Cr(acac)$_3$ precursor and reaction for 2 minutes before addition of the Ni(acac)$_2$ precursor.

Table 6-2 List of trimetallic nanoalloy compositions synthesised including the actual mass used anf the composition obtained by XRF analysis.

Nanoalloy composition (in the form NiM^{1}M^2)	Mass of Ni(acac)$_2$ / mg	Mass of M^1(acac)$_n$ / mg	Mass of M^2(acac)$_n$ / mg	Nanoalloy composition obtained (from XRF)
Ni$_{0.5}$Cu$_{0.3}$Co$_{0.2}$	26.0	15.8	10.5	Ni$_{0.52}$Cu$_{0.32}$Co$_{0.16}$
Ni$_{0.4}$Cu$_{0.3}$Co$_{0.3}$	21.0	16.4	15.6	Ni$_{0.41}$Cu$_{0.36}$Co$_{0.23}$
Ni$_{0.46}$Cu$_{0.27}$Co$_{0.27}$	23.6	14.1	13.9	Ni$_{0.45}$Cu$_{0.33}$Co$_{0.22}$
Ni$_{0.5}$Cu$_{0.3}$Fe$_{0.2}$	26.0	16.0	14.0	Ni$_{0.49}$Cu$_{0.30}$Fe$_{0.21}$
Ni$_{0.5}$Co$_{0.3}$Fe$_{0.2}$	25.5	15.8	14.1	Ni$_{0.56}$Co$_{0.26}$Fe$_{0.18}$
Ni$_{0.5}$Co$_{0.3}$Fe$_{0.2}$	26.0	15.8	14.2	Ni$_{0.58}$Co$_{0.24}$Fe$_{0.18}$
Ni$_{0.5}$Cu$_{0.3}$Cr$_{0.2}$	25.9	15.9	14.0	Ni$_{0.63}$Cu$_{0.36}$Cr$_{0.01}$

6.1.2.2 Synthesis of Water Soluble Platinum Nanoparticles[128]

Ethylene glycol (3 mL) and silver nitrate (0.04 M, 0.5 mL) where mixed in a flask for 15 min and then argon gas was bubbled into the flask for 20 min before heating to 160° C and refluxing for 2 hr, under argon.

After the solution had refluxed for 2 hr, chloroplatinic acid hydrate (0.0625 M, 20 µL) was injected into the flask, sequentially followed by polyvinylpyrrolidone (0.375 M, 40 µL) until a total of 1.5 mL of chloroplatinic acid hydrate and 3 mL of polyvinylpyrrolidone had been added. The solution was left to react at this temperature (160° C) for a further 15 minutes, under stirring, and a dark-brown solution of Pt nanoparticles was obtained. This was washed with ~ 25 mL acetone and centrifuged at 4000 rpm until the solid dropped out of solution. Then the solid product was re-dispersed in ethanol/hexane (1:3 volume ratio) and centrifuged at 3000 rpm, once the nanopartciles had settled out the solution was removed, this process was repeated several times. After washing the nanoparticles were dispersed in milli-pore water (18.2 Ω) with an approximate density of 1 mg mL^{-1}.

6.1.2.3 Ru(acac)$_3$ Synthesis[113]

Ruthenium(III) chloride hydrate (0.5 g, 2.2 mmol as Ru) was dissolved in a mixture of 25 cm^3 of water and 50 cm^3 of ethanol. The reddish brown solution was refluxed, under inert conditions, for 5 h. The colour of the solution turned dark green and then deep blue. Then an excess amount of ligand (0.73 g, 7.26 mmol) was introduced quickly into the 'ruthenium blue solution' and the mixture was refluxed until its colour turned red (about 2.5 hr). The mixture was cooled, and a portion of sodium hydrogencarbonate (added in order to neutralize the liberated hydrogen ions; then the mixture was refluxed again for 2 h, before cooling and adding another portion of sodium hydrogencarbonate before refluxing for another 2 h. Once cooled, the solution was concentrated to *ca. 25* cm^3 on a rotary evaporator. The precipitate was collected by and dried under a vacuum. The precipitate is extracted with *ca. 20* cm^3 portions of benzene. The deep red benzene extract was passed through a column

of alumina, and the column was washed with benzene. The eluent was concentrated to dryness then recrystallized from ethanol.

ESI-MS: positive ion *m/z*: 400.0454 ([M+H]$^+$), calc. for $C_{15}H_{22}O_6Ru$: 400.049 (error 0.0 mDa) *m/z*: 422.0263 ([M+Na]$^+$), calc. for $C_{15}H_{21}NaO_6Ru$: 422.0278 (error 1.0 mDa)

Elemental analysis: for $C_{15}H_{21}O_6Ru$: Calc. C 45.22, H 5.31, N 0, Rest 49.47 %. Found C 45.23, H 5.53, N 0, Rest 49.24 %.

6.1.3   Characterisation

6.1.3.1   Powder X-Ray Diffraction (XRD)

Powder diffraction patterns were obtained using an Oxford Diffraction Supernova diffractometer with a Mo Kα radiation source (0.71073 Å) operating in powder diffraction mode. Data was collected to 2θ = 45° with an exposure time of 100 s. Samples of the solid ligand stabilised nanoparticles were loaded onto a micro-loop for analysis.

6.1.3.2   X-Ray Fluorescence Spectroscopy (XRF)

A Horiba X-ray Analytical Microscope AGT-7000 was used for analysis and data processing. A small amount of solid sample was placed onto a Pespex block (to ensure a low background signal). No filter was used. A 10 μm beam size, potential of 15 kV, current of 0.9 mA, acquisition time of 300 s and process time of 6 were used. Multiple points (ca. 20) were analysed for each sample and an average taken.

6.1.3.3   Transition Electron Microscopy (TEM) / Energy Dispersive X-ray Spectroscopy(EDX)/ Electron Diffraction

TEM and electron diffraction images were obtained using a JEOL JEM-2010 transmission electron microscope, equipped with an EDAX Phoenix EDS x-ray

spectrometer, operated at a voltage of 200 kV. Liquid nitrogen was used during analysis to reduce decomposition of the organic ligands and so contamination of the sample. Prior to analysis, nanoparticles were dispersed in hexane and sonicated for 5 minutes to disperse the particles. Samples were prepared by placing a drop of the dispersed nanoparticle solution on a gold or copper holey carbon grid and allowing the solvent to evaporate.

EDX analysis was recorded at a 10 kV accelerating voltage. A tilt stage was used to try to reduce contribution from the sample holder. EDX of the trimetallic nanoalloys was carried out by Dr Robert Mitchell (JEOL nanocentre).

6.1.3.4 *Mass Spectroscopy*

Mass spectroscopy was carried out by Mr Karl Heaton.

Mass spectrometry measurements were performed on a Bruker micrOTOF MS (ESI).

6.1.3.5 *Elemental Analysis*

Elemental Analyses were performed by Dr Graeme McAllister

Elemental analyses were performed using an Exeter Analytical Inc. CE-440 analyser.

6.2   Chapter 3 Experimental (HER)

6.2.1   Materials and reagents

P25 TiO_2 was purchased from Degussa and the Nitric acid and Sulphuric acid from Fluka. Sodium sulphate anhydrous and sodium hydroxide were purchased from Sigma Aldrich.

6.2.1.1   Preparation of Electrolyte Solutions for Proton Reduction

All electrochemical solutions used mili-pore water (18.2 Ω).

Electrochemical measurements at pH 1 were carried out in a solution of 0.1 M H_2SO_4 (1.38 mL in 250 mL) and 0.1 M Na_2SO_4 (3.55 g in 250 mL).

Electrochemical measurements at pH 13 were carried out in a solution of 0.1 M NaOH (1 g in 250 mL) and 0.1 M Na_2SO_4 (3.55 g in 250 mL).

Electrochemical measurements at pH 7 were carried out in a solution of 0.1 M phosphate buffer (1.20 g sodium phosphate monobasic and 2.13 g sodium phosphate dibasic) and 0.1 M Na_2SO_4 (3.55 g in 250 mL).

6.2.2   Electrode fabrication

6.2.2.1   Preparation of TiO_2 Thin Films on FTO Coated Glass Electrodes[159]

P25 (c.a. 0.05 g) was placed in a sample tube with nitric acid (0.1 M, 0.15 mL) and sonicated for 10 min. FTO electrodes submerged in acetone were sonicated for 10 minutes and then rinsed with acetone, before repeating the procedure with ethanol and then mili-pore water (18.2 Ω). Finally, the FTO was dried using compressed air before use. Adhesive tape was used to mask the area of the electrode not being covered by the TiO_2 and to control the film thickness.

A 2 μL drop of the TiO$_2$ dispersion was placed on the FTO and a glass slide was then used to spread the TiO$_2$ dispersion over the electrode (the total TiO$_2$ dispersion in the film is less than the total applied). The film was left to dry at room temperature, for approximately 10 min. Then the tape was removed and the surface it had covered was wiped with acetone to ensure it was clean. The electrode was subsequently dried at 80 °C for 6 hr, then heated to 450 °C and held at temperature for 0.5 hr (1 °C min^{-1} heating rate) before being allowed to cool to room temperature.

6.2.2.2   Deposition of Nanoparticles onto TiO$_2$ Films

The surface of the FTO, not covered by the TiO$_2$ film, was again masked with tape and 20 μL of a 1 mg mL^{-1} nanoparticle solution was deposited onto the TiO$_2$ film. This was then left to dry in air for 3 hr before removing the tape and wiping the surface it covered with acetone. Finally, the electrodes were heated to 450 °C and held at temperature for 2 hr (1 °C min^{-1} heating rate) and then allowed to cool to room temperature, before being tested.

6.2.2.3   Preparation of Electrodes by Supporting Preformed Nanoparticles on Carbon Rods

Ligand stabilised alloy nanoparticles in a hexane solution (1 or 0.1 mg mL^{-1}) were drop cast onto the end of polished (with P1200 grade paper) carbon rods (length = 1 cm; diameter = 0.3 cm). The amount of solution deposited was varied to give catalyst loadings ranging from 14 to 283 μg cm^{-2}. This was then heated, at a rate of 1 °C min^{-1}, to 450 ° C and held for 3 hours, to remove the ligands.

The sides of the carbon rod were then insulated, using nail polish, to ensure only the end of the carbon rod supporting the nanoparticles was exposed to the electrolyte solution. Giving a geometric surface area of 0.071 cm^2.

6.2.3   Characterisation

6.2.3.1   HR-SEM

HR-SEM analysis was conducted by Stuart Micklethwaite (LENFF, Leeds).

HR-SEM was carried out on electrodes after calcination and after 20 cycles between -200 mV and -1200 mV vs Ag/AgCl, in pH 1 0.1 M H_2SO_4 / 0.1 M Na_2SO_4. The carbon rod electrode was cut to a length of 0.3 cm prior to analysis, so the electrodes would fit on the SEM stage.

6.2.4   Electrochemical Setup

Electrochemical analysis was carried out using a BASi Epsilon-EC potentiostat. EIS measurements were carried out on a Bio-Logic potentiostat. EC-Lab software was used for analysis and the data was modelled using non-linear least-squares fit analysis and equivalent electrical circuits.

A single compartment electrochemical cell was used for all measurements. A silver/silver chloride reference electrode and a platinum wire/mesh counter electrode (1 cm × 5 cm) were used. Measurements were recorded at pH 1 (0.1 M sulphuric acid and 0.1 M sodium sulfate solution), pH 7 (0.1 M phosphate buffer and 0.1 M sodium sulfate) and pH 13 (0.1 M sodium hydroxide and 0.1 M sodium sulfate). Argon (or nitrogen for EIS measurements) was bubbled through the solution for 20 minutes before taking measurements and an argon atmosphere was maintained during runs. The working electrode was rotated at a rate of 4000 rpm.

CV and LSV measurements were recorded between 0 V and -1 V vs RHE at a scan rate of 20 mV s^{-1} and 1 mV s^{-1} respectively. CPE measurements were recorded at a potential of -0.5 V vs RHE for 12 hours.

EIS measurements were carried out in the frequency region from 100,000 to 0.01 Hz (6 frequency points per decade) with amplitude of 10 mV root mean square at room temperature.

6.3 *Chapter 4 Experimental (CO$_2$ Reduction)*

6.3.1 Materials and Reagents

Sodium bicarbonate, sodium phosphate monobasic and sodium phosphate dibasic were purchased from Sigma Aldrich. The CO$_2$ source was a 5% methane, carbon dioxide BOC gas cylinder.

All electrochemical solutions used mili-pore water (18.2 Ω).

The electrolyte solution was 0.5 M NaHCO$_3$ (10.5 g), with 0.1 M phosphate buffer (1.20 g sodium phosphate monobasic and 2.13 g sodium phosphate dibasic) to maintain a pH of 7.

6.3.2 Electrode Fabrication

Graphite sheets (1.5 cm by 1 cm) were placed in concentrated hydrochloric acid for 1 hour and then rinsed thoroughly with mili-pore water (18.2 Ω), before sonicating in milipore water for 10 minutes. Then the graphite sheets where polished with p1200 grade sand paper and rinsed again with milipore water. Then they were masked in nail polish to leave a 0.5 cm ^{2} (1cm by 0.5 cm) area uncovered at one end. Ligand stabilised alloy nanoparticles in a hexane solution (0.1 mg mL^{-1}) were drop cast onto the uncovered area. This was left to dry in air (ca 10 min) before heating, at a rate of 1 °C min^{-1}, to 450 ° C and held for 3 hours, to remove the ligands.

6.3.3 Electrochemical Setup

Electrochemical analysis was carried out using a BASi Epsilon-EC potentiostat. EIS measurements were carried out on a Bio-Logic potentiostat.

A dual compartment electrochemical cell was used for all measurements. The counter electrode was in a separate compartment to the working and reference electrodes, separated by a glass frit infiltrated with Nafion. A silver/silver chloride

reference electrode and a platinum mesh (1 cm × 5 cm) auxiliary electrode were used. Measurements were recorded in a solution of 0.5 M sodium hydrogen carbonate and 0.1 M phosphate buffer. CO_2 was bubbled through the solution for 30 minutes before taking measurements.

CV measurements were taken between 0 and -1.8 V vs Ag/AgCl at a scan rate of 20 mV s^{-1}. CPE measurements were recorder for 5 hours at potentials ranging from -1 V to -1.4 V.

6.3.4 GC Setup

Gas analysis was performed using a Shimadzu Corporation GC-2014. Gases were separated on a 25 cm long column packed with 5 Å molecular sieves and detection was performed using a thermal conductivity detector (TCD). 50 µL of gas was autosampled every 15 minutes over a time course of 6 – 24 hours. Gas samples were analysed using the following conditions; 20 mL min^{-1} gas, 90 °C column temperature and 120 °C detector temperature. Under these conditions the retention time of H_2 is 1.5 min, O_2 2.3 min and N_2 3 min. Peak areas were analysed by integration using Shimadzu GC Solutions – GC Postrun software.

GC H_2 calibration was carried out by Miss Danielle Jowett (PhD student).

GC calibration for H_2 was performed by a series of injections of known volumes and pressures of gas. The H_2 source was a BOC 99.99% H_2 cylinder. Using a Schlenk line with mercury manometer, a Schlenk tube with suba seal was evacuated and refilled with argon 3 times. The Schlenk was evacuated again, and the manifold closed off from the vacuum pump to hold a static vacuum. A H_2 balloon was fitted with a needle and inserted into the Schlenk, and removed when the manometer had dropped by an appreciable amount (200 – 500 mm). The pressure of H_2 in the Schlenk was measured from the manometer using a ruler and recorded. H_2 was removed via an argon purged gas syringe and inserted into the GC, each pressure was run three times to obtain an average H_2 peak area. Using the pressure and volume of gas injected, the number of moles of H_2 in each injection was calculated. The area of the chromatogram peak at 1.5 min was analysed, and plotted against the number of moles of H_2 to obtain a calibration curve.

6.3.5   NMR set-up

NMR measurements were done by Mr Ben Coulson (PhD student).

NMR spectra were acquired on a Bruker AVANCE 500 (128 scans, operating at 500.23 MHz). Solvent suppression was applied to reduce the size of the water peak and enable the smaller CO_2 reduction product peaks to be observed.

Appendix 1 – Chapter 2 Supplementary Data

A1.1 NiCu

Table A 1 XRD 2θ peak positions for the (111) and (200) reflections in $Ni_{1-x}Cu_x$ (x = 0, 0.3, 0.5 or 0.7) nanoalloys.

	2θ position / °	
	(111)	(200)
Ni	20.15	23.29
$Ni_{0.7}Cu_{0.3}$	19.52	22.58
$Ni_{0.5}Cu_{0.5}$	19.66	22.69
$Ni_{0.3}Cu_{0.7}$	16.71	19.59
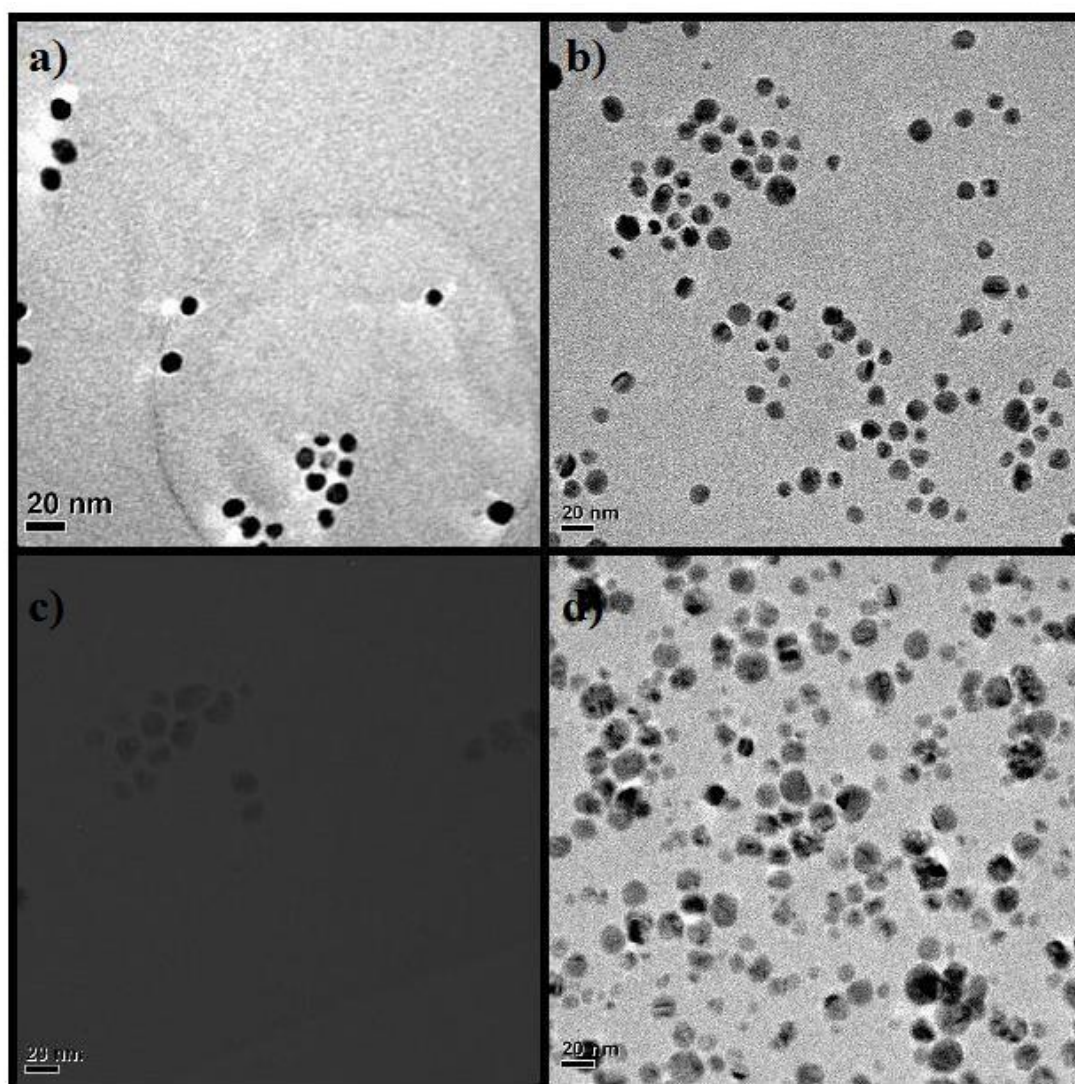
Figure A 1 TEM images recorded at 50 kV of nanoparticles with composition a) $Ni_{0.7}Cu_{0.3}$, b) $Ni_{0.5}Cu_{0.5}$, c) $Ni_{0.3}Cu_{0.7}$ and d)) Ni_0Cu_1.
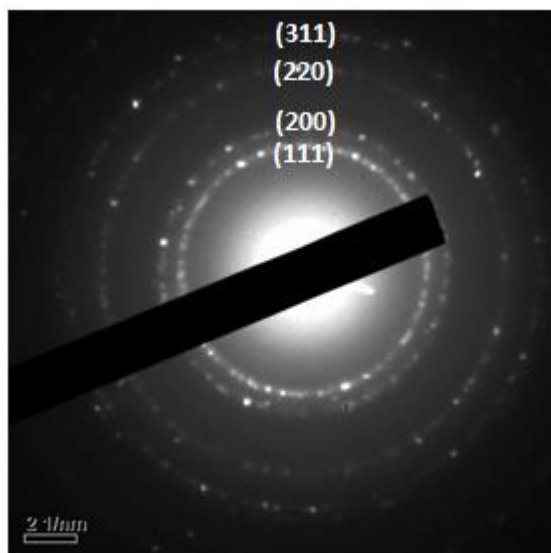
Figure A 2 Electron diffraction of $Ni_{0.5}Cu_{0.5}$ nanoalloys.

A1.2 NiCo
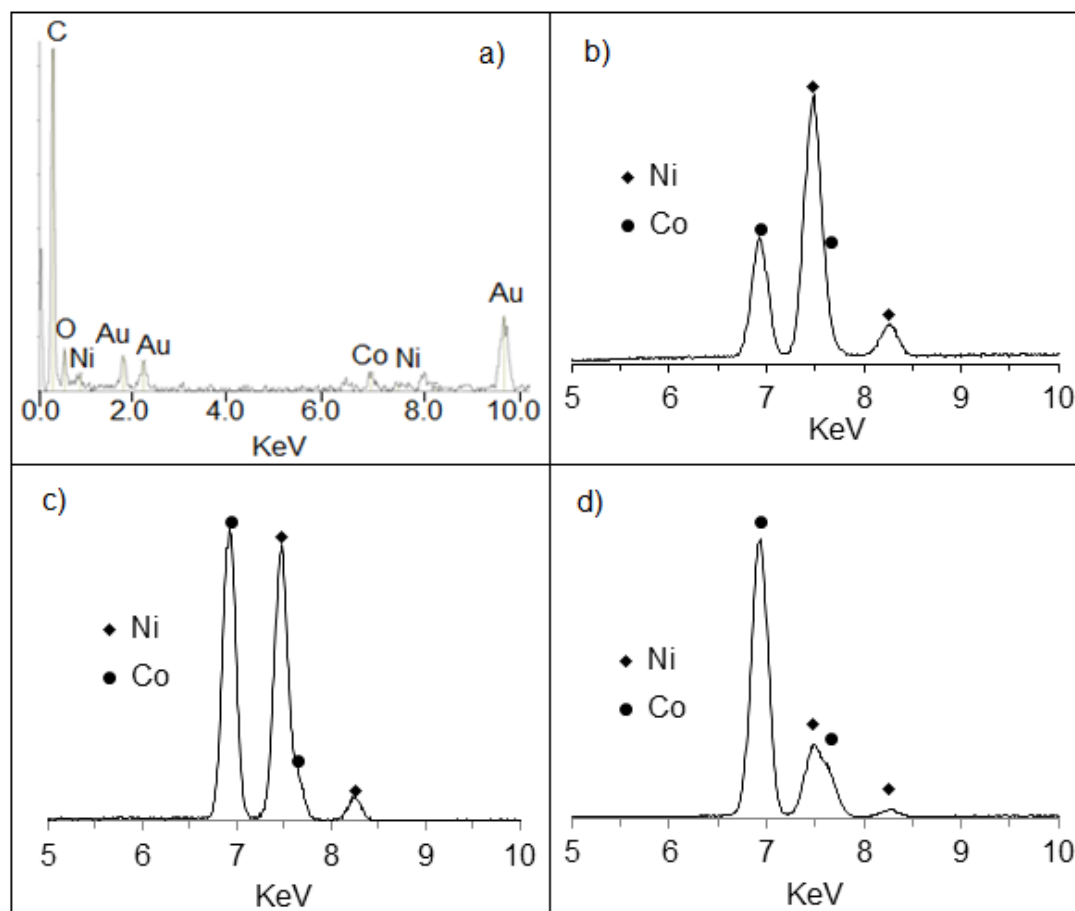
Figure A 3 a) EDX spectrum of a $Ni_{0.5}Co_{0.5}$ nanoparticle and XRF spectrum of b) $Ni_{0.7}Co_{0.3}$, c) $Ni_{0.5}Co_{0.5}$ and d) $Ni_{0.3}Co_{0.7}$.
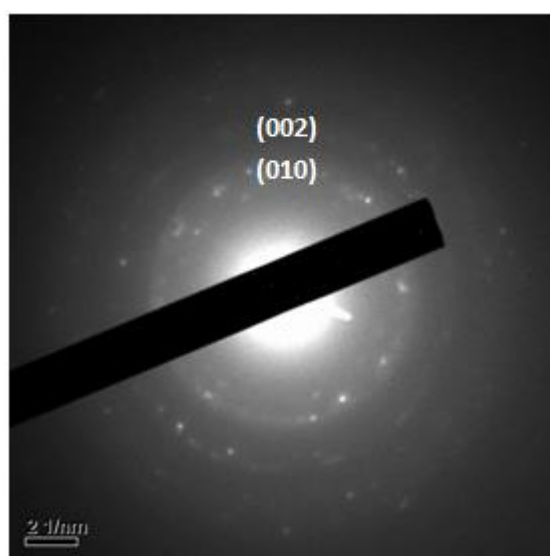
Figure A 4 Electron diffraction of $Ni_{0.5}Co_{0.5}$ nanoalloys.

A1.3 NiCr
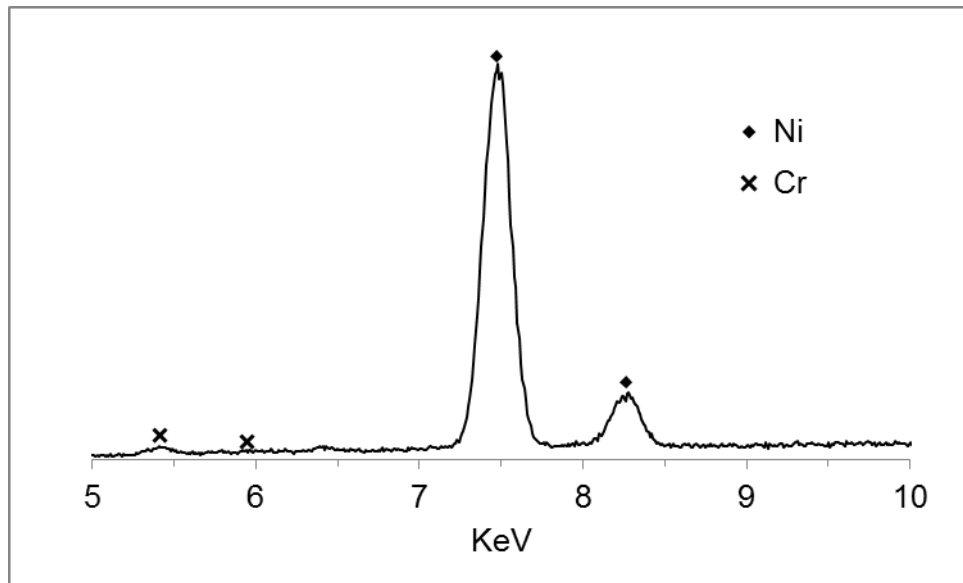
Figure A 5 XRF of $Ni_{0.5}Cr_{0.5}$ nanoalloy, the presence of less than 1 % Cr incorporated.

A1.4 NiMo
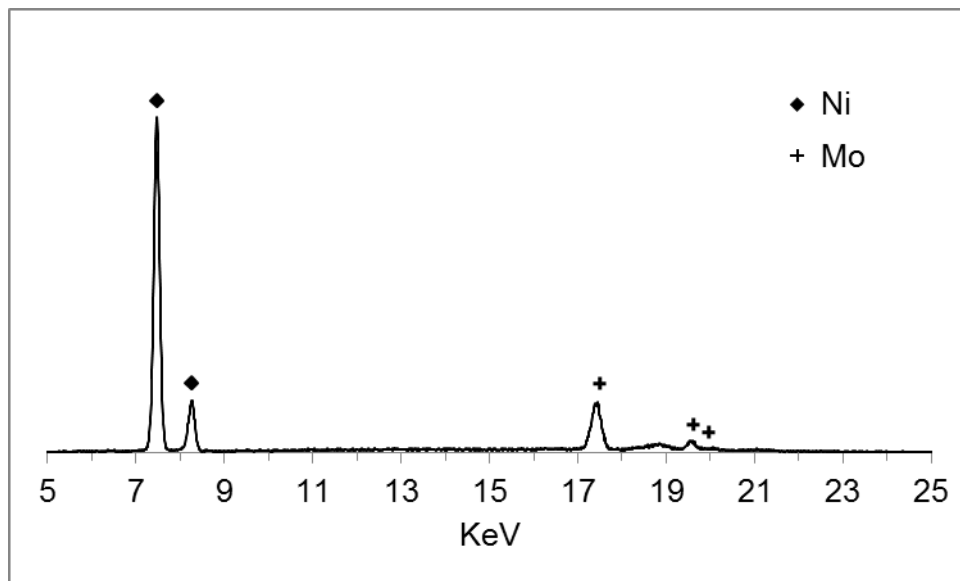
Figure A 6 XRF of $Ni_{0.5}Mo_{0.5}$ nanoalloy

A1.5 NiCuCo
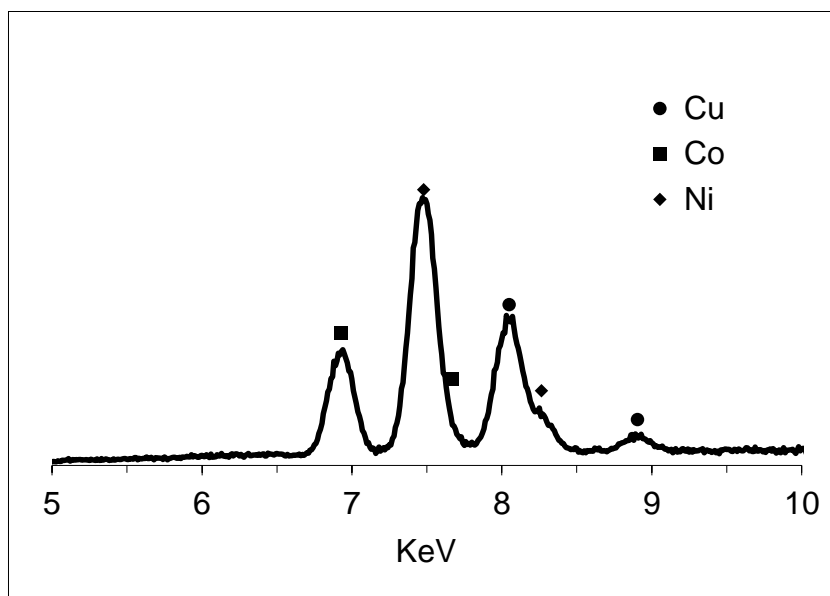
Figure A 7 XRF spectrum of $Ni_{0.5}Cu_{0.3}Co_{0.2}$ alloy nanoparticles, giving an average composition of $Ni_{0.52}Cu_{0.32}Co_{0.16}$.
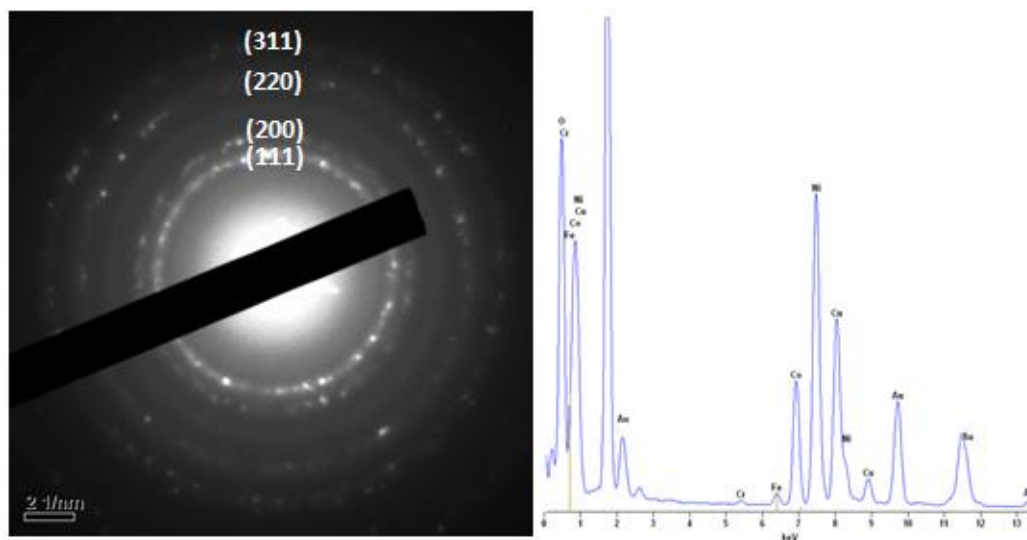
Figure A 8 Electron diffraction (left) and EDX (right) of $Ni_{0.5}Cu_{0.3}Co_{0.2}$ nanoalloys.

A1.6 NiCuFe
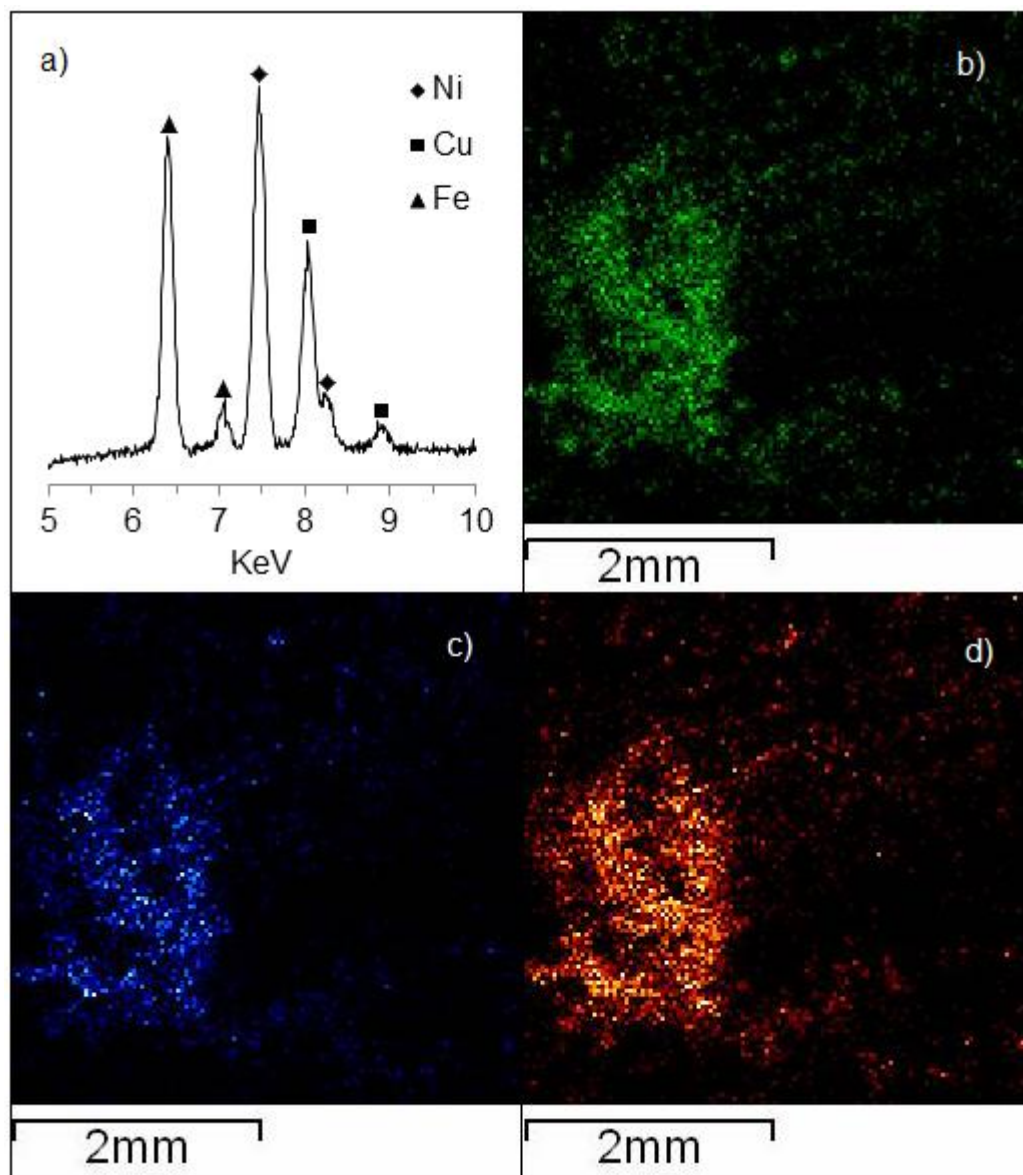
Figure A 9 a) XRF spectrum of $Ni_{0.5}Cu_{0.3}Fe_{0.2}$ alloy nanoparticles, giving an average composition of and elemental mapping images of b) Ni, c) Cu and d) Fe.
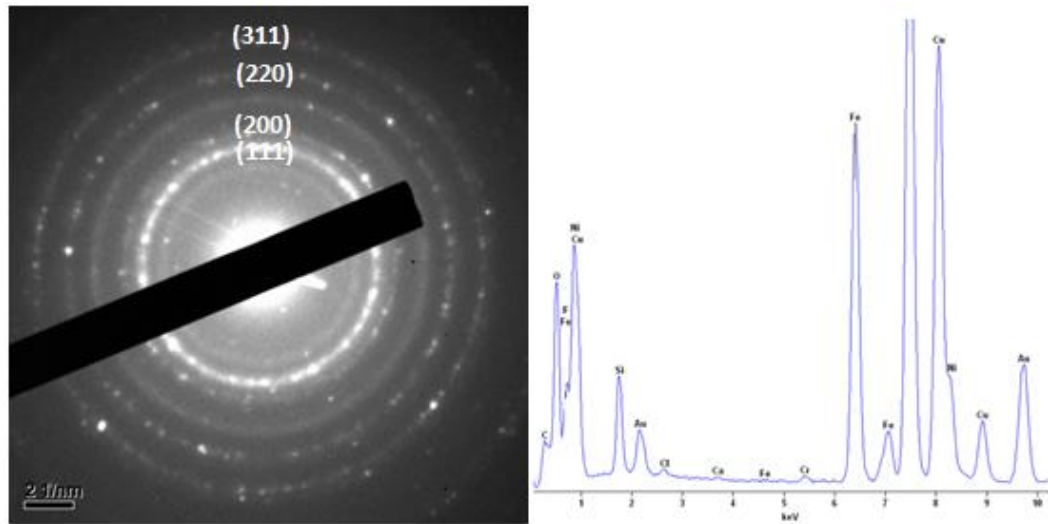
Figure A 10 Electron diffraction (left) and EDX (right) of $Ni_{0.5}Cu_{0.3}Fe_{0.2}$ nanoalloys.

A1.7 NiCoFe
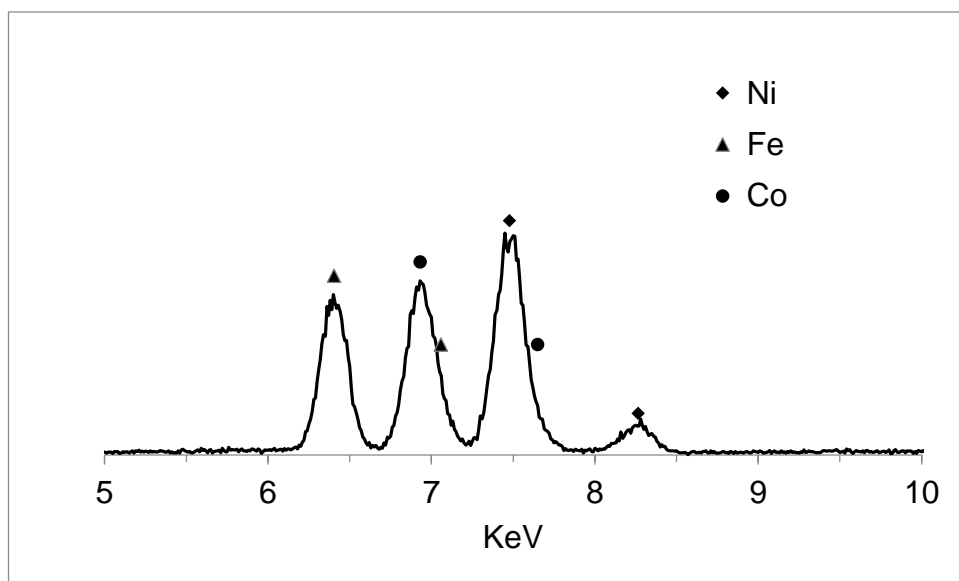
Figure A 11 XRF spectrum of $Ni_{0.5}Cu_{0.3}Co_{0.2}$ alloy nanoparticles, giving an average composition of $Ni_{0.56}Co_{0.24}Fe_{0.18}$.
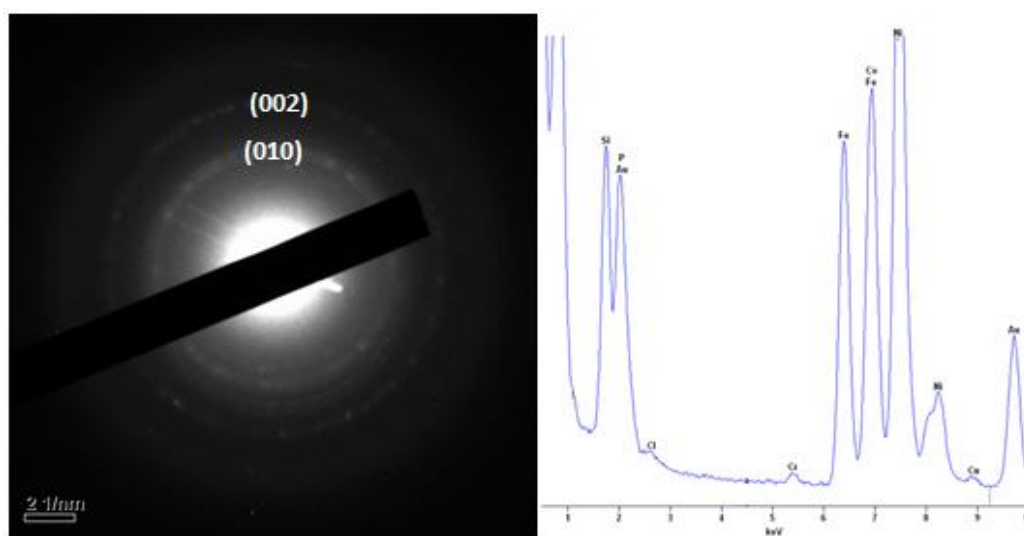
Figure A 12 Electron diffraction (left) and EDX (right) of $Ni_{0.5}Co_{0.3}Fe_{0.2}$ nanoalloys.

Apppendix 2 - Chapter 3 Supplementary Data

A2.1 Rotation Rate Determination
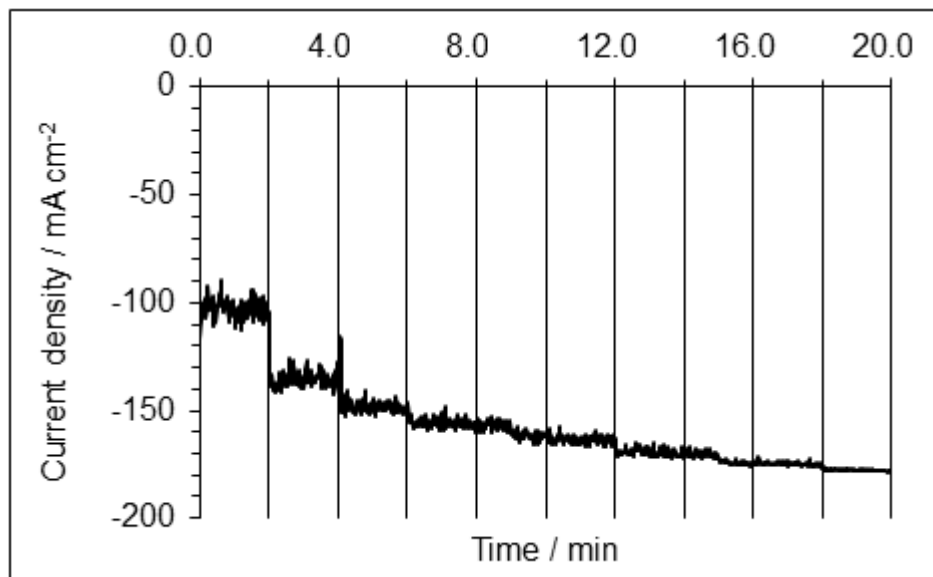
Figure A 13 Current density with increasing rotation rate; starting from 0 rpm and increasing by 500 rpm every 2 minutes to 4500 rpm.

A2.2 Calculation of a Monolayer Loading on a Carbon Rod Electrode:

Diameter of the carbon rod $= 0.3$ cm^2

Surface area $= 0.0707$ cm^2 $= 7.07 \times 10^{-6}$ m^2

For a 10 nm nanoparticle, cross sectional area $= 78.54$ nm$^2 = 7.85 \times 10^{-17}$ m^2

The number of nanoparticles on the carbon rod $= 7.07 \times 10^{-6}$ m$^2 / 7.85 \times 10^{-17}$ m^2

$= 9 \times 10^{10}$

Volume of a nanoparticle $= 5.24 \times 10^{-25}$ m^3

Density of nickel $= 8907$ Kg m^{-3}

Therefore, the mass of a nanoparticle $= 8907$ m$^{-3} \times 5.24 \times 10^{-25}$ m^3

$= 4.66 \times 10^{-21}$ Kg

The mass of all the nanoparticles on the surface $= 4.66 \times 10^{-21}$ Kg $\times 9 \times 10^{10}$

$= 4.2 \times 10^{-10}$ Kg $= 0.42$ µg

A2.3 EDX Analysis of Electrodes
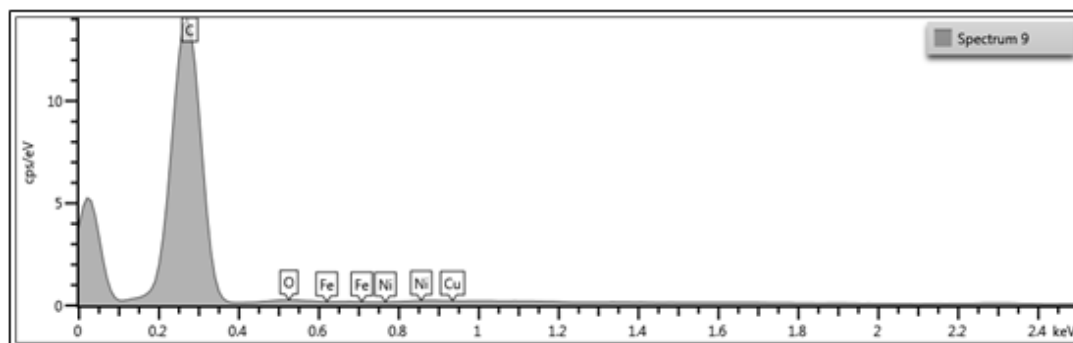
Figure A 14 EDX spectrum of the $Ni_{0.5}Cu_{0.3}Fe_{0.2}$ electrode after 20 CV cycles in 0.1 M H_2SO_4 / 0.1 M Na_2SO_4, pH 1. The expected peak positions for Ni, Cu and Fe are shown however, the signal is swamped by the carbon from the rod preventing quantitative analysis of the nanoalloy composition.

A2.4 Electrocatalytic Data for NiFe Nanoalloys
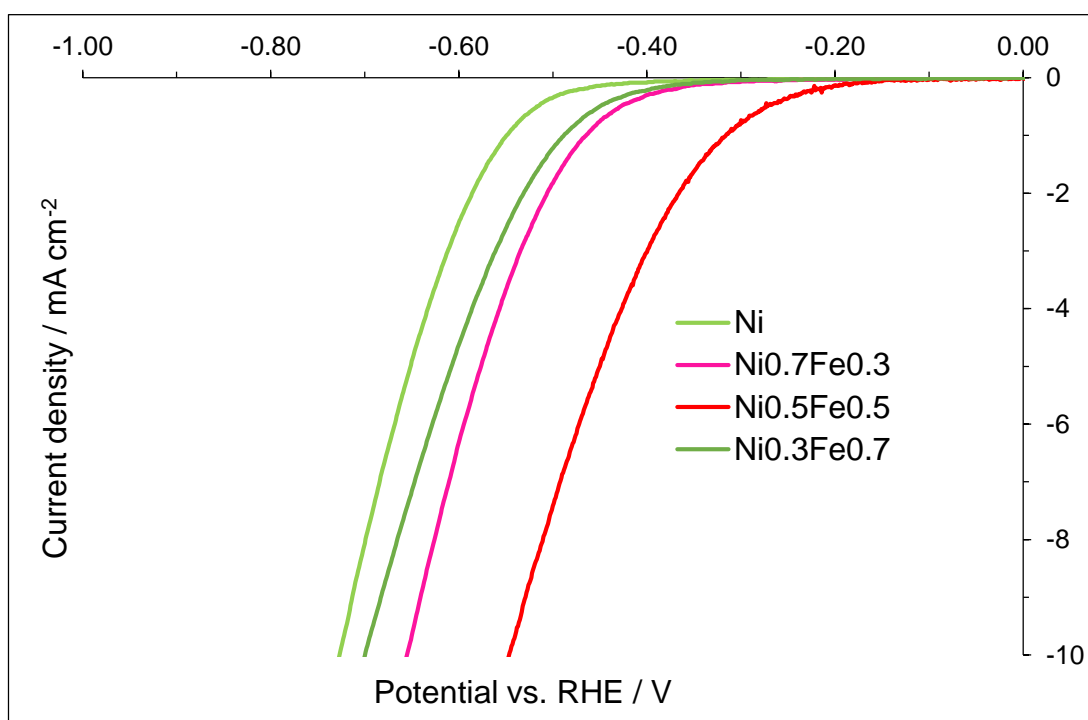
Figure A 15 Electrocatalytic activities of $Ni_{1-x}Fe_x$ nanoalloys (where x = 0, 0.3 0.5 and 0.7).

A2.5 EIS Equivalent Circuit Data at Various Overpotentials in pH 1

Table A 2 EIS fit data for a two time constant parallel equivalent circuit at various overpotentials in pH 1.

η = -100 mV	Ni	$Ni_{0.5}Cu_{0.5}$	$Ni_{0.5}Co_{0.5}$	$Ni_{0.5}Cu_{0.3}Co_{0.2}$	$Ni_{0.5}Cu_{0.3}Fe_{0.2}$	$Ni_{0.5}Co_{0.3}Fe_{0.2}$
R_s / Ohm cm^2	2.64	1.98	2.09	1.86	1.17	1.67
CPE_1 / Fs$^{(a-1)}$	3.80E-05	3.05E-05	2.11E-05	2.14E-05	3.83E-05	1.45E-05
a_1	0.86	0.88	0.91	0.89	0.86	0.93
R_1 / Ohm cm^2	1.20	1.04	0.94	1.33	1.55	0.88
τ_1 / s	8.70E-06	7.68E-06	6.84E-06	7.54E-06	1.13E-05	5.52E-06
CPE_2 / F s$^{(a-1)}$	1.55E-05	2.19E-05	1.19E-05	1.04E-05	1.04E-05	1.65E-05
a_2	1	1	1	1	1	0.92
R_2 / Ohm cm^2	1923.84	1589.16	4291.08	1779.96	1067.04	1141.86
τ_2 / s	2.98E-02	3.48E-02	5.11E-02	1.85E-02	1.11E-02	7.23E-03
χ^2	2.77E-02	2.81E-02	2.98E-02	3.74E-02	1.22E-02	7.02E-03

η = -300 mV	Ni	$Ni_{0.5}Cu_{0.5}$	$Ni_{0.5}Co_{0.5}$	$Ni_{0.5}Cu_{0.3}Co_{0.2}$	$Ni_{0.5}Cu_{0.3}Fe_{0.2}$	$Ni_{0.5}Co_{0.3}Fe_{0.2}$
R_s / Ohm cm^2	2.08	1.98	2.06	1.87	1.17	1.68
CPE_1 / Fs$^{(a-1)}$	8.57E-06	2.18E-05	2.33E-05	1.77E-05	4.71E-05	1.89E-05
a_1	0.67	0.92	0.91	0.92	0.85	0.92
R_1 / Ohm cm^2	0.80	0.89	1.02	0.85	1.49	1.04
τ_1 / s	2.19E-08	7.63E-06	8.28E-06	5.81E-06	1.21E-05	7.63E-06
CPE_2 / F s$^{(a-1)}$	2.39E-05	2.39E-05	1.25E-05	7.21E-06	1.46E-05	8.82E-06
a_2	0.91	0.96	1	0.92	1	0.92
R_2 / Ohm cm^2	1190.16	755.16	2466.48	1001.88	720.84	340.68
τ_2 / s	1.44E-02	1.65E-02	3.08E-02	7.61E-03	1.05E-02	2.89E-03
χ^2	4.55E-02	1.18E-02	3.20E-02	7.17E-03	1.48E-02	9.42E-03

η = -500 mV	Ni	$Ni_{0.5}Cu_{0.5}$	$Ni_{0.5}Co_{0.5}$	$Ni_{0.5}Cu_{0.3}Co_{0.2}$	$N_{0.5}iCu_{0.3}Fe_{0.2}$	$Ni_{0.5}Co_{0.3}Fe_{0.2}$
R_s / Ohm cm^2	2.83	2.00	2.10	1.89	1.33	1.76
CPE_1 / Fs$^{(a-1)}$	3.93E-05	3.47E-05	2.43E-05	1.70E-05	4.62E-05	3.30E-05
a_1	0.85	0.89	0.91	0.95	0.85	0.88
R_1 / Ohm cm^2	0.94	1.09	1.01	1.24	1.28	1.67
τ_1 / s	6.17E-06	1.06E-05	8.58E-06	1.18E-05	1.02E-05	1.35E-05
CPE_2 / F s$^{(a-1)}$	2.16E-05	2.75E-05	1.48E-05	2.20E-05	1.96E-05	1.34E-05
a_2	1	1	1	0.94	1	1
R_2 / Ohm cm^2	19.18	136.20	122.16	472.98	14.48	26.50
τ_2 / s	4.14 E-04	3.75E-03	1.81E-03	5.25E-03	2.84E-04	3.55E-04
χ^2	3.45E-02	1.28E-02	3.71E-02	2.82E-02	2.16E-02	1.53E-02

A2.6 EIS at pH 13, comparison at various overpotentials
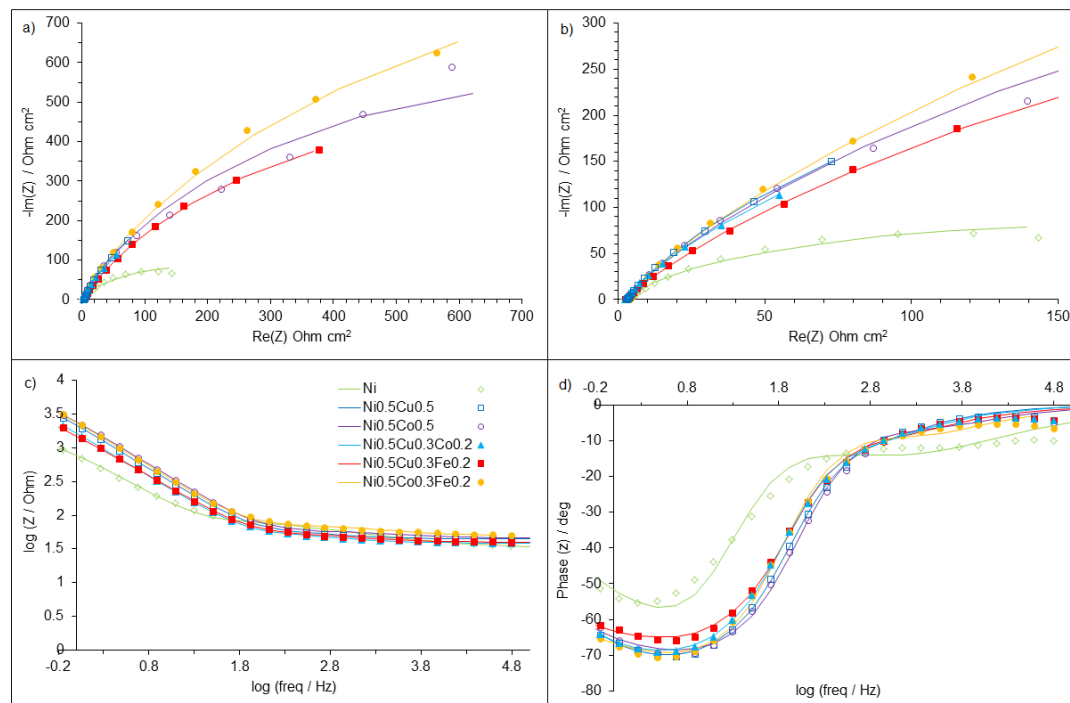
Figure A 16 EIS data at an overpotential of -100 mV in 0.1 M NaOH pH 13. The symbols are the experimental data and the lines are the fits a) Nyquist plot for all frequencies, b) zoomed in image of Nyquist plot at high frequencies, c) Bode impedance plot and d) Bode phase plot.
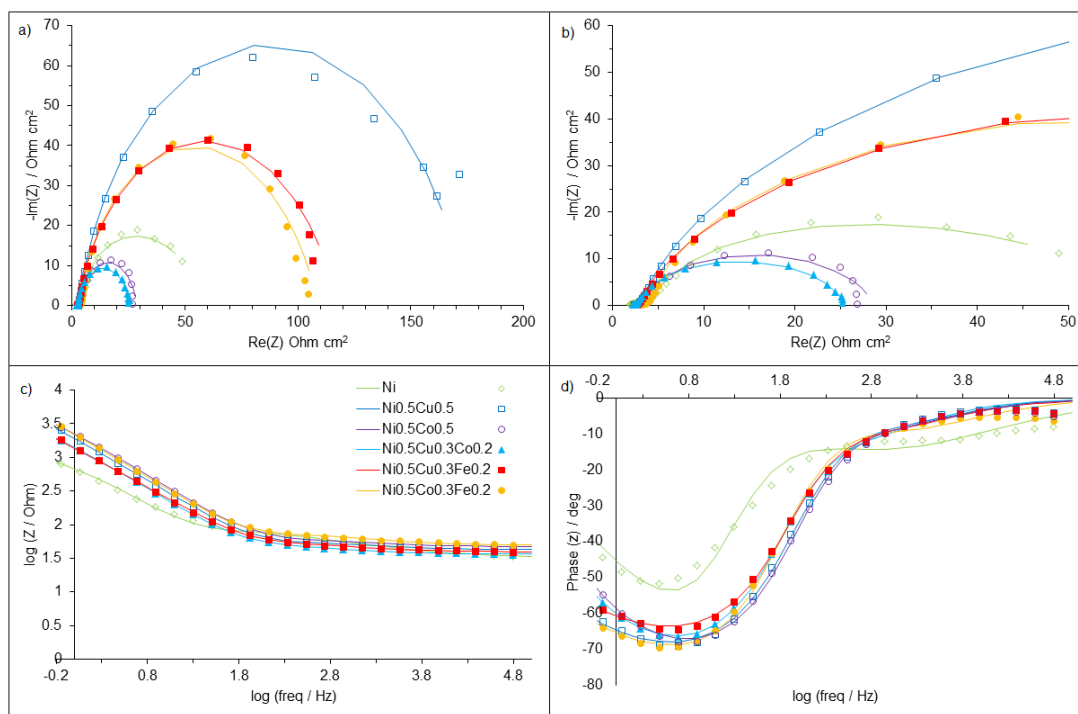
Figure A 17 EIS data at an overpotential of -300 mV in 0.1 M NaOH pH 13. The symbols are the experimental data and the lines are the fits a) Nyquist plot for all frequencies, b) zoomed in image of Nyquist plot at high frequencies, c) Bode impedance plot and d) Bode phase plot.
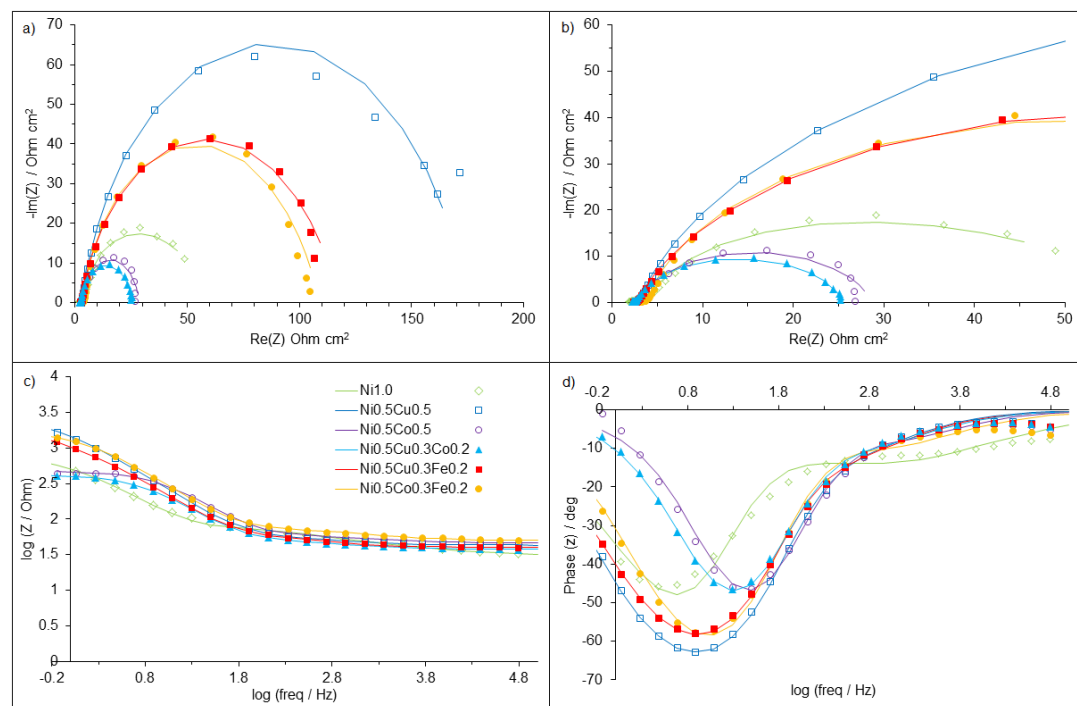
Figure A 18 EIS data at an overpotential of -500 mV in 0.1 M NaOH pH 13. The symbols are the experimental data and the lines are the fits a) Nyquist plot for all frequencies, b) zoomed in image of Nyquist plot at high frequencies, c) Bode impedance plot and d) Bode phase plot.

A2.7 EIS Equivalent Circuit Data at Various Overpotentials in pH 13

Table A 3 EIS fit data for a two time constant parallel equivalent circuit at various overpotentials in pH 13.

| η = -100 mV	Ni	$Ni_{0.5}Cu_{0.5}$	$Ni_{0.5}Co_{0.5}$	$Ni_{0.5}Cu_{0.3}Co_{0.2}$	$Ni_{0.5}Cu_{0.3}Fe_{0.2}$	$Ni_{0.5}Co_{0.3}Fe_{0.2}$
R_s / Ohm cm^2	1.73	2.63	2.70	2.30	2.35	2.50
CPE_1 / Fs$^{(a-1)}$	1.30E-04	8.28E-05	7.64E-05	1.15E-04	1.45E-04	3.91E-05
a_1	0.54	0.78	0.68	0.74	0.68	0.60
R_1 / Ohm cm^2	2.78	1.79	0.96	1.72	1.46	1.39
τ_1 / s	1.77E-07	1.05E-05	8.47E-07	8.17E-06	3.31E-06	6.26E-08
CPE_2 / F s$^{(a-1)}$	2.17E-04	1.69E-05	2.53E-05	2.49E-05	2.75E-05	6.34E-05
a_2	0.81	1	0.97	1	0.98	0.88
R_2 / Ohm cm^2	235.56	979.32	1658.82	978.12	1463.04	2143.98
τ_2 / s	7.07E-03	1.66E-02	3.03E-02	2.44E-02	3.25E-02	3.64E-02
χ^2	2.11E-02	1.89E-02	5.49E-02	1.96E-02	2.68E-02	5.49E-02

η = -300 mV	Ni	$Ni_{0.5}Cu_{0.5}$	$Ni_{0.5}Co_{0.5}$	$Ni_{0.5}Cu_{0.3}Co_{0.2}$	$Ni_{0.5}Cu_{0.3}Fe_{0.2}$	$Ni_{0.5}Co_{0.3}Fe_{0.2}$
R_s / Ohm cm^2	1.82	2.55	2.82	2.13	2.35	2.70
CPE_1 / Fs$^{(a-1)}$	9.23E-05	1.01E-04	7.82E-05	9.02E-05	1.62E-04	5.65E-05
a_1	0.60	0.73	0.74	0.73	0.68	0.62
R_1 / Ohm cm^2	2.55	1.27	1.49	0.89	1.68	1.44
τ_1 / s	4.81E-07	4.27E-06	4.20E-06	2.56E-06	4.48E-06	2.03E-07
CPE_2 / F s$^{(a-1)}$	2.48E-04	2.15E-05	1.85E-05	6.11E-05	2.46E-05	5.33E-05
a_2	0.8	1	1	0.91	1	0.91
R_2 / Ohm cm^2	112.44	1078.50	551.16	394.02	772.68	1479.24
τ_2 / s	3.50E-03	2.32E-02	1.02E-02	9.22E-03	1.90E-02	2.98E-02
χ^2	3.37E-02	3.29E-02	3.17E-02	1.92E-02	4.94E-02	5.04E-02

η = -500 mV	Ni	$Ni_{0.5}Cu_{0.5}$	$Ni_{0.5}Co_{0.5}$	$Ni_{0.5}Cu_{0.3}Co_{0.2}$	$N_{0.5}iCu_{0.3}Fe_{0.2}$	$Ni_{0.5}Co_{0.3}Fe_{0.2}$
R_s / Ohm cm^2	1.76	2.58	2.567	2.25	2.31	2.82
CPE_1 / Fs$^{(a-1)}$	1.26E-04	9.67E-05	1.10E-05	8.89E-05	4.26E-05	2.08E-05
a_1	0.59	0.78	0.77	0.78	0.78	0.74
R_1 / Ohm cm^2	2.54	2.08	0.67	1.31	0.68	1.17
τ_1 / s	6.24E-07	1.48E-05	2.43E-07	8.39E-06	1.70E-06	5.51E-07
CPE_2 / F s$^{(a-1)}$	2.64E-04	1.96E-05	1.10E-05	8.89E-05	4.26E-05	2.08E-05
a_2	0.59	0.78	0.77	0.78	0.78	0.74
R_2 / Ohm cm^2	52.51	170.34	25.52	22.04	111.24	102.48
τ_2 / s	2.27E-03	3.34E-03	5.02E-04	7.76E-04	2.18E-03	2.11E-03
χ^2	2.99E-02	4.31E-02	3.38E-02	3.14E-02	1.79E-02	4.11E-02

Appendix 3 – Chapter 4 Supplementary Data

A3.1 Calculating Faradaic Efficiency

Moles expected for 100 % FE of a 1 electron reaction =

$$\frac{\text{Average Current (A)} \ \times \ \text{Time (s)}}{\text{Faraday constant (96490 C mol}^{-1})}$$

For multiple electron transfer, divide by the number of electrons.

To get concentration for 100 % FE, divide the moles by the volume (12 mL for solution or 5 mL for the headspace).

The solubility of hydrogen in water is 0.79 mmol dm^{-3}, therefore this was subtracted from the expected 100 % FE concentration.

Abbreviations

ADF-STEM	Annular dark field scanning transmission electron microscopy
CPE	Controlled potential electrolysis
CTAB	Cetyltrimethyl ammonium bromide
CV	Cyclic voltammetry
EDX	Energy dispersive X-ray spectroscopy
fcc	Face centred cubic
FE	Faradaic efficiency
FTO	Fluorine doped tin oxide
GC	Gas chromatography
hcp	Hexagonal close packed
HER	Hydrogen evolution reaction
HOR	Hydrogen oxidation reaction
HR-SEM	High resolution scanning electron microscopy
IR	Infrared
ITO	Indium doped tin oxide
LSV	Linear sweep voltammetry
NHE	Normal hydrogen electrode
NMR	Nuclear magnetic resonance
OER	Oxygen evolution reaction
ORR	Oxygen reduction reaction
PV	Photovoltaic
rds	Rate determining step
RHE	Reversible hydrogen electrode
SHE	Standard hydrogen electrode
TEM	Transmission electron microscopy
UV	Ultra violet
XRD	X-ray diffraction
XRF	X-ray fluorescence

Terms

a	Lattice parameter
c	Lattice parameter
d	Interplannar spacing
D	Crystallite size
E	Potential / V
F	Faraday constant (96490 C mol^{-1})
ΔG^0	Standard free energy
i	Current density / mA cm^{-2}
i^0	Exchange current density / mA cm^{-2}
I	Current / mA
k	Scherrer constant
R	Gas constant (8.314 J K^{-1} mol^{-1})
T	Temperature / K
α	Transfer coefficient
β	Full peak width at half maximum for an XRD diffract graph or the structure factor for an electrolytic cell
θ	Bragg diffraction angle
η	Overpotential
ρ	Density

References

1.   A. Kudo and Y. Miseki, *Chem. Soc. Rev.*, 2009, **38**, 253-278.

2.   M. G. Walter, E. L. Warren, J. R. McKone, S. W. Boettcher, Q. Mi, E. A. Santori and N. S. Lewis, *Chem. Rev.* , 2010, **110**, 6446-6473.

3.   M. Ni, M. K. H. Leung, D. Y. C. Leung and K. Sumathy, *Renewable Sustainable Energy Rev.*, 2007, **11**, 401-425.

4.   S. Chen and L.-W. Wang, *Chem* Mater**, 2012, **24**, 3659-3666.

5.   M. Y. Tsang, N. E. Pridmore, L. J. Gillie, Y. H. Chou, R. Brydson and R. E. Douthwaite, *Adv. Mater.*, 2012, **24**, 3406-3409.

6.   K. Sayama and H. Arakawa, *J. Photochem. Photobiol. A*, 1994, **77**, 243-247.

7.   T. Puangpetch, T. Sreethawong and S. Chavadej, *Int. J. Hydrogen Energy*, 2010, **35**, 6531-6540.

8.   U. Siemon, D. Bahnemann, J. J. Testa, D. Rodriguez, M. I. Litter and N. Bruno, *J. Photochem. Photobiol. A*, 2002, **148**, 247-255.

9.   M. Gratzel, *Acc. Chem. Res.*, 1981, **14**, 376-384.

10.   M. Maicu, M. C. Hidalgo, G. Colon and J. A. Navio, *J. Photochem. Photobiol. A*, 2011, **217**, 275-283.

11.   S. Y. Reece, J. A. Hamel, K. Sung, T. D. Jarvi, A. J. Esswein, J. J. H. Pijpers and D. G. Nocera, *Science*, 2011, **334**, 645-648.

12.   K. Sivula and M. Gratzel, in *Photoelectrochemical Water Splitting Materials, Processes and Architectures*, eds. L. Peter and H.-J. Lewerenz, The Royal Society of Chemistry, 2013, p. 4.

13.   H. S. Jeon, J. H. Koh, S. J. Park, M. S. Jee, D.-H. Ko, Y. J. Hwang and B. K. Min, *J. Mater. Chem. A*, 2015, **3**, 5835-5842.

14.   O. Khaselev and J. A. Turner, *Science*, 1998, **280**, 425-427.

15.   J. Luo, J.-H. Im, M. T. Mayer, M. Schreier, M. K. Nazeeruddin, N.-G. Park, S. D. Tilley, H. J. Fan and M. Gratzel, *Science*, 2014, **345**, 1593-1596.

16.   T. Arai, S. Sato and T. Morikawa, *Energy Environ. Sci.*, 2015, **8**, 1998-2002.

17.   K. P. Kuhl, E. R. Cave, D. N. Abram and T. F. Jaramillo, *Energy Environ. Sci.*, 2012, **5**, 7050-7059.

18.   M. Zeng and Y. Li, *J. Mater. Chem. A*, 2015, **3**, 14942-14962.

19.   C. C. L. McCrory, S. Jung, I. M. Ferrer, S. M. Chatman, J. C. Peters and T. F. Jaramillo, *J. Am. Chem. Soc.*, 2015, **137**, 4347-4357.

20.   T. R. Cook, D. K. Dogutan, S. Y. Reece, Y. Surendranath, T. S. Teets and D. G. Nocera, *Chem. Rev.*, 2010, **110**, 6474-6502.

21.   W. Zhu, Y.-J. Zhang, H. Zhang, H. Lv, Q. Li, R. Michalsky, A. A. Peterson and S. Sun, *J. Am. Chem. Soc.*, 2014, **136**, 16132-16135.

22.   Y. Chen and M. W. Kanan, *J. Am. Chem. Soc.*, 2012, **134**, 1986-1989.

23.	K. J. Schouten and M. Koper, in *Photoelectrochemical Water Splitting Materials, Processes and Architectures* eds. L. Peter and H.-J. Lawerenz, The Royal Society of Chemistry, 2013.

24.	M. Gattrell, N. Gupta and A. Co, *J. Electroanal. Chem.*, 2006, **594**, 1-19.

25.	W.-F. Chen, K. Sasaki, C. Ma, A. Frenkel, N. Marikovic, J. T. Muckerman, Y. M. Zhu and R. R. Adzic, *Angew. Chem. Int. Ed.*, 2012, **51**, 6131-6135.

26.	E. Navarro-Flores, Z. W. Chong and S. Omanovic, *J. Mol. Catal. A: Chem.*, 2005, **226**, 179-197.

27.	D. E. Brown, M. N. Mahmood, M. C. M. Man and A. K. Turner, *Electrochim. Acta*, 1984, **29**, 1551-1556.

28.	E. J. Popczun, J. R. McKone, C. G. Read, A. J. Biacchi, A. M. Wiltrout, N. S. Lewis and R. E. Schaak, *J. Am. Chem. Soc.*, 2013, **135**, 9267-9270.

29.	T. M. Muster, A. Trichi, T. A. Markley, D. Lau, P. Martin, A. Bradbury, A. Bendavid and S. Dligatch, *Electrochim. Acta*, 2011, **56**, 9679-9699.

30.	S. Guerin, B. E. Hayden, C. E. Lee, C. Mormiche, J. R. Owen and A. E. Russell, *J. Comb. Chem.*, 2004, **6**, 149-158.

31.	S. D. Beattie and J. R. Dahn, *J. Electrochem. Soc.*, 2005, **152**, C542-C548.

32.	S. H. Baeck, T. F. Jaramillo, C. Brandli and E. W. McFarland, *J. Comb. Chem.*, 2002, **4**, 563-568.

33.	J. J. Hanak, H. W. Lehmann and R. K. Wehner, *J. Appl. Phys.*, 1972, **43**, 1666-1673.

34.	S. Guerin, B. E. Hayden, D. Pletcher, M. E. Rendall and J.-P. Suchsland, *J. Comb. Chem.*, 2006, **8**, 679-689.

35.	T. He, E. Kreidler, L. Xiong, J. Luo and C. J. Zhong, *J. Electrochem. Soc.*, 2006, **153**, A1637-A1643.

36.	M. K. Carpenter, T. E. Moylan, R. S. Kureja, M. H. Atwan and M. M. Tessema, *J. Am. Chem. Soc.*, 2012, **134**, 8535-8542.

37.	C. Wang, M. F. Chi, D. G. Li, D. v. d. Vliet, G. F. Wang, Q. Y. Lin, J. F. Mitchell, K. L. More, N. M. Markovic and V. R. Stamenkovic, *ACS Catal.*, 2011, **1**, 1355-1359.

38.	J. Luo, L. Wang, D. Mott, P. N. Njoki, N. Kariuki, C.-J. Zhong and T. He, *J. Mater. Chem.*, 2006, **16**, 1665-1673.

39.	B. Fang, B. N. Wanjala, J. Yin, R. Loukrakpam, J. Luo, X. Hu, J. Last and C.-J. Zhong, *Int. J. Hydrogen Energy*, 2012, **37**, 4627-4632.

40.	B. N. Wanjala, B. Fang, J. Luo, Y. S. Chen, J. Yin, M. H. Engehard, R. Loukrakpam and C. J. Zhong, *J. Am. Chem. Soc.*, 2011, **133**, 12714-12727.

41.	J. A. Zhao, K. Jarvis, P. Ferreira and A. Manthiram, *J. Power Sources*, 2011, **196**, 4515-4523.

42.	Y. Zhang, W. Huang, S. E. Habas, J. N. Kuhn, M. E. Grass, Y. Yamada, P. Yang and G. A. Somorjai, *J. Phys. Chem. C.* , 2008, **112**, 12092-12095.

43.	U. A. Paulus, A. Wokaun, G. G. Scherer, T. J. Schmidt, V. Stamenkovic, V. Radmilovic, N. M. Markovic and P. N. Ross, *J. Phys. Chem. B.*, 2002, **106**, 4181-4191.

44.   H.-J. Kim, C.-W. Kim, D. Punnoose, C. V. V. M. Gopi, S.-K. Kim, K. Prabakar and S. S. Rao, *Appl. Surf. Sci.*, 2015, **328**, 78-85.

45.   Z. Zou, J. Ye and H. Arakawa, *Int. J. Hydrogen Energy*, 2003, **28**, 663-669.

46.   X. Zou and Y. Zhang, *Chem. Soc. Rev.*, 2015, **44**, 5148-5180.

47.   B. Parkingson and J. Turner, in *Photoelectrochemical Water Splitting Materials, Processes and Architectures*, ed. H.-J. Lewerenz, The Royal Society of Chemistry, 2013, pp. 1-17.

48.   S. Trasatti, *J. Electroanal. Chem.*, 1972, **39**, 163-184.

49.   M. H. Miles, *J. Electroanal. Chem.*, 1975, **60**, 89-96.

50.   M. A. Dominguez-Crespo, E. Ramirez-Meneses, A. M. Torres-Huerta, V. Garibay-Febles and K. Philippot, *Int. J. Hydrogen Energy*, 2012, **37**, 4798-4811.

51.   H. J. Miao and D. L. Piron, *Electrochim. Acta*, 1993, **38**, 1079-1085.

52.   I. Herraiz-Cardona, E. Ortega, J. G. a. Anton and V. Pe´rez-Herranz, *Int. J. Hydrogen Energy*, 2011, **36**, 9428-9438.

53.   R. Solmaz, A. Doner, I. Sahin, A. O. Yuce, G. Kardas, B. Yazici and M. Erbil, *Int. J. Hydrogen Energy*, 2009, **34**, 7910-7918.

54.   R. Solmaz, A. Doner and G. Kardas, *Int. J. Hydrogen Energy*, 2009, **34**, 2089-2094.

55.   H. Vrubel and X. L. Hu, *Angew. Chem. Int. Ed.*, 2012, **51**, 12703-12706.

56.   R. B. Levy and M. Boudart, *Science*, 1973, **181**, 547-549.

57.   W.-F. Chen, C.-H. Wang, K. Sasaki, N. Marikovic, W. Xu, J. T. Muckerman, Y. Zhu and R. R. Adzic, *Energy Environ. Sci.*, 2013, **6**, 943-951.

58.   J. R. McKone, B. F. Sadtler, C. A. Werlang, N. S. Lewis and H. B. Gray, *ACS Catal.*, 2013, **3**, 166-169.

59.   C. Wan, Y. N. Regmi and B. M. Leonard, *Angew. Chem. Int. Ed.*, 2014, **53**, 6407-6410.

60.   B. J. Murphy, F. Sargent and F. A. Armstrong, *Energy Environ. Sci.*, 2014, **7**, 1426.

61.   S. Ogo, K. Ichikawa, T. Kishima, T. Matsumoto, H. Nakai, K. Kusaka and T. Ohhara, *Science*, 2013, **339**, 682-684.

62.   N. Wang, M. Wang, L. Chen and L. Sun, *Dalton Trans.*, 2013, **42**, 12059-12071.

63.   C. Greco, *Dalton Trans.*, 2013, **42**, 13845.

64.   P. Du and R. Eisenberg, *Energy Environ. Sci.*, 2012, **5**, 6012.

65.   A. K. Das, M. H. Engelhard, R. M. Bullock and J. A. S. Roberts, *Inorg. Chem.*, 2014, **53**, 6875-6885.

66.   B. C. M. Martindale, G. A. M. Hutton, C. A. Caputo and E. Reisner, *J. Am. Chem. Soc.*, 2015, **137**, 6018-6025.

67.   K. Fan, F. Li, L. Wang, Q. Daniel, E. Gabrielsson and L. Sun, *Phys. Chem. Chem. Phys.*, 2014, **16**, 25234-25240.

68.   B. E. Barton and T. B. Rauchfuss, *J. Am. Chem. Soc.*, 2010, **132**, 14877-14885.

69.   M. Wang, L. Chen and L. Sun, *Energy Environ. Sci.*, 2012, **5**, 6763-6778.

70.   R. Ferrando, J. Jellinek and R. L. Johnston, *Chem. Rev.*, 2008, **108**, 845-910.

71.   R. Simpraga, G. Tremiliosi, S. Y. Qian and B. E. Conway, *J. Electroanal. Chem.*, 1997, **424**, 141-151.

72.   A. Damian and S. Omanovic, *J. Power Sources*, 2006, **158**, 464-476.

73.   J. R. McKone, E. L. Warren, M. J. Bierman, S. W. Boettcher, N. S. Lewis and H. B. Gray, *Energy Environ. Sci.*, 2011, **4**, 3573-3583.

74.   S. Martinez, M. Metikos-Hukovic and L. Valek, *J. Mol. Catal. A: Chem.*, 2006, **245**, 114-121.

75.   M. Metikos-Hukovic, Z. Grubac, N. Radic and A. Tonejc, *J. Mol. Catal. A: Chem.*, 2006, **249**, 172-180.

76.   M. Jafarian, O. Azizi, F. Gobal and M. G. Mahjani, *Int. J. Hydrogen Energy*, 2007, **32**, 1686-1693.

77.   M. J. Giz, S. C. Bento and E. R. Gonzalez, *Int. J. Hydrogen Energy*, 2000, **25**, 621-626.

78.   J. M. Yan, X. B. Zhang, S. Han, H. Shioyama and Q. Xu, *J. Power Sources*, 2009, **194**, 478-481.

79.   G. Chen, S. Desinan, R. Rosei, F. Rosei and D. Ma, *Chem. Eur. J.*, 2012, **18**, 7925-7930.

80.   L. D. Rogatis, T. Montini, B. Lorenzut and P. Fornasiero, *Energy Environ. Sci.*, 2008, **1**, 501-509.

81.   S. Canaguier, V. Artero and M.Fontecave, *Dalton Trans.*, 2008, 315-325.

82.   Q. Zhou, J. Jiang, Q. Zhong, Y. Wang, K. Li and H. Liu, *J. Alloys Compd.*, 2013, **563**, 171-175.

83.   C. D. Windle and R. N. Perutz, *Coord. Chem. Rev.*, 2014, **256**, 2562-2570.

84.   G. A. Olah, *Catal. Lett.*, 2004, **93**, 1-2.

85.   X.-M. i. Liu, G. Q. Lu, Z.-F. Yan and J. Beltramini, *Ind. Eng. Chem. Res.*, 2003, **42**, 6518-6530.

86.   L. Lyu, F. Jin, H. Zhong, H. Chen and G. Yao, *RSC Adv.*, 2015, **5**, 31450-31453.

87.   Y. Li, S. H. Chan and Q. Sun, *Nanoscale*, 2015, **7**, 8663-8683.

88.   W. Lv, R. Zhang, P. Gao and L. Lei, *J. Power Sources*, 2014, **253**, 276-281.

89.   C. W. Li and M. W. Kanan, *J. Am. Chem. Soc.*, 2012, **134**, 7231-7234.

90.   R. D. Tilley and D. A. Jefferson, *J. Mater. Chem.*, 2002, **12**, 3809-3813.

91.   M. A. Dominguez-Crespo, E. Ramı´rez-Meneses, V. Montiel-Palma, A. M. T. Huerta and H. D. Rosales, *Int. J. Hydrogen Energy*, 2009, **34**, 1664-1676.

92.   D. Ferrer, A. Torres-Castro, X. Gao, S. Sepulveda-Guzman, U. Ortiz-Mendez and M. Jose-Yacaman, *Nano Lett.*, 2007, **7**, 1701-1705.

93.   M. C. Fromen, J. Morillo, M. J. Casanove and P. Lecante, *Europhys. Lett.*, 2006, **73**, 885-891.

94.   F. Baletto, C. Mottet and R. Ferrando, *Phys. Rev. Lett.*, 2003, **90**, 135504-135501-135504-135504.

95.   D. Cheng, W. Wang and S. Huang, *J. Phys. Chem. B.*, 2006, **110**, 16193-16196.

96.   H. Lv, Z. Xi, Z. Chen, S. Guo, Y. Yu, W. Zhu, Q. Li, X. Zhang, M. Pan, G. Lu, S. Mu and S. Sun, *J. Am. Chem. Soc.*, 2015, **137**, 5859-5862.

97.   J. Ahmed, B. Kumar, A. M. Mugweru, P. Trinh, K. V. Ramanujachary, S. E. Lofland, Govind and A. K. Ganguli, *J. Phys. Chem. C*, 2010, **114**, 18779-18784.

98.   C. Wang, M. F. Chi, G. F. Wang, D. v. d. Vliet, D. G. Li, K. More, H. H. Wang, J. A. Schlueter, N. M. Markovic and V. R. Stamenkovic, *Adv. Funct. Mater.*, 2011, **21**, 147-152.

99.   Y. Herbani, T. Nakamura and S. Sato, *J. Colloid Interface Sci.*

, 2012, **375**, 78-87.

100.   H. Bonnemann and R. M. Richards, *Eur. J. Inorg. Chem.*, 2001, 2455-2480.

101.   S. Carenco, S. Labouille, S. Bouchonnet, C. Boissière, X.-F. L. Goff, C. Sanchez and N. Mézailles, *Chem. Eur. J.*, 2012, **18**, 14165-14173.

102.   N. Toshima and T. Yonezawa, *New J. Chem.*, 1998, **22**, 1179-1201.

103.   C. M. Wylie, R. M. Shelton, G. J. P. Fleming and A. J. Davenpor, *Dental Mater.*, 2007, **23**, 714-723.

104.   in *Alloy Phase Diagrams*, ed. H. Baker, 1992, vol. 3.

105.   C. Burda, X. B. Chen, R. Narayanan and M. A. El-Sayed, *Chem. Rev.*, 2005, **105**, 1025-1102.

106.   J. Pelleg, E. Elish and D. Mogilyanski, *Metall. Mater. Trans. A*, 2005, **36A**, 3187-3194.

107.   R. Brayner, T. Coradin, F. Fievet-Vincent, J. Livage and F. Fievet, *New J. Chem.*, 2005, **29**, 681-685.

108.   O. D. Jayakumar, H. G. Salunke and A. K. Tyagi, *Solid State Commun*, 2009, **149**, 1769-1771.

109.   M. Kumar, A. Pathak, M. Singh and M. L. Singla, *Thin Solid Films*, 2010, **519**, 1445-1451.

110.   G. Viau, F. Fievet-Vincent and F. Fievet, *Solid State Ionics*, 1996, **84**, 259-270.

111.   K. L. Wu, X.-W. Wei, X.-M. Zhou, D.-H. Wu, X.-W. Liu, Y. Ye and Q. Wang, *J. Phys. Chem. C*, 2011, **115**, 16268-16274.

112.   T. A. Aljohani, B. E. Hayden and A. Anastasopoulos, *Electrochim. Acta*, 2012, **76**, 389-393.

113.   A. Endo, M. Kajitani, M. Mukaida, K. Shimizu and G. P. Sato, *Inorg. Chim. Acta*, 1988, **150**, 25-34.

114.   C. Wang, W. Li, X. Lu, S. Xie, F. Xiao, P. Liu and Y. Tong, *Int. J. Hydrogen Energy*, 2012, **37**, 18688-18693.

115.   F. Rosalbino, G. Scavino and M. A. Grande, *J. Electroanal. Chem.*, 2013, **694**, 114-121.

116.   W.-W. Zhang, Q.-Q. Cao, J.-L. Xie, X.-M. Ren, C.-S. Lu, Y. Zhou, Y.-G. Yao and Q.-J. Menga, *J. Colloid Interface Sci.*, 2003, **257**, 237-243.

117.   A. Kumar, J. T. Miller, A. S. Mukasyan and E. E. Wolf, *Appl. Catal., A*, 2013, **467**, 593-603.

118.   K. V. Manukyan, A. Cross, S. Rouvimov, J. Miller, A. S. Mukasyan and E. E. Wolf, *Appl. Catal., A*, 2014, **476**, 47-53.

119.   M. Srivastava, A. K. Ojha, S. Chaubey, P. K. Sharma and A. C. Pandey, *Mater. Chem. Phys.*, 2010, **120**, 493-500.

120.   Y. Li, H. Wang, L. Xie, Y. Liang, G. Hong and H. Dai, *J. Am. Chem. Soc.*, 2011, **133**, 7296-7299.

121.   W.-F. Chen, J. T. Muckerman and E. Fujita, *Chem. Commun.*, 2013, **49**, 8896-8909.

122.   R. Guidelli, R. G. Compton, J. M. Feliu, E. Gileadi, J. Lipkowski, W. Schmickler and S. Trasatti, *Pure Appl. Chem.*, 2014, **86**, 245-258.

123.   E. Reisner, D. J. Powell, C. Cavazza, J. C. Fontecilla-Camps and F. A. Armstrong, *J. Am. Chem. Soc.*, 2009, **131**, 18457-18466.

124.   M. K. Nazeeruddin, A. Kay, I. Ridicio, R. Humphybaker, E. Muller, P. Laska, N. Vlachopoulos and M. Gratzel, *J. Am. Chem. Soc.*, 1993, **115**, 6382-6390.

125.   P. Cuendet, K. K. Rao, M. Gratzel and D. Hall, *Biochimie*, 1986, **68**, 217-221.

126.   E. Favry, D. Wang, D. Fantauzzi, J. Anton, D. S. Su, T. Jacob and N. Alonso-Vante, *Phys. Chem. Chem. Phys.*, 2011, **13**, 9201-9208.

127.   N. Alexeyeva, A. Sarapuu, K. Tammeveski, F. J. Vidal-Iglesias, J. Solla-Gullon and J. M. Feliu, *Electrochim. Acta*, 2011, **56**, 6702-6708.

128.   N. V. Long, M. Ohtaki, T. D. Hien, J. Randy and M. Nogami, *Electrochim. Acta*, 2011, **56**, 9133-9143.

129.   U. A. Paulus, T. J. Schmidt, H. A. Gasteriger and R. J. Behm, *J. Electroanal. Chem.*, 2001, **495**, 134-145.

130.   S. Sugawara, K. Tsujita, S. Mitsushima, K. Shinohara and K. Ota, *Electrocatal.*, 2011, **2**, 60-68.

131.   A. Habrioux, D. Diabate, J. Rousseau, T. W. Napporn, K. Servat, L. Guetaz, A. Trokourey and K. B. Kokoh, *Electrocatal.*, 2010, **1**, 51-59.

132.   B. N. Wanjala, R. Loukrakpam, J. Luo, P. N. Njoki, D. Mott, C. J. Zhong, M. H. Shao, L. Protsailo and T. Kawamura, *J. Phys. Chem. C*, 2010, **114**, 17580-17590.

133.   C. Wang, G. F. Wang, D. v. d. Vliet, K. C. Chang, N. M. Markovic and V. R. Stamenkovic, *Phys. Chem. Chem. Phys.*, 2010, **12**, 6933-6939.

134.   M. R. G. d. Chialvo and A. C. Chialvo, *J. Electroanal. Chem.*, 1998, **448**, 87-93.

135.   M. M. Jaksic, *Int. J. Hydrogen Energy*, 2001, **26**, 559-578.

136.   S. G. Neophytides, S. Zafeiratos, G. D. Papakonstantinou, J. M. Jaksic, F. E. Paloukis and M. M. Jaksic, *Int. J. Hydrogen Energy*, 2005, **30**, 131-147.

137.   H. Ezaki, M. Morinaga and S. Watanabe, *Electrochim. Acta*, 1993, **38**, 557-564.

138.   H. Ezaki, M. Morinaga, S. Watanabe and J. Saito, *Electrochim. Acta*, 1994, **39**, 1769-1773.

139.   J. G. Highfield, K. Ogiro and B. Grushko, *Electrochim. Acta*, 2001, **47**, 465-481.

140.   Basics of Electrochemical Impedance Spectroscopy - *http://www.gamry.com/application-notes/EIS/basics-of-electrochemical-impedance-spectroscopy/*, Accessed 23rd April, 2015.

141.   T. Pajkossy, *J. Electroanal. Chem.*, 1994, **364**, 111-125.

142.   S. Omanovic and M. Metikos-Hukovic, *Thin Solid Films*, 1995, **266**, 31-35.

143.   M. Metikos-Hukovic and A. Jukic, *Electrochim. Acta*, 2000, **45**, 4159-4170.

144.   Z. Xie, P. He, L. Du, F. Dong, K. Dai and T. Zhang, *Electrochim. Acta*, 2013, **88**, 390-394.

145.   R. J. Lim, M. Xie, M. A. Sk, J.-M. Lee, A. Fisher, X. Wang and K. H. Lim, *Catal. Today*, 2014, **233**, 169-180.

146.   Y. Hori, K. Kikuchi and S. Suzuki, *Chem. Lett.*, 1985, 1695-1698.

147.   Y. Hori, K. Kikuchi, A. Murata and S. Suzuki, *Chem. Lett.*, 1986, 897-898.

148.   Y. Hori, A. Murata, R. Takahashi and S. Suzuki, *J. Chem. Soc., Chem. Commun.*, 1988, 17-19.

149.   Y. Hori, A. Murata and R. Takahashi, *J. Chem. Soc., Faraday Trans.*, 1989, **85**, 2309-2326.

150.   A. A. Peterson and J. K. Norskov, *J. Phys. Chem. Lett.*, 2012, **3**, 251-258.

151.   A. A. Peterson, F. Abild-Pedersen, F. Studt, J. Rossmeisl and J. K. Norskov, *Energy Environ. Sci.*, 2010, **3**, 1311-1315.

152.   P. Li, H. Jing, J. Xu, C. Wu, H. Peng, J. Lu and F. Lu, *Nanoscale*, 2014, **6**, 11380-11386.

153.   G. R. Fulmer, A. J. M. Miller, N. H. Sherden, H. E. Gottlieb, A. Nudelman, B. M. Stoltz, J. E. Bercaw and K. I. Goldberg, *Organometallics*, 2010, **29**, 2176-2179.

154.   H. Shibata, J. A. Moulijn and G. Mul, *Catal. Lett.*, 2008, **123**, 186-192.

155.   I. Ali, N. Ullah and S. Omanovic, *Int. J. Electrochem. Sci.*, 2014, **9**, 7198-7205.

156.   Y. Hori, A. Murata and R. Takahashi, *J. Phys. Chem. B.*, 1997, **101**, 7075-7081.

157.   S. Back, H. Kim and Y. Jung, *ACS Catal.* , 2015, **5**, 965-971.

158.   W. J. Durand, A. A. Peterson, F. Studt and F. Abild-Pedersen, *Surf. Sci.*, 2011, **605**, 1354-1359.

159.   E. Reisner, J. C. Fontecilla-Camps and F. A. Armstrong, *Chem. Commun.*, 2009, 550-552.